

# UC Santa Barbara

## UC Santa Barbara Electronic Theses and Dissertations

### Title

Testing the WIMP hypothesis with the LUX dark matter detector

### Permalink

<https://escholarship.org/uc/item/1xw3r0nq>

### Author

Nehrkorn, Curt

### Publication Date

2017

Peer reviewed|Thesis/dissertation

UNIVERSITY of CALIFORNIA  
Santa Barbara

**Testing the WIMP hypothesis with the LUX dark matter detector**

A dissertation submitted in partial satisfaction of the  
requirements for the degree of

Doctor of Philosophy

in

Physics

by

Curt Nehr Korn

Committee in charge:

Professor Harry Nelson, Chair  
Professor Jeffrey Richman  
Professor Mark Srednicki

January 2018

The dissertation of Curt Nehr Korn is approved:

---

Professor Jeffrey Richman

---

Professor Mark Srednicki

---

Professor Harry Nelson, Chair

December 2017

Copyright © 2018  
by Curt Nehr Korn

## Acknowledgements

Without the support and camaraderie of the many people I'll attempt to recognize here, this work would have been not only impossible, but no fun at all. So, here goes:

Harry Nelson, my research advisor, is someone I often find myself trying to emulate, both as a scientist and as a person. He is as tireless a champion of his students and colleagues as he is a promoter of physics and the joys of fundamental research. I have learned so much from Harry, and I am so grateful.

I thank my committee-members Jeffrey Richman and Mark Srednicki for their time and their feedback on this dissertation. Both have also taught me in their excellent graduate courses—Jeff for two quarters of stimulating particle physics, Mark for two quarters of Jackson-fueled fun. I am honored to count them among my advisors.

Through the inevitable ups and downs of graduate school, I am fortunate to have had the supportive friendship of fellow UCSB students. In no particular order, and with apologies to anyone accidentally omitted: Teddy, Netta, Stacy, Ben, Kim, Seth, David, Zach, Ruwan, Shankari, Christina, Jessica, Carol—thank you for sharing with me the many phases of grad school, from problem sets to dinner parties, from frisbee games (directly) to urgent care visits, from trivia nights to choral concerts.

At UCSB, I had the great privilege of working alongside Harry and a crack team of dark matter hunters. Mike Witherell and Carmen Carmona are now continuing the search elsewhere, but I am grateful for all that I've learned from them. I thank Dean White and Suzanne Kyre for their invaluable expertise and patience (and Dean again for his company in the wintry northern reaches of Minnesota . . . those tonnes of lead bricks weren't about to lift themselves!). I thank Melih Solmaz for being a reliable research and conversation partner. I thank Sally "Sunny" Shaw, the newest UCSB recruit but a LUX veteran, for the unflagging dedication and competence she brings to the team. Finally, both in South Dakota and at UCSB, Scott Haselschwardt has been a pillar of good sense and productivity. I have benefited from his stabilizing influence and keen insight in more instances than can be listed here, but especially in the development of the Run4 likelihood models and our many struggles to keep LUX running.

Working as part of the LUX collaboration has spoiled me with even more colleagues, mentors, and friends. Onsite in Lead, the many months spent shepherding the detector through times of both calm and rebellion were made immeasurably brighter by Alex L., Mongkol, Rachel, Carlos, Simon, Lea, Maria Francesca, Brian L., Jeremy, James M., Sally, Cham, Tomasz, Elizabeth, Eryk, Dev, Nicole, Jon, Attila, Richard, Kim, Alex M., Vladimir, Rick, Alex B., Wei, Christina, Samuel, Dongqing, Tom, Dan A., Matthew, and so many others. At SURF, Robyn, Oren, and Dave T. were a constant source of support and good cheer. Doug, Mark, and Markus—it's difficult to imagine South Dakota without you.

Coaxing a result out of the Run4 dataset required the manic dedication of a number of LUXers; thank you Evan, Scotts, Aaron, Lucie, Elizabeth, Richard, Wing, Kim, and Jeremy for contributing your gifts to this endeavor. Additionally, I acknowledge Henrique for his enormously helpful input to the SD paper-writing effort. I thank Mani, Mike

Woods, Surge, Brian, James, Aaron, and Jacob for welcoming me into their LUX group at UC Davis; likewise, I thank Evan, Scott, Elizabeth, Kate, Lucie, Simon, Daniel, Kevin O., Attila, Dan, Kevin L., and Mike Witherell for making me feel at home at LBL.

My family has loved and supported me through thesis-writing and my whole life. Thank you Mel, Mama and Papa, and Grandpa and Renee for everything, and in particular for instilling in me a passion for learning, teaching, and teamwork. Grace, thank you for counseling me through frustrations and cheering me through successes, for sharing your statistical wisdom, for visiting me in the dead of South Dakotan winter, and for sitting through  $\sim 10^{45}$  breathless retellings of the dark matter story. You can add this one to the list.

# Curriculum Vitæ

Curt Nehr Korn

## Education

- 2017            Ph.D. in Physics, University of California, Santa Barbara
- 2011            A.B. in Physics, Harvard University, Cambridge, MA

## Research Experience

- 2012–17        Graduate student researcher, UCSB
- *Advisor:* Harry Nelson
  - Dark matter searches with the LUX experiment
- 2009–11        Undergraduate researcher, Harvard University
- *Advisor:* Masahiro Morii
  - Particle physics studies with the ATLAS detector

## Teaching Experience

- 2011–12        Teaching Assistant, UCSB Physics Dept.
- 2008–11        Tutor, Recent Immigrant Term-time Enrichment, Harvard

## Selected Publications

“Limits on spin-dependent WIMP-nucleon cross section obtained from the complete LUX exposure,” D. S. Akerib et al. (LUX Collaboration), *Phys. Rev. Lett.* 118, 251302 (2017), arXiv:1705.03380 [astro-ph.CO].

“Results from a search for dark matter in the complete LUX exposure,” D. S. Akerib et al. (LUX Collaboration), *Phys. Rev. Lett.* 118, 021303 (2017), arXiv:1608.07648 [astro-ph.CO].

“Improved Limits on Scattering of Weakly Interacting Massive Particles from Reanalysis of 2013 LUX Data,” D. S. Akerib et al. (LUX Collaboration), *Phys. Rev. Lett.* 116, 161301 (2016), arXiv:1512.03506 [astro-ph.CO].

# Abstract

## Testing the WIMP hypothesis with the LUX dark matter detector

by

Curt Nehrorn

According to current estimates, the dark matter (DM) in our universe outweighs standard baryonic matter by a factor of five. Galaxies, including the Milky Way, are enveloped in dark halos responsible for their past formation and their present rotational dynamics. Despite the progress made by astrophysicists in identifying DM's gravitational influence, its composition is unknown. Uncovering the particle nature of DM is therefore one of the main projects in fundamental physics. Experiments such as the Large Underground Xenon (LUX) seek to directly observe DM particles in the galactic halo as they collide with nuclei in target materials. LUX was operated at the Sanford Underground Research Facility (SURF) in Lead, South Dakota from April 2013 to May 2016. Though no evidence for DM events was found, the collected data allowed world-leading constraints to be placed on the interaction rate between DM particles and nucleons. Here we explore the WIMP (Weakly Interacting Massive Particle) hypothesis, and go through the signal models relevant to direct detection experiments like LUX. We describe the design and operation of the LUX detector, its calibration, as well as expected sources of background events and techniques employed to mitigate them. Data analysis and the implementation

of models used in the profile likelihood ratio (PLR) procedure for setting frequentist confidence intervals are also discussed in detail. Finally, LUX limits on spin-dependent WIMP-nucleon scattering are given special attention.

# Contents

<b>1</b>	<b>Introduction</b>	<b>1</b>
1.1	Evidence for dark matter . . . . .	2
1.1.1	Galactic rotation curves . . . . .	4
1.1.2	Bullet Cluster and other hints . . . . .	7
1.1.3	$\Lambda$ CDM . . . . .	8
1.2	Candidates . . . . .	14
1.2.1	WIMPs . . . . .	15
1.2.2	Non-WIMP candidates . . . . .	18
<b>2</b>	<b>Detection of dark matter</b>	<b>20</b>
2.1	Detection schemes . . . . .	21
2.1.1	A note on the status of the field . . . . .	23
2.2	Principles of direct detection . . . . .	24
2.2.1	WIMP-nucleus scattering . . . . .	24
2.2.2	Kinematics . . . . .	25
2.2.3	WIMP event rates in detectors . . . . .	26
2.2.4	Standard Halo Model . . . . .	30
2.2.5	Form factors . . . . .	37
2.2.6	Particle interactions . . . . .	40
<b>3</b>	<b>The LUX experiment</b>	<b>48</b>
3.1	Time projection chambers . . . . .	48
3.2	Liquid xenon physics . . . . .	52
3.3	The LUX detector . . . . .	56
3.3.1	Design and operation . . . . .	56
3.3.2	Electronics and data acquisition . . . . .	62
3.3.3	Data processing framework . . . . .	65
3.4	Calibrations . . . . .	71
3.4.1	Krypton-83m . . . . .	71
3.4.2	Tritium . . . . .	73
3.4.3	Deuterium-deuterium neutron beam . . . . .	74
3.5	Backgrounds . . . . .	77

<b>4</b>	<b>LUX muon veto</b>	<b>81</b>
4.1	Cosmic ray muons . . . . .	82
4.1.1	Muon-induced neutrons . . . . .	82
4.1.2	Cherenkov Radiation . . . . .	83
4.2	LUX muon veto system . . . . .	85
4.2.1	Water tank and purification system . . . . .	85
4.2.2	PMTs . . . . .	87
4.2.3	Electronics and data acquisition . . . . .	87
4.2.4	Commissioning and operation . . . . .	90
4.2.5	Preliminary analysis . . . . .	93
<b>5</b>	<b>LUX Results</b>	<b>96</b>
5.1	LUX WIMP search timeline . . . . .	97
5.2	WS2013 . . . . .	99
5.2.1	Data quality . . . . .	101
5.2.2	Event selection . . . . .	103
5.2.3	NR model and efficiency . . . . .	105
5.2.4	Limits . . . . .	108
5.3	WS2014–2016 . . . . .	110
5.3.1	Electric drift field . . . . .	112
5.3.2	Position reconstruction implications . . . . .	114
5.3.3	Addressing field variation effects on electron-ion recombination . . . . .	119
5.3.4	Additional selection cuts . . . . .	124
5.3.5	Blinding scheme . . . . .	124
5.3.6	Limits . . . . .	126
<b>6</b>	<b>Profile Likelihood Statistics</b>	<b>129</b>
6.1	Introduction . . . . .	129
6.1.1	Frequentist and Bayesian intervals . . . . .	130
6.1.2	Profile likelihood ratio test statistic . . . . .	134
6.1.3	Applying the PLR to LUX . . . . .	140
6.2	LUX WS2013 Likelihood . . . . .	145
6.3	LUX WS2014–16 Likelihood . . . . .	152
6.4	Combined Analysis . . . . .	156
6.5	Review of LUX PDFs . . . . .	161
6.5.1	WS2013 . . . . .	161
6.5.2	WS2014–16 . . . . .	162
<b>7</b>	<b>Limits on spin-dependent WIMP scattering from full LUX dataset</b>	<b>174</b>
7.1	Introduction . . . . .	175
7.2	The LUX detector and WS2014–16 run . . . . .	175
7.3	The Dataset and Selection . . . . .	178
7.4	Signal model construction . . . . .	180

7.4.1	Spin-dependent coupling between WIMPs and Xe nuclei . . . . .	180
7.4.2	Nuclear recoil spectra . . . . .	185
7.5	Statistical Analysis . . . . .	186
7.6	Results . . . . .	188
7.6.1	Ramifications for particle physics models . . . . .	197
7.7	Conclusion . . . . .	207
<b>A</b>	<b>Annual velocity modulation</b>	<b>208</b>
<b>B</b>	<b>Cut-and-count limits with likelihood ratios</b>	<b>212</b>
	<b>Bibliography</b>	<b>219</b>

# List of Figures

1.1	Overlaid rotation curves from 21 Sc galaxies, presented by Rubin, Ford, and Thonnard in their 1980 review paper [1]. Despite differences in their size and luminosity, the galaxies all feature the same flatness in their rotation curves at high radii, suggesting the presence of a dark matter halo.	4
1.2	Rotation curve of a dwarf spiral galaxy from [2], a favorite of dark matter review papers (e.g. Refs. [3, 4]). The solid curve shows the fit of a dark matter halo model to the data. Contributions to the total curve from individual components of the galactic model are represented by dotted (gas), dashed (visible matter), and dot-dashed (dark halo) curves. . . . .	6
1.3	Bullet Cluster merger, taken from [5]. At left, Magellan images of the merger, illustrating the distribution of galaxies. At right, <i>Chandra</i> X-ray map of the intracluster plasma. Green contours show the results of the weak lensing gravitational mass reconstructions. . . . .	7
1.4	<i>Top:</i> Mollweide projection of the Planck 2013 CMB temperature map (Credit: ESA and the Planck Collaboration). <i>Bottom:</i> Angular power spectrum from [6], showing the observed $D_l^{TT} \equiv l(l+1)C_l/2\pi$ values and the curve predicted by the best-fit $\Lambda$ CDM model, with residuals in the bottom panel. . . . .	12
1.5	Comoving (i.e. adjusted for Hubble expansion) number density $Y$ of WIMPs over time $t$ , calculated from eq. 1.17 by Feng. Figure taken from Ref. [7]. The black solid curve shows time evolution for a WIMP with $\langle\sigma_A v\rangle$ that reproduces the observed relic density $\Omega_\chi$ (right axis). The contours of the colored bands are calculated using alternate values of $\langle\sigma_A v\rangle$ (altering the “correct” value by one, two, and three orders of magnitude). The dashed black curve shows the Boltzmann suppression of WIMP density in the case of thermal equilibrium. . . . .	17

2.1	Illustrative Feynman diagrams for the three approaches to DM detection, beneath images of representative experiments. At left, the collider search technique is shown with an LHC graphic (credit: CERN) and diagram with Standard Model (SM) particles inelastically scattering to produce DM particles ( $\chi$ ). At right, the Feynman diagram is flipped, and DM self-annihilates to produce SM particles, conceivably visible to indirect detection observatories like the Fermi LAT (image credit: NASA). Finally, shown in the center, an image of LUX represents the field of direct detection, schematically illustrated by a Feynman diagram obtained by rotating the others $90^\circ$ , wherein a DM particle scatters against a SM particle (image credit: Matt Kapust, South Dakota Science and Technology Authority). . . . .	22
2.2	Minimum WIMP velocities $v_{\min}$ required to produce nuclear recoils $E_R$ for various WIMP masses and target materials. . . . .	28
2.3	WIMP speed distributions in the rest frame of the halo (black curve) and in the rest frame of the Earth (green). For the solid green curve, the annually averaged Earth velocity is used. Distributions at the time of the Earth's minimum and maximum relative speeds are shown as green dashed and green dotted curves, respectively. For simplicity, the escape velocity truncation has not been included in these calculations. The region beyond the standard $v_{\text{esc}} = 544$ km/s value is indicated by the shaded red area under the (halo-frame) $f(v)$ curve, which only accounts for less than 0.7% of the total probability. The loss of this velocity tail only becomes significant for detectors where energy thresholds require $v_{\min}$ near $v_{\text{esc}}$ . See Fig. 2 of Ref. [8] for a demonstration of how the uncertainty on $v_{\text{esc}}$ affects the sensitivity of various detectors. . . . .	35
2.4	SHM mean inverse WIMP speeds for various WIMP masses and target materials, using the parameters indicated in Table 2.1, and a time-averaged $\langle v_{\text{obs}}(t) \rangle = 230$ km/s. If we were to ignore the form factor in eq. 2.19, this spectrum would determine the shape of the differential rate. . . . .	36
2.5	Nuclear form factors for various detector target isotopes, using the Helm charge density model. . . . .	39
2.6	Differential event rate for SI scattering, normalized to WIMP-nucleon cross section $\sigma_N^{\text{SI}} = 1$ zb. A wide range is used on the axes showing both extremes of the spectra, such that the effects of the form factor bounces can be seen in the heavier nuclei (for higher mass WIMPs). . . . .	44
2.7	Integrated event rate for SI scattering, normalized to WIMP-nucleon cross section $\sigma_N^{\text{SI}} = 1$ zb. The curves show the total number of expected events in a year-long exposure of a 1000 kg detector, integrating the spectrum above $E_R$ . . . . .	45

3.1	Cartoon of the TPC detection principle. Particle collisions produce scintillation and ionization, measured as S1 (prompt photons) and S2 (electroluminescence) PMT signals, respectively. The shaded blue region represents the LXe, with GXe situated above. The striped circles are the cathode and anode high voltage grids, which generate the electric drift field. The LXe within this field is called the “active volume.” PMTs are arranged in two arrays, one beneath the active volume (in the LXe), and one above (in the GXe). . . . .	50
3.2	Cross-sectional drawing of the LUX cryostats. Taken from Ref. [9]. . . .	57
3.3	Drawing of the LUX detector internals, with critical components labeled. Taken from Ref. [9]. . . . .	60
3.4	Flowchart depicting the signal path, starting at the LUX PMTs and traversing the data acquisition system. Taken from Ref. [10]. . . . .	62
3.5	Example of a low-energy event ( $\sim 1.5$ keV <sub>ee</sub> ) as seen in the raw datas. Each POD channel corresponds to a single PMT. Taken from Ref. [10]. .	63
3.6	Schematic of the LUX data processing framework. Taken from Ref. [11].	65
3.7	Illustration of position reconstruction in LUX. Panels a) and b) show the reconstructed positions of events from calibration data, obtained from an iterative fit, colored according to the fraction of S2 pulse area appearing in the PMT indicated with an “X”. Panels c) and d) show the corresponding light response functions used in the reconstruction algorithm. Taken from Ref. [12]. . . . .	67
3.8	At left: reconstructed $(x, y)$ positions of uniformly distributed calibration data. The stripes of high event density are the result of gate grid wires concentrating electron trajectories into tight bands, an effect shown at right. Taken from Ref. [12]. . . . .	68
3.9	At left: relative variation in S1 and S2 pulse areas as a function of position, obtained from the monoenergetic $^{83\text{m}}\text{Kr}$ calibration data. At right: effect of applying pulse area corrections to raw data. The pulse area distributions of uncorrected data are shown as blue histograms; areas corrected for $z$ -dependent variation only are shown in red; areas corrected for $z$ and $(x, y)$ variation are shown in black. Taken from Ref. [13]. . . . .	72
3.10	At left: scatter plot of $^3\text{H}$ calibration data, using fitted values of $g_1$ and $g_2$ to convert from $S1$ to $n_\gamma$ and from $S2$ to $n_e$ , respectively. Contours (lines, in this case) of deposited energy are drawn, according to eq. 3.9. At right: the same data, collected into bins of energy, and compared against the theoretical $^3\text{H}$ beta spectrum. The fall-off at low energy shows the detection threshold, driven by the S1 detection efficiency. Taken from Ref. [14]. . . . .	73

3.11	At left: ER band from the $^3\text{H}$ data, drawn in the traditional discrimination space of $S1$ vs. $\log_{10}(S2/S1)$ . The scatter plot shows the calibration data, and the solid black line shows a fit to the Gaussian mean of $\log_{10}(S2/S1)$ in each $S1$ bin (solid black dots). The dashed black lines show the 10% and 90% ER band contours. Analogous quantities are shown in red for the NR band, as measured by the deuterium-deuterium neutron calibration. At right: the underlying quanta responsible for the shape of the ER band (see Sec. 3.2). Taken from Ref. [14]. . . . .	74
3.12	At left: spatial distribution of single-scatter events from the DD calibration data, where the $y'$ axis is parallel to the direction of the neutron beam. Events within the indicated box are selected to reduce contamination from neutrons that have been scattered outside the detector (and thus do not have the 2.45 MeV energy of those in the collimated beam). At right: the nuclear recoil band, indicated by the black 10%, mean, and 90% lines calculated from the DD data (comprising the scatter plot). The contours in red come from simulated data using the model parameters tuned by the calibration analysis. Taken from Ref. [15]. . . . .	75
3.13	Spatial distribution of low-energy background events, predicted by the model (left) and observed in the first LUX exposure (right). Binning in squared radius ensures equal projected volume of the bins. The unit DRU <sub>ee</sub> is the differential rate unit, using the electron equivalent energy scale: events $\text{kg}^{-1} \text{day}^{-1} \text{keV}_{\text{ee}}^{-1}$ . Taken from Ref. [16]. . . . .	79
4.1	Spectrum of Cherenkov light in water from a 300 GeV muon. The UV range of PMT sensitivity is shaded in orange. . . . .	84
4.2	At left: wide-angle view of the LUX water tank interior. Three of the veto system vertical PMT strings are visible. Note also the gray, horizontal acrylic tube, which was raised during DD calibrations to allow neutrons to reach the TPC (see Sec. 3.4.3). At right: close-up of a Hamamatsu R7081 10" PMT, mounted at the lowest level of one of the four vertical strings. . . . .	86
4.3	Schematic of the veto system electronics. . . . .	88
4.4	Annotated photos of the veto system electronics rack. . . . .	88
4.5	Annotated photo of the electronics responsible for the hardware trigger hold-off for the veto system. . . . .	90
4.6	Single photoelectron spectra of water tank PMT (South 3) at three different bias voltages. . . . .	91
4.7	At left: replacement high voltage supplies for the veto PMTs. At right: the bottom West PMT makes a break for it, as captured by a submersible camera. . . . .	92
4.8	At left: PMT quantum efficiency, taken from the Hamamatsu data sheet. A parameterization of this curve was implemented in the GEANT4 model. At right, a plot of simulated quantum efficiency, shown as a validation of the implementation. . . . .	93

4.9	Top: Visualization of a simulated photon (green) reflecting off the Tyvek-lined tank walls. The veto PMT photocathodes are shown as pink hemispheres. At bottom right: experimentally measured reflectivity of different Tyvek products, obtained from the Daya Bay experiment. A parameterization of the green “thin tyvek” curve was implemented in the GEANT4 model. At bottom left, a plot of simulated reflectivity, shown as a validation of the implementation. . . . .	94
4.10	Waveforms of the LUX TPC and veto PMT channels in a coincident muon event, shown respectively as gray-scale and color curves. Accounting for a trigger time offset, the events are simultaneous. The mess of LXe PMT waveforms shows a massive S1 pulse, followed immediately by a sprawling wake of extracted electrons; meanwhile the water PMTs exhibit a crisp, high-coincidence level Cherenkov signal. . . . .	95
5.1	2D histogram of all $\sim 93$ million WS2013 triggers, plotted in a simple parameter space spanned by the total pulse area and total pulse length of the event. Pulse length is measured in ADC samples ( $= 10 \text{ ns} = .01 \mu\text{s}$ ). The color scale is omitted, but measures logarithmic event density (red is high, blue low). See text for descriptions of outlined regions. . . . .	100
5.2	For each bin in the 2D parameter space of Fig. 5.1, an average quantity is calculated. At left: the total pulse area of the prior event. At right: the number of S2 pulses per event (including single electrons) identified by the pulse classifying algorithm. . . . .	100
5.3	Schematic of the NR simulations validating the DD results. . . . .	105
5.4	Signal yields and detection efficiency for NRs, as a function of recoil energy (taken from Ref. [17]). In all three panels, the simulation results are shown as a solid black curve (best-fit Lindhard), green and yellow bands ( $\pm 1\sigma$ and $\pm 2\sigma$ Lindhard) and dashed curve (Bezrukov). In the top two panels, the DD measurements of charge and light yield are shown as black circular markers with error bars—these measurements determine the model parameters used in the simulations. In the bottom panel, the NR detection efficiency is calculated as described in the main text. The other curves show the efficiencies of individual selection criteria (for the nominal Lindhard model): in red, S2 detection efficiency; in green, S1 detection efficiency (including the two-PMT coincidence requirement); in blue, combined S1 and S2 detection efficiency. The final efficiency curves account for the additional thresholds on $S1$ and $S2_{\text{raw}}$ . In the WIMP signal models, LUX is assumed to be 0% efficient at detecting signals below $1.1 \text{ keV}_{\text{nr}}$ , the lowest energy probed by the DD light yield measurement—this region is therefore grayed out in the bottom panel. . . . .	107

5.5	Top: final data from the WS2013 analysis, plotted in $S1-\log_{10}S2$ space. Data points with gray markers fall at the edge of the fiducial volume ( $r > 18$ cm), whereas solid black points are located more radially inward. The blue lines indicate the mean (solid), 10th and 90th percentile (dashed) contours of the ER band. The red contours show the same quantities for the NR model. Grey curves show the combined energy scale. Bottom: 90% confidence level upper limits on SI WIMP-nucleon cross section. The black curve shows the WS2013 result (expected sensitivity bands in green and yellow), whereas the gray curve shows the result from the first analysis [18]. Both figures taken from Ref. [17], which also contains the references for the other experimental limits shown. . . . .	109
5.6	Edges of the LUX TPC active volume in the S2 coordinate system, as deduced from $^{83\text{m}}\text{Kr}$ calibration data. Taken from Ref. [19]. Recall from Sec. 3.3.3 that reconstructed $(x, y)$ position measures the point of electron emission at the liquid surface. . . . .	112
5.7	Field lines and equipotential contours calculated from a 2D electrostatic model of the LUX detector, for WS2013 (left) and WS2014–16 (right). Taken from Ref. [19]. . . . .	113
5.8	An example of field map data: the regular grid of points in real space (at left) is transformed into S2 space (at right), with field strength values indicated. Taken from Ref. [19]. . . . .	116
5.9	Demonstration of the C3PO field map interpolation algorithm. At left, $r^2-z$ (top) and $x-y$ (bottom) histograms of the uniformly distributed positions fed as inputs into the program. At right, the calculated S2-space position distributions are shown, based on an August, 2016 field map. . . . .	117
5.10	The electric field strength, calculated for each point sampled in Fig. 5.9, is plotted against the true $z$ position, projecting all values of radius and azimuth. The scale of the variation in $z$ large, with the breadth of the correlation showing subdominant dependence of $E_{\text{drift}}$ on $(x, y)$ position. . . . .	118
5.11	Time evolution of the modeled electric charge density and field. At left, the average charge density on the PTFE walls, with an exponential fit shown in red. The indicated discontinuity marks the time of a test where the cathode grid was grounded. At right, the drift field strength in each $z$ -slice over time. Both figures taken from Ref. [19]. . . . .	122
5.12	ER (blue) and NR (red) bands, shown as the mean and 10th/90th percentile $S2$ values for a given $S1$ , calculated from NEST models of each WS2014–16 exposure segment. The calibration data ( $^3\text{H}$ for ER, DD for NR) is shown as histograms in each panel. Note that the NEST fitting procedure was performed with ER calibration data only; the resulting parameters were used in the NR model, and found to be in good agreement with the DD calibration data (of which multiple $z$ -positions were available only in the first and final DD datasets). . . . .	123

5.13	Final data from the WS2014–16 analysis, plotted in $S1$ – $\log_{10}S2$ space. Data points with hollow markers fall at the edge of the fiducial volume ( $r_{S2,\text{fid.}} - r_{S2} < 1$ cm), whereas solid black points are located more radially inward. The blue lines indicate the mean (solid), 10th and 90th percentile (dashed) contours of the ER band. The red contours show the same quantities for the NR model. Green curves show the combined energy scale. Multiple instances of the dashed curves indicate the deviation of the ER and NR models over the 16 exposure bins. The salt has been removed from this data, as have pathological events discovered after the unblinding. Taken from Ref. [20]. . . . .	127
5.14	Upper limits on SI WIMP-nucleon cross section, derived from the WS2014–16 and WS2013 datasets (thick black line, with expected sensitivity shown as green and yellow bands). The kink at $\sim 40$ GeV arises from the power constraint applied at $-1\sigma$ . The WS2014–16 result (before combination with WS2013) is also shown, as a gray line. Note that WS2014–16 outperforms the earlier result for higher masses (due to the greater exposure), but because of background events at small $S1$ , WS2014–16 is less constraining of light WIMPs than WS2013. The grey shaded areas show regions of favored CMSSM parameter space [21]. Taken from Ref. [20], which contains references to the other experimental results shown. . . . .	128
6.1	At left: illustration of a confidence belt, taken from Ref. [22]. The interceptions of the $x = x_0$ line with the edges of the belt determine the confidence interval bounds. At right: 3D visualization of a confidence belt, taken from Ref. [23]. Note that Cranmer uses $\theta$ instead of $\mu$ to represent the model parameter, so that the green band in the $x$ – $\theta$ plane represents the confidence belt (as shown in the left plot). Blue regions under the PDF curves indicate the integrated areas that equal $\alpha$ , the bounds of which determine the edges of the belt. . . . .	133
6.2	Illustration of a test statistic PDF. For the PLR test statistic, higher $q$ indicates greater disagreement between the data and test hypothesis. . .	138
6.3	Inverted hypothesis testing for confidence interval construction. In the left panel, calculations of $p(\sigma)$ are performed as in Fig. 6.2, at multiple values of $\sigma$ . This information is condensed in the $p$ value curve in the right panel, from which $\sigma_{\text{UL}}$ may be found by solving $p(\sigma) = 1 - \alpha$ . In addition to the $p$ value curve obtained from the observed dataset, a blue curve is shown representing the median $p(\sigma)$ values of an ensemble of datasets drawn from a fixed alternate hypothesis. For example, when setting an upper limit, this alternate hypothesis would be that the signal cross section is zero. . .	140

6.4	$p$ -value curve for 100 GeV WIMP, neutron-only spin-dependent coupling. The solid black line shows $p_{\text{obs}}$ as a function of the POI (here abbreviated “xsec”). The dashed black line shows $p$ for a median dataset drawn from the background-only model, and the green and yellow bands show the $\pm 1$ - and $\pm 2$ - s.d. quantiles. . . . .	141
6.5	$p(\sigma)$ values for a two-sided PLR TS. The best-fit $\hat{\sigma}$ falls near the peak of the curve. . . . .	142
6.6	WS2014–16 dependence of $n_s$ on $k_{\text{Lind.}}$ , shown for two WIMP masses. This introduces uncertainty on the WIMP detection rate at a given signal cross section in the likelihood model. Note that the small uncertainty on $k_{\text{Lind.}}$ (see Tab. 6.2) means that the NP is effectively constrained to within $\sim 4\%$ of the nominal value. Even for small WIMP masses, where the effect is most prominent, this translates to only $\sim 20\%$ uncertainty in the detection rate. . . . .	149
6.7	Projection of the background onto the $S1$ axis (blue), with the WS2014–16 data shown in black. . . . .	157
6.8	Projection of the background model onto the $\log_{10} S2$ axis (blue), with the WS2014–16 data shown in black. . . . .	157
6.9	Projection of the background model onto the $S1$ – $\log_{10} S2$ plane (blue), with the WS2014–16 data shown in black. . . . .	158
6.10	Projection of the background model onto the $r_{S2}$ axis (blue), with the WS2014–16 data shown in black. . . . .	158
6.11	Projection of the background model onto the $z_{S2}$ axis (blue), with the WS2014–16 data shown in black. . . . .	159
6.12	Projection of the background model onto the $\phi_{S2}$ axis (blue), with the WS2014–16 data shown in black. . . . .	159
6.13	Projection of the background model onto the date bin axis (blue), with the WS2014–16 data shown in black. Note that the date bins do not each have equal live time: date bins 1 and 2 each contain $\sim 47$ livedays, whereas date bins 3 and 4 contain double and triple that exposure time, respectively. The background rate is thus roughly constant. . . . .	160
6.14	Uniform spatial distribution (in real space) converted into S2 coordinates: $f_{\text{unif.}}^t(\mathbf{r}_{S2})$ , radius vs. drift time in slices of azimuth and date. Describes WIMP, $^8\text{B}$ , $\beta$ , and accidental coincidence populations. . . . .	163
6.15	Low- $z$ Compton scatters: $f_{\gamma, \text{bottom}}^t(\mathbf{r}_{S2})$ , radius vs. drift time in slices of azimuth and date. . . . .	163
6.16	Other Compton scatters: $f_{\gamma, \text{rest}}^t(\mathbf{r}_{S2})$ , radius vs. drift time in slices of azimuth and date. . . . .	164
6.17	ER distribution $f_{\text{ER}}^{t,z}(S1, \log_{10} S2)$ for Comptons and betas. Note that the band is pushed up at lower drift times (higher $z$ ), where the drift field is stronger. . . . .	164
6.18	$f_{\text{acc.}}(S1, \log_{10} S2)$ , which is taken to be independent of drift and date. . .	165

6.19	NR distribution $f_{8\text{B}}^{t,z}(S1, \log_{10} S2)$ for $^8\text{B}$ neutrinos. Variation with electric field is expected to be small. . . . .	165
6.20	NR distribution $f_{\chi}^{t,z}(S1, \log_{10} S2)$ for 5 GeV WIMPs. Plots normalized to expected events per bin per zb per day per kg. . . . .	166
6.21	NR distribution $f_{\chi}^{t,z}(S1, \log_{10} S2)$ for 7 GeV WIMPs. . . . .	166
6.22	NR distribution $f_{\chi}^{t,z}(S1, \log_{10} S2)$ for 10 GeV WIMPs. . . . .	167
6.23	NR distribution $f_{\chi}^{t,z}(S1, \log_{10} S2)$ for 12 GeV WIMPs. . . . .	167
6.24	NR distribution $f_{\chi}^{t,z}(S1, \log_{10} S2)$ for 14 GeV WIMPs. . . . .	168
6.25	NR distribution $f_{\chi}^{t,z}(S1, \log_{10} S2)$ for 17 GeV WIMPs. . . . .	168
6.26	NR distribution $f_{\chi}^{t,z}(S1, \log_{10} S2)$ for 21 GeV WIMPs. . . . .	169
6.27	NR distribution $f_{\chi}^{t,z}(S1, \log_{10} S2)$ for 33 GeV WIMPs. . . . .	169
6.28	NR distribution $f_{\chi}^{t,z}(S1, \log_{10} S2)$ for 50 GeV WIMPs. . . . .	170
6.29	NR distribution $f_{\chi}^{t,z}(S1, \log_{10} S2)$ for 100 GeV WIMPs. . . . .	170
6.30	NR distribution $f_{\chi}^{t,z}(S1, \log_{10} S2)$ for 200 GeV WIMPs. At higher WIMP masses, the spectrum is essentially the same. . . . .	171
6.31	Wall model: projection of $f_{\text{wall}}^{t=1}(\mathbf{r}_{S2}, S1, \log_{10} S2)$ onto $S1\text{-}\log_{10} S2$ plane. . . . .	171
6.32	Wall model: projection of $f_{\text{wall}}^{t=1}(\mathbf{r}_{S2}, S1, \log_{10} S2)$ onto $R\text{-}\log_{10} S2$ plane, where $R$ is a crude correction of radius that approximates true position. This shows how smaller S2 area leads to greater radial uncertainty (and therefore greater penetration into the fiducial volume). . . . .	172
6.33	Wall model: projection of $f_{\text{wall}}^{t=1}(\mathbf{r}_{S2}, S1, \log_{10} S2)$ onto $x_{S2}\text{-}y_{S2}$ plane, in slices of drift time. Note the azimuthal asymmetry, and the shrinking of the detector at greater drift times. . . . .	173
7.1	LUX total efficiency (black), averaged over the entire exposure. NR model uncertainties are illustrated by the gray band, indicating $\pm 1\sigma$ variation. The vertical dashed line represents the analysis threshold of 1.1 keV (the lowest DD calibration point), below which we conservatively take the LUX efficiency to be zero. Sample WIMP spectra are plotted in color, with values corresponding to the right-hand y-axis. dru is the differential rate unit ( $\text{events kg}^{-1}\text{d}^{-1}\text{keV}^{-1}$ ), and the spectra have each been calculated with WIMP-nucleon cross section = 1 pb. Spectra for WIMP-proton and -neutron scattering are given by the red and blue curves, respectively, for three WIMP masses: 5 GeV $c^{-2}$ (dotted), 50 GeV $c^{-2}$ (dash-dotted), and 1000 GeV $c^{-2}$ (dashed). Structure functions from [24] are used for this calculation. . . . .	179

7.2	90% CL upper limits on WIMP-neutron (left) and WIMP-proton (right) cross section. Results from this analysis are shown in thick black (“LUX WS2013+WS2014–16”), with the range of expected sensitivity indicated by the green (1- $\sigma$ ) and yellow (2- $\sigma$ ) bands. Solid gray curves show the previously published LUX WS2013 limits [25]. Constraints from other LXe TPC experiments are also shown, including XENON100 [26] and PandaX-II [27]. In the left panel, model-dependent (axial-vector mediator with indicated couplings) LHC search results are represented by dashed lines, with CMS [28] in light blue, and ATLAS [29] in dark blue. As calculated by a new profile likelihood scan of the MSSM7 [30], favored parameter space is shown as dark (1- $\sigma$ ) and light (2- $\sigma$ ) peach regions; an earlier calculation using the MSSM-15 [31] is shown in gray, with analogous shading of confidence levels. In the right panel, the DAMA allowed region (as interpreted in [32]) is shown in pink (the analogous neutron-only region is above the bounds of the plot). Such an interpretation is in severe tension with this result, as well as the PICO-2L [33] and PICO-60 [34] constraints. Selected limits from indirect searches at neutrino observatories (Super-Kamiokande [35] and IceCube [36]) are plotted as dashed lines. . . . .	190
7.3	Fig. 7.2a, enlarged for visibility. . . . .	191
7.4	Fig. 7.2b, enlarged for visibility. . . . .	192
7.5	90% CL exclusions on coupling parameters $a_n$ and $a_p$ for 50 GeV $c^{-2}$ and 1000 GeV $c^{-2}$ WIMPs. Ellipse boundaries are colored as in Fig. 7.2: this result (thick black), LUX WS2013 (gray), PandaX-II (purple), and PICO-60 (blue). Geometrically, Eq. 7.27 describes a rotated ellipse when the sum is performed over multiple isotopes with distinct $\sigma_p^A/\sigma_n^A$ , as is the case for LXe experiments. PICO-60 considers only $^{19}\text{F}$ (for which $\langle \mathbf{S}_n \rangle \sim 0$ ), and thus sets limits only on $a_p$ . The innermost region (bounded by LUX and PICO-60) represents parameter space not in tension with experimental data. The model-dependency of the LHC results is apparent in this plane, as the CMS excluded region (shown as a green band) is restricted to the $a_n = a_p$ line (see main text for important caveat). This line is absent from the lower panel since, in this treatment, CMS is insensitive to WIMPs at the TeV mass scale. MSSM7 favored regions from the GAMBIT scan are also shown, with a red contour at the 2- $\sigma$ level for visibility. The degeneracies assumed in the MSSM7 Lagrangian lead to the tight correlation between $a_n$ and $a_p$ . This scan includes a range of possible WIMP masses (unlike the mass-specific experimental exclusions), and thus appears identically in each panel, noting the change in axis scale. Additionally, the scans include models with sub-dominant relic densities, for which experimental limits are rescaled accordingly. . . . .	193
7.6	Fig. 7.5a, enlarged for visibility. . . . .	194
7.7	Fig. 7.5b, enlarged for visibility. . . . .	195

7.8	95% CL exclusion regions in the mass-mass plane for axial vector $Z'$ mediated coupling simplified models. Shaded area bounded by the black curve shows LUX combined results (newly calculated); the red curves show CMS results from [28]; the blue curves show the PICO results [34]. For the latter two results, the solid curves comprise points taken from analogous plots in the respective publications, whereas the dashed lines are calculated from the 90% CL cross section limits according to the procedure described in the text (these are shown simply as a cross-check of the method). . . . .	201
7.9	Effect of relic density rescaling on LUX limits, taken from Ref. [37] (where $M_R$ refers to $M_{\text{med}}$ ). At left, the rescaling procedure is illustrated by showing the raw LUX 95% CL bound with fixed $\rho_\chi$ (purple), the region where the calculated $\Omega_\chi/\Omega_{\text{DM}}^{\text{obs}} > 1$ (red), and the rescaled LUX limit (orange). Near $m_\chi = 80$ GeV, all three contours overlap by construction: here, the calculated $\Omega_\chi/\Omega_{\text{DM}}^{\text{obs}} = 1$ , which matches the assumption implicit in the purple curve, so that the rescaling multiplier is unity. Elsewhere, this is not true, and the discrepancy is corrected for by the rescaling. The purple region is estimated from LUX’s first SI result [18] (since this publication predates Refs. [17, 25, 38]), and furthermore differs from Fig. 7.8 by a factor of $(1/0.25)^{2 \times 1/4} = 1/2$ due to the different values of $g_q$ assumed. Still, the constraint is very close to that shown in Fig. 7.8, and the rescaled result is thus a good approximation of what might be obtained by applying this procedure to the most recent LUX bounds. The left panel also shows the “perturbativity bound” $m_\chi < \sqrt{4\pi}M_{\text{med}}/g_\chi$ , which ensures that the $\chi Z'$ Yukawa interaction is perturbative. In the right panel, the rescaled constraint contours are shown for various choices of mediator couplings. . . . .	204
7.10	Comparison of SD WIMP-nucleon cross sections when the running of the couplings is taken into account, taken from Ref. [39]. These corrections should be applied to LHC constraints when comparing them to direct detection limits. . . . .	205
7.11	WIMP–neutron cross section limits, identical to Fig. 7.3 except for the LHC contours. The transparent CMS and ATLAS dashed curves are the same as in Fig. 7.3 (and as shown in Refs. [28] and [29], respectively). The solid dashed curves have been scaled by the correction factor shown in Fig. 7.10, following the procedure laid out in Ref. [39]. The effect is most pronounced at small cross sections since these correspond to large mediator mass. . . . .	206
A.1	Relative Earth velocity $v_{\text{obs}}(t)$ during the LUX WS2014–16 exposure. Line color indicates the relative data-taking efficiency: lighter periods show times of calibration or detector shut-down, darker periods indicate closer to 100% efficiency. . . . .	209

A.2	Efficiency plot and SD recoil spectra as in Fig. 7.1. The fainter curves have been calculated using the correct WS2014–16 value of $\langle v_{\text{obs}}(t) \rangle$ (230 km/s), and the darker curves using the WS2013 value (245 km/s). A visible change is only apparent in the 5 GeV WIMP curves, since the tail of the Maxwellian distribution is responsible for the recoil spectra at these energies. . . . .	211
B.1	$\Lambda$ as a function of $(S1, \log_{10} S2)$ , for a 50 GeV WIMP. This is the result of dividing a normalized Fig. 6.28 by a normalized Fig. 6.17 and taking the natural logarithm. (The blotchiness is only the result of smoothing a histogram with limited statistics.) Making a cut $\Lambda > \Lambda_c$ would be equivalent to making a cut in $(S1, \log_{10} S2)$ -space defined by closed regions satisfying $\Lambda > \Lambda_c$ . . . . .	213
B.2	PDFs in $\Lambda$ for background events (blue) and signal events (red), in the case of a 50 GeV WIMP. One could imagine cutting at $\Lambda > 5$ to achieve high background rejection. . . . .	214
B.3	Acceptance curve for ER background and 50 GeV WIMP. We can see that making a cut on $\Lambda$ that achieves 40% signal acceptance will eliminate $1 - 10^{-3} = 99.9\%$ of background events. . . . .	214
B.4	Signal acceptance as a function of WIMP mass, following a cut on $\Lambda$ that achieves 99.9% rejection of ER background events. Since the NR spectrum converges to a roughly constant shape as WIMP mass increases, the signal acceptance reaches a plateau. The NR and ER bands are better separated at lower energies, leading to the superior acceptance of light WIMPs for constant ER rejection. . . . .	215
B.5	In blue: a range of 90% CL upper limits on SI WIMP-nucleon cross section from an approximate cut-and-count analysis of the WS2014–16 dataset. The lower edge of the band is defined by a FC $b = 15$ expected limit, the upper edge uses $b = 1$ . In green: the $1-\sigma$ range of expected limits from the full PLR analysis. . . . .	218

# List of Tables

1.1	A sample of Planck 2015 $\Lambda$ CDM fit results, taken from [6]. Note that these parameters are not the direct output of the likelihood search, which scans over a minimal set of independent parameters. Instead, these are derived quantities, calculated from the minimal set, assumptions (e.g. $\Omega = 1$ and $w_\Lambda = -1$ ), and auxiliary measurements. . . . .	11
2.1	Astronomical velocities relevant to the calculation of WIMP event rates in Earth-based detectors. Symbols and quantities from two popular references are shown for comparison. In this work and in the LUX publications, we use the starred* values (indicated only when values are not in agreement). Vector quantities are shown in Galactic coordinates $(x, y, z) = x\hat{\mathbf{x}} + y\hat{\mathbf{y}} + z\hat{\mathbf{z}}$ , where $\hat{\mathbf{x}}$ points towards the Galactic Center, $\hat{\mathbf{y}}$ towards the direction of disk rotation, and $\hat{\mathbf{z}}$ towards the North Galactic Pole [40]. . .	33
3.1	LUX reduced quantities and associated units. . . . .	69
5.1	LUX detector parameters in WS2013 and WS2014–16. In the first row, the voltages are given in ascending order of grid height in the TPC: bottom PMT shield (B), cathode (C), gate (G, with    indicating the position of the liquid surface), anode (A), top PMT shield (T). Drift field magnitudes are listed as “nominal” values, calculated from an idealized geometry. In reality, deviations from these values arise from grid geometry effects [11] and due to charge accumulation on the PTFE reflector panels (observed only in WS2014–16 [19]). The S2 gain $g_2$ (and related quantity $\epsilon_{ee}$ ) and S1 gain $g_1$ are calculated via a “Doke plot” analysis, described in Refs. [11, 17]. Ranges are shown for WS2014–16 values to reflect their variation over the course of exposure. . . . .	98
5.2	Key quantities and features of the two WIMP search analyses. Note that the WS2014–16 fiducial mass is averaged over the exposure (since the mapping of S2 coordinates to real space coordinates was time varying, but the fiducial volume definition was fixed in S2 coordinates, the true fiducial volume changed over time as well). . . . .	111

5.3	NEST parameters for the WS2014–16 ER and NR models. Data transcribed from Ref. [41]. Where shown, error bars do not represent formal uncertainties, but rather heuristic ranges of values yielding good agreement between model and calibration data; these parameters do not enter into the profile likelihood as constrained nuisance parameters. . . . .	121
6.1	Notation used in this chapter pertaining to the statistical modeling of LUX data. . . . .	135
6.2	Nuisance parameters in the WS2013 likelihood model. Constraints are Gaussian with means and standard deviations indicated. Event counts are after cuts and analysis thresholds. The best-fit model has zero contribution from the signal PDF. In this case the signal-model parameters simply float to the central values of their constraints, and so are not listed. . . . .	146
6.3	Model parameters in the best fit to WS2014–16 data for an example $50 \text{ GeV } c^{-2}$ WIMP mass. Constraints are Gaussian with means and standard deviations indicated. Fitted event counts are after cuts and analysis thresholds. . . . .	153

# Chapter 1

## Introduction

The quest to understand dark matter offers nothing in the way of guarantees. The inscrutable substance represents one of the greatest mysteries in contemporary physics, with its composition unknown and its existence occasionally called into doubt. Furthermore, to answer the question asked by taxi drivers and state politicians alike, its detection would furnish no obvious technological boon.

Still, scientists band together in ever greater numbers, pooling their expertise, resources, and graduate students in an effort to solve the missing mass puzzle. Perhaps this is no surprise, since illuminating the dark matter would reveal secrets of the universe at both its smallest and largest scales. And although healthy scientific skepticism is certainly alive and well, the astrophysical evidence in support of the dark matter hypothesis is striking in its richness and diversity.

## 1.1 Evidence for dark matter

The first hints of dark matter were uncovered in the 1930s, notably by Oort [42] and Zwicky [43]. The latter is often credited with its discovery, having speculated that the unexpectedly high velocity dispersion observed among the galaxies of the Coma cluster could be a result of “dunkle Materie.” To explain this phenomenon, he calculated:

[...] the average density in the Coma system would have to be at least 400 times larger than that derived on the grounds of observations of luminous matter. If this would be confirmed we would get the surprising result that dark matter is present in much greater amount than luminous matter. [43]

As is noted in [44], Zwicky’s large estimate is inflated by a factor of 8, due to the value of the Hubble constant assumed in his calculations.

Zwicky invoked the virial theorem to arrive at his conclusions, which relates the time averaged total kinetic and potential energies ( $T$  and  $U$ , respectively) of a stable system. For gravitationally bound systems,

$$\langle T \rangle_\tau = -\frac{1}{2} \langle U \rangle_\tau \quad . \quad (1.1)$$

For observational purposes, it is useful to assume ergodicity and replace the time averages with ensemble averages ( $\langle \rangle_\tau \rightarrow \langle \rangle_N$ ). We can approximate the Coma cluster as a spherical gas with uniform density to obtain

$$U = -\frac{3}{5} \frac{GM^2}{R} \quad , \quad (1.2)$$

where  $G$  is the gravitational constant,  $M$  is the total mass of the cluster, and  $R$  the

radius. Making the further approximation that all  $N$  galaxies in the cluster have equal mass  $m = M/N$ , we find

$$\langle T \rangle_\tau = \frac{1}{2} \sum_i^N m_i \langle v_i^2 \rangle_\tau \quad (1.3)$$

$$= \frac{m}{2} \sum_i^N \langle v^2 \rangle_N \quad (1.4)$$

$$= \frac{M}{2} \langle v^2 \rangle_N \quad . \quad (1.5)$$

Substituting these results into eq. 1.1, we derive an expression for the total mass of the cluster in terms of velocity dispersion:

$$M = \frac{5}{3} \frac{R \langle v^2 \rangle_N}{G} \quad . \quad (1.6)$$

This is the formula used by Zwicky to arrive at the now famous conclusion: the mass predicted by the gravitational properties of the system far outweighed that deduced from the system's luminosity.

Though this line of reasoning might have been the first indication of dark matter's existence, it was not until some 40 years later that a consistent picture began to emerge, connecting the disparate observations of high mass-to-light ratios. The groundbreaking work of Vera Rubin and others investigating the rotation of galaxies was central to this endeavor.

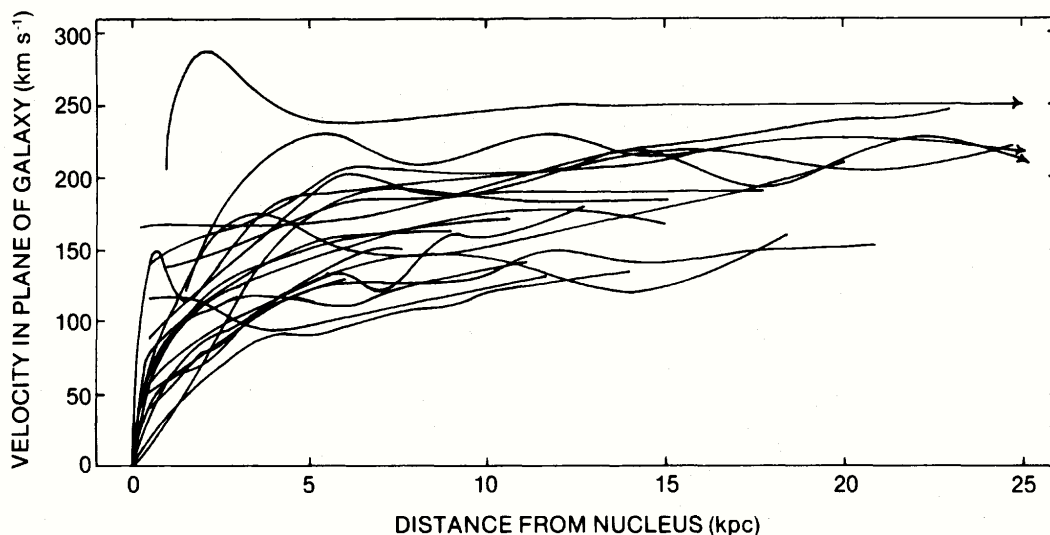


Figure 1.1: Overlaid rotation curves from 21 Sc galaxies, presented by Rubin, Ford, and Thonnard in their 1980 review paper [1]. Despite differences in their size and luminosity, the galaxies all feature the same flatness in their rotation curves at high radii, suggesting the presence of a dark matter halo.

### 1.1.1 Galactic rotation curves

Whereas Zwicky’s observations concerned the dynamics of galaxy clusters, the most famous evidence for dark matter comes from a smaller scale: the rotational motion of galaxies themselves. Rotation curves are the graphs relating the circular velocity of galactic constituents to their galactic radius (i.e. distance from the center of the galaxy), which can be notated functionally as  $v(r)$ . From Newton’s second law, we have:

$$v(r) = \sqrt{\frac{GM(r)}{r}} \quad , \quad (1.7)$$

where  $M(r)$  denotes the mass enclosed within radius  $r$ . As  $r$  increases and  $M(r)$  approaches the constant total mass of the galaxy, it follows that  $v(r)$  will fall as  $1/\sqrt{r}$ .

In practice, these curves are constructed by measuring the Doppler shift of emission

lines from gas clouds located at a range of galactic radii. In their early work, Rubin and Ford made use of a spectrograph to map the velocity distribution of H II regions in M31 [45]. Given the distribution of luminous mass in M31, they expected to observe the drop-off in the rotation curve at high radius. Instead, the curve remained flat out to their farthest measurements, implying a mass distribution at odds with the density profile suggested by luminous matter. Specifically, referring to eq. 1.7, we see that at high radius  $M(r) \propto r$  (or equivalently,  $\rho(r) \propto r^{-2}$ ). This discrepancy was borne out in subsequent studies, which found similarly flat rotation curves in a survey of many spiral galaxies (see e.g. Refs. [1, 46]). Fig. 1.1 shows a collection of 21 such rotation curves. In the discussion section of [1], Rubin *et al.* summarize:

This form for the rotation curves implies that the mass is not centrally condensed, but that significant mass is located at large  $R$ . The integral mass is increasing at least as fast as  $R$ . The mass is not converging to a limiting mass at the edge of the optical image. The conclusion is inescapable that nonluminous matter exists beyond the optical galaxy. [1]

Later surveys used the 21-cm line from neutral hydrogen to construct galactic rotation curves out to even higher radii, well beyond the optical disk. Fig. 1.2, taken from [2], is often showcased as an iconic example from this body of research. However, the original authors (Begeman *et al.*) did not see the data as being incontrovertible evidence for dark matter (hereafter “DM”); instead, they argued that their observations could be more accurately described by an alternative theory: modified Newtonian dynamics (MOND).

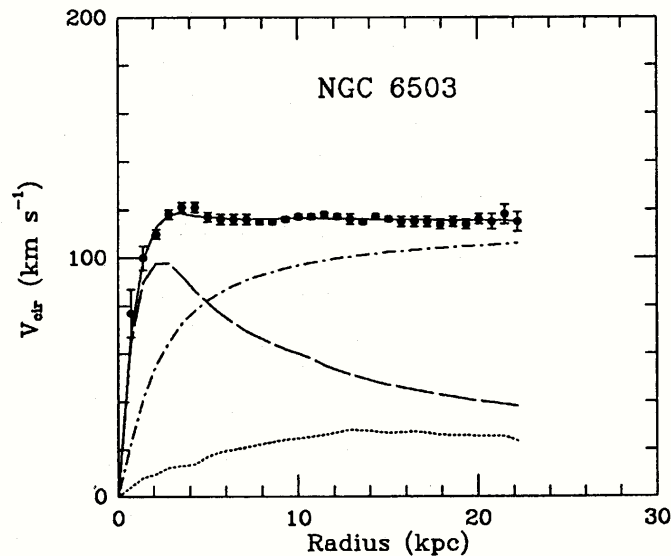


Figure 1.2: Rotation curve of a dwarf spiral galaxy from [2], a favorite of dark matter review papers (e.g. Refs. [3, 4]). The solid curve shows the fit of a dark matter halo model to the data. Contributions to the total curve from individual components of the galactic model are represented by dotted (gas), dashed (visible matter), and dot-dashed (dark halo) curves.

A full discussion of MOND is beyond the scope of this work, but the motivation for the theory warrants mention. In principle, the discrepancies between the observed luminous mass and the dynamics of galaxies can be resolved by:

- (i) Assuming the validity of Newtonian dynamics at galactic scales, and inferring the presence of invisible mass.
- (ii) Assuming that the majority of mass is luminous matter, and introducing modifications to Newtonian dynamics.

MOND theories follow the latter logical tack; the dark matter hypothesis, the former. First introduced by M. Milgrom in 1983 [47], MOND demonstrates good agreement with observed galactic dynamics (e.g. rotation curves) when tuning only one or two free model

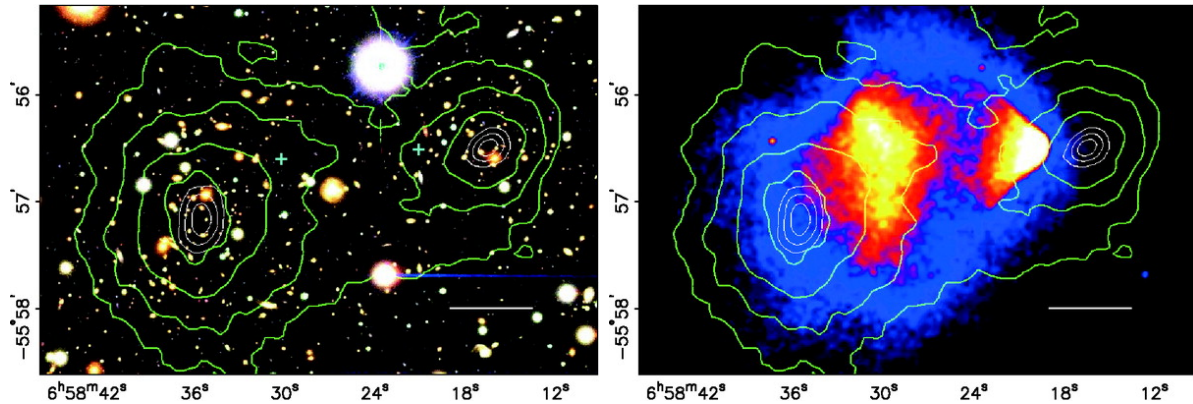


Figure 1.3: Bullet Cluster merger, taken from [5]. At left, Magellan images of the merger, illustrating the distribution of galaxies. At right, *Chandra* X-ray map of the intracluster plasma. Green contours show the results of the weak lensing gravitational mass reconstructions.

parameters [2]. However, the theory runs into problems when confronted with systems like galaxy clusters.

### 1.1.2 Bullet Cluster and other hints

The Bullet Cluster (1E 0657–558) arguably constitutes the most dramatic astrophysical phenomenon in support of the DM hypothesis, and strongly disfavors the simplest MOND formulations. This system is actually a merger: two galaxy clusters colliding in the plane of the sky. Galaxies within clusters are sufficiently sparsely distributed that they are largely unaffected by cluster mergers: they continue on their relative trajectories unscathed. The intracluster plasma, on the other hand, behaves more like a liquid, and experiences ram pressure during a cluster merger. The plasma, which is the dominant source of luminous matter in clusters, is thus separated from the galaxies during the collision. Therefore, if there is no DM, one would expect the mass distribution in the merger

to match the spatial distribution of the hot plasma, and not that of the galaxies. Under the DM hypothesis, the DM would dominate the mass of the cluster, and its distribution (as a similarly collisionless cluster component) would trace that of the galaxies. This latter hypothesis was resoundingly confirmed in 2006 by Clowe *et al.* in [5], where weak lensing data was analyzed to reconstruct the gravitational potential of the merger. The two peaks of this potential were compared to *Chandra* X-ray data (which maps the hot plasma clouds) and the optical images of galaxies. From the original paper:

Both peaks are [...] within  $1 \sigma$  of the luminosity centroid of the respective component's galaxies [...]. Both peaks are also offset at  $\sim 8 \sigma$  from the center of mass of their respective plasma clouds. They are skewed toward the plasma clouds, and this is expected because the plasma contributes about one-tenth of the total cluster mass [...] [5]

See Fig. 1.3 for the striking visualization of this result.

Before continuing to an overview of dark matter's place in the standard model of cosmology, it is worth noting that there are numerous other astrophysical datasets bolstering the case for dark matter. Bertone *et. al* offer a comprehensive survey in [4], and J. Feng provides a succinct list of key findings in [7].

### 1.1.3 $\Lambda$ CDM

Analogous to the Standard Model of particle physics, the “Lambda cold dark matter” ( $\Lambda$ CDM) model is a powerful theoretical framework. Its most fundamental formulation is

a 6-parameter description of Big Bang cosmology, grounded mathematically in Einstein’s general relativity (GR). To review (closely following [4]), the Einstein field equations,

$$R_{\mu\nu} - \frac{1}{2}g_{\mu\nu}R = \frac{8\pi G}{c^4}T_{\mu\nu} + \Lambda g_{\mu\nu} \quad , \quad (1.8)$$

relate the geometry of space-time (LHS) to its energy content (RHS). Here,  $R_{\mu\nu}$  is the Ricci tensor,  $R$  the Ricci scalar, and  $g_{\mu\nu}$  the metric tensor.  $T_{\mu\nu}$  is the stress-energy tensor,  $G$  the familiar Newtonian gravitational constant, and  $c$  the speed of light in vacuum. Finally,  $\Lambda$  is the eponymous “lambda,” referred to as the cosmological constant. The metric used to solve the field equations is constructed under the assumption of the cosmological principle; i.e., the universe is homogeneous and isotropic when considered with sufficiently coarse granularity (in practice, observational evidence confirms homogeneity and isotropy at  $\gtrsim 100$  Mpc length scales). The resulting Friedmann-Lemaître-Robertson-Walker (FLRW) metric is characterized by the generic line element:

$$ds^2 = -c^2 dt^2 + a(t)^2 \left( \frac{dr^2}{1 - kr^2} + r^2 d\Omega^2 \right) \quad . \quad (1.9)$$

The scale factor  $a(t)$  allows for the time-dependent expansion (or contraction) of space, and  $k$  encodes the curvature. Flat geometry corresponds to  $k = 0$ , open (hyperbolic) geometry to  $k = -1$ , and closed (hyperspherical) geometry to  $k = +1$ . Current observational evidence supports the hypothesis that  $k = 0$ , or at least very nearly so.

Solving 1.8 with 1.9 and substituting the Hubble “constant”  $H(t) \equiv \dot{a}(t)/a(t)$  yields the Friedmann equation:

$$H^2 = \frac{8\pi G}{3}\rho - \frac{k}{a^2} \quad . \quad (1.10)$$

Here, we have absorbed the cosmological constant into the total energy density:

$$\rho \equiv \sum_i \rho_i + \frac{\Lambda c^2}{8\pi G} \quad , \quad (1.11)$$

where  $\rho_i$  are the densities of distinct components of the universe (e.g. matter, radiation).

This fluid interpretation of  $\Lambda$  suggests the presence of “dark energy,” an intrinsic energy density of space. Another tensor component of the solution to 1.8, the acceleration equation, can be expressed as

$$\frac{\ddot{a}}{a} = -\frac{4\pi G}{3} \left( \rho + \frac{3p}{c^2} \right) \quad , \quad (1.12)$$

if we specify an equation of state  $p_\Lambda = -\rho_\Lambda c^2$  and include this in the total pressure  $p$ .

Unlike matter and radiation, for which the proportionality constant  $w \equiv p/\rho c^2 \geq 0$ , dark energy exhibits *negative* pressure, accelerating the expansion of the universe<sup>1</sup> (provided  $\Lambda > 0$ ). That the universe is expanding at an accelerating rate was first discovered from Type Ia supernova observations in 1998 [48, 49], indicating the presence of enough dark energy to counteract the deceleration generated gravitationally by the matter in the universe (dark and otherwise).

The accounting of the universe’s energy budget is usually performed in terms of the critical density  $\rho_c$ :

$$\rho_c = \frac{3H^2}{8\pi G} \quad , \quad (1.13)$$

that is, the density required to ensure a flat universe ( $k = 0$ ; see Eq. 1.10). Abundances

---

<sup>1</sup>A note for the non-cosmologists: though positive pressure might naively be expected to encourage the expansion of space, its effect is the opposite. In a homogeneous universe, there are no pressure gradients, and thus no corresponding forces.

Table 1.1: A sample of Planck 2015  $\Lambda$ CDM fit results, taken from [6]. Note that these parameters are not the direct output of the likelihood search, which scans over a minimal set of independent parameters. Instead, these are derived quantities, calculated from the minimal set, assumptions (e.g.  $\Omega = 1$  and  $w_\Lambda = -1$ ), and auxiliary measurements.

Parameter	Symbol	Fit value
Baryonic matter density	$\Omega_b$	$0.0488 \pm 0.0003$
Cold dark matter density	$\Omega_c$	$0.2601 \pm 0.0022$
Total matter density	$\Omega_m = \Omega_c + \Omega_b$	$0.3089 \pm 0.0062$
Dark energy density	$\Omega_\Lambda$	$0.6911 \pm 0.0062$
Critical density	$\rho_c$	$(8.62 \pm 0.12) \times 10^{-27} \text{ kg/m}^3$

of individual species  $i$  can then be expressed as fractions of  $\rho_c$ :

$$\Omega_i \equiv \frac{\rho_i}{\rho_c} \quad . \quad (1.14)$$

In a flat universe, we therefore have:

$$\Omega \equiv \sum_i \Omega_i = 1 \quad . \quad (1.15)$$

See Table 1.1 for the best estimates of these densities from recent observational data. In particular, note that dark matter is found to constitute over 80% of matter density at cosmological scales. On the other hand, the total energy density is dominated by dark energy ( $\Omega_\Lambda/\Omega \sim 70\%$ ). Familiar baryonic matter therefore accounts for a shockingly small fraction of the *stuff* in our universe.

Observationally, the most powerful handle on the free parameters in  $\Lambda$ CDM is the cosmic microwave background (CMB). In the thermal history of the universe following the Big Bang, “recombination” refers to the epoch during which temperatures had decreased sufficiently to permit the binding of free electrons to protons, effectively decou-

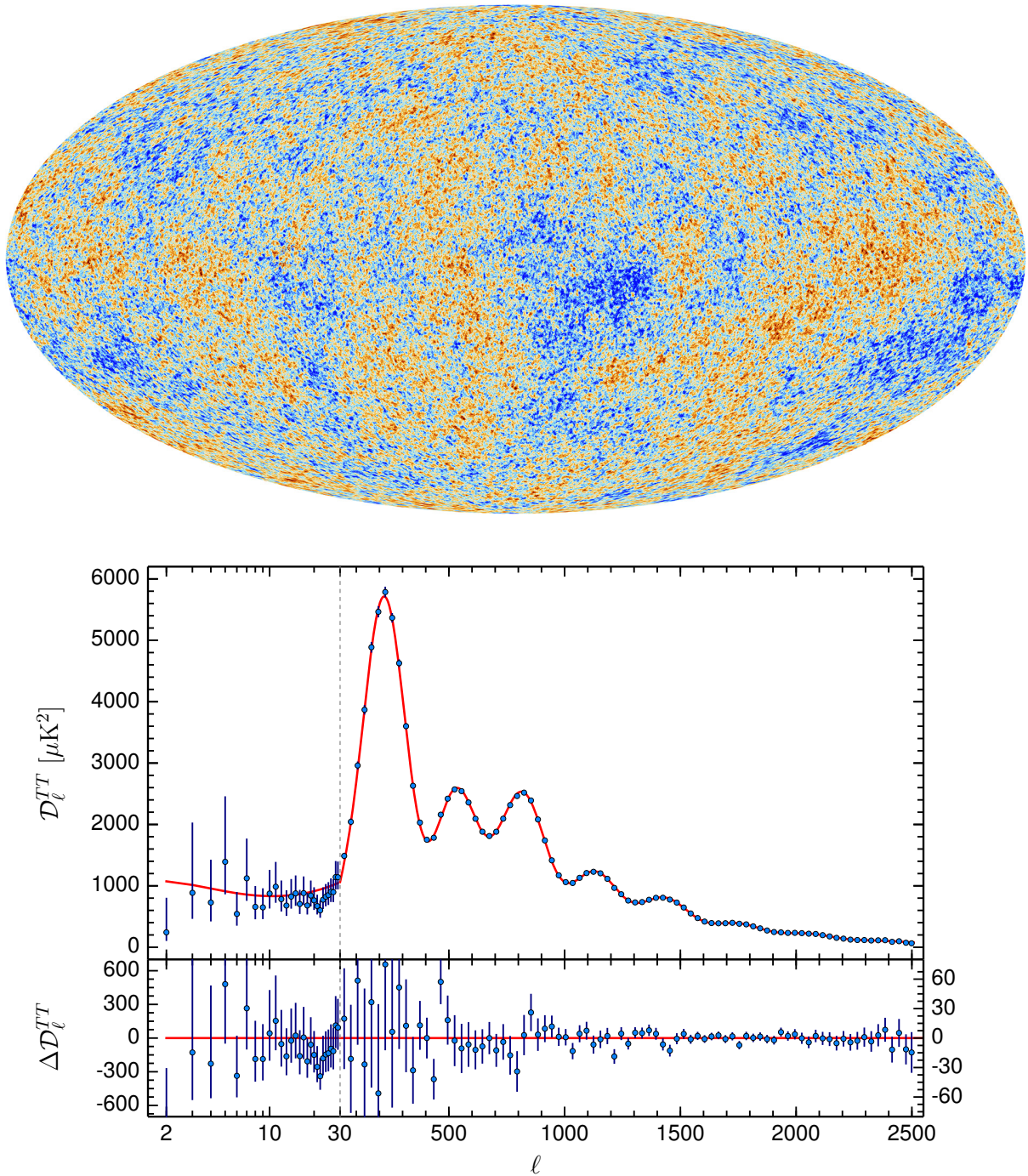


Figure 1.4: *Top*: Mollweide projection of the Planck 2013 CMB temperature map (Credit: ESA and the Planck Collaboration). *Bottom*: Angular power spectrum from [6], showing the observed  $D_\ell^{TT} \equiv l(l+1)C_l/2\pi$  values and the curve predicted by the best-fit  $\Lambda\text{CDM}$  model, with residuals in the bottom panel.

pling baryons from photons [50, 51]. The relic radiation from this event is visible today as the CMB, a (nearly) isotropic field of black-body photons sapped of their original energy as the expansion of space elongated their wavelengths. In the current epoch, the spectral radiance matches the distribution expected from Planck’s law for a black-body with  $T = 2.72548 \pm 0.00057$  K [52]. The fine temperature anisotropies in the CMB, now mapped out in great detail by a succession of experiments with dramatically increasing sensitivity, are an invaluable source of information regarding density fluctuations in the early universe, which in turn impose strong constraints on the parameters of  $\Lambda$ CDM [53].

Fig. 1.4 shows two versions of the Planck data. The finely detailed CMB temperature map dataset is compressed into the more manageable angular power spectrum via Fourier analysis:

$$\frac{\Delta T}{T}(\theta, \phi) = \sum_{l=2}^{+\infty} \sum_{m=-l}^{+l} a_{lm} Y_{lm}(\theta, \phi) \quad , \quad (1.16)$$

where the multipole expansion is done using spherical harmonics  $Y_{lm}$ . Assuming Gaussian fluctuations, the  $m$ -averaged  $C_l \equiv \langle |a_{lm}|^2 \rangle$  give the variance of the harmonic coefficients (which have mean of 0), and thus encode all of the statistical information in the observed  $\frac{\Delta T}{T}(\theta, \phi)$ . The parameters listed in Tab. 1.1 are found by a fit of the model to the  $C_l$  data.

The CMB is not the only probe astronomers have for inferring the parameters of  $\Lambda$ CDM. The Dark Energy Survey (DES) analyzes the clustering of galaxies and weak gravitational lensing to constrain the  $\Omega_m$  parameter. Recent results from DES are largely in agreement with the Planck values [54].

## 1.2 Candidates

Dark matter is remarkable for its importance in physics at such disparate length scales—so far, we have looked at its influence on vast astronomical bodies, but it may also be the key to understanding the microscopic world of fundamental particles. Supersymmetry (SUSY), a theoretical extension to the Standard Model (SM), predicts the existence of a spectrum of as yet undiscovered particles. These particles would be “superpartners” to the familiar quark, lepton, and boson fields of the SM, and the lightest among them might be stable. In the framework of Big Bang cosmology, this lightest supersymmetric particle (LSP) would have been created in the early universe along with the other forms of matter and energy we see now. Unable to decay or interact with SM particles save through gravity and the weak force, LSPs would persist in the universe to present day, perhaps explaining the existence of DM.

The LSP is one of many theoretical candidates that have been proposed to explain the nature and origin of DM. It falls into the broader category of WIMPs (Weakly Interacting Massive Particles), which need not necessarily be described by the SUSY framework. Still, the supersymmetric WIMP is an appealing candidate because of its potential to fit nicely into two seemingly unrelated physics puzzles: the hierarchy problem of the SM, and the mystery of dark matter.

### 1.2.1 WIMPs

WIMPs, in spite of their humble acronym, have gained a devoted following among theorists and experimentalists alike. This is due in part to the mathematical coincidence known as the “WIMP miracle,” wherein if one assumes weak-scale coupling and mass properties for the WIMP, its production in the early universe would result in roughly the  $\Omega_{\text{DM}}$  density observed today. This calculation of the thermal relic density is carefully outlined in the reviews of Jungman *et al.* [3] and Feng [7], so only the main points will be summarized here.

In the aftermath of the Big Bang, the hot and dense universe was populated by particles popping into and out of existence. Our WIMP,  $\chi$ , would be participating in this frenzy, annihilating to lighter particles via  $\chi\bar{\chi} \rightarrow \bar{l}l$  and similarly being produced via  $\bar{l}l \rightarrow \chi\bar{\chi}$ . The production processes occur provided the temperature  $T$  is significantly greater than the WIMP mass  $m_\chi$ , a guaranteed condition in the very young universe. In this era, the number density  $n$  of WIMPs is at a thermal equilibrium value  $n_{\text{eq}}$  determined by statistical mechanics. Eventually, as time progresses and the universe cools,  $T < m_\chi$  and the WIMPs become Boltzmann suppressed:  $n_{\text{eq}} \propto e^{-m_\chi/T}$ . However, the universe is not just getting colder; it is also blowing up. The expansion of space, given by the Hubble parameter  $H$ , prevents WIMPs from completely disappearing by reducing their concentration to the extent that annihilation becomes improbable. This is called “freeze-out”: the WIMP population drops out of thermal equilibrium because the rate of annihilation  $\langle\sigma_A v\rangle$ —i.e. the thermally averaged annihilation cross section—becomes

smaller than the rate of spatial expansion  $H$ .

Mathematically, these competing processes contribute to the rate of change of WIMP number density as

$$\frac{dn}{dt} = -3Hn - \langle\sigma_A v\rangle (n^2 - n_{\text{eq}}^2) \quad , \quad (1.17)$$

a Boltzmann equation of equilibrium. As Jungman *et al.* point out, ignoring the second two terms on the right-hand side leaves a description of the Hubble expansion alone, which can be solved to yield the expected relationship  $n \propto a^{-3}$ . Reinstating these terms, we now have the full description of the effects of Hubble expansion as well as  $\chi\bar{\chi}$  annihilation. Since equation 1.17 governs the time evolution of  $n(t)$ , the relic density can be calculated from its solution. Figure 1.5 shows approximate solutions calculated by Feng in Ref. [7] for a 100 GeV WIMP. The fact that the value of  $\langle\sigma_A v\rangle$  which reproduces the observed DM density is on the order of electroweak scale interactions is a “striking coincidence” [3]; and as Feng notes, even for those unmoved by SUSY or the hierarchy problem, it “independently provides a strong motivation for new particles at the weak scale” [7].

Though WIMPs have been popular candidates for many years now, their conspicuous absence from experimental DM searches have left some skeptical as to their supposedly miraculous theoretical motivation. A recent review of the status of WIMPs has found that most of the simplest formulations of WIMPs (requiring no new particles other than the WIMP itself) will be put to a final test by current or proposed next-generation detectors [55].

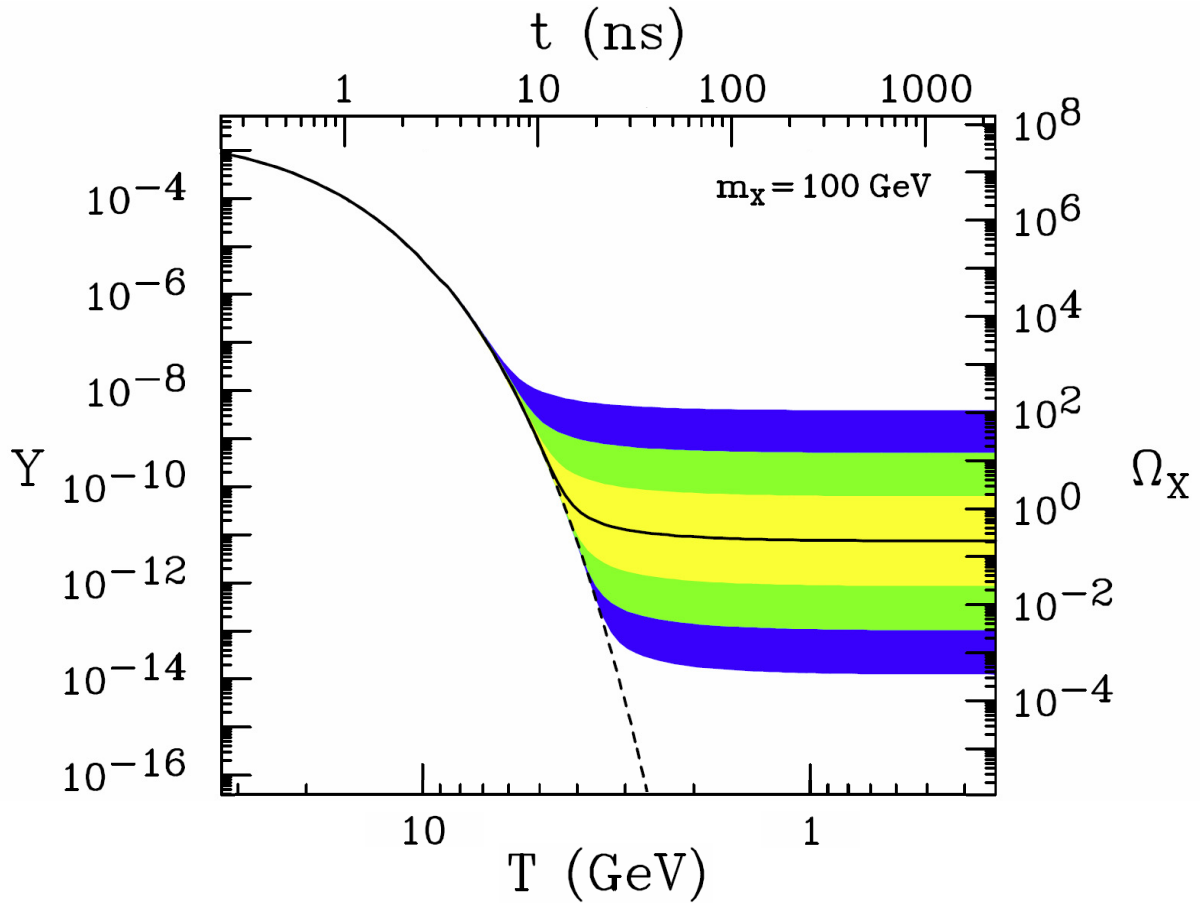


Figure 1.5: Comoving (i.e. adjusted for Hubble expansion) number density  $Y$  of WIMPs over time  $t$ , calculated from eq. 1.17 by Feng. Figure taken from Ref. [7]. The black solid curve shows time evolution for a WIMP with  $\langle\sigma_{AV}\rangle$  that reproduces the observed relic density  $\Omega_\chi$  (right axis). The contours of the colored bands are calculated using alternate values of  $\langle\sigma_{AV}\rangle$  (altering the “correct” value by one, two, and three orders of magnitude). The dashed black curve shows the Boltzmann suppression of WIMP density in the case of thermal equilibrium.

## 1.2.2 Non-WIMP candidates

WIMPs are by no means the only theoretical DM constituent being searched for in current experiments. Feng’s review comprehensively explores other options, including axions and sterile neutrinos. Unlike WIMPs, neither of these candidates naturally produce the correct relic DM density. Still, they address *other* issues in particle physics, unrelated (at least at face value) to the gauge hierarchy problem: sterile neutrinos offer an explanation to the question of neutrino mass, whereas axions have been introduced to tackle the strong CP problem [7].

Other theories hold that DM can be explained without introducing any new particles at all. MACHOs (Massive Astrophysical Compact Halo Objects) were proposed as a particularly reactionary alternative to WIMPs, and would consist of baryonic matter. However, microlensing surveys have ruled out MACHOs as being significant components of the halo DM for a wide range of MACHO masses [56]. That said, the recent LIGO detection of black hole mergers [57] has sparked interest in the possibility of primordial black holes providing some of the dark matter. Though many mass ranges are ruled out, primordial black holes in the “intermediate-mass range” ( $M_{\odot} < M < 10^3 M_{\odot}$ ) can still account for some the DM [58]. Carr *et al.* conclude that this and the “sublunar” mass range may soon be ruled out as well, but that Planck-mass scale black holes are viable candidates and will not be constrained by near-term experiments.

It is possible that some combination of all of these candidates are responsible for the observed  $\Omega_{\text{DM}}$ . However, observational constraints imposed on a single hypothetical

species are typically calculated under the assumption that it alone constitutes the DM. The details of this calculation in the case of WIMP dark matter are explored in the next chapter.

## Chapter 2

# Detection of dark matter

The “discovery” of dark matter, from an astrophysical perspective, has already been accomplished. Debate rages over the rightful attribution of this accolade: Fritz Zwicky’s daughter Barbarina Zwicky continues to wage a fierce battle for her father’s legacy [59], notwithstanding the tendency of modern authors (including this one) to favor Rubin’s efforts [60].<sup>1</sup> Irrespective of this controversy, however, the question of dark matter’s composition is decidedly unanswered. If “discovery” describes the ascertaining of DM’s existence, then “detection” must be the unveiling of DM’s particle nature.

---

<sup>1</sup>It appears that B. Zwicky scored a minor victory in the case of Ref. [60]. In the publicly available online version of the article, the title reads (as of this writing) “How Vera Rubin confirmed dark matter” instead of “How Vera Rubin discovered dark matter,” as it appeared in the original print edition. (Additionally, an online commenter self-identified as “barbarina zwicky” lambasts the author for advancing a smear campaign against her father.) However, the HTML title field still retains the “discovered,” so Google searchers will see the original title’s wording in the hyperlink.

## 2.1 Detection schemes

Experiments designed to detect dark matter fall into three main categories:

**Production:** Colliders like the LHC produce exotic particles via high-energy inelastic scattering. Detectors like CMS and ATLAS are used to reconstruct what particles were created in the collisions. If a WIMP were generated in such a collision, it would appear as missing energy in the event reconstruction.

**Indirect detection:** Cosmic rays are in general a useful probe of astrophysical processes. If many DM particles were concentrated in a high-density region (e.g. in the Sun, after scattering from protons and becoming gravitationally trapped), they could annihilate and produce a tell-tale resonance in the spectrum of radiation emanating from this region. Earth- and space-based laboratories are capable of observing such a signal.

**Direct detection:** Perhaps the most conceptually straightforward of the three techniques, experiments in this category seek to observe collisions between galactic DM particles and atoms in a target material. Since the Earth is constantly passing through the dark halo, a sensitive enough detector should be able to detect such a collision. To mitigate non-WIMP backgrounds from cosmic rays, direct detection experiments must be deployed underground, where the rock overburden acts as a radiation shield.

Figure 2.1 pictorially portrays the three approaches to DM detection. An ideal de-

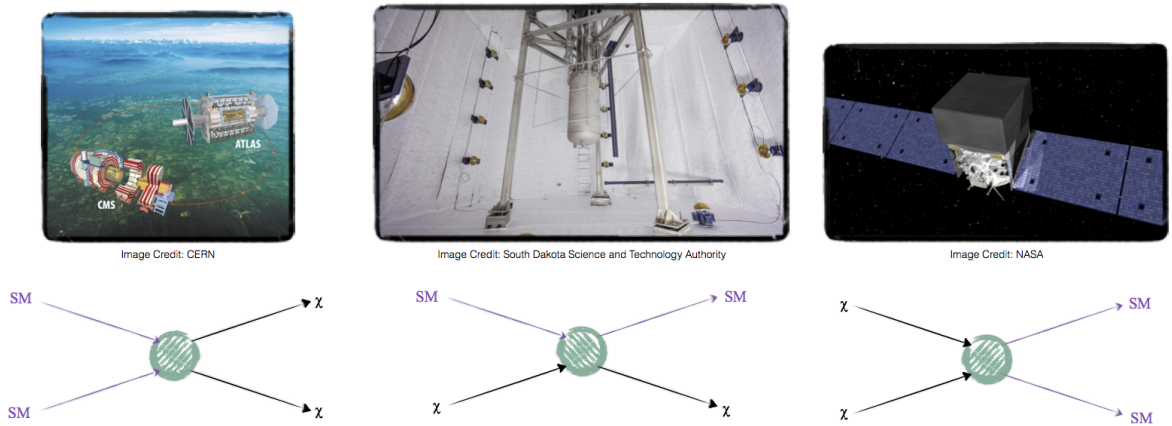


Figure 2.1: Illustrative Feynman diagrams for the three approaches to DM detection, beneath images of representative experiments. At left, the collider search technique is shown with an LHC graphic (credit: CERN) and diagram with Standard Model (SM) particles inelastically scattering to produce DM particles ( $\chi$ ). At right, the Feynman diagram is flipped, and DM self-annihilates to produce SM particles, conceivably visible to indirect detection observatories like the Fermi LAT (image credit: NASA). Finally, shown in the center, an image of LUX represents the field of direct detection, schematically illustrated by a Feynman diagram obtained by rotating the others  $90^\circ$ , wherein a DM particle scatters against a SM particle (image credit: Matt Kapust, South Dakota Science and Technology Authority).

tection scenario would involve experiments in multiple categories seeing signals: for example, a new particle discovery at the LHC could be corroborated by an underground detector reporting detection of a WIMP with consistent mass and coupling properties. This would imply that the particle created in anthropogenic high-energy collisions exists cosmogenically in the galaxy.

Experiments designed for different detection schemes are often said to be “complementary,” capable not only of validating one another’s results, but also of testing hypotheses to which the other is insensitive. If, for example, DM particles are too massive to be produced at the LHC, direct and indirect detection experiments might still be able to see a signal. In fact, DM searches within just the direct detection category also exhibit complementarity, due to differences in their target materials. Section 2.2 will explore the specific mechanisms giving rise to these differences in sensitivity.

### 2.1.1 A note on the status of the field

Despite the diversity of detectors built to glimpse the dark matter particle, success has been elusive. There have been a few false alarms, but only one group remains steadfast in its claim of detecting a WIMP signal: the DAMA/LIBRA direct detection collaboration interprets an observed annual modulation in their event rate as originating from WIMPs [61] (see section 2.2.4 for an explanation of annual modulation). Though null results of countless other experiments cast considerable doubt on this conclusion, Bernabei *et al.* assert that no systematic effect proposed so far can satisfactorily explain their data.

They suggest that their sodium-iodide detector is, by a lucky quirk of nuclear physics and effective field theory, uniquely suited to detecting WIMPs. Efforts are ongoing to replicate these results using a different NaI detector [62, 63], and the scientific community is, on the whole, fairly skeptical of the claim.<sup>2</sup>

As LUX is a direct detection experiment, details of the theory and current status of the other two search techniques are largely beyond the scope of this work. J. Gaskins provides a thorough review of indirect detection searches in Ref. [64], and recent LHC results interpreted as DM constraints can be found in Ref. [28] (CMS) and Ref. [29] (ATLAS). Suffice it to say here that no one has found anything conclusive yet.

## 2.2 Principles of direct detection

### 2.2.1 WIMP-nucleus scattering

The direct detection of WIMPs is contingent on the possibility of WIMP-nucleus scattering. In collisions between WIMPs and nuclei in the target material of a detector, the kinetic energy of the recoiling nucleus  $E_R$  can be experimentally measured via a number of calorimetry techniques. The observed nuclear recoil energy spectrum (and, in turn, the total event rate) depends on the differential WIMP-nucleus cross section  $d\sigma/dE_R$ , a quantity incorporating information from particle physics matrix elements, kinematic phase space, and also nuclear physics. In their review paper, Jungman *et al.* symbolically

---

<sup>2</sup>David Cline, the late stalwart of many particle physics and DM experiments, minced no words at the 2014 UCLA Dark Matter conference when he declared the DAMA/LIBRA results “bad science.”

express this conceptual compartmentalization as [3]

$$\frac{d\sigma}{dq^2} = \frac{G_F^2 C}{v^2} F^2(q) \quad , \quad (2.1)$$

where  $G_F$  is the Fermi constant,  $v$  is the WIMP velocity (in the detector rest frame),  $q$  is the momentum transfer, the dimensionless  $C$  encodes the particle physics model input, and the form factor  $F^2(q)$  contains the nuclear physics (sometimes referred to as the “coherence loss”). This expression can be derived by application of Fermi’s Golden Rule for two-body elastic scattering<sup>3</sup>, assuming that the particle physics process is independent of momentum transfer ( $dC/dq^2 = 0$ , where the matrix element is embedded in  $C$ ). In this section, these components will be examined in a top-down approach: first, the kinematics of the effective WIMP-nucleus elastic scattering is explored, incorporating the effects of WIMP velocity distribution models; next, the nuclear physics of form factors is discussed; and finally, the particle physics of WIMP-quark coupling is reviewed.

### 2.2.2 Kinematics

In elastic scattering, the momentum transfer is

$$q = \mu v \sqrt{2(1 - \cos \theta)} \quad , \quad (2.2)$$

where  $\theta$  is the scattering angle in the center-of-mass reference frame, and

$$\mu \equiv m_A m_\chi / (m_A + m_\chi) \quad (2.3)$$

---

<sup>3</sup> Inelastic scattering is also theoretically feasible, whether through excitation of the target nucleus [65], or of the DM particle itself [66].

is the WIMP-nucleus reduced mass (with  $m_A$  indicating the mass of a nucleus of mass number  $A$ , and  $m_\chi$  the WIMP mass). Therefore the nuclear recoil energy is

$$E_R = \frac{q^2}{2m_A} = \frac{\mu^2 v^2}{m_A} (1 - \cos \theta) \quad . \quad (2.4)$$

From this we can see that assuming  $dC/dq^2 = 0$  is equivalent to assuming  $dC/d\cos\theta = 0$ , i.e. that the fundamental WIMP-nucleon scattering cross-section is isotropic. This is a reasonable assumption, since for cold (non-relativistic) dark matter, we are operating in the low-momentum exchange regime [67]. Additionally, and of primary interest to direct detection experimentalists, we can write an expression for the differential cross section in terms of recoil energy:

$$\frac{d\sigma}{dE_R} = \frac{d\sigma}{dq^2} \frac{dq^2}{dE_R} \quad (2.5)$$

$$= \frac{2m_A G_F^2 C}{v^2} F^2(E_R) \quad . \quad (2.6)$$

### 2.2.3 WIMP event rates in detectors

In practice, we aim to experimentally measure the rate  $R$  of WIMP events in our detector (or, failing that, set statistical upper limits on it). Suppose that we are immersed in a halo with local mass density  $\rho_\chi$ , composed of WIMPs of mass  $m_\chi$ , all moving at the speed  $v = v_\chi$  (in the detector rest frame). In that case, the differential rate in our detector

(number of events per unit time per unit energy) will be

$$\frac{dR}{dE_R} = (\# \text{ nuclei in detector}) \times (\text{WIMP flux}) \times (\text{WIMP-nucleus cross section}) \quad (2.7)$$

$$= (N_T) \times \left( v_\chi \frac{\rho_\chi}{m_\chi} \right) \times \left( \frac{d\sigma}{dE_R} \Big|_{v=v_\chi} \right) \quad (2.8)$$

$$= C \frac{2 G_F^2 m_A N_T \rho_\chi}{m_\chi} F^2(E_R) \frac{H(v_\chi - v_{\min}(E_R))}{v_\chi} \quad (2.9)$$

Eq. 2.9 is written such that  $C$  represents our unknown quantity, where everything else is a physical constant or modeled quantity (with the exception of  $m_\chi$ , the WIMP mass<sup>4</sup>).

This equation is therefore at the core of hypothesis testing, as it links our theoretical unknowns with what we actually measure. The Heaviside step function  $H$  has been explicitly included in 2.9 to emphasize that given a fixed recoil energy  $E_R$ , there exists a minimum WIMP velocity  $v_{\min}$  for which the scattering event can occur. Put another way, a given velocity  $v$  will result in a maximum recoil energy in the case of back-to-back scattering ( $\cos \theta = -1$ ). From eq. 2.4, we see then that

$$v_{\min}(E_R) = \sqrt{\frac{E_R m_A}{2\mu^2}} \quad (2.10)$$

Fig. 2.2 shows  $v_{\min}$  for a variety of WIMP masses, for the commonly used or proposed target elements Xe, Ge, Ar, Si, and He (listed in descending order of atomic weight). If we consider a detector with energy threshold  $E_R = 5$  keV, these plots show how fast a WIMP must be moving to induce a signal. As might be expected, lighter WIMPs require

<sup>4</sup>Experiments will typically set limits on  $C$  as a function of WIMP mass by scanning over a range of  $m_\chi$ , constructing signal models according to eq. 2.9 for each value, and interpolating the results.

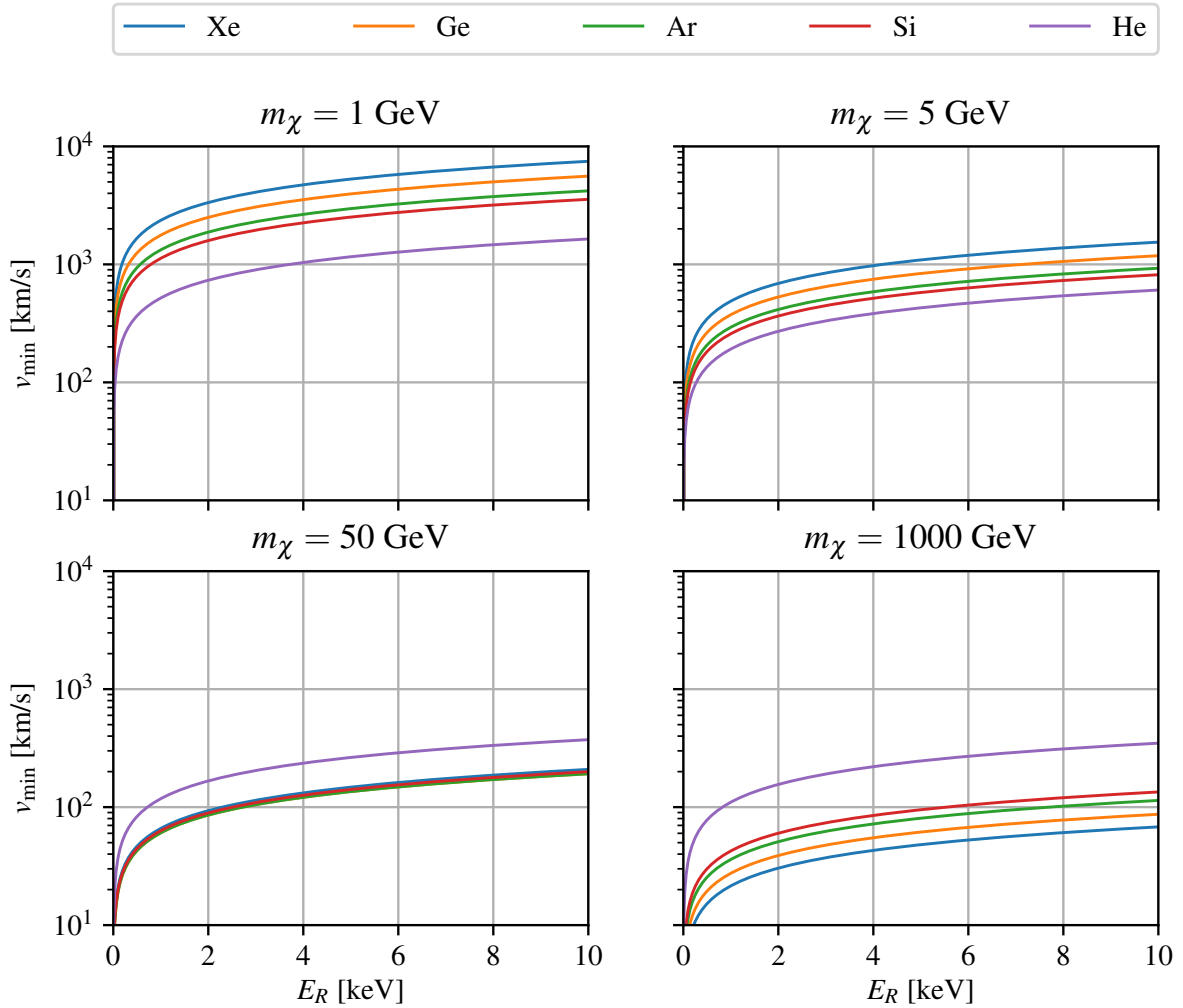


Figure 2.2: Minimum WIMP velocities  $v_{\min}$  required to produce nuclear recoils  $E_R$  for various WIMP masses and target materials.

much higher velocities in order to be detected, for all target materials. At a given WIMP mass, however, the best-suited target material (at least from a kinematic standpoint) is the one which has  $m_A$  closest to  $m_\chi$ . This can be verified by solving  $dv_{\min}/dm_A = 0$ , which indeed yields  $m_A = m_\chi$ . For this reason, xenon detectors have an advantage when it comes to detecting heavy WIMPs. On the other hand, in the case of light WIMPs ( $m_\chi \sim \mathcal{O}(1\text{GeV})$ ), Xe detectors (and most others) are only sensitive to very high-velocity particles. Liquid helium detectors are therefore being developed to explore this region of WIMP parameter space [68].

### What about WIMP-electron scattering?

Before taking a more careful approach to modeling the velocity of galactic WIMPs, it is worth understanding the focus on elastic nuclear scattering. In a generic scenario where WIMPs couple with equal strength to quarks and leptons, the  $C$  quantity should be roughly the same when describing WIMP-nucleon or WIMP-electron scattering. However, the factor of  $m_A$  in eq. 2.6 is replaced by the electron mass  $m_e$ , meaning the scattering rate from electrons suffers a large ( $m_e/m_A \sim 10^{-5}$ ) suppression relative to the nuclear scattering rate. In this scenario, then, WIMP detectors would be far more likely to see nuclear recoils than electron recoils.

On the other hand, the possibility of “leptophilic” dark matter has been proposed [69], in part to explain the discrepancy between the putative DAMA/LIBRA signal and the null results of other experiments. In this scenario, WIMPs would couple exclusively to leptons. By construction, tree level WIMP-quark interactions are forbidden; however,

in most cases allowed by a general effective field theory (EFT) description, coupling to quarks would arise from virtual lepton loops, and WIMP-nucleus scattering would still dominate [70]. (In those few cases where loop diagrams do not contribute, Kopp *et al.* also found that their leptophilic model was a poor fit to the DAMA/LIBRA data.)

These arguments hold for WIMPs at the GeV to TeV scales, but WIMP-electron scattering does become a viable detection mechanism for especially light WIMPs (MeV to GeV scale) [71–73]. This approach is kinematically favorable not only because of the small electron mass, but because bound electrons have a high typical velocity  $\alpha c$  and can absorb a large fraction of a light WIMP’s kinetic energy in inelastic collisions (ionization, atomic or band-gap transitions).

## 2.2.4 Standard Halo Model

Eq. 2.9 is a useful starting point, but requires a major simplifying assumption: namely, WIMPs at the galactic radius of our solar system travel at a single velocity with negligible variation. In fact, this assumption was made in the pioneering work of Goodman and Witten [67], who chose a typical WIMP velocity of  $v = 200$  km/s to assess the feasibility of direct detection experiments. Looking at Fig. 2.2 again, this would require sub-keV energy thresholds for most detectors attempting to see  $< 5$  GeV WIMPs.

Since those exploratory calculations of 1985, however, far more sophisticated models of the galactic dark halo have been developed. These models suggest a probability density function (PDF)  $f(v)$  describing the distribution of WIMP speeds relative to an Earth-

based detector. Generalizing eq. 2.8 to account for this, we must integrate over all WIMP velocities that can generate a recoil  $E_R$ , weighting the integrand by the appropriate PDF:

$$\frac{dR}{dE_R} = (N_T) \times \left( \frac{\rho_\chi}{m_\chi} \right) \times \left( \int_{v_{\min}(E_R)}^{\infty} dv f(v) v \frac{d\sigma}{dE_R} \Big|_v \right) \quad (2.11)$$

$$= C \frac{2 G_F^2 m_A N_T \rho_\chi}{m_\chi} F^2(E_R) \int_{v_{\min}(E_R)}^{\infty} \frac{dv}{v} f(v) \quad . \quad (2.12)$$

In fact, we can recover eq. 2.9 from eq. 2.12 by specifying

$$f(v) = \delta(v - v_\chi) \quad . \quad (2.13)$$

The approximate functional form for  $f(v)$  most commonly used by direct detection experimentalists was first introduced by Druiker, Freese, and Spergel [74] just a few months after Goodman and Witten’s paper. In the rest frame of the halo, the velocity PDF is taken to be a Maxwell-Boltzmann distribution, which follows naturally from a few simplifying assumptions. Most importantly, it can be argued [74, 75] that as the galactic halo was formed by the gravitational collapse of a diffuse DM cloud, WIMP velocities were thermally randomized in a process called “violent relaxation” [76]. WIMPs do not, by definition, interact frequently with baryonic matter, and thus will have preserved this ancient velocity distribution. This model, which describes the halo as an isotropic and isothermal sphere, is referred to as the “standard halo model” (SHM).<sup>5</sup>

In its simplest form, then, the distribution for WIMP velocities in the rest frame of

---

<sup>5</sup>Empirically testing the accuracy of the SHM using tracer stars in the galactic halo is the subject of current research [77]. Preliminary findings hint at a departure from the Maxwell-Boltzmann velocity distribution, shifted to slightly slower velocities than the commonly assumed model.

the halo is

$$f(\vec{v}) = \frac{1}{N} e^{-v^2/v_0^2} \quad , \quad (2.14)$$

where  $v_0$  is the most probable speed, and  $N = \pi^{3/2}v_0^3$  is a normalization constant. Note that this is a multivariate distribution for the 3 velocity components; to obtain the PDF for the speed  $v = |\vec{v}|$  used in eq. 2.12, we must integrate over angles:

$$f(v) = \int_0^{4\pi} f(\vec{v}) v^2 d\Omega \quad (2.15)$$

$$= \frac{4\pi v^2}{N} e^{-v^2/v_0^2} \quad . \quad (2.16)$$

Though certainly an improvement over Goodman and Witten’s delta function approximation, this distribution still ignores a few subtleties. First of all, we expect the distribution to be cut off at the escape velocity of the galaxy  $v_{\text{esc}}$ : WIMPs traveling faster than this speed will not be gravitationally bound to the galaxy, and will therefore not be present in the equilibrated ensemble. Second, the motion of the Earth relative to the bulk distribution of the halo must be considered when calculating event rates in an Earth-bound laboratory. Lewin and Smith systematically tackle both of these mathematical hurdles in their 1996 review [78], which remains an invaluable reference. However, integral calculations in Ref. [78] contain a small error involving the geometric projection of the Earth’s solar orbit onto the galactic plane [79], and more recent calculations (e.g. Savage *et al.* [40] and McCabe [8]) are now the standard.

Following the notation of Ref. [8], we can define the distribution of WIMP velocity  $\vec{v}$

Quantity	Savage <i>et al.</i> [40]		McCabe [8]	
	symbol	value [km/s]	symbol	value [km/s]
Local Standard of Rest velocity	$\mathbf{v}_{\text{LSR}}$	(0, 220, 0)*	$\vec{v}_0$	various
Peculiar velocity of Sun (relative to above)	$\mathbf{v}_{\odot,\text{pec}}$	(10, 13, 7)*	$\vec{v}_{\otimes}$	(11.1, 12.24, 7.25)
Earth's orbital speed around Sun	$V_{\oplus}$	29.8	$v_{\oplus}$	29.8
Earth velocity relative to halo	$\mathbf{v}_{\text{obs}} = \mathbf{v}_{\text{LSR}} + \mathbf{v}_{\odot,\text{pec}} + \mathbf{V}_{\oplus}$		$\vec{v}_e = \vec{v}_0 + \vec{v}_{\otimes} + \vec{v}_{\oplus}$	
Galactic escape velocity	$v_{\text{esc}}$	650	$v_{\text{esc}}$	544*

Table 2.1: Astronomical velocities relevant to the calculation of WIMP event rates in Earth-based detectors. Symbols and quantities from two popular references are shown for comparison. In this work and in the LUX publications, we use the starred\* values (indicated only when values are not in agreement). Vector quantities are shown in Galactic coordinates  $(x, y, z) = x\hat{\mathbf{x}} + y\hat{\mathbf{y}} + z\hat{\mathbf{z}}$ , where  $\hat{\mathbf{x}}$  points towards the Galactic Center,  $\hat{\mathbf{y}}$  towards the direction of disk rotation, and  $\hat{\mathbf{z}}$  towards the North Galactic Pole [40].

relative to an observer on Earth as

$$f_{\oplus}(\vec{v}, \vec{v}_{\text{obs}}) = f(\vec{v} + \vec{v}_{\text{obs}}) = \begin{cases} \frac{1}{N} e^{-(\vec{v} + \vec{v}_{\text{obs}})^2 / v_0^2} & |\vec{v} + \vec{v}_{\text{obs}}| < v_{\text{esc}} \\ 0 & |\vec{v} + \vec{v}_{\text{obs}}| > v_{\text{esc}} \end{cases}, \quad (2.17)$$

where truncating the distribution affects the normalization constant:

$$N = \pi^{3/2} v_0^3 \left[ \text{erf}(x_{\text{esc}}) - \frac{2x_{\text{esc}}}{\sqrt{\pi}} e^{-x_{\text{esc}}^2} \right] \quad (2.18)$$

(using  $x_{\text{esc}} \equiv v_{\text{esc}}/v_0$ ). The original distribution is simply boosted into the frame of the observer, whose relative velocity  $\vec{v}_{\text{obs}}$  is the vectorial sum of the “local standard of rest” (LSR) velocity (i.e. the circular motion of the galaxy near the solar system), the “peculiar velocity” of the Sun relative to the LSR, and the time-varying orbital velocity of the Earth around the Sun. See Table 2.1 for a catalog of useful notation definitions, as

well as numerical values for the astrophysical parameters of the SHM. Figure 2.3 shows the Maxwellian speed distribution in the frame of the WIMP halo and of the Earth.

With these adjustments in mind, we can rewrite eq. 2.12 as

$$\frac{dR}{dE_R} = C \frac{2 G_F^2 m_A N_T \rho_\chi}{m_\chi} F^2(E_R) \int_{v_{\min}(E_R)}^{\infty} \frac{d^3\vec{v}}{v} f_{\oplus}(\vec{v}, \vec{v}_{\text{obs}}) \quad , \quad (2.19)$$

where  $v$  is the WIMP velocity in the frame of the detector, and the escape velocity truncation is taken care of by definition 2.17. The integral over velocities, called  $\zeta(E_R)$  in Ref. [8] and  $\eta(E, t)$  in [40], yields the average inverse speed of WIMPs that can generate nuclear recoils of a given energy. Both references provide analytic solutions (Appendix B of Ref. [8] also considers an optional exponential ramp-down of the distribution near  $v_{\text{esc}}$ ). Significantly, this quantity is time-varying, since the relative WIMP velocity rises and falls as the Earth moves in concert with and in opposition to the Sun’s circular velocity, depending on the time of year. Some experiments seek to exploit this variation, looking for annual modulation of event rates. In low-background experiments that see only a handful of signal-like events in a years-long exposure, an average value for  $v_{\text{obs}}$  is used instead. This is the strategy used to calculate  $\zeta(E_R)$  in Fig. 2.4. The same target isotopes are considered as in Fig. 2.2, though the  $x$ -axis ( $E_R$ ) range has been expanded and converted to logarithmic scale. This spectrum would completely define the shape of differential rate if there were no coherence loss; that is, if the WIMP were incapable of “seeing” the individual protons and neutrons inside the nucleus.

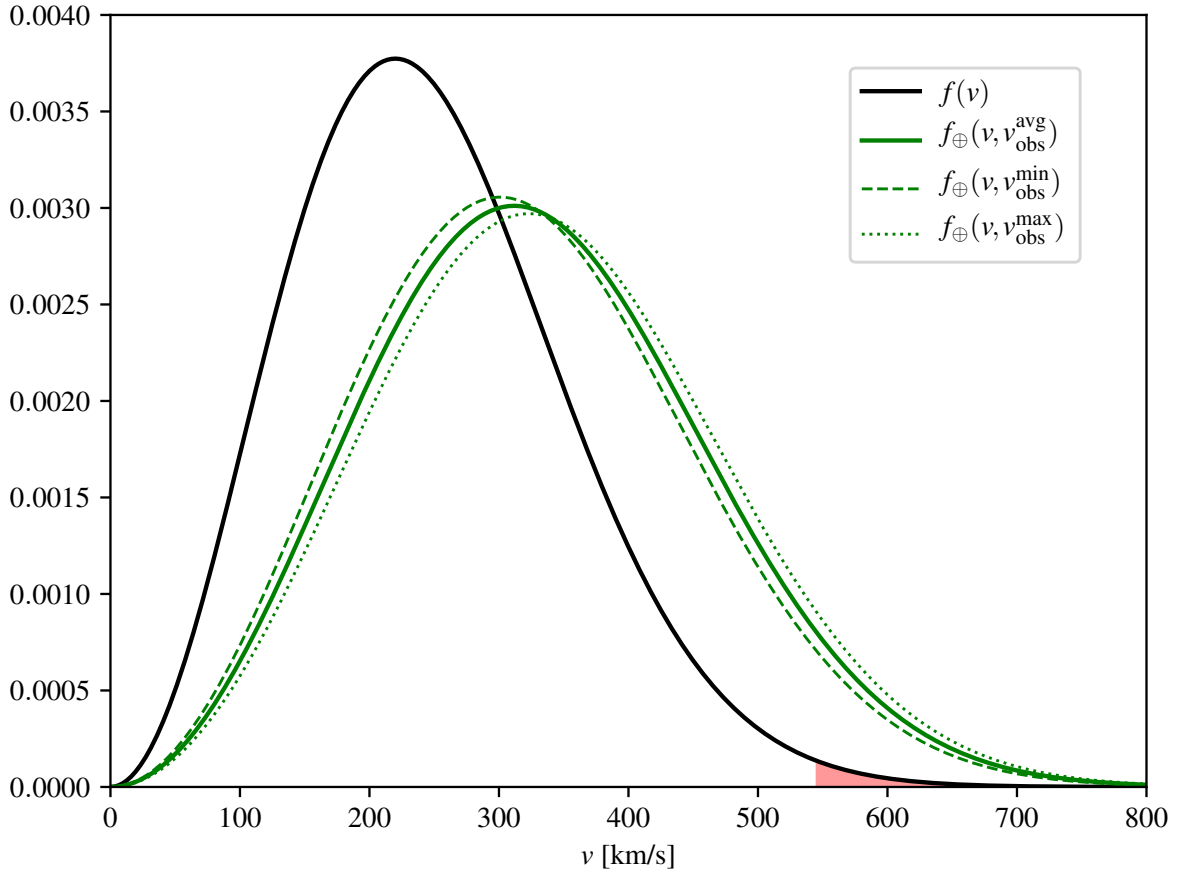


Figure 2.3: WIMP speed distributions in the rest frame of the halo (black curve) and in the rest frame of the Earth (green). For the solid green curve, the annually averaged Earth velocity is used. Distributions at the time of the Earth’s minimum and maximum relative speeds are shown as green dashed and green dotted curves, respectively. For simplicity, the escape velocity truncation has not been included in these calculations. The region beyond the standard  $v_{\text{esc}} = 544$  km/s value is indicated by the shaded red area under the (halo-frame)  $f(v)$  curve, which only accounts for less than 0.7% of the total probability. The loss of this velocity tail only becomes significant for detectors where energy thresholds require  $v_{\text{min}}$  near  $v_{\text{esc}}$ . See Fig. 2 of Ref. [8] for a demonstration of how the uncertainty on  $v_{\text{esc}}$  affects the sensitivity of various detectors.

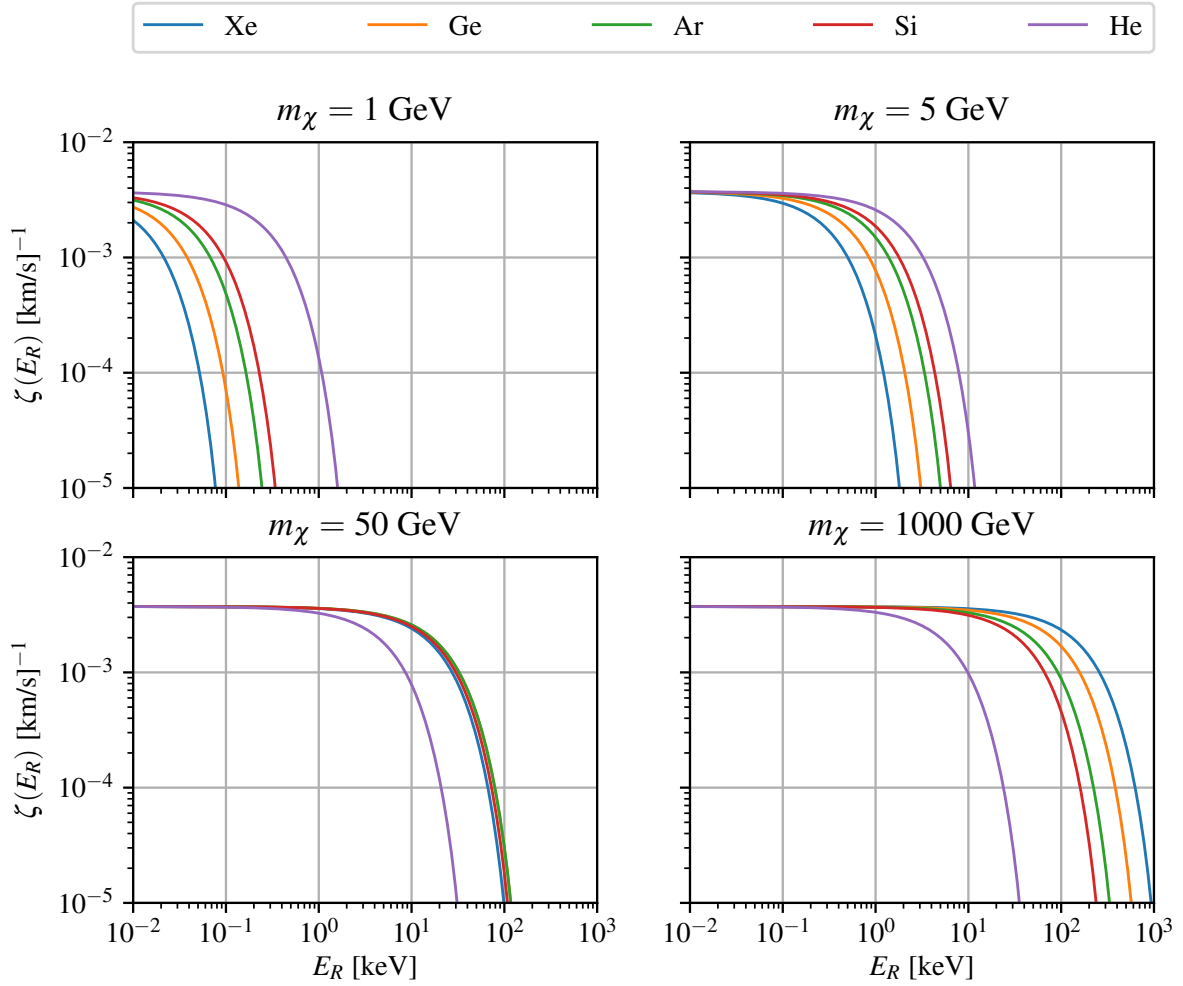


Figure 2.4: SHM mean inverse WIMP speeds for various WIMP masses and target materials, using the parameters indicated in Table 2.1, and a time-averaged  $\langle v_{\text{obs}}(t) \rangle = 230$  km/s. If we were to ignore the form factor in eq. 2.19, this spectrum would determine the shape of the differential rate.

### 2.2.5 Form factors

The necessity for the form factor  $F$  arises when the wavelength  $h/q$  of the momentum transfer is on the same scale as the effective nuclear radius  $r_n$ . In this regime, the nucleus can no longer be treated as a monolithic unit and the particle physics factor  $C$  must be corrected. If the WIMP-nucleus coupling is spin-independent (SI), then this correction is adequately approximated by the Helm form factor [80].<sup>6</sup> As with the choice of the SHM velocity distribution, this model strikes an attractive balance between simplicity and accuracy and has become the standard for experimentalists, allowing for consistency across results. That being said, equally convenient (i.e. having analytical solutions) but more accurate models have been proposed [82].

Following Lewin and Smith [78] and working in the first Born approximation, the form factor is given by the Fourier transform of the density of scattering sites in the nucleus. Spin-dependent (SD) scattering requires a careful and detailed nuclear calculation to achieve acceptable accuracy, and is given thorough treatment in Chapter 7. For SI

---

<sup>6</sup>J. Engel endorses this form factor in Ref. [81] for the purposes of DM searches, noting its similarity to that derived from the Woods-Saxon density distribution. Confusingly, Jungman *et al.* therefore dub it the “Woods-Saxon” form factor, though apparently the jargon has since changed back to “Helm.”

scattering, as discussed, we will use Helm's model:

$$\rho_0(r) = \begin{cases} 3/(4\pi r_n^3) & r < r_n \\ 0 & r > r_n \end{cases} \quad (2.20)$$

$$\rho_1(r) = \frac{1}{(2\pi s^2)^{3/2}} e^{-r^2/2s^2} \quad (2.21)$$

$$\rho(\vec{r}) = \int \rho_0(\vec{r}') \rho_1(\vec{r} - \vec{r}') d^3 \vec{r}' \quad . \quad (2.22)$$

Essentially, this density model  $\rho(\vec{r})$  is just a uniform sphere ( $\rho_0$ ) extending out to the nuclear radius  $r_n$ , normalized to unity, and smeared by a gaussian ( $\rho_1$ ) with thickness parameter  $s$  to smooth out the unphysical cut-off at  $r_n$ . The Fourier transform of the spherically symmetric distribution,

$$F(q) = \frac{4\pi}{q} \int_0^\infty r \sin(qr) \rho(r) dr \quad , \quad (2.23)$$

is given by the product of the individual transforms of  $\rho_0$  and  $\rho_1$ , thanks to the convolution theorem:

$$F(q) = F_0(q) \times F_1(q) \quad (2.24)$$

$$= 3 \frac{j_1(qr_n)}{qr_n} \times e^{-(qs)^2/2} \quad , \quad (2.25)$$

where the solution is obtained using the spherical Bessel function

$$j_1(x) = \frac{\sin x}{x^2} - \frac{\cos x}{x} \quad . \quad (2.26)$$

Given values for  $r_n$  and  $s$ , eq. 2.25 can be readily calculated and implemented in Equ-

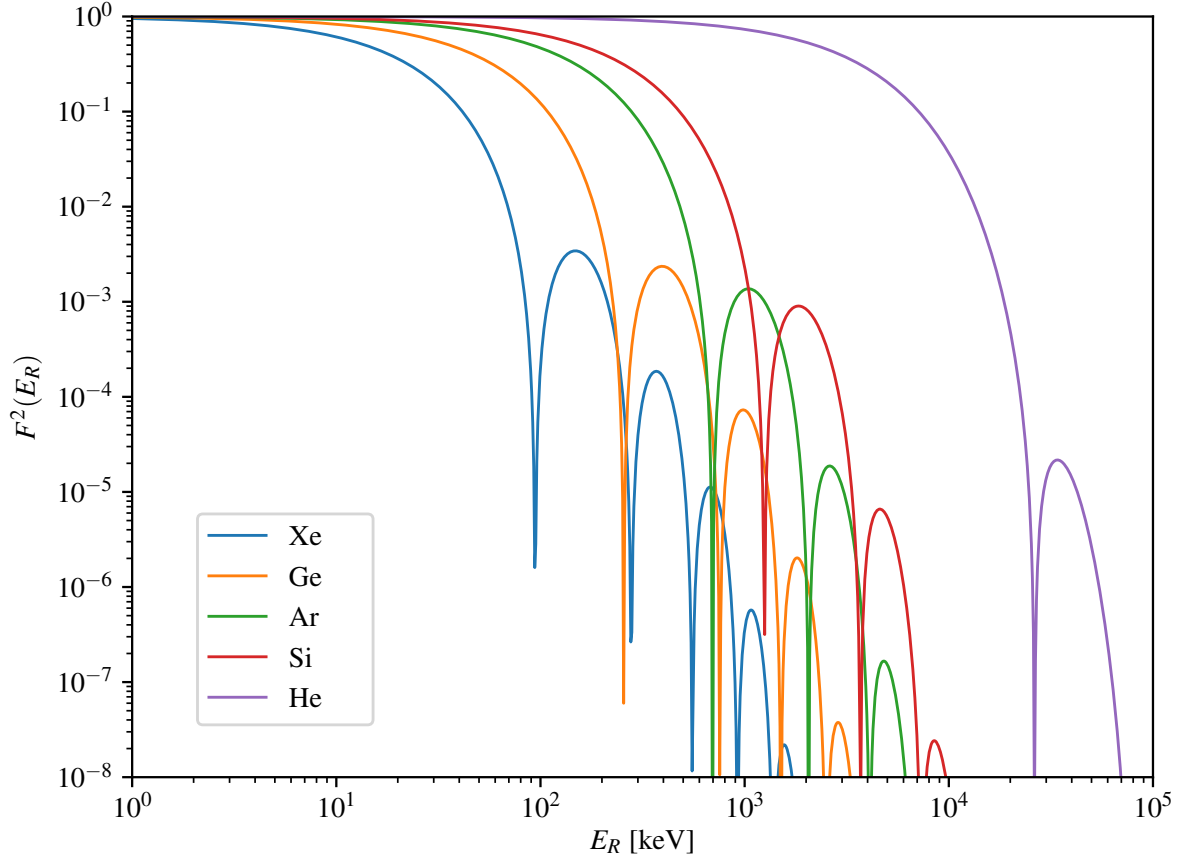


Figure 2.5: Nuclear form factors for various detector target isotopes, using the Helm charge density model.

tion 2.19. (Note that natural units are used here;  $qr_n/\hbar c$  is the appropriate dimensionless quantity.)

Figure 2.5 shows the form factors of our usual suite of target materials as a function of  $E_R$  (using 2.4 to convert to  $q$ ). For these calculations, Lewin and Smith’s parameterization for the nuclear radius are used [78]:

$$r_n = \sqrt{c^2 + \frac{7}{3}\pi^2 a^2 - 5s^2} \quad , \quad (2.27)$$

with

$$c/[1 \text{ fm}] = 1.23A^{1/3} - 0.60 \quad , \quad (2.28)$$

using  $a = 0.52 \text{ fm}$  and  $s = 0.9 \text{ fm}$ . These values are obtained from fits to muon scattering data, making the assumption that the nucleon distribution mimics the charge distribution in the nucleus. Comparing these form factors to the naive recoil spectra specified by the WIMP velocity model (Fig. 2.4), it is clear that for xenon, the form factor plays a significant role for WIMPs of mass greater than 50 GeV. The unmodified recoil spectrum for a 1 TeV WIMP begins falling off near 100 keV, whereas at this momentum transfer, the form factor suppression is already at the level of a few orders of magnitude. As we will see in the next section, for SI scattering, this apparent disadvantage for heavier nuclei is counterbalanced by a boost in the cross section that comes from having so many nucleons coherently contributing to the matrix element.

## 2.2.6 Particle interactions

The standard approach to modeling the couplings between WIMPs and the quarks and gluons in a nucleon is to use an effective Lagrangian, categorizing hypothetical interactions by their properties under parity transformation. The effective operators are thus scalar (1), pseudo-scalar ( $\gamma^5$ ), vector ( $\gamma^\mu$ ), axial vector ( $\gamma^5\gamma^\mu$ ), or tensor ( $\sigma^{\mu\nu}$ ). These interactions can be connected to a specific particle physics theory, such as SUSY. For example, J. Engel *et al.* explicitly calculate coupling coefficients under the minimal

supersymmetric extension to the SM of the following Lagrangian density [83]:

$$\mathcal{L} = \frac{g^2}{2M_W^2} \sum_q \left( \bar{\chi} \gamma^5 \gamma^\mu \chi \bar{q} \gamma_\mu [V_q + A_q \gamma^5] q + \bar{\chi} \chi S_q \frac{m_q}{M_W} \bar{q} q + \bar{\chi} \gamma^5 \chi P_q \bar{q} \gamma^5 q \right) . \quad (2.29)$$

Here,  $\chi$  and  $q$  are the WIMP and quark fields, with  $q$  also acting as an index for quark type, and the operator coefficients  $V_q$ ,  $A_q$ ,  $S_q$ , and  $P_q$  can be calculated by evaluating the relevant Feynman diagrams (see eq. 3.6 of [83]).

A more general approach, however, is to leave these coefficients as they are, assuming as little as possible about the fundamental theory. In Refs. [84, 85], for example, all Lorentz-invariant combinations of operators are considered. As it turns out, in the non-relativistic limit of direct detection experiments, vector and scalar couplings reduce to spin-independent (SI) interactions, whereas spin-dependent (SD) interactions arise from axial vector coupling. Other operators are suppressed at these low energies by momentum dependent terms, and are not typically considered among the main results published by direct detection experimentalists (with notable exceptions, discussed below).

Having defined effective WIMP-quark coupling coefficients, the next task is to translate these to WIMP-nucleon coupling parameters. Once again, though, we can either (i) explicitly relate these coefficients under the assumption of an effective model (scalar, vector, axial vector), using knowledge of quark structure in nucleons, or (ii) accept the effective WIMP-nucleon coefficients as given, remaining agnostic to the underlying theory. Option (ii) is usually adopted by direct detection experiments, but option (i) is necessary for comparing results to collider searches. Ref. [86] provides a convenient

framework for this kind of comparison, employing a simplified model in which the WIMP is a Dirac fermion whose interactions with quarks are governed by  $s$ -channel exchange of a  $Z'$  mediator.

With effective WIMP-nucleons now in hand, it is useful to express the WIMP-nucleon cross section in the zero momentum transfer limit:

$$\sigma_{p,n} \equiv \int_0^{4\mu_{p,n}^2 v^2} \frac{d\sigma(q=0)}{dq^2} dq^2 \quad (2.30)$$

$$= 4 G_F^2 \mu_{p,n}^2 C_{p,n} \quad , \quad (2.31)$$

where the subscript  $p, n$  indicates either a proton or a neutron. This has been calculated from the generic eq. 2.1, integrating over the range of possible  $q$ . Alternatively, in the case of SI interactions, we could also write:

$$\sigma_{p,n}^{\text{SI}} = \frac{4\mu_{p,n}^2 f_{p,n}^2}{\pi} \quad (2.32)$$

using the effective WIMP-proton(neutron) coupling constants  $f_{p,n}$ . This standard cross section can be defined for WIMP-nucleus scattering as well, giving for an isotope with mass number  $A$  and atomic number  $Z$  [3]:

$$\sigma_A^{\text{SI}} = \frac{4\mu_A^2}{\pi} [Z f_p + (A - Z) f_n]^2 \quad (2.33)$$

from which, making the typical assumption that  $f_p = f_n \equiv f_N$  for SI interactions,

$$\sigma_A^{\text{SI}} = \frac{4\mu_A^2 A^2 f_N^2}{\pi} \quad (2.34)$$

$$= \left( \frac{\mu_A A}{\mu_N} \right)^2 \sigma_N^{\text{SI}} \quad , \quad (2.35)$$

plugging in eq 2.32 in the second line. Here, at last, is the oft-touted  $A^2$  enhancement that benefits heavy nuclei in SI scattering sensitivity. For especially heavy WIMPs,  $\mu_A^2 \rightarrow m_A^2 \propto A^2$ , and this becomes a  $A^4$  boost. This property comes about from the coherent addition of nucleon matrix elements in SI scattering (it is absent in SD interactions), an assumption that is valid at low momentum transfer, and corrected for at higher  $q$  by the form factor, as discussed in Sec. 2.2.5.

We can relate  $\sigma_A^{\text{SI}}$  to  $C_A^{\text{SI}}$  via 2.31:

$$C_A^{\text{SI}} = \frac{\sigma_A^{\text{SI}}}{4G_F^2 \mu_A^2} = \frac{A^2 \sigma_N^{\text{SI}}}{4G_F^2 \mu_N^2} \quad , \quad (2.36)$$

which allows us to express the differential SI WIMP-nucleus scattering rate (eq. 2.19) in terms of the WIMP-nucleon zero-momentum transfer cross section:

$$\frac{dR}{dE_R} = \sigma_N^{\text{SI}} \frac{A^2 m_A N_T \rho_\chi}{2m_\chi \mu_N^2} F^2(E_R) \int_{v_{\min}(E_R)}^\infty \frac{d^3\vec{v}}{v} f_\oplus(\vec{v}, \vec{v}_{\text{obs}}) \quad . \quad (2.37)$$

This is an appealing form for this expression, as it allows for the construction of a signal model (for a given WIMP mass) normalized by the physical unknown that is the WIMP-nucleon cross section for arbitrary target isotopes. This puts all direct detection experiments on common ground, provided that they use the same astrophysical parameters (of the SHM) and nuclear form factor calculations. That way, even if either of

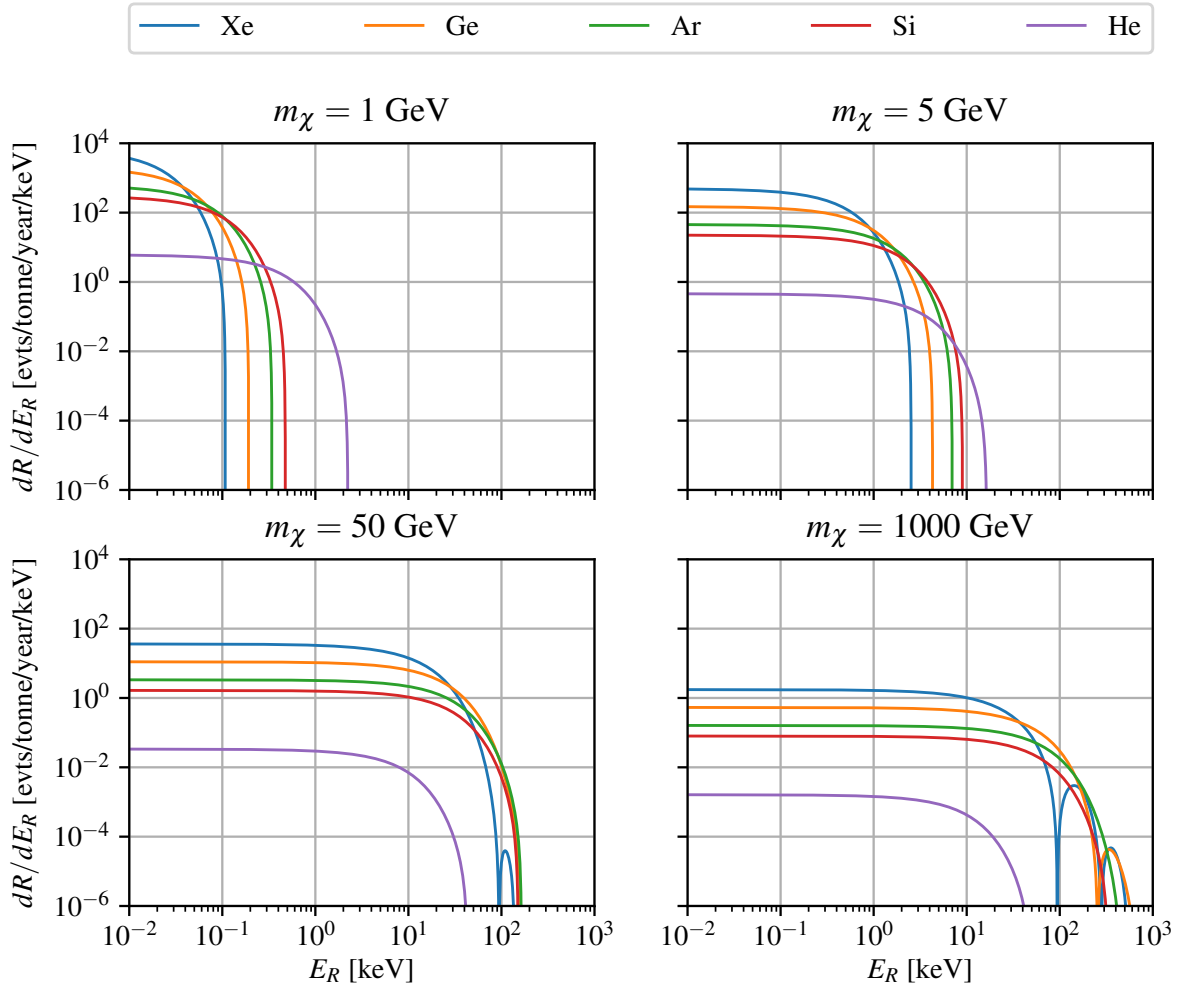


Figure 2.6: Differential event rate for SI scattering, normalized to WIMP-nucleon cross section  $\sigma_N^{\text{SI}} = 1 \text{ zb}$ . A wide range is used on the axes showing both extremes of the spectra, such that the effects of the form factor bounces can be seen in the heavier nuclei (for higher mass WIMPs).

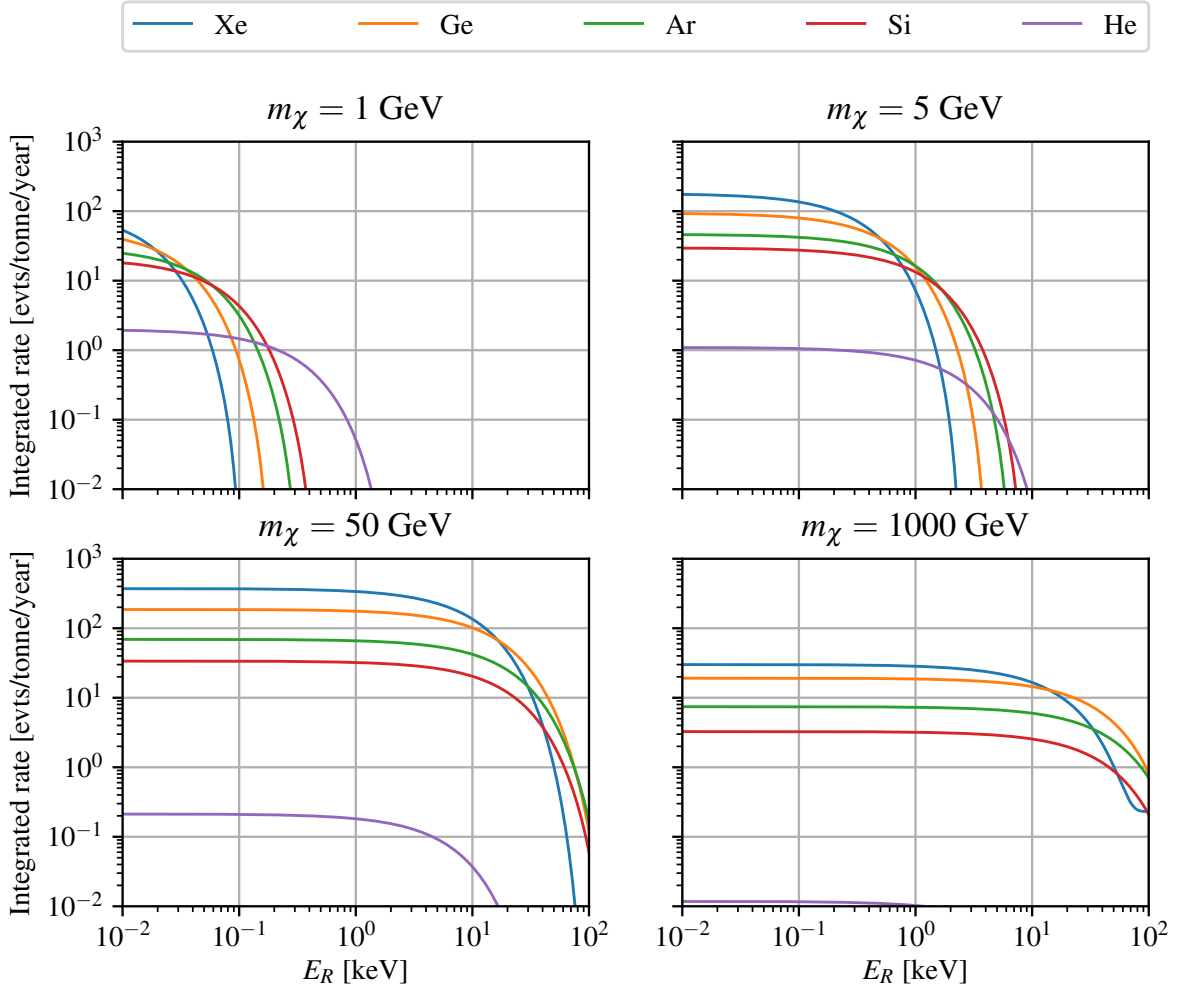


Figure 2.7: Integrated event rate for SI scattering, normalized to WIMP-nucleon cross section  $\sigma_N^{\text{SI}} = 1 \text{ zb}$ . The curves show the total number of expected events in a year-long exposure of a 1000 kg detector, integrating the spectrum above  $E_R$ .

these models carry significant uncertainty, comparisons between direct detection results are still apples-to-apples. Comparisons to LHC or indirect DM searches, however, must acknowledge the caveat that direct detection results have some model-dependence.

Figure 2.6 shows the results of eq. 2.37 after fixing  $\sigma_N^{\text{SI}} = 1$  zb. Figure 2.7 shows the total integrated rate as a function of detection threshold  $E_R$ . For a 50 GeV WIMP, then, a tonne-scale Xe detector with a 3 keV threshold would expect to see hundreds of events per year, given  $\sigma_N^{\text{SI}} = 1$  zb. The best upper limits on 50 GeV WIMPs are currently closer to 0.1 zb ( $10^{-46}$  cm<sup>2</sup>) [20], which would imply tens of events per year. For lighter WIMPs, the top two panels show the advantages that come with using a low-mass target nucleus, assuming reasonable ( $\sim 1$  keV) detection thresholds.

So far, we have closely examined only the SI interaction. It is customary to assume that only SI or SD scattering is possible, and to set limits accordingly (though in principle both could occur). SD scattering is given special treatment in Chapter 7, and a notable difference in that analysis is that the WIMP-proton and WIMP-neutron couplings are not assumed to be identical. The form factors used are also far more complex, necessitating detailed nuclear modeling.

Not considered in this work, but an area of active research, are non-relativistic EFT operators other than the vanilla SI and SD ones. As mentioned, these potential interactions (in which WIMPs might couple, for example, to the angular momentum of the nucleus) would be subdominant to SI and SD coupling; however, SI and SD interactions could be suppressed by some cancelation mechanism, leaving only these operators as a di-

rect detection probe. Fitzpatrick *et al.* thoroughly catalog all possible EFT operators in Ref. [87], presenting new form factors to describe the relevant nuclear responses. In total, the 14 operators and pairwise interference of matrix elements lead to a 28-dimensional space of coupling coefficients. With so many free parameters, it is no wonder that some authors have devised scenarios in which the DAMA WIMP interpretation squares with the null results of other experiments [88, 89]. Still, an exhaustive analysis of this parameter space using inputs from direct and indirect DM searches finds significant tension with the DAMA claim [90]. Even so, the EFT operators make a compelling case for supporting a diversity of DM experiments with different target materials.

# Chapter 3

## The LUX experiment

### 3.1 Time projection chambers

The LUX detector is a dual-phase time projection chamber (TPC), capable of reconstructing the 3D position of a particle interaction occurring within its active volume. “Dual-phase” refers to the use of both liquid xenon (LXe) and gaseous xenon (GXe) in the detector. In general, the target material need not be xenon; dual-phase argon TPCs are also employed in DM searches [91, 92] and helium TPCs have been proposed [68]. Single-phase TPCs are commonly used in high energy particle physics detectors, where they were first developed [93].

Fig. 3.1 illustrates how the LUX TPC operates. First, an incident particle (perhaps a WIMP!) travels through the liquid target, colliding with a Xe atom and depositing energy (see Sec. 2.2.2 for the case of WIMP-nucleus elastic scattering). This energy is released by the recoiling particle in the form of prompt scintillation, ionization, and heat. Whereas

some detection techniques make use of the thermal excitation channel, this information is lost in LXe TPCs. Instead, the scintillation photons and ionization electrons constitute the observable quanta. The former can be detected by photomultiplier tubes (PMTs), shown in Fig. 3.1 as colored circles at the top and bottom of the TPC cylinder. This primary signal is referred to as S1. As for the liberated ionization electrons: in the presence of an induced electric field, some escape recombination with Xe ions and drift vertically to the surface of the liquid. Here, a stronger electric field is applied (omitted from the figure) in order to extract the electrons into the gas phase. As this cloud of electrons is accelerated through the GXe, a second light signal (S2) is generated via electroluminescence (also called proportional scintillation).

The S1 and S2 signals in the PMTs are read out via amplification and digitization electronics, resulting in the voltage pulses drawn along the right side of Fig. 3.1. The total energy deposited in the event can be estimated by the magnitude of these pulse areas, which are proportional to the energy quanta. The  $z$  position of the interaction site is inferred from the time delay separating the S2 from the S1 (called the “drift time”), using the drift velocity of electrons in LXe. In the ideal case of perfectly vertical field geometry, this relationship is simply linear: depth below liquid surface is given by drift time times drift velocity. Meanwhile, the  $(x, y)$  position of the event can be reconstructed from the distribution of S2 photons incident on the top PMT array. Although electroluminescence is an isotropic photon emission process, the proximity of the top PMTs to the S2 production sites allows for  $(x, y)$  localization. In other words, geometric efficiency

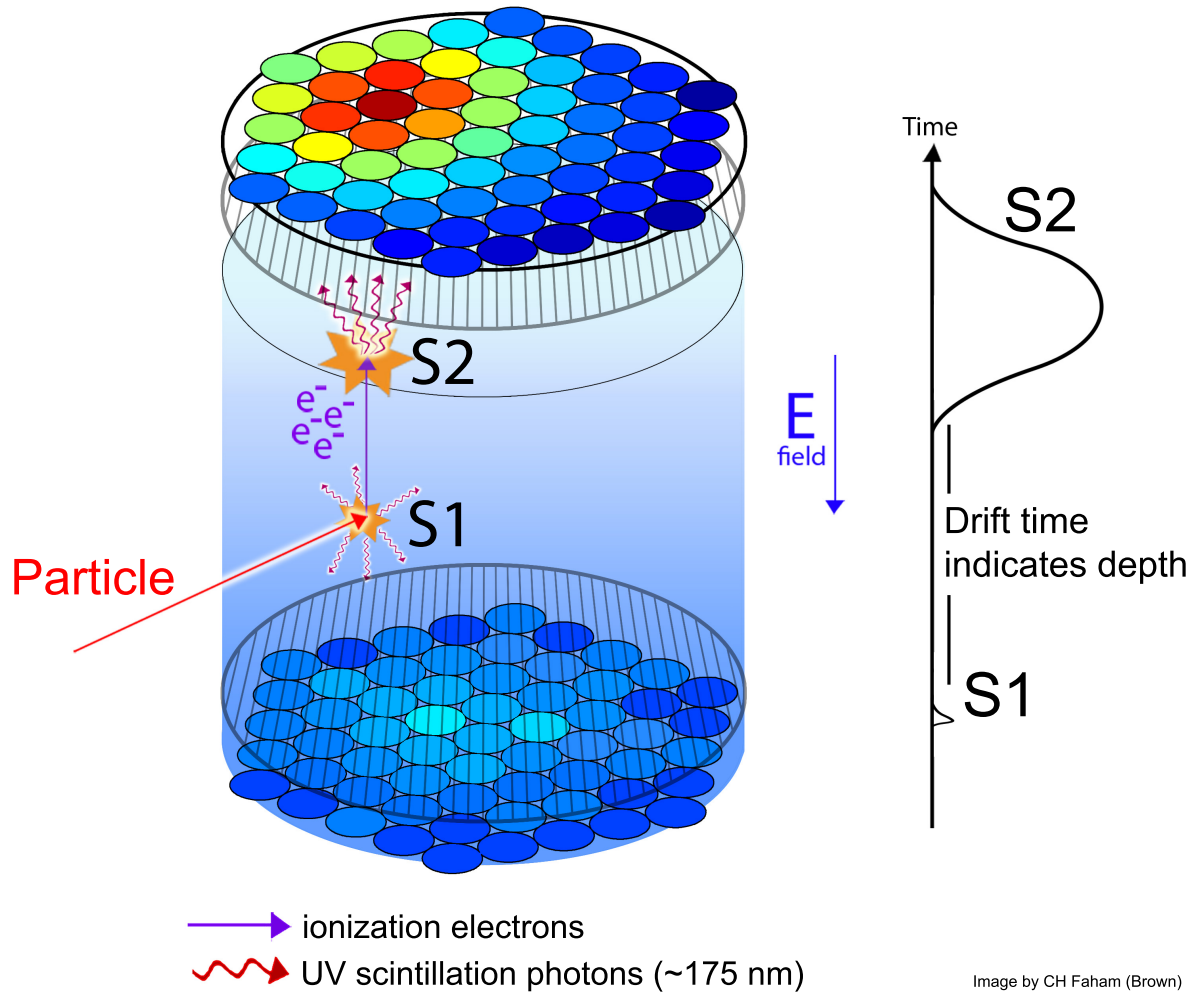


Figure 3.1: Cartoon of the TPC detection principle. Particle collisions produce scintillation and ionization, measured as S1 (prompt photons) and S2 (electroluminescence) PMT signals, respectively. The shaded blue region represents the LXe, with GXe situated above. The striped circles are the cathode and anode high voltage grids, which generate the electric drift field. The LXe within this field is called the “active volume.” PMTs are arranged in two arrays, one beneath the active volume (in the LXe), and one above (in the GXe).

causes the hit pattern illustrated in Fig. 3.1. Again assuming perfectly vertical drift field lines, the  $(x, y)$  position of the S2 production site will match that of the original interaction.

The data collected from the LUX PMTs is therefore rich in information, capturing the energy and 3D position of particle collisions within the active volume. Both of these observables are important for the identification of potential WIMP events. Recoil energy has been discussed in the previous chapter, and position within the detector is crucial for rejecting background events originating from radioactive sources outside the detector. Such events are concentrated near the TPC boundaries, since most gammas and X-rays are incapable of penetrating deep into the LXe bulk.

Beyond position and energy, however, yet another quantity vital to signal identification is available: the ratio of S2 light to S1 light. The distribution of this ratio differs for electronic recoil (ER) and nuclear recoil (NR) scattering events, where the latter is the object of most WIMP searches. ERs, on the other hand, occur when the incident particle scatters off a bound electron. Beta, X-ray, and gamma radiation—responsible for the vast majority of the background events in LUX that pass selection cuts—all generate ERs. Thus, distinguishing ERs from NRs is another tool used to mitigate background noise and enhance sensitivity to DM particles.

## 3.2 Liquid xenon physics

As mentioned, an energy deposition in LXe is partitioned into three channels. The recoiling electron or nucleus travels along a track, leaving ionized and excited Xe atoms<sup>1</sup> in its wake, as well as heat. This process is modeled simply by

$$E_{\text{dep}} = fW(n_i + n_{\text{ex}}) \quad , \quad (3.1)$$

where the total deposited energy  $E_{\text{dep}}$  is equal to the work function  $W$  times the total number of quanta produced, i.e. the sum of  $n_i$  (number of electron-ion pairs) and  $n_{\text{ex}}$  (number of excitons). The quenching factor  $f$  accounts for the fraction of energy lost to heat. In ER collisions, this fraction is small enough to be ignored [95], such that  $f_{\text{ER}} \equiv 1$  and the  $\sim 5\%$  heat loss is included in the definition of  $W = 13.7 \pm 0.2$  eV [96]. The quenching factor for NRs  $f_{\text{NR}}$  is significantly smaller than unity, since the recoiling nucleus will participate in secondary NRs that fall below the excitation threshold  $W$ . The microphysics of this process is described by the Lindhard theory [97], and although the NR quenching factor varies with  $E_{\text{dep}}$ , a typical value is  $f_{\text{NR}} \sim 1/4$ .

Note that  $n_i$  and  $n_{\text{ex}}$  refer to the initial quanta produced along the track of the recoiling particle. Naively, we might expect the number of observed S1 photons to be directly proportional to  $n_{\text{ex}}$ , since de-excitation of excitons produces the 178 nm light (“vacuum ultraviolet” or VUV photons) which the PMTs detect as S1. Similarly, we would expect the size of the S2 signal to go as  $n_i$  (note that electroluminescence also

<sup>1</sup>In fact, these excitons are unstable dimers  $\text{Xe}_2^*$ , though the details of this chemistry can be safely ignored for our purposes. However, it should be noted that S1 pulse shape discrimination between ERs and NRs can be achieved by exploiting some of these details:  $\text{Xe}_2^*$  occurs in either a triplet ( $\tau = 3$  ns) or singlet state ( $\tau = 24$  ns), which are generated in different proportions for ERs and NRs [94].

generates 178 nm photons). In this simplified picture, then, the exciton-ion ratio

$$\alpha \equiv \frac{n_{\text{ex}}}{n_{\text{i}}} \quad (3.2)$$

uniquely governs the ratio of S2 and S1 signals. For NRs, this ratio is roughly unity [96], whereas for ERs,  $\alpha \sim 0.2$  (energy is primarily funneled into the ionization channel) [98]. Although this fundamental difference in  $\alpha$  plays a significant role in discriminating between ERs and NRs (based on their charge-to-light ratio), another process also has an effect: following ionization, some electrons will *recombine* with Xe ions to produce another batch of Xe excitons, effectively stealing from the S2 signal and enhancing the S1.

If a fraction  $r$  of the initial electron-ion pairs recombine, then we have:

$$n_{\gamma} = n_{\text{ex}} + r n_{\text{i}} = (\alpha + r)n_{\text{i}} \quad (3.3)$$

$$n_{\text{e}} = (1 - r)n_{\text{i}} \quad (3.4)$$

where  $n_{\text{e}}$  and  $n_{\gamma}$  are the number of electrons and photons that escape the interaction site, respectively. It is these quantities that determine the S1 and S2 signal sizes:

$$S1 = g_1 n_{\gamma} \quad (3.5)$$

$$S2 = g_2 n_{\text{e}} \quad (3.6)$$

The italicized pulse sizes  $S1$  and  $S2$  are measured in units of “detected photons” (phd), and are normalized to correct for position-dependent inefficiencies. The S1 gain  $g_1$  is the

probability that a scintillation photon leaving the interaction site will strike a PMT photocathode and produce a photoelectron (phe); it is therefore a product of the geometrical light collection efficiency and the averaged PMT quantum efficiency. On the other hand, the S2 gain  $g_2$  depends on the efficiency with which drifted electrons are extracted from the liquid into the gas phase ( $\epsilon$ ) as well as the average pulse size (in phd) of a single extracted electron (SE):

$$g_2 = \epsilon \times \text{SE} \tag{3.7}$$

Extraction efficiency depends on the applied electric field, as does SE, which depends further on detector geometry and GXe pressure. In LUX,  $g_1 \sim 0.1$  phd/photon and  $g_2 \sim 12$  phd/electron, as derived from calibrations discussed later in this chapter.

The recombination fraction  $r$  depends strongly on the ionization density of the track, and also on electric field. Modeling this quantity in a probabilistic framework—for the purpose of simulating both WIMP NR signals as well as ER backgrounds—is the subject of ongoing research. The Noble Element Simulation Technique (NEST) software represents the most substantive effort in this endeavor [99], and is employed extensively in LUX analyses. Comprehensive treatments of this topic can be found in Refs. [14, 96, 100–103]. Suffice it to say here that since NRs are typified by shorter tracks with greater ionization density than ERs,  $r$  is to some extent invariant under changes of electric field for nuclear recoils. As for the more sprawling ER tracks, increasing the electric field has the effect of improving an electron’s chances of escaping recombination. Thus, the region in  $S1$ – $S2$  space populated by ERs varies significantly with electric field [104]. For both ERs and

NRs, the effect also depends on  $E_{\text{dep}}$ . This subtlety holds serious ramifications for the second LUX exposure, where deformations in the electric field geometry led to spatially varying charge and light yields.

The effects of recombination can, however, be ignored when reconstructing energy from the combined S1+S2 detector response. From eqs. 3.3 and 3.4, we can see that  $n_\gamma + n_e = n_{\text{ex}} + n_i$ , which makes intuitive sense under the assumption that all excitons and electron-ion pairs each result in an escaping photon or electron with perfect efficiency.<sup>2</sup>

In that case, for ERs, we can rewrite eq. 3.1 as:

$$E_{\text{dep}} = W(n_\gamma + n_e) \quad (3.8)$$

$$= W\left(\frac{S1}{g_1} + \frac{S2}{g_2}\right) \quad (3.9)$$

We can do the same for NRs, by restoring the quenching factor  $f$  back into the equation. This is a more complicated procedure, however, since  $f$  is itself energy-dependent. This is where the Lindhard theory enters, which will be discussed briefly later in this chapter. However, we may not know whether a particular event is the result of an NR or an ER. Thus, if energy is reconstructed under the assumption of an ER (i.e.  $f = 1$ ), then this is reflected in the unit  $\text{keV}_{\text{ee}}$  (where “ee” stands for “electron equivalent”). Similarly, if the energy calculation assumes a NR deposition, then the unit  $\text{keV}_{\text{nr}}$  is used.

---

<sup>2</sup>This is known to be a simplification, as so-called Penning effects can quench the photon production from excitons [105]. These are taken into account in the NEST model [99].

## 3.3 The LUX detector

### 3.3.1 Design and operation

In designing a dark matter detector, the primary goal is sensitivity to WIMP signals. This means optimizing efficiencies and driving down thresholds, but also reducing potential backgrounds. Another concern, of course, is that the detector must live in the real world: pragmatic matters such as cost, ease of operation, and safety must be considered as well. The LUX detector paper [9] goes through the design choices motivated by these criteria in detail, highlights of which will be reviewed in this section.

The location of LUX's deployment is arguably its most fascinating design choice. While active, the LUX TPC was housed inside a 70,000 gallon water tank, itself nestled nearly a mile underground in a gold mine turned science lab.<sup>3</sup> Background mitigation drives both of these extreme measures: the 4850 feet of rock overburden shield LUX from cosmogenic radiation (muons in particular, discussed in Chap. 4), while the water buffer blocks gamma rays and neutrons emanating from the cavern rock (see Sec. 3.5). In addition to these dramatic radiation shields, background mitigation was achieved by careful screening of materials used in the construction of detector components. The copper used in the major structural elements shown in Fig. 3.2 are an example of this, as are the titanium cryostats themselves [107].

In order to have a liquid xenon detector, one must have liquid xenon. In its active

---

<sup>3</sup>The Sanford Underground Research Facility (SURF, formerly the Homestake gold mine) in Lead, South Dakota, is home to LUX as well as a number of other low-background experiments. Most auspiciously, the cavern occupied by LUX was once host to Ray Davis's Nobel-winning neutrino experiment [106].

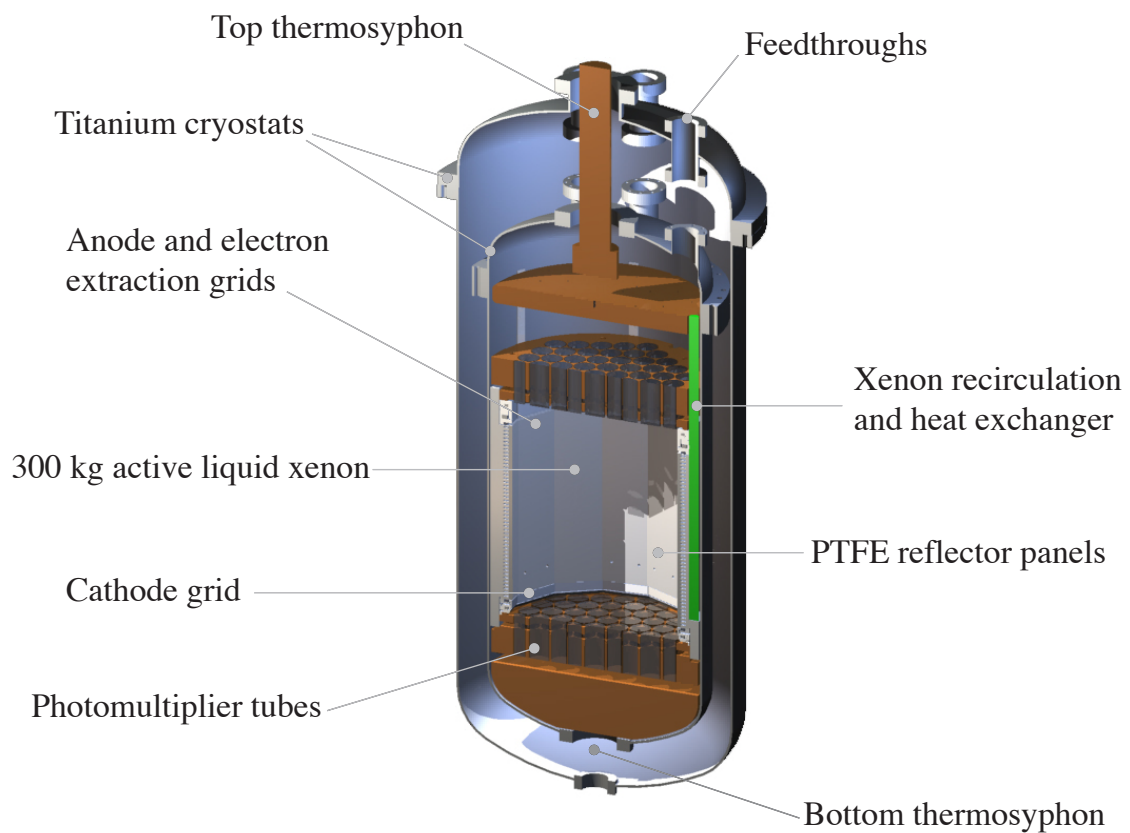


Figure 3.2: Cross-sectional drawing of the LUX cryostats. Taken from Ref. [9].

volume (i.e. the region enclosed by the detector walls between the high voltage grids establishing the drift field), LUX contained  $\sim 250$  kg LXe kept at roughly 175 K (at  $\sim 2$  atm). This temperature is far more convenient cryogenically speaking than the millikelvin levels required by crystal germanium detectors like CDMS. A thermosyphon (TS) system is used to cool LUX, powered by gravity and a reservoir of liquid nitrogen situated *above* the detector. Closed loops of nitrogen gas are thermally coupled to the reservoir as well as the detector below; gas is thus liquefied at the top of the loop, falls to the warmer detector, where it evaporates and subsequently rises back up to the reservoir. The  $N_2$  pressure in the TS loops can be adjusted, effectively tuning the cooling power. Low and high power electric heaters supplement this system, for temperature fine control and rapid detector warmup, respectively.

Xenon has no naturally occurring long-lived radioactive isotopes, so pure Xe is an excellent target material. In practice, though, even research-grade Xe contains the unstable contaminants  $^{85}\text{Kr}$  (11 year half-life) and  $^{39}\text{Ar}$  (269 year half-life) in concentrations problematic for WIMP searches. Both isotopes decay (mostly) via “naked” beta emission with  $< 1$  MeV Q-values, and would generate an unacceptable number of ER events. LUX therefore developed and carried out a Xe purification program to reduce the concentration of these contaminants to manageable levels. Using a charcoal adsorption-based chromatography system to separate the gases, a factor of nearly 40 reduction in  $^{85}\text{Kr}$  concentration was achieved [108].

Even safely ensconced within the LUX detector, Xe is vulnerable to contamination

from outgassing detector components. Oxygen and other electronegative impurities capture ionization electrons as they drift to the liquid level, reducing the S2 detection efficiency. To combat this, Xe was constantly cycled through a circulation system in the gas phase, passing through a heated zirconium getter before reentering the detector through a series of heat exchangers [109]. A sampling system in line with the gas circulation plumbing allowed for regular monitoring of Xe purity [110, 111], demonstrating efficient purification by the getter. Noble contaminants like Kr and Ar, however, cannot be extracted by the getter—an air leak reintroducing these background sources to the Xe would necessitate recovery and transportation of the Xe to the gas chromatography setup. As such, great precautions were taken in procedures involving manipulation of the circulation system.

Figure 3.3 shows a closer look at the LUX detector internals. PTFE (polytetrafluoroethylene) panels surround the TPC, possessing high VUV reflectivity and enhancing S1 detection efficiency. The five high voltage (HV) grids are also shown, as well as the field rings that shape the drift field. The bottommost grid shields the PMTs from the great potential established by the cathode, directly above it. The cathode-gate potential is responsible for the drift field in the LXe, with the gate grid situated just below the liquid level. Just above the liquid level, the anode is positioned; the gate-anode potential creates the extraction field that allows for S2 light production. Finally, the topmost grid shields the PMT array from the anode. For details on the construction and performance of the HV grids, see Ref. [112].

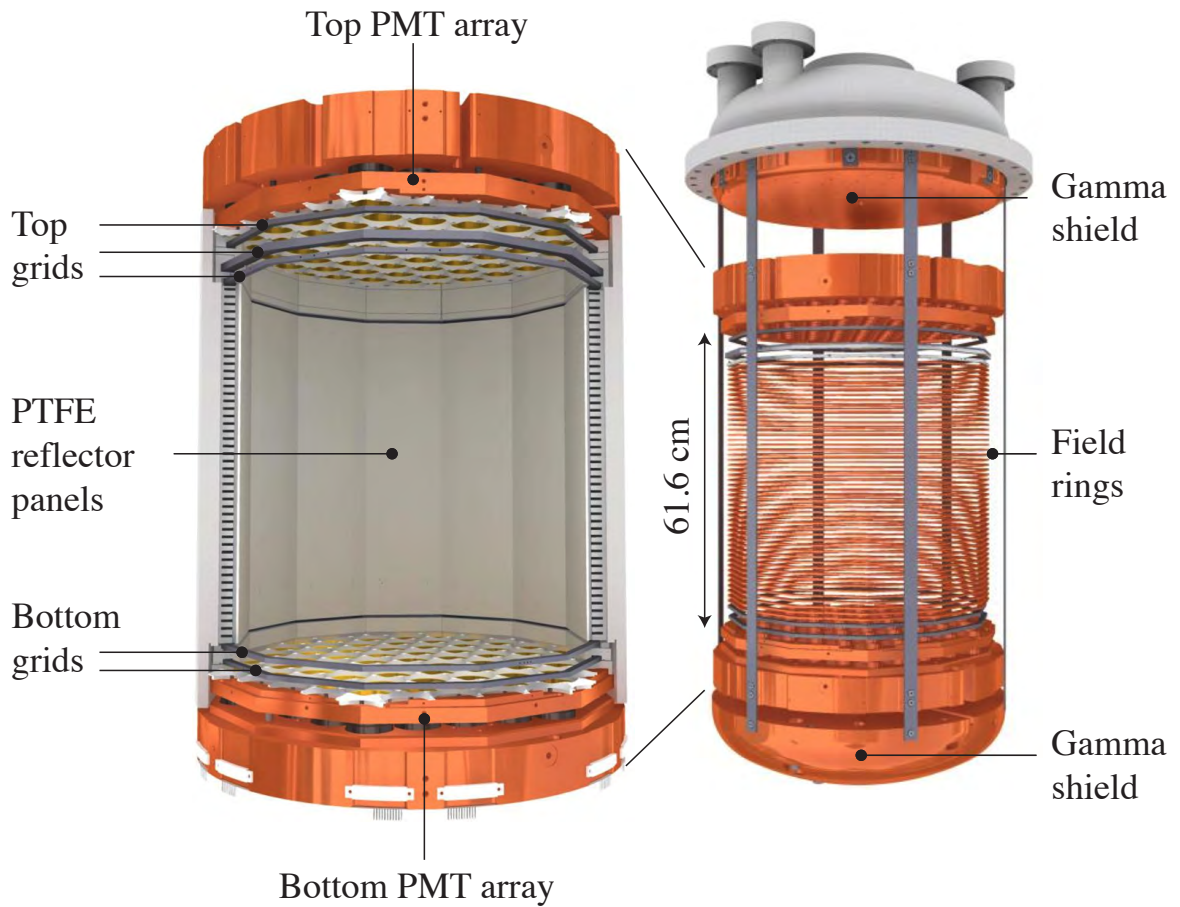


Figure 3.3: Drawing of the LUX detector internals, with critical components labeled. Taken from Ref. [9].

The LUX PMT arrays were designed to answer the age-old question: if a WIMP collides with a Xe nucleus in a TPC but no one is there to see it, does it make any light? LUX used 122 Hamamatsu R8778 PMTs—61 in the top array and 61 in the bottom—to detect 178 nm photons emitted in the S1 and S2 light production processes. The Hamamatsu R7887 PMTs have a typical quantum efficiency of 33%, and were developed with low radioactivity as a key goal. Information on the LUX PMTs, their commissioning, and performance can be found in Ref. [113]. In the LUX WIMP searches, the PMTs were biased to voltages between -1 kV and -2 kV, to achieve gains of  $\sim 4 \times 10^6$  (for an average single photoelectron pulse area of  $\sim 16$  mVns at the PMT output).

An important distinction should be made between the traditional units of phe (photoelectrons) and the LUX units of phd (detected photons). It was discovered that a single VUV photon incident on the R7887 PMT photocathode could induce the emission of *two* electrons [114]. In such a scenario, the signal size would be quantified as 2 phe but only 1 phd. The probability of double phe emission can be as high as  $\sim 20\%$  for VUV photons, but is zero for the blue LED light used in gain calibrations. This means the average single phe (sphe) size as measured by the LED calibration is lower than the average pulse size for a single detected VUV photon. Single phd calibrations were therefore performed using VUV light to calculate the LUX PMT gains (see Ref. [11]).

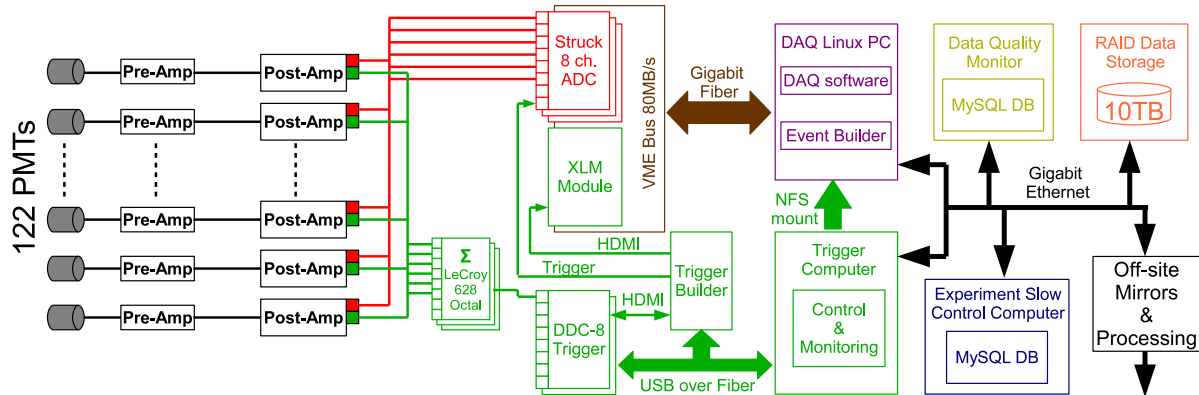


Figure 3.4: Flowchart depicting the signal path, starting at the LUX PMTs and traversing the data acquisition system. Taken from Ref. [10].

### 3.3.2 Electronics and data acquisition

The design and performance of the LUX analog and digital electronics are documented in Refs. [10, 115, 116]. As shown in Fig. 3.4, raw PMT signals are shaped and amplified by two sets of amplifiers and subsequently split into two copies. One copy of the voltage waveforms passes through the LUX FPGA-based trigger system [10, 116], which generates a flag when it identifies an event of interest in the datasream. The other copy of the data is sent to the analog to digital converters (ADCs), where it is written to disk. Each PMT has its own channel in the recorded data, though as can be seen in Fig. 3.4, PMT channels are summed into groups for the triggering logic.

Unlike with traditional “online” trigger systems, LUX data can be recorded without a trigger condition being met. Trigger information is digitized alongside the PMT waveforms in dedicated ADC channels, allowing for offline use in compressing the raw data into blocks of event-level data. Note, however, that the data acquisition system (DAQ) does allow for online triggering: this was referred to as “VPTG mode,” short for “Valid

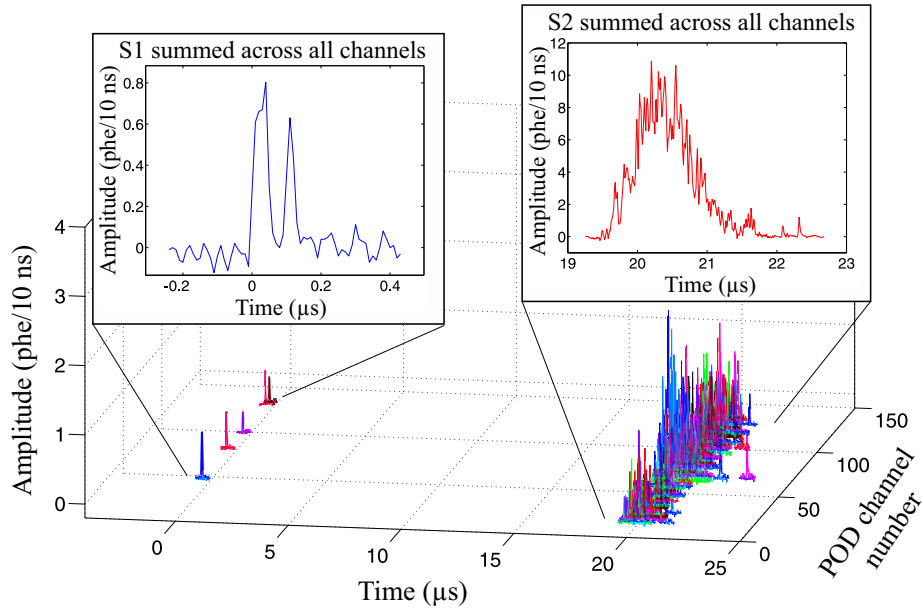


Figure 3.5: Example of a low-energy event ( $\sim 1.5 \text{ keV}_{ee}$ ) as seen in the raw datas. Each POD channel corresponds to a single PMT. Taken from Ref. [10].

Pulse Trigger Gate.” This mode was not used for TPC data-taking, the reasoning being that if an unforeseen systematic bias in the trigger was rejecting events of interest to some future analysis, potentially valuable data would be lost forever. In the offline triggering mode, the raw data would always be saved, and such an analysis could still be performed even if there were a problem with the trigger.

Still, with 122 channels of PMT voltage data being digitized at 100 MHz, it would not be feasible to store *every* 14-bit sample over the course of a years-long WIMP search.<sup>4</sup> Instead, the ADCs were operated in “POD” mode, meaning “Pulse Only Digitization.” When the voltage in a certain channel exceeds the POD detection threshold, samples are written to a memory bank from the buffer until the POD end threshold is reached. A fixed

<sup>4</sup>This would require roughly an exabyte of storage, and would be wildly impractical from a data processing perspective.

number of samples preceding and succeeding this range are also recorded. The thresholds are tuned to achieve high efficiency for single photoelectron (sphe) digitization while also rejecting baseline noise. The POD detect threshold of 1.5 mV used in the WIMP searches resulted in a typical sphe acceptance of  $> 95\%$  [11].

Figure 3.5 shows an example of a low-energy S1+S2 event as seen in the raw data output of the ADCs. A small S1 pulse, lasting fewer than 20 samples ( $0.2 \mu\text{s}$ ), appears as roughly 5 sphe scattered amongst as many PMT channels. 20  $\mu\text{s}$  later—corresponding to an event depth of about 3 cm below the liquid level—the taller and broader S2 pulse can be seen. This channel-wise POD data, written in discrete sequences corresponding to ADC memory bank downloads, is saved in binary files with the `.dat` extension. This is the rawest and least filtered form of the LUX data. Binary files with the `.evt` extension are the output of the event-building stage of data processing: this algorithm searches for trigger channel flags, and collects all PODs occurring within .5 ms of the trigger (before or after), saving them into an event object. A trigger hold-off of 1 ms ensures that PODs are not duplicated in separate events. The width of this event window is driven by the maximum drift time in LUX. `.evt` files differ from `.dat` files only in their organization and their omission of POD data not occurring near a trigger. Further data reduction is necessary for the purposes of expedient WIMP search analyses.

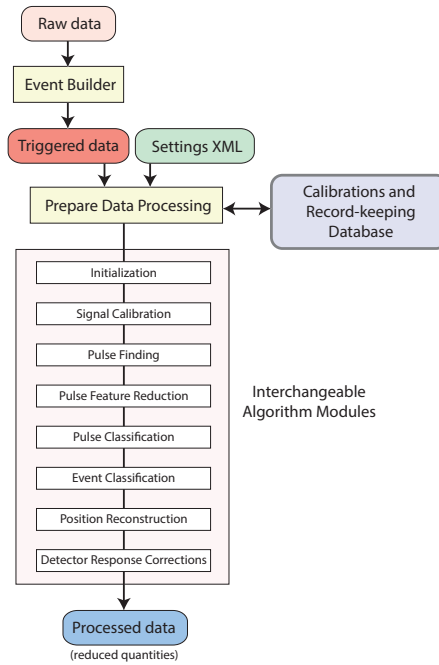


Figure 3.6: Schematic of the LUX data processing framework. Taken from Ref. [11].

### 3.3.3 Data processing framework

The LUX data processing framework (DPF) extracts essential information from the raw data and saves it in output `.rq` binary files (“RQs” meaning “reduced quantities”). RQs are calculated and stored for each event, and include quantities at the event-level (e.g. number of identified pulses, trigger timestamp), pulse-level (e.g. area, width, type), and channel-level (pulse area fraction in a given PMT). The DPF has a modular structure: data reduction algorithms are implemented as modules, called sequentially by a Python wrapper, and incrementally add condensed information to the output `.rq` file. In this way, modules can be written in any programming language, and can be easily swapped out for alternate versions. In a given data processing run, the choices of which modules to use (and also what their input parameters should be) are specified in an `.xml` file.

The DPF will generate an ID unique to that configuration, which is saved in a MySQL database. Figure 3.6 shows the organization of the LUX DPF.

Initial modules in the DPF prepare the data for RQ calculation: baselines are subtracted; ADC counts are converted to phd/sample, using PMT gains; PODs from different channels that overlap in time are summed into the imaginatively named SUMPODs. A pulse-finding algorithm then scans the SUMPOD data, using boxcar filters of different widths to ensure identification of both large S2s as well as tiny sphe. Pulse-level quantities can now be calculated, including area, width, spike count, etc. A pulse classification algorithm then determines the *type* of the pulse, which can be “S1” or “S2”, but also “sphe” or “SE”, “other”, or in some algorithm versions, a merger of two pulses. This algorithm is crucial to the identification of so-called *golden events*, which arise predominantly from single-scatter interactions, the signature of a WIMP event. Gammas and neutrons often scatter more than once in the active volume, thus producing multiple S2s. Selecting for golden events, which consist of only one valid S2 following one valid S1, thus immediately rejects a significant number of background events.

Following the identification of S2 and S1 pulses, the position reconstruction module is run. This module is based on the Mercury algorithm developed for the ZEPLIN-III DM detector, another LXe TPC [117]. The LUX technique is described in the recently released Ref. [12]. Essentially, the algorithm makes use of light response functions (LRFs) and the S2 pulse area fractions in each PMT to search for the maximum likelihood  $(x, y)$  position of S2 generation. The LRFs are calculated in advance for each PMT by iterative

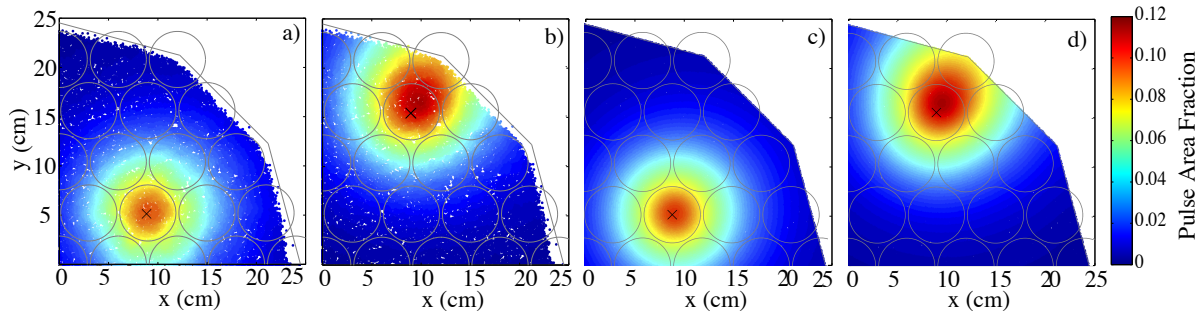


Figure 3.7: Illustration of position reconstruction in LUX. Panels a) and b) show the reconstructed positions of events from calibration data, obtained from an iterative fit, colored according to the fraction of S2 pulse area appearing in the PMT indicated with an “X”. Panels c) and d) show the corresponding light response functions used in the reconstruction algorithm. Taken from Ref. [12].

application of the fitting algorithm, using events from calibration data. Figure 3.7 shows the empirical and parametrized LRFs for two PMTs. Note that the LRFs for the higher radius PMT (panels b) and d)) exhibit radial asymmetry. This is a result of the highly reflective PTFE panels significantly altering the distribution of light. Including this effect in the LRFs represents an improvement of the LUX method over the ZEPLIN-III algorithm.

Figure 3.8a shows the reconstructed positions of uniformly distributed events selected from a calibration run. Interestingly, the striped pattern is not an artifact of the reconstruction, but rather a real clustering of electron extraction sites resulting from the positions of the HV grid wires. Figure 3.8b illustrates the origin of this effect: drifting electrons are bunched into narrow bands as they pass the gate grid (with wires running through the page), en route to the liquid-gas boundary, where S2 photon production begins. This phenomenon clearly limits the validity of the assumption that an S2 production site matches the  $(x, y)$  position of the original energy deposition. A further complication

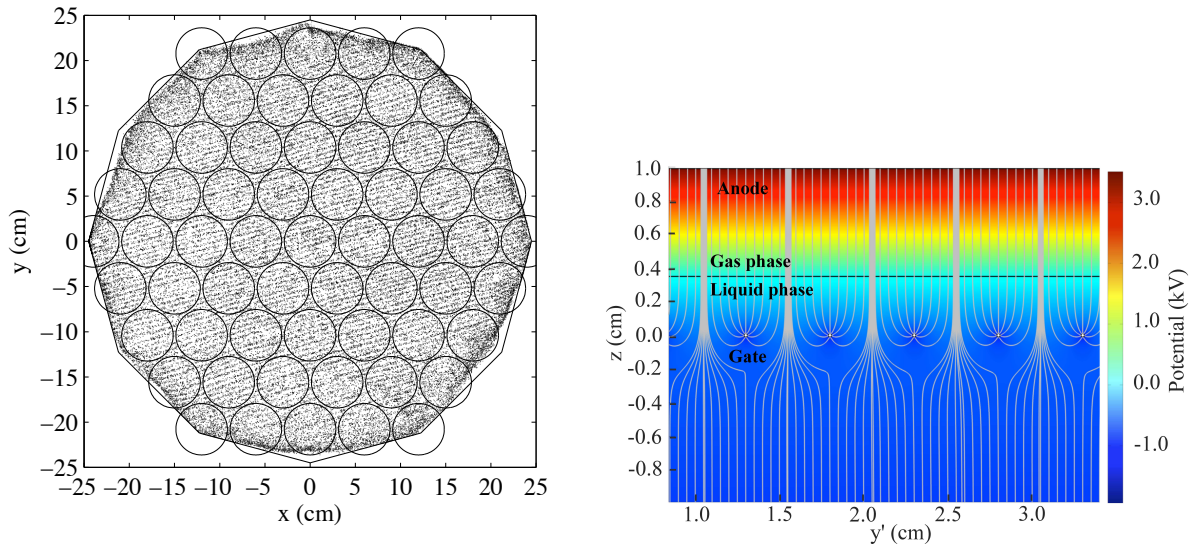


Figure 3.8: At left: reconstructed  $(x, y)$  positions of uniformly distributed calibration data. The stripes of high event density are the result of gate grid wires concentrating electron trajectories into tight bands, an effect shown at right. Taken from Ref. [12].

is the geometry of the drift field, which in the first LUX exposure was slightly “fringed.” Consequently, the radius of S2 production was slightly less than that of the scattering event. This effect was modeled and accounted for in the data processing, resulting in a set of corrected coordinates  $\{x, y\}$  as well as a set of raw coordinates  $\{x_{S2}, y_{S2}\}$  (see Table 3.1). In the second LUX data-taking run, the field geometry was more seriously distorted, requiring more careful treatment (discussed in Chap. 5).

The final major stage of data processing corrects pulse quantities for spatially varying detector efficiencies, known as “flat-fielding” in 2D imaging. In LUX, these are called “area corrections” (since we are correcting pulse areas) as opposed to the aforementioned “position corrections.” For S1 pulses, this correction normalizes the area to what would be observed (on average) if the same number of scintillation photons originated at the

Symbol	Unit	Description
$S1$	phd	Total number of detected photons (obtained from summed pulse area) corresponding to prompt scintillation VUV light.
$S2$	phd	Total number of detected photons (obtained from summed pulse area) corresponding to electroluminescence VUV light (proportional to charge). Sometimes notated $S2_{\text{raw}}$ to distinguish from $S2$ .
$S1$	phd	$S1$ , corrected for position-dependent detector efficiencies. Geometrical light collection efficiency dominates the correction factor (see Sec. 3.4.1). Sometimes notated $S1_c$ or $S1_{\text{corr}}$ .
$S1_{\text{spike}}$	phd	$S1$ (obtained from counting single photon peaks in PMT waveforms), corrected for position-dependent detector efficiencies.
$S2$	phd	$S2$ , corrected for position-dependent detector efficiencies. Electron lifetime dominates the correction factor (see Sec. 3.4.1). Sometimes notated $S2_c$ or $S2_{\text{corr}}$ .
$\mathbf{r}_{S2} = \{x_{S2}, y_{S2}, z_{S2}\}$	{cm, cm, $\mu\text{s}$ }	Reconstructed position of interaction, in the uncorrected $S2$ coordinate space. Also commonly seen in cylindrical coordinates $\{r_{S2}, \phi_{S2}, z_{S2}\}$ . Note that $z_{S2}$ is the drift time, sometimes notated as $t_{S2}$ or $t_{\text{drift}}$ .
$\mathbf{r} = \{x, y, z\}$	{cm, cm, cm}	Reconstructed position of interaction, corrected for electric field effects. Also commonly seen in cylindrical coordinates $\{r, \phi, z\}$ .

Table 3.1: LUX reduced quantities and associated units.

center of the TPC. S1 photon detection efficiency primarily varies with  $z$  position; because of total internal reflection at the liquid-gas interface, most S1 light is predominantly collected in the bottom PMTs. As such, S1 photons emitted near the bottom PMT array are  $\sim 50\%$  more likely to be detected than those originating near the liquid surface. S2 pulse areas also vary with  $z$  (for fixed  $n_e$ ), since longer drift times incur greater losses of charge to electronegative impurities. This loss is totally cancelled in the correction, as if the event occurred exactly at the center of the gate grid. Note that some  $(x, y)$  dependence exists as well, to some extent for S1 but more significantly for S2 pulse area efficiencies. As indicated in Table 3.1, corrected pulse areas are notated in italics:  $S1$  and  $S2$ .

Since electron lifetime (a function of LXe purity) can vary over the course of a long WIMP search exposure, the area corrections must be updated as well. Thus, date-dependent area correction maps are stored in a database which is queried by the DPF in the course of determining IQs (important quantities) required by the various data reduction modules. The LRFs, for example, can also change over time, as can PMT gains. These and other detector parameters are calculated and monitored using various calibration techniques, allowing for consistent and accurate estimation of key event observables by the DPF.

## 3.4 Calibrations

LUX has pioneered a number of novel calibration methods. The inherent difficulty in calibrating the ER response of LXe detectors lies in one of their great strengths: self-shielding. Gamma rays from sources external to the detector cannot penetrate far into the fiducial volume with high efficiency. Thus, for a high statistics calibration of detector response to events occurring in the central volume, radioactive sources must be introduced into the Xe itself. This is a frightening prospect, and runs counter to every onsite shifter's best instincts. The only ways such calibrations can be executed without compromising the WIMP search by irrevocably contaminating the Xe are (*i*) using a short-lived isotope that decays away rapidly, or (*ii*) ensuring the isotope is bound in a molecular form that is efficiently extracted by the getter. Calibrations using metastable krypton-83 ( $^{83\text{m}}\text{Kr}$ ) follow the first approach; those using tritium ( $^3\text{H}$ ) in the form of tritiated methane ( $\text{CH}_3\text{T}$ ) follow the second.

### 3.4.1 Krypton-83m

$^{83\text{m}}\text{Kr}$  decays to  $^{83}\text{Kr}$  in a two-stage process, releasing a total of 41.5 keV. The first transition of 32.1 keV has a half-life of 1.83 hours; it is followed by a 9.4 keV transition with a fleeting 154 ns half-life. This decay structure is convenient for a number of reasons. First of all, the monoenergetic total transition is well outside the range of WIMP scatters, so there is nearly no risk of contaminating the region of interest (the smaller secondary transition is never spatially or temporally isolated from the first). Second, the short

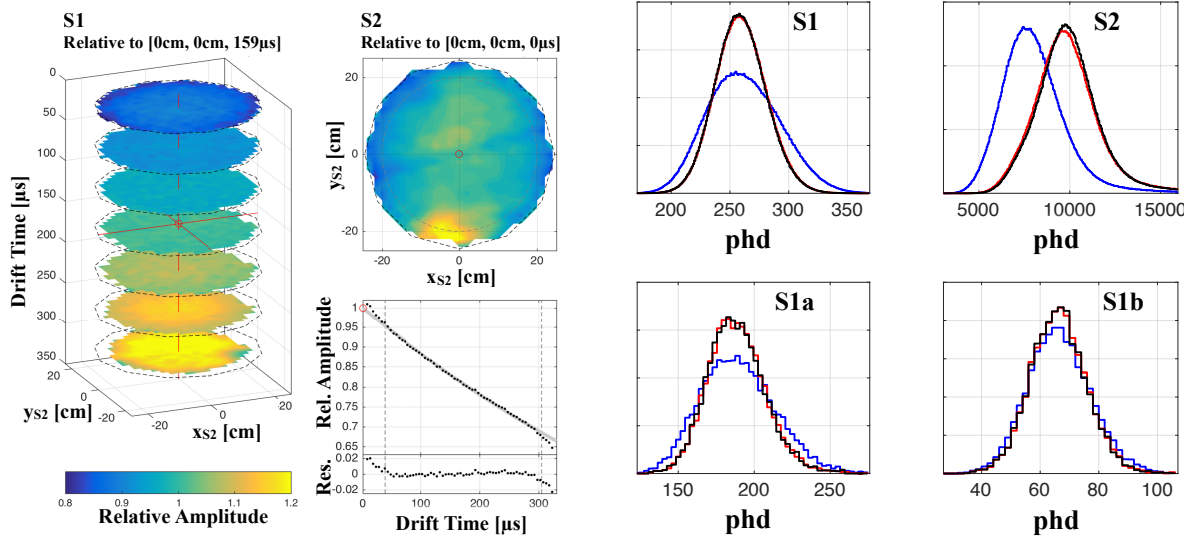


Figure 3.9: At left: relative variation in S1 and S2 pulse areas as a function of position, obtained from the monoenergetic  $^{83\text{m}}\text{Kr}$  calibration data. At right: effect of applying pulse area corrections to raw data. The pulse area distributions of uncorrected data are shown as blue histograms; areas corrected for  $z$ -dependent variation only are shown in red; areas corrected for  $z$  and  $(x, y)$  variation are shown in black. Taken from Ref. [13].

1.83 hour half-life allows for a quick return to baseline trigger rate following an injection, leaving the DAQ system free of clutter.

The LUX experience with  $^{83\text{m}}\text{Kr}$  is documented in the newly released Ref. [13]. In short, it became the workhorse of the WIMP search calibration techniques. Featuring a monoenergetic signal, distributed uniformly in the LXe, this calibration allowed for the calculation of the area correction maps referred to in Sec 3.3.3. The results of these calculations are shown in Fig 3.9. Furthermore, the events shown in Fig. 3.8a are from a  $^{83\text{m}}\text{Kr}$  calibration: these datasets are used in the calculation of the LRFs vital to position reconstruction. As an added bonus, the double decay structure can be resolved in the S1 pulses for a fraction of events, allowing for studies of the electric field geometry (since recombination statistics for the low-energy ERs from the first transition are less affected

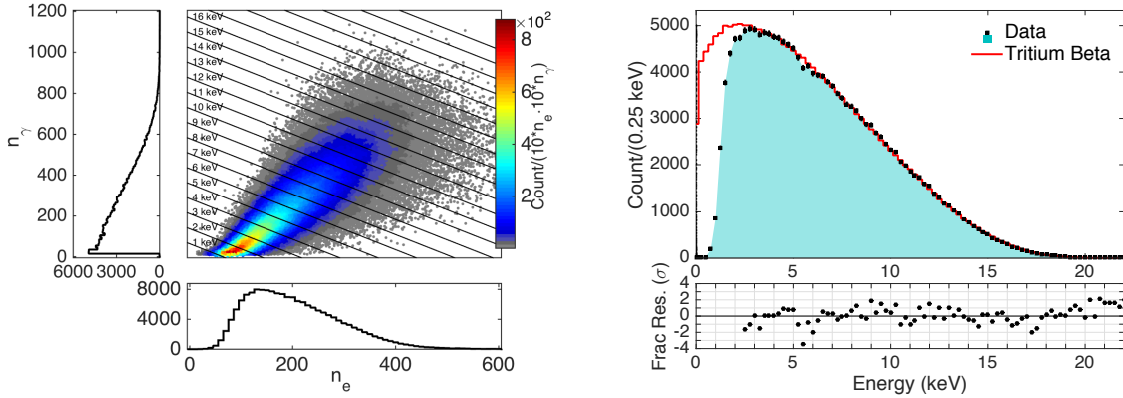


Figure 3.10: At left: scatter plot of  ${}^3\text{H}$  calibration data, using fitted values of  $g_1$  and  $g_2$  to convert from  $S1$  to  $n_\gamma$  and from  $S2$  to  $n_e$ , respectively. Contours (lines, in this case) of deposited energy are drawn, according to eq. 3.9. At right: the same data, collected into bins of energy, and compared against the theoretical  ${}^3\text{H}$  beta spectrum. The fall-off at low energy shows the detection threshold, driven by the S1 detection efficiency. Taken from Ref. [14].

by field variation than the higher energy second transitions).

### 3.4.2 Tritium

Unlike short-lived  ${}^{83\text{m}}\text{Kr}$ , tritium has a 12.3 year half-life. Additionally, its beta decay spectrum—with a 18.6 keV Q-value—has significant overlap with the WIMP nuclear recoil range. This makes it ideal for calibrating ER backgrounds, but it also means that it must be efficiently removed from the Xe before WIMP search data taking can resume. In Ref. [14], the LUX technique is described, whereby a six-hour purification time constant was achieved during removal. Figure 3.10 shows the observed spectrum in  $n_e$ - $n_\gamma$  space as well as combined energy space, from which a measurement of the detector  $g_1$  and  $g_2$  can be made.

Figure 3.13a shows the tritium ER band. This spectral shape is the primary dis-

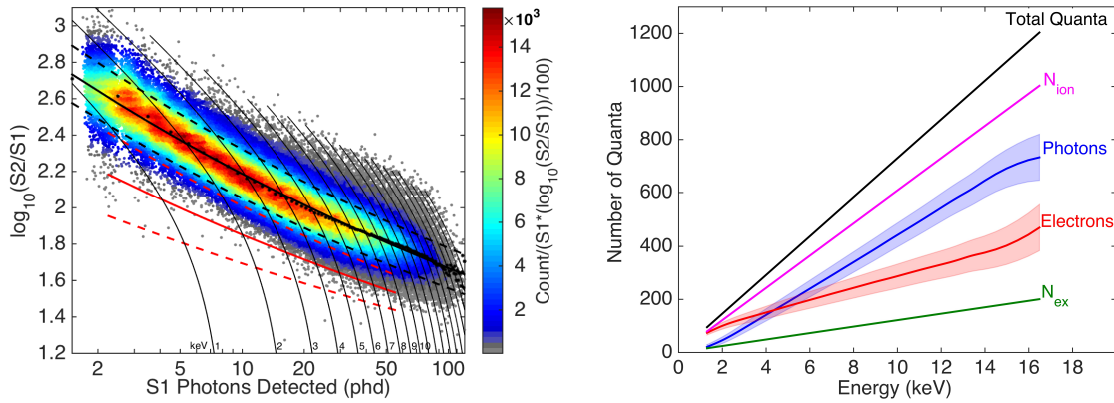


Figure 3.11: At left: ER band from the  $^3\text{H}$  data, drawn in the traditional discrimination space of  $S1$  vs.  $\log_{10}(S2/S1)$ . The scatter plot shows the calibration data, and the solid black line shows a fit to the Gaussian mean of  $\log_{10}(S2/S1)$  in each  $S1$  bin (solid black dots). The dashed black lines show the 10% and 90% ER band contours. Analogous quantities are shown in red for the NR band, as measured by the deuterium-deuterium neutron calibration. At right: the underlying quanta responsible for the shape of the ER band (see Sec. 3.2). Taken from Ref. [14].

criminant between low-energy ER backgrounds and NR signal events. In Fig. 3.13b, the deduced effects of recombination physics are shown. As discussed in Sec. 3.2, the initial number of ions produced is not necessarily the same as the observed number of electrons, due to the recombination of electron-ion pairs. In the plot, these numbers quickly diverge, as the assumed  $n_{\text{ion}}/n_{\text{ex}} = 5$  ratio is taken to be constant, but the reconstructed  $n_e/n_\gamma$  is clearly energy dependent. See Ref. [101] for an in-depth exploration of the LUX ER band and the effects of recombination fluctuations.

### 3.4.3 Deuterium-deuterium neutron beam

Between the  $^{83\text{m}}\text{Kr}$  and  $^3\text{H}$  calibrations, a remarkably accurate picture of LUX's response to ER events can be constructed. However, in order to refine the expected distribution

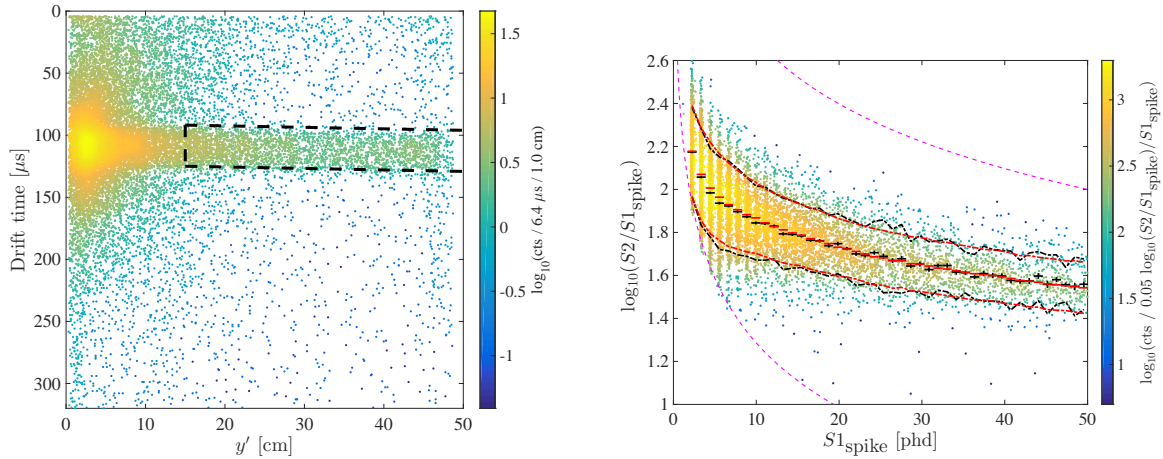


Figure 3.12: At left: spatial distribution of single-scatter events from the DD calibration data, where the  $y'$  axis is parallel to the direction of the neutron beam. Events within the indicated box are selected to reduce contamination from neutrons that have been scattered outside the detector (and thus do not have the 2.45 MeV energy of those in the collimated beam). At right: the nuclear recoil band, indicated by the black 10%, mean, and 90% lines calculated from the DD data (comprising the scatter plot). The contours in red come from simulated data using the model parameters tuned by the calibration analysis. Taken from Ref. [15].

of WIMP signal events, an NR calibration must also be performed. Following the first data-taking run, LUX employed a deuterium-deuterium (DD) fusion generator to fire a collimated beam of 2.45 MeV neutrons into the TPC. The generator was positioned outside the water tank, but an acrylic tube of air was suspended in the water and aligned with the beam, to allow neutrons to penetrate into the LXe space. Figure 3.12a shows the spatial distribution of events observed during the DD campaign, showing the definition of the beam shape. Closer to the wall, though, events caused by neutrons that have scattered outside of the TPC contaminate the monoenergetic data; the indicated box shows a selection used to reduce this background.

Although the neutrons in the beam have a known energy, they scatter off of Xe nuclei with a known angular distribution, depositing variable amounts of energy. However, if one

selects for double-scatter events, the reconstructed vertex positions allow for calculation of the scattering angle of the first interaction. This kinematically constrains the deposited energy of the first nuclear recoil. Although the S1s of the two interactions overlap, provided they are sufficiently separated in  $z$ , the S2s can be resolved. Thus, events from the double-scatter sample can be used to deduce the charge yield of NRs as a function of deposited energy. With this measurement in hand, the single-scatters can then be examined to determine the light yield. The full analysis is quite nuanced, and presented in Ref. [15].

The NR band shown in Fig. 3.12b is calculated empirically from the calibration data, but the result of a simulation is shown as well. Having a reliable NR model for MC simulations is desirable, since the WIMP recoil spectra are not well approximated by that of the DD neutrons. Since charge and light yield are effective parameters, more fundamental parameters of the NR model in NEST must be tuned to reproduce the data. To review, the observable nuclear recoil energy is expressed as a fraction of the total:

$$E_{\text{NR}} = \frac{W(n_e + n_\gamma)}{L} \quad (3.10)$$

where we have replaced the factor of  $f$  with the conventional Lindhard quenching factor  $L$ .<sup>5</sup>  $L$  is energy dependent, modeled as

$$L = \frac{k g(\epsilon)}{1 + k g(\epsilon)} \quad , \quad (3.11)$$

---

<sup>5</sup>Once again, we are ignoring the effects of biexcitonic quenching for clarity, though these are considered in the NEST model.

where  $\epsilon$  is a dimensionless form of the energy,

$$\epsilon = 11.5 (E_{\text{NR}}/\text{keV}_{\text{nr}}) Z^{-7/3} \quad , \quad (3.12)$$

and  $g(\epsilon)$  is a measure of the electronic stopping power relative to the nuclear stopping power, parametrized in Ref. [78] as

$$g(\epsilon) = 3\epsilon^{0.15} + 0.7\epsilon^{0.6} + \epsilon \quad . \quad (3.13)$$

Finally,  $k$  is a constant of proportionality between the electronic stopping power and the velocity of the recoiling nucleus [15, 97]. This parameter was measured to be  $k = 0.1735 \pm 0.0060$  in the analysis of the DD calibration data. The uncertainty on  $k$  is taken into account in the WIMP signal model used in the limit-setting technique discussed in Chap. 6.

### 3.5 Backgrounds

The expected sources of background events in the LUX WIMP search have already been alluded to. Radioactivity in detector components, in contaminants in the LXe, in the cavern rock, as well as cosmic rays all have the potential to generate events in the TPC. However, after narrowing the search region to low-energy single-scatter events in a fiducial detector volume, many backgrounds are instantly weeded out. What remains are almost entirely ER backgrounds—Compton scattering gamma rays from detector components, beta decays from radon daughters in the Xe, beta decays from  $^{85}\text{Kr}$ , and cosmogenic  $^{127}\text{Xe}$  electron capture decays. NR backgrounds come from neutrons, produced in  $(\alpha, n)$

reactions (predominantly in the PMTs) or by cosmogenic muon interactions in the water or cavern rock.

All of these background sources are described in detail in the LUX publication Ref. [16]. As described there, the neutron background is so small as to be negligible for the purposes of constructing a background model. The water shield effectively blocks thermal neutrons and gammas from the cavern rock, and the underground location suppresses the muon flux such that only 0.1 events are expected from muon-induced neutrons, in a 100 kg-year exposure.

The low-energy ER event rate due to Compton scattering of gammas originating in detector materials is calculated with the GEANT4-based [118] LUXSIM [119] software, using the results of the screening assays to estimate the activity of various detector components. This estimate is refined by performing a fit to the observed high-energy ER spectrum, where the radioisotopes  $^{238}\text{U}$ ,  $^{232}\text{Th}$  (and their daughters),  $^{40}\text{K}$ , and  $^{60}\text{Co}$  are modeled. The concentration of radon daughters, on the other hand, is constrained from fits to the observed  $\alpha$  particle energy spectrum.  $^{85}\text{Kr}$  event rates can be deduced from the observed concentration of  $^{\text{nat}}\text{K}$  (as measured by the sampling system), the assumed abundance of  $^{85}\text{Kr}$  and its beta decay spectrum.

While exposed to cosmic rays and thermal neutrons aboveground, the LUX Xe was activated. Of the unstable isotopes generated in these processes, only  $^{127}\text{Xe}$  has the ability to produce low-energy single-scatter events in the WIMP search data. With a half-life of 36 days, however, it was only a significant background source during the

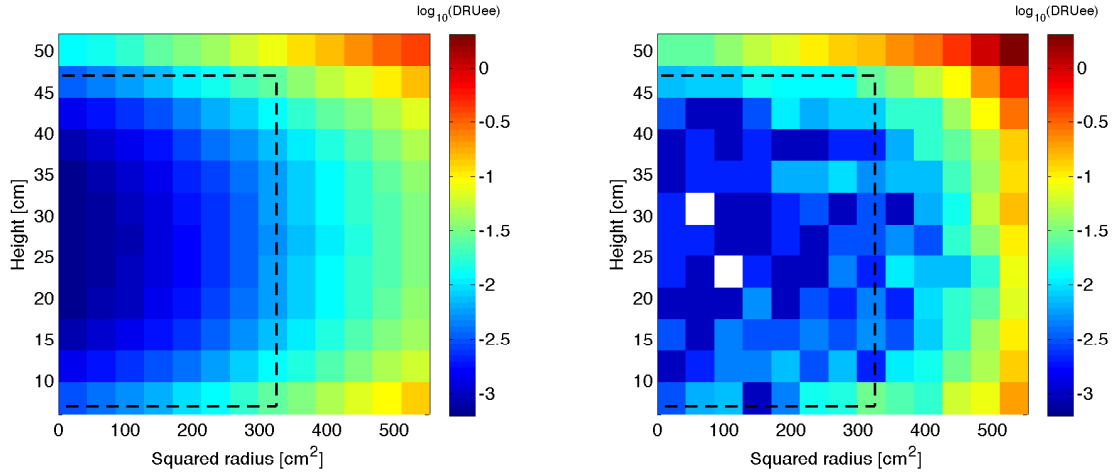


Figure 3.13: Spatial distribution of low-energy background events, predicted by the model (left) and observed in the first LUX exposure (right). Binning in squared radius ensures equal projected volume of the bins. The unit DRUee is the differential rate unit, using the electron equivalent energy scale: events  $\text{kg}^{-1} \text{day}^{-1} \text{keV}_{ee}^{-1}$ . Taken from Ref. [16].

first LUX data-taking run (once underground, the Xe experiences no activation, and the residual  $^{127}\text{Xe}$  decays away). Unlike the other intra-Xe background sources,  $^{127}\text{Xe}$  decays via electron capture. Ordinarily, the full energy of the nuclear deexcitation of the  $^{127}\text{I}$  daughter is visible—either 203 keV (53% probability) or 375 keV (47% probability)—and the event is well outside the low-energy search region. However, the 375 keV nuclear transition has a 17% chance of occurring via  $\gamma$  emission. With a mean free path of 2.6 cm in LXe, this gamma has a finite probability of escaping the TPC undetected. In that case, if the original captured electron came from the L shell or higher, the subsequent atomic transitions would release X-rays or Auger electrons and result in a clean low-energy event. Owing to the requirement that the gamma escape, this background source is not uniformly distributed in the detector volume, but instead concentrated near the edges (similar to the gamma distribution).

An additional background source not discussed in Ref. [16] arises from interactions occurring very close to the PTFE reflector panels, referred to as wall events. Under ideal conditions, these events would be rejected by a fiducial radius cut. However, due to the affinity of PTFE to absorb ionization electrons, these events can suffer severe S2 suppression; since  $(x, y)$  position reconstruction depends on the S2 signal, the resolution is poor for these events, and some will statistically leak into the fiducial volume.<sup>6</sup> The rate and distributions of these events are difficult to model from first principles. Therefore, empirical estimates are calculated using control samples of the search data. This is discussed briefly in Chap. 6, though a much more complete treatment can be found in Ref. [120].

Another background to WIMP searches in general is coherent nuclear scattering from neutrinos. In LUX, these interactions are expected to produce only  $\sim 0.2$  detectable events in the full exposure. However, as next-generation experiments grow in size and sensitivity, neutrinos will eventually become an irreducible background. One might think that muon-induced neutrons also represent a similar challenge, but unlike neutrinos, muons can be readily detected. The muon veto system in LUX was designed to observe muons passing through the water shield, enabling the rejection of coincident events in the Xe TPC as WIMP signal candidates.

---

<sup>6</sup>Ref. [16] catalogs backgrounds to the first published LUX WIMP search, in which a strict radial cut was enforced. The wall background is only significant for more relaxed fiducial volume definitions.

# Chapter 4

## LUX muon veto

As discussed in the previous chapter, the LUX water shield effectively blocks gammas and neutrons generated from radioactivity in the cavern rock. The “fast” neutron ( $1 \text{ MeV} < E < 8 \text{ MeV}$ ) background is created by  $^{238}\text{U}$  fission as well as in uranium and thorium chain ( $\alpha, n$ ) reactions. The flux of these neutrons near the LUX TPC is suppressed by  $\sim 22$  orders of magnitude, thanks to the LUX water tank [16]. In contrast, muon-induced neutrons have a much harder energy spectrum, reaching to the GeV scale [121]—these are only shielded by a factor of  $\sim 10^3$  by the water. Still, such neutrons are significantly rarer than fast neutrons, and are not expected to produce any events in the TPC. Even so, had LUX discovered a population of NR events during the WIMP search, being able to demonstrate that these were not muon-related phenomena would have significantly bolstered a DM detection claim.

## 4.1 Cosmic ray muons

A longtime favorite of particle physics outreach demonstrations and undergraduate laboratory experiments, the mu “who ordered that?” lepton is not at all welcome near DM detectors. Muons are generated in cosmic ray collisions in the upper atmosphere, and bombard the Earth’s surface with a flux of roughly  $1 \text{ muon cm}^{-2} \text{ min}^{-1}$ . Though not themselves likely to fake a WIMP signal, the trail of ionization they leave in LUX would clutter the data acquisition system. Moreover, secondary particles produced in showers from collisions outside the detector include fast neutrons—a dangerous background source, owing to their propensity to create single-scatter NRs in the TPC.

Moving underground significantly reduces the threat posed by muons: the Davis cavern at SURF is located 4850 ft below the surface, or 4.3 km.w.e. (kilometers water equivalent), and enjoys a  $10^7$  suppression of the muon flux compared to the surface. That any muons survive the trip at all is remarkable in itself—unlike high energy electrons, which rapidly lose energy to bremsstrahlung, the heavier muons are not as susceptible to braking radiation and can penetrate deep into the Earth (see e.g. Refs. [122, 123]). At depths greater than 10 km.w.e., the muon flux is dominated by the products of neutrino interactions with the rock (see Fig. 24.6 of Ref. [122]).

### 4.1.1 Muon-induced neutrons

At the LUX depth of 4.3 km.w.e., the average muon energy is about 300 GeV. In Ref. [121], Mei and Hime calculate the differential muon spectrum as a function of depth,

and from this derive the resulting muon-induced neutron rate and energy distribution. Neutrons can be generated by a number of mechanisms (see e.g. Ref. [124]), so numerous physics models must be juggled to make accurate predictions. The LUX estimate of 0.1 single-scatter NRs per 100 kg-year exposure from muon-induced neutrons is calculated using the Mei and Hime results. Two thirds of this background source arises from neutron production in the water shield itself [16]—by instrumenting the water tank with PMTs, then, such events can be tagged and vetoed.

### 4.1.2 Cherenkov Radiation

When a charged particle passes through a medium at a velocity greater than the local phase velocity of light, a shockwave is generated from the rapid distortion of the electromagnetic field. The resulting coherent light is dubbed Cherenkov radiation, and forms the basis of a wide variety of particle detection techniques (the IceCube detector [125] being a particularly fascinating example). The Frank-Tamm formula gives the spectral density of Cherenkov light (per unit length) produced by a particle with charge  $q$  traveling at velocity  $\beta$  through a medium with permeability  $\mu(\omega)$  and refractive index  $n(\omega)$  [126]:

$$\frac{d^2 E}{dx d\omega} = \frac{q^2}{4\pi} \mu(\omega) \left( 1 - \frac{1}{\beta^2 n^2(\omega)} \right) \omega \quad . \quad (4.1)$$

With a few approximations, this can be used to estimate the light yield of a typical muon traveling through the LUX water tank. Specifically, we can take  $\mu(\omega) \approx \mu_0$  (a valid approximation for water) and fix  $n = 1.33$ , since the refractive index of water is largely independent of wavelength in the UV range to which the water tank PMTs are

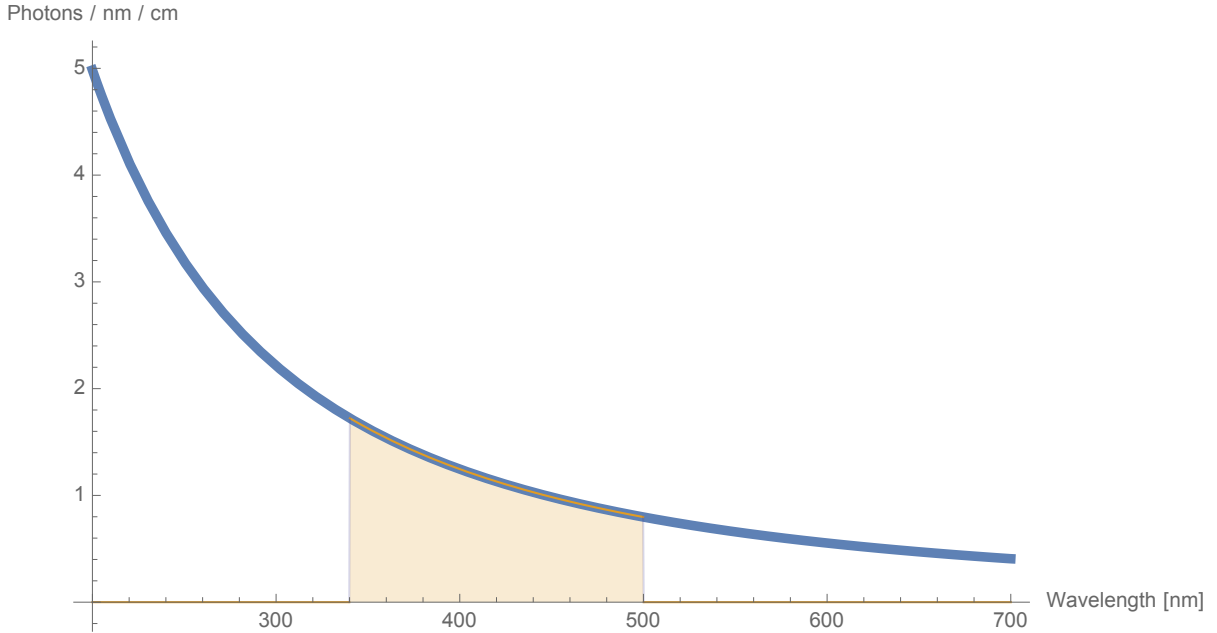


Figure 4.1: Spectrum of Cherenkov light in water from a 300 GeV muon. The UV range of PMT sensitivity is shaded in orange.

sensitive. Thus, applying the chain rule twice to eq. 4.1 gives the number of photons emitted per unit track length, per unit wavelength:

$$\frac{d^2 N}{dx d\lambda} = \frac{2\pi z^2 \alpha}{\lambda^2} \left( 1 - \frac{1}{\beta^2 n^2} \right) , \quad (4.2)$$

where  $\alpha$  is the fine structure constant, and the charge is now expressed as a multiple of the elementary charge:  $q = ze$ . This equation can be easily integrated over a range of wavelengths to calculate  $dN/dx$ .

For example, consider a 300 GeV ( $\beta \sim 1 - 10^{-7}$ ) muon passing through the LUX water tank. Figure 4.1 shows the corresponding Cherenkov spectrum calculated from eq. 4.2, with the shaded area indicating the approximate range of wavelengths to which the LUX water tank PMTs are sensitive. The integral over this range comes out to  $\sim 190$  photons per cm of water traversed by the muon. Since the water tank is 6 m tall, this

comes to a typical yield of  $\sim 10^5$  detectable photons emitted by a through-going muon. The 20 PMTs cover a combined  $\sim 0.4\%$  of the total surface area of the tank, so one would expect 400 photons to strike photocathodes, resulting in a total of  $\sim 100$  prompt photoelectrons per muon event (accounting for PMT quantum efficiency). Because of the reflectivity of the tank walls, a photon has an average of 5–6 chances to strike a PMT (from the mean of the negative binomial distribution, assuming  $\sim 85\%$  reflective walls and no absorption in the water), so this signal would be boosted to hundreds of detected photoelectrons per through-going muon. The parameters used in this simple calculation inform the basic specifications of the LUX muon veto system, since  $\mathcal{O}(10^2)$  phe/muon allows for high efficiency tagging. Indeed, a similar setup was used with great success in the Super-Kamiokande outer detector [127].

## 4.2 LUX muon veto system

The LUX muon veto system comprised the LUX water tank (and its internal lining of reflective Tyvek sheets), 20 Hamamatsu R7081 10" PMTs, HV supply, signal pickoff box, a dedicated electronics rack with amplifiers and triggering logic modules, 8 ADC channels, and analysis software integrated into the LUX data processing framework.

### 4.2.1 Water tank and purification system

Figure 4.2 shows a wide-angle view of the interior of the LUX water tank before it was filled, capable of holding 70,000 gallons of ultra-pure water. The water is treated before



Figure 4.2: At left: wide-angle view of the LUX water tank interior. Three of the veto system vertical PMT strings are visible. Note also the gray, horizontal acrylic tube, which was raised during DD calibrations to allow neutrons to reach the TPC (see Sec. 3.4.3). At right: close-up of a Hamamatsu R7081 10" PMT, mounted at the lowest level of one of the four vertical strings.

being pumped into the tank, and is continuously recirculated through the purification system, designed by South Coast Water Co. The recirculation purification system includes a series of deionizing resin beds, with one treatment specifically targeting U/Th impurities. UV lamps destroy any organic compounds, and two filters (1 and 0.2  $\mu\text{m}$ ) remove particulate contaminants. A membrane degasification system removes dissolved gases such as  $\text{O}_2$  and, more importantly,  $\text{Rn}$ . To help prevent radon contamination of the water through various entry points in the tank (e.g. flanges with instrumentation and plumbing feedthroughs), an overpressure purge of  $\text{N}_2$  is applied, using boil-off gas from the liquid nitrogen dewars supplying the cryogenic LUX systems.

In addition to these measures, during a fill of the tank, domestic water is processed through additional water softening, filtration, and reverse osmosis units before entering the recirculation purification system. During the WIMP search campaigns, the LUX

water was kept at nearly  $18 \text{ M}\Omega\text{-cm}$  resistivity, at  $\sim 23 \text{ }^\circ\text{C}$ . For reference, pure water at  $25 \text{ }^\circ\text{C}$  has  $18.2 \text{ M}\Omega\text{-cm}$  resistivity [128]. The dissolved  $\text{O}_2$  concentrations (measured as a tracer of radon gas) were reduced to below the detection threshold of the system ( $< 1 \text{ ppb}$ ).

### 4.2.2 PMTs

Twenty Hamamatsu R7081 10" PMTs were used to instrument the water tank. A water-tight housing protected the electronics base, to which positive bias voltage was supplied. This allowed the photocathode to be grounded, and safely exposed to the water (see Ref. [113]). The performance of the LUX veto system PMTs was characterized prior to their installation by M. Hanhardt in Ref. [129]. The veto system PMTs were arranged in four vertical strings along the interior of the water tank, each string consisting of four suspended PMTs facing radially inward (towards LUX) and a fifth on the floor facing upward. Because positive high voltage was supplied, a single RG-58 cable attached to the PMT base carried both the bias HV and the fast signal pulses. Outside the water tank, a "pickoff" circuit capacitively separated the AC signal from the DC voltage. The signal was then routed to the amplification, triggering, and digitization electronics.

### 4.2.3 Electronics and data acquisition

A schematic of the veto system analog electronics system, which featured both custom-built amplifiers and standard NIM products, is shown in Fig. 4.3. Annotated photos of the

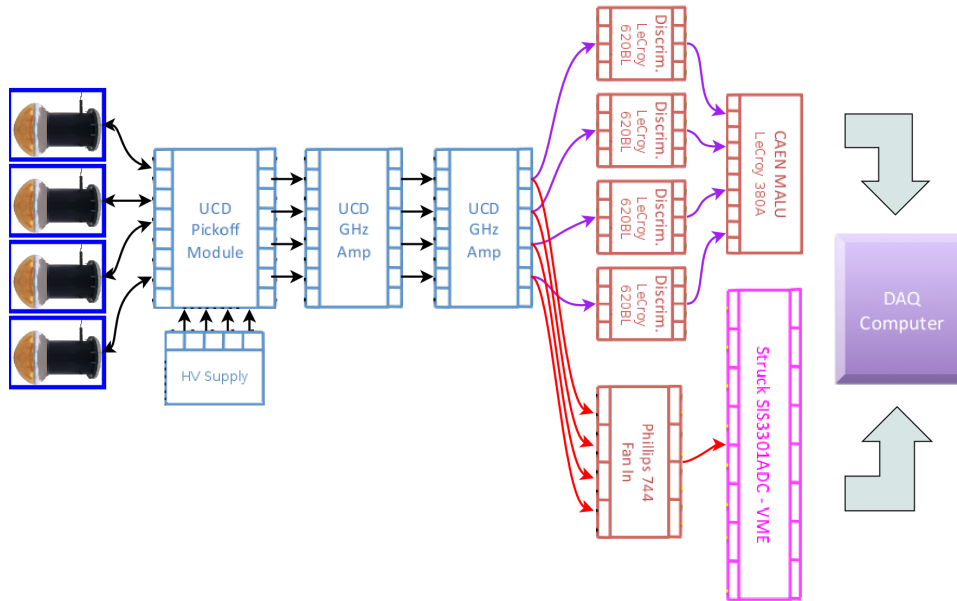


Figure 4.3: Schematic of the veto system electronics.

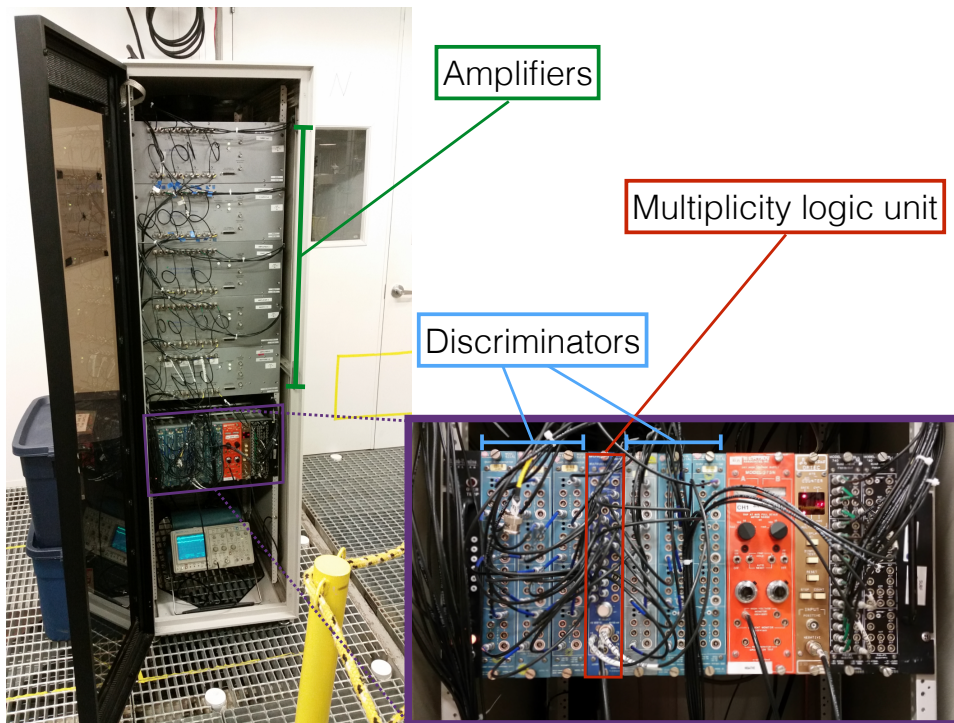


Figure 4.4: Annotated photos of the veto system electronics rack.

main components are shown in Fig. 4.4. The system functioned similarly to the signal processing electronics of the TPC PMTs (see Sec. 3.3.2), with copies of the amplified signals being sent to both trigger logic and ADCs. Unlike the TPC signals, however, the veto data was digitized in VPTG mode; i.e., a trigger condition must be met for data to be stored.

The veto system trigger was configured with the goal of flagging muon events with high efficiency while rejecting the many pulses due to noise and other backgrounds. The amplified signals of each veto PMT were passed on to discriminators that would generate a NIM pulse when a threshold of  $-30$  mV (approximately the height of a sphe pulse) was surpassed. These 20 discriminator signals were collected by a LeCroy 380A multiplicity logic unit, which would in turn generate a NIM pulse when a configurable coincidence requirement was reached. This signal was then sent to the LUX VPTG logic, permitting veto PMT data to be recorded by the Struck ADCs. The diagram in Fig. 4.3 omits a hardware component that was added to the veto circuitry: the trigger hold-off. Shown in gory detail in Fig. 4.5, this component imposed a mandatory dead-time following any veto trigger, preventing pulses from being double-counted.

Another distinction between the veto system and TPC signals was the ganging scheme: whereas each of the 122 TPC PMTs was allotted its own digitizer channel, the 20 veto PMTs received only 8 ADC channels. Channels were therefore summed according to the vertical position of the PMT: the top row was summed into one channel, the same for the second highest row, and etc., though the bottom (upward facing) PMTs were left

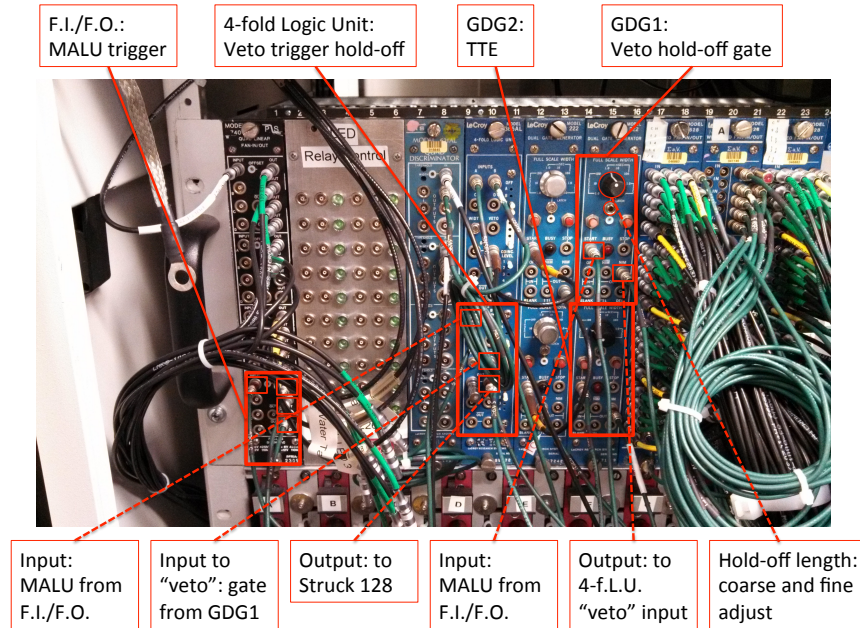


Figure 4.5: Annotated photo of the electronics responsible for the hardware trigger hold-off for the veto system.

as individual channels. This channel grouping can actually be seen at the right edge of zoomed inset of Figure 4.4, where four green-labeled LEMO cables enter a fan-in/fan-out module, and a single white-labeled cable (destined for the digitizers) emerges. Note that this channel ganging was used for the data acquisition, but not in the triggering logic.

#### 4.2.4 Commissioning and operation

Early underground commissioning of the water tank PMTs consisted of HV bias and tank light-tightness tests. These diagnostics revealed a problem with a crimp in the PMT base, which caused sparking and open circuits in a number of channels. Luckily, this was readily fixed, and all 20 PMTs were operational when the tank was filled with water. Testing for

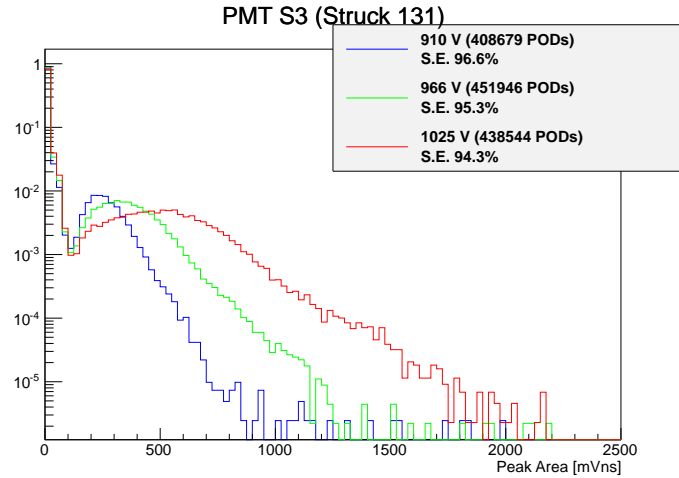


Figure 4.6: Single photoelectron spectra of water tank PMT (South 3) at three different bias voltages.

light tightness was painstaking work, requiring one person watching the PMT count rate (note the brown Ortec unit in Fig. 4.4) while another crawled between the tank surface and the floor grating, shining a flashlight at potential light leak locations.

Other tests probed the response of the veto system: the trigger rate at various coincidence levels was examined, and single photoelectron calibrations were performed using blue LEDs mounted in the water tank (see Fig. 4.6). For the second LUX exposure, an intermediate bias voltage was chosen, to ensure that the majority of single photoelectron pulses passed the relatively high POD threshold imposed at the ADCs.<sup>1</sup> The coincidence threshold for the trigger was set to  $N > 3$  in a 400 ns time window. The system was online throughout data-taking of this science run.

During the first underground LUX exposure, the veto system operation was more exploratory and intermittent. Though useful data was collected, continuous performance

<sup>1</sup>Subsequent studies of saturation effects imply that this choice might interfere with more detailed analyses of muon events; at the time, though, it was feared that the veto system might miss events worth vetoing.

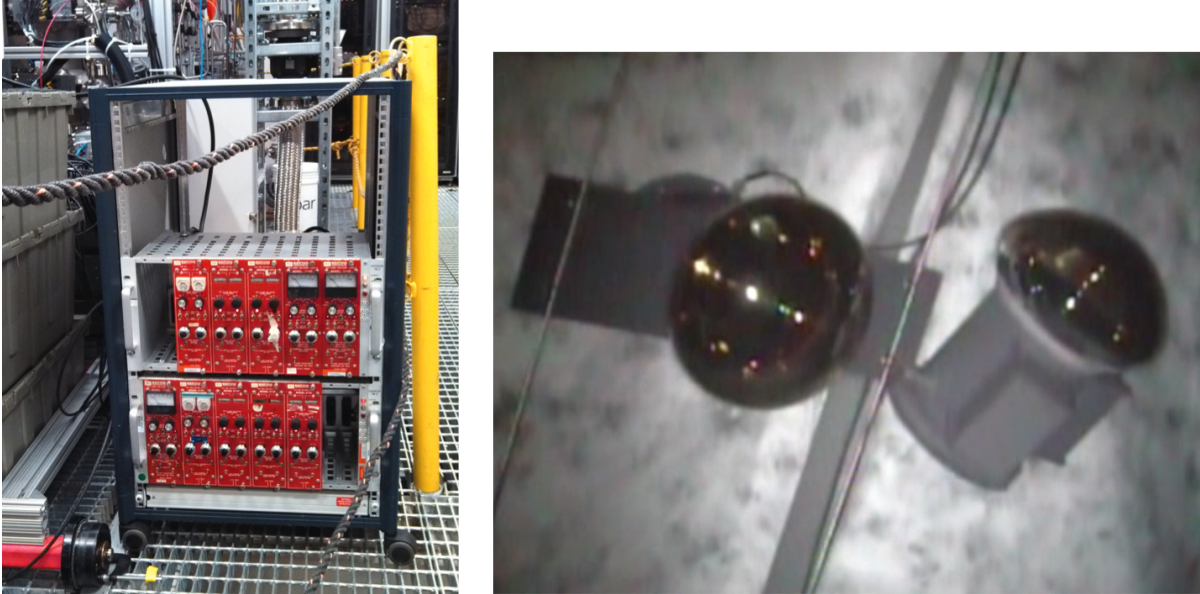


Figure 4.7: At left: replacement high voltage supplies for the veto PMTs. At right: the bottom West PMT makes a break for it, as captured by a submersible camera.

was hampered by the failure of two high voltage supplies, necessitating the procurement of a tertiary backup option. Figure 4.7a shows this setup, consisting of 10 Bertan positive HV NIM modules. (For the later science run, a new HV supply with both positive and negative capabilities was acquired and used to bias both the LXe and water PMTs.) Additionally, not all PMTs survived the entire LUX experience. One channel became too noisy to be useful, and another PMT was unable to be biased to high voltage without tripping. Most spectacularly, the floor-mounted PMT at the bottom of the West string became detached from one of its ballast weights, allowing it to float freely until becoming entangled in the PMT above it (see Fig. 4.7b). Rather than drain the entire water tank to rescue this PMT, it was deactivated for the remainder of LUX activities. Its dedicated ADC channel was, however, put to good use—the multiplicity count (as measured by the logic unit in the trigger system) was digitized, allowing for validation studies and

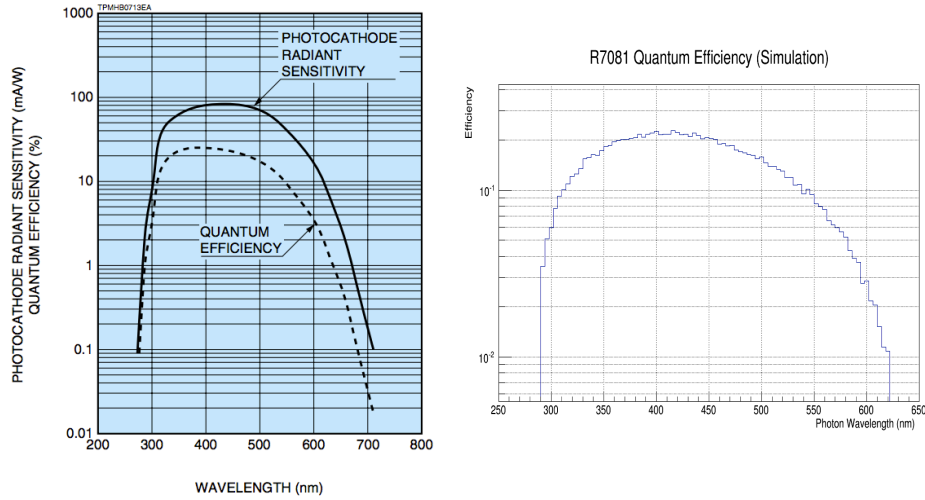


Figure 4.8: At left: PMT quantum efficiency, taken from the Hamamatsu data sheet. A parameterization of this curve was implemented in the GEANT4 model. At right, a plot of simulated quantum efficiency, shown as a validation of the implementation.

convenient analysis cuts.

### 4.2.5 Preliminary analysis

Despite some of the setbacks experienced in the first LUX run, the veto system performed its stated purpose in the second run, flagging events with significant light production in the water tank (though, no such events passed selection cuts in the WIMP search). Beyond this, though, efforts are ongoing to extract physics information from the wealth of data collected. As can be seen in Figures 4.8 and 4.9, geometry and material properties in the GEANT4 simulations have been updated to better match reality. This allows for calculations of expected system response to muon events much more sophisticated than the back-of-the-envelope estimate shown in Sec. 4.1.2.

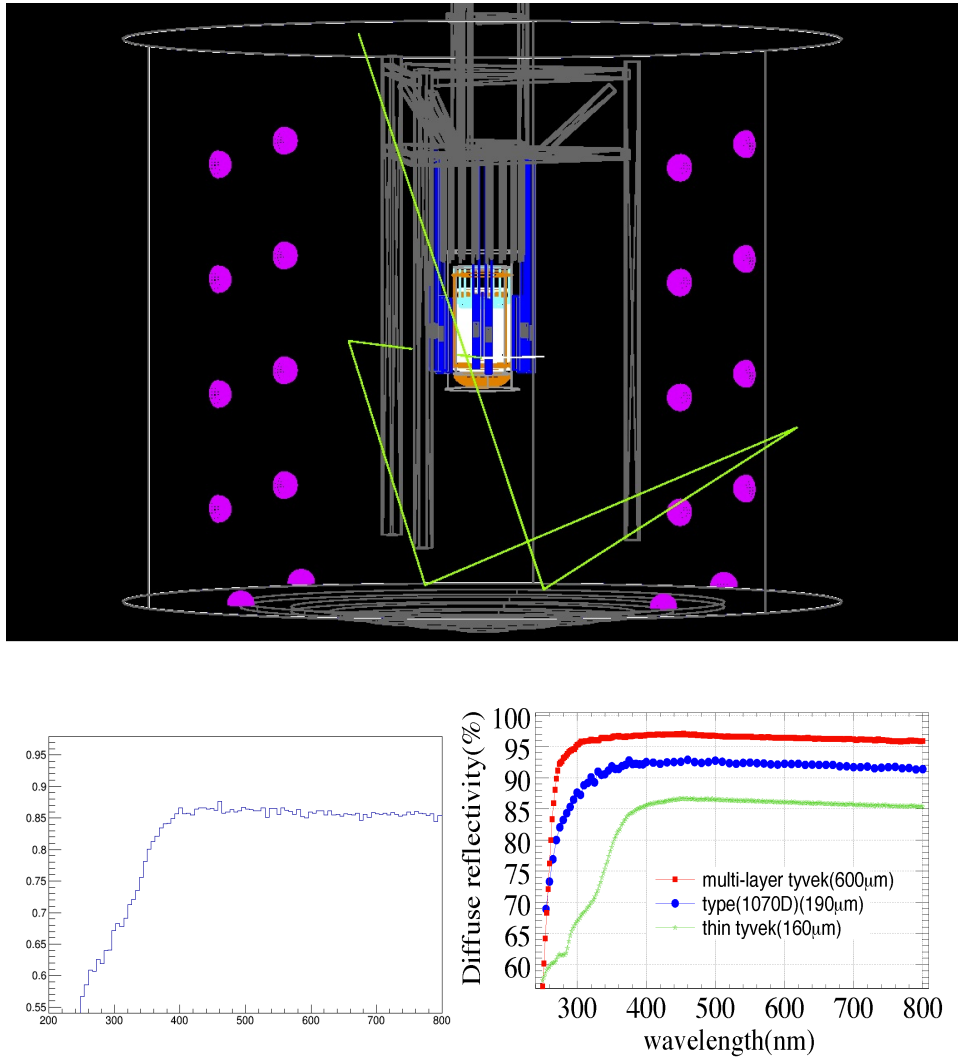


Figure 4.9: Top: Visualization of a simulated photon (green) reflecting off the Tyvek-lined tank walls. The veto PMT photocathodes are shown as pink hemispheres. At bottom right: experimentally measured reflectivity of different Tyvek products, obtained from the Daya Bay experiment. A parameterization of the green “thin tyvek” curve was implemented in the GEANT4 model. At bottom left, a plot of simulated reflectivity, shown as a validation of the implementation.

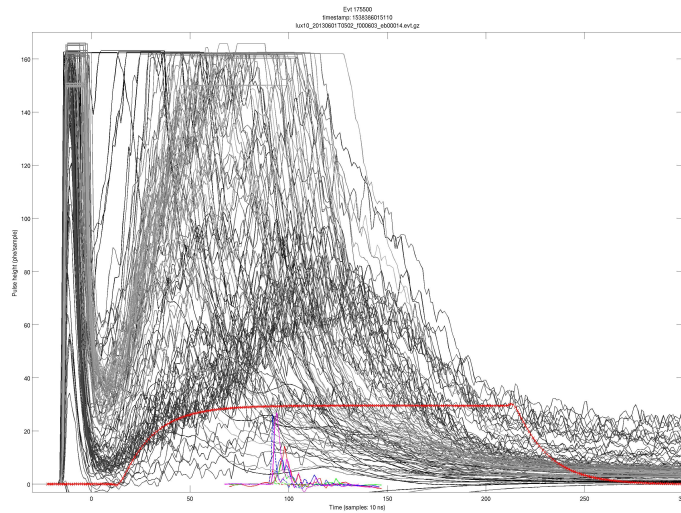


Figure 4.10: Waveforms of the LUX TPC and veto PMT channels in a coincident muon event, shown respectively as gray-scale and color curves. Accounting for a trigger time offset, the events are simultaneous. The mess of LXe PMT waveforms shows a massive S1 pulse, followed immediately by a sprawling wake of extracted electrons; meanwhile the water PMTs exhibit a crisp, high-coincidence level Cherenkov signal.

The early studies of the veto data itself revealed a puzzling pileup of legitimate events with small time separation. These occasional bursts of light in the tank were hypothesized to be the result of flashing PMTs—sparking of some sort in the base of a PMT, as seen in Super-Kamiokande—though this was never confirmed. This phenomenon, as well as electronics noise and saturation effects, make the study of the veto system data a nontrivial exercise. Still, an encouraging result of the early work was the identification of coincident muon events in the LUX TPC and veto system (see Fig. 4.10 for an example). More recent studies leveraging the full power of the GEANT4 simulations show promising progress in the effort to see interesting physics in the veto data, and will be presented in forthcoming publications.

# Chapter 5

## LUX Results

In short: LUX did not find WIMPs.

The LUX detector was operated underground for over three years, though this metric hardly captures the tremendous effort invested. Hundreds of person-years were spent in LUX's conception, construction, and operation, while countless more went towards the analysis of the WIMP search data. Notwithstanding LUX's "failure" to detect dark matter, the endeavor is still regarded as a success. First of all, the technologies and expertise developed for LUX, ranging from cryogenics to calibrations, will be vital tools in the larger next-generation detectors. Furthermore, the very absence of an observed dark matter signal, combined with the unprecedented sensitivity of LUX, allowed for new statistical constraints to be placed on WIMP properties. This information has bearing on theoretical models of DM, on past detection claims, and the direction of future searches. However, it is no small task to extract this information from the raw LUX data. With

hundreds of millions of triggers to sift through, a variety of selection criteria must be imposed to narrow the sample down to events of interest. This process is the focus of this chapter.

## 5.1 LUX WIMP search timeline

Three primary results have been published by the LUX collaboration. These results are presented as upper limits on WIMP-nucleon scattering cross section as a function of WIMP mass, under the assumption of spin-independent (SI) coupling. As discussed in Chap. 2, LXe detectors like LUX are most sensitive to WIMPs in this coupling scenario, which is why exclusions on SI cross section are the first analyses to be performed. The first two LUX publications reporting SI WIMP limits—Refs. [17, 18]—concern the data of a months-long exposure taken in the spring and summer of 2013, within a year of LUX’s underground deployment, known as Run3. A preliminary, rapid analysis was reported in Ref. [18]. Improvements to the analysis were made in Ref. [17], including an expanded fiducial volume, refined background model, more sophisticated statistical analysis, and superior calibration information. This “re-analysis” of the Run3 data will be referred to as WS2013 (as in Ref. [20]), where WS stands for “WIMP search”.

Following the data-taking period of WS2013, the first tritium and DD neutron calibrations were carried out (see Secs. 3.4.2 and 3.4.3). Additionally, a grid “conditioning” campaign was attempted, with the goal of raising the grids to higher voltages than attainable in WS2013 due to the onset of light production. The conditioning, in which

Parameter	WS2013 value	WS2014–16 value
HV grid voltages [kV] (B, C, G    A, T)	-2, -10, -1.5    +3.5, -1	-2, -8.5, +1    +7, -1
Nominal drift field	-0.18 kV/cm	-0.21 kV/cm
Nominal extraction field (in liquid) in gas	(-3.07) -6.02 kV/cm	(-3.68) -7.21 kV/cm
$\epsilon_{ee}$ (electron extraction efficiency)	$(49 \pm 3)\%$	$(73 \pm 4)\%$
$g_2$ [phd/ $n_e$ ]	$12.1 \pm 0.8$	$18.9 \pm 0.8 - 19.7 \pm 2.4$
$g_1$ [phd/ $n_\gamma$ ]	$0.117 \pm 0.003$	$0.100 \pm 0.002 - 0.097 \pm 0.001$

Table 5.1: LUX detector parameters in WS2013 and WS2014–16. In the first row, the voltages are given in ascending order of grid height in the TPC: bottom PMT shield (B), cathode (C), gate (G, with || indicating the position of the liquid surface), anode (A), top PMT shield (T). Drift field magnitudes are listed as “nominal” values, calculated from an idealized geometry. In reality, deviations from these values arise from grid geometry effects [11] and due to charge accumulation on the PTFE reflector panels (observed only in WS2014–16 [19]). The S2 gain  $g_2$  (and related quantity  $\epsilon_{ee}$ ) and S1 gain  $g_1$  are calculated via a “Doke plot” analysis, described in Refs. [11, 17]. Ranges are shown for WS2014–16 values to reflect their variation over the course of exposure.

grids were held at high voltages in a burn-in style approach (see Ref. [112]), was in some respects successful. Notably, the electron extraction efficiency was improved, due to the greater potential difference achievable between the gate and anode grids.

Table 5.1 shows the differences between the WS2013 detector conditions and those of the longer exposure, termed WS2014–16, taken following the grid conditioning campaign. The improvement in  $\epsilon_{ee}$  can be seen, along with a corresponding boost in S2 gain  $g_2$ . A marginal increase in the cathode-gate potential difference was also achieved, though this was negligible compared to an unanticipated consequence of the grid conditioning: charge buildup on the PTFE reflector panels surrounding the TPC. This effect severely altered the drift field geometry, introducing a major challenge to the WS2014–16 analysis. Nevertheless, the WS2014–16 dataset was combined with WS2013 to produce the limits shown in Ref. [20]. All three papers, at the time of their publication, reported world-leading constraints on SI WIMP–nucleon cross section. The final LUX limit was only recently surpassed by the XENON1T [130] and PandaX-II [131] collaborations.

## 5.2 WS2013

The WS2013 analysis, first presented in Ref. [17], is also thoroughly documented in Ref. [11]. However, key elements will be summarized here, as they form the backbone of the more complex WS2014–16 analysis.

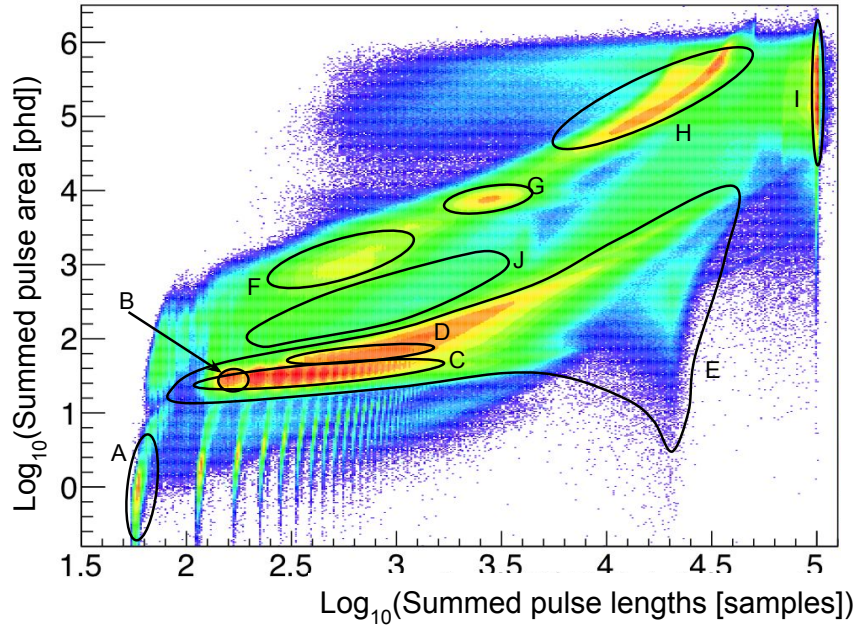


Figure 5.1: 2D histogram of all  $\sim 93$  million WS2013 triggers, plotted in a simple parameter space spanned by the total pulse area and total pulse length of the event. Pulse length is measured in ADC samples ( $= 10 \text{ ns} = .01 \mu\text{s}$ ). The color scale is omitted, but measures logarithmic event density (red is high, blue low). See text for descriptions of outlined regions.

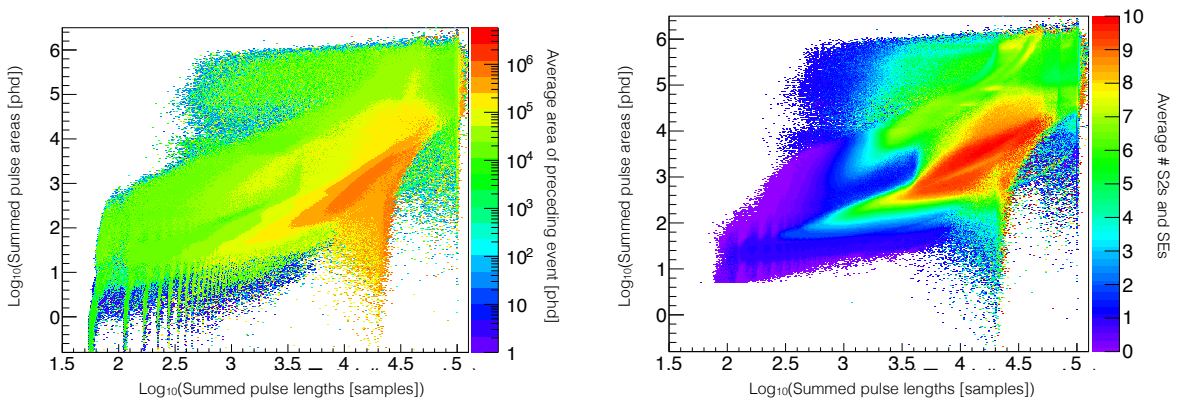


Figure 5.2: For each bin in the 2D parameter space of Fig. 5.1, an average quantity is calculated. At left: the total pulse area of the prior event. At right: the number of S2 pulses per event (including single electrons) identified by the pulse classifying algorithm.

### 5.2.1 Data quality

The WS2013 dataset contains 95 live days of data. Figure 5.1 visualizes the collected events in a 2D histogram: on the  $x$ -axis, the sum of the lengths of all pulses in the event; on the  $y$ -axis, the sum of the pulse areas. In spite of the simplicity of the reduced quantities considered, this perspective offers a quick view of the various event types common in the LUX data. There are too many features to enumerate in detail, though a few populations of interest are labeled in the plot, and explained here:

- (A) **sphe:** Events containing only one single photoelectron pulse. As expected, then, the total area is  $\sim 1$  phd. Similar narrow streaks with small total pulse area can be seen to the right; these are simply events consisting of  $N$  sphe pulses. Ordinarily, the LUX trigger would not flag these pulses for event construction because it is tuned to identify S2 pulses; however a coincident trigger from the veto system would cause an event to be built.
- (B) **SE:** Events containing one pulse due to the S2 of a single extracted electron. As can be seen, SE pulses are typically 25 phd in area,  $1.5 \mu\text{s}$  in length.
- (C)  $1 \times \text{SE} + N \times \text{sphe}$ : Events containing a single SE pulse in addition to some number of sphes.
- (D)  $2 \times \text{SE} + N \times \text{sphe}$ : Events containing two SE pulses in addition to some number of sphes.
- (E) **e-train:** The events in populations (B–D) often fall in the broader category of the

“electron train” (or just “e-train”). In this phenomenon, seen by XENON10 as well [132], a large S2 pulse will precipitate a prolonged period (milliseconds) of frequent liquid electron S2s. This effect is thought to be caused by a combination of mechanisms. For one, electrons not initially extracted will thermalize at the liquid surface, and can be randomly emitted into the gas until absorbed by electronegative impurities. Another cause might be secondary ionization electrons, generated by the photoionization of impurities as a result of the initial large S2 [133].

- (F) **Sub-cathode S1s:** Interactions occurring below the cathode grid, in the “reverse field region.” Ionization electrons will not drift upwards, but instead towards the bottom PMT shield grid, so no S2 is generated. However, due to the proximity of the events to the bottom PMT array, the S1 pulse is often quite large.
- (G)  **$^{83\text{m}}\text{Kr}$ :** Standard S1+S2 events generated during the monoenergetic krypton calibration runs.
- (H) **High energy:** Large pulse area ERs due to single and multiple scatters.
- (I) **Maximum event length:** High energy events that mark the start of an electron train. Because PODs are distributed throughout the maximum 1 ms event window, the distribution is cut off at the right edge, and this population is effectively an overflow bin.
- (J) **Gas events:** S1s and S2s arising from interactions in the gaseous Xe between the anode and top PMT shield grid. Gas S1 pulses are wider than their LXe coun-

terparts, and often conjoined with the S2 that results from ionized electrons being dragged down to the anode. Since the electric field here is weaker than between the gate and anode, the proportional scintillation is correspondingly less intense.

The plots in Fig. 5.2 show the means of other event quantities for each bin in the area-length parameter space. In particular, the e-train events are discernible by the large number of S2s and SEs they contain, and by the greater than average size of preceding events. Other, more colorfully named event topologies were also discovered in the LUX data, including “electron burps” and “the snowman.” These, and many of the populations listed above, are rejected with very high efficiency by the event selection criteria of the analysis.

### 5.2.2 Event selection

The most important ingredient to event selection is the requirement of a single scatter, utilizing the pulse finding and classification described in Sec. 3.3.3. The definition of single scatter events, which are also called “golden events,” is:

1. One valid S1, followed by one valid S2 within the 1000  $\mu\text{s}$  event window.
2. S1 must register in  $\geq 2$  PMTs, corresponding to at least 2 raw sphe.
3.  $S2 > 55$  digital photons, as measured by a “spike count” of PMT traces. (A stronger threshold is used in the analysis cuts.)
4. Additional S2s prior to the S1 and additional S1s subsequent to S2 are allowed.

5. S2 pulse area  $>$  S1 pulse area.

About 95% of triggers are rejected by the golden event requirements. The efficiency of the golden event classification for NRs is discussed in great detail in Sec. 5.2.3.

Fake single scatters can be caused by the misreconstruction of noisy events. Particularly problematic are events falling in the tail of an electron train, where random coincidences of single photoelectrons can mimic an S1 pulse and be paired with a small (several electrons) S2. A cleanliness cut was developed to mitigate this kind of event, based on the total pulse area of the S1 and S2 pair (“good area”) relative to the total area of other pulses in the event (“bad area”). Also, periods of detector instability (including abnormal trigger rates) were excluded from the final data sample.

Finally, defining a fiducial volume and energy range narrows the sample to a region of interest (ROI) for the WIMP search. In the WS2013 analysis, the fiducial volume was a cylinder of radius 20 cm and an extent in depth given by the drift time range  $[38, 305] \mu\text{s}$  (corresponding to  $z$  positions between 8.5 and 48.6 cm above the bottom PMT array).<sup>1</sup> A  $[1,50]$  phd  $S1$  window limits the ROI to roughly  $< 10 \text{ keV}_{ee}$ . Note that despite the two-PMT coincidence requirement for S1 pulses, position-dependent area corrections can result in  $S1 < 2$  phd. A threshold of  $S2_{\text{raw}} > 165$  phd was also introduced, corresponding to 6.7 extracted electrons, targeting wall background events with incomplete charge collection. Following all of these cuts, 591 events remain in the final WS2013 dataset.

---

<sup>1</sup>Recall from Chap. 3 that in WS2013, corrected position coordinates were used, accounting for a small distortion of the drift field.

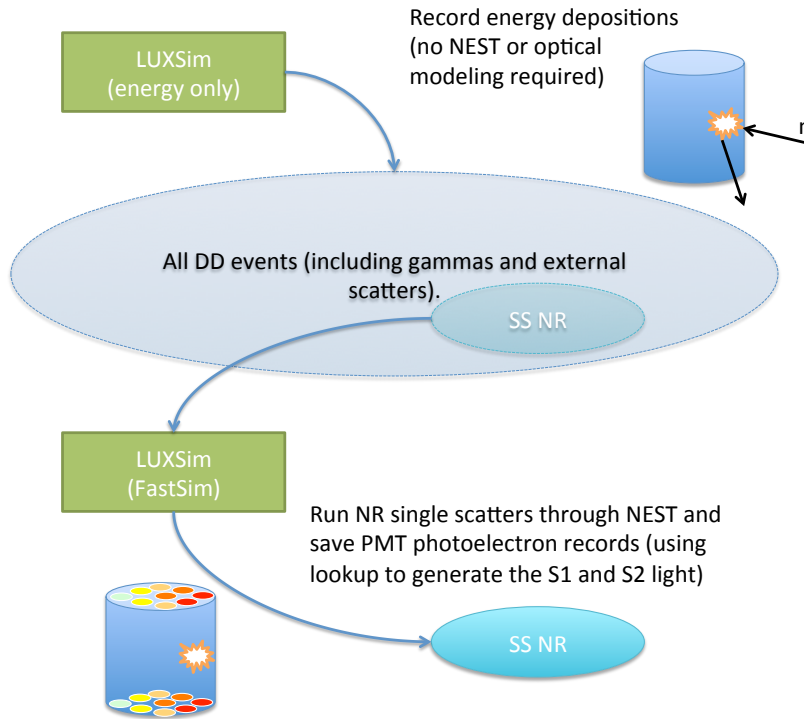


Figure 5.3: Schematic of the NR simulations validating the DD results.

### 5.2.3 NR model and efficiency

To assess the cost to signal detection efficiency that comes with all of the above cuts, simulated NR events were passed through the DPF and subjected to the selection. As discussed in Sec. 3.4.3, the NEST model was carefully tuned to reproduce the measured NR signal yields in LXe. A validation of the final model parameters was performed using the strategy shown in Fig. 5.3. First, DD neutrons are propagated through the water tank and into LUX, in an energy-only LUXSIM run. This means recording all energy depositions in the LXe: their positions, their type (ER or NR), and the kinetic energy of the recoiling particle. Gammas can be produced in some inelastic interactions, and need not be fully simulated. The output of this simulation is processed, with single-scatter

NRs being identified (via a clustering algorithm) and stored for further use.

The output of the first stage is then used as input for another LUXSIM run, this time invoking the FastSim technique. In this simulation, the NRs are passed through NEST, which generates the number of electrons and photons escaping the interaction site, according to the tuned Lindhard theory and appropriate recombination statistics. Then, rather than proceed with the computationally expensive task of tracking optical photons, a  $^{83\text{m}}\text{Kr}$ -based lookup table is used to simulate the response of each PMT to the S1 and S2. This is the FastSim component—the mapping of photons to a raw S1, and likewise for ionization electrons and raw S2, as a function of interaction position. Finally, a further simulation of signal processing and noise converts the PMT records into the LUX `.evt` file format, which allows the simulated data to be analyzed in the DPF just like actual data. The results of this validation of the NR model are shown in Ref. [15].

For the WIMP search efficiency calculation, a simpler simulation scheme was undertaken. NRs were sprinkled throughout the fiducial volume at a range of energies, and the NEST+FastSim+DPF sequence was carried out. The fraction of NR events passing cuts at each sampled energy therefore determined the estimated efficiency. This process was repeated for 6 versions of the NR model: the nominal Lindhard result of the DD analysis, four more Lindhard models derived from the  $\pm 1\sigma$  and  $\pm 2\sigma$  uncertainties on the model parameters, and a distinct model parameterization following the work of Bezrukov [134]. The results are shown in Fig. 5.4, alongside the charge yield measurements of the DD calibration.

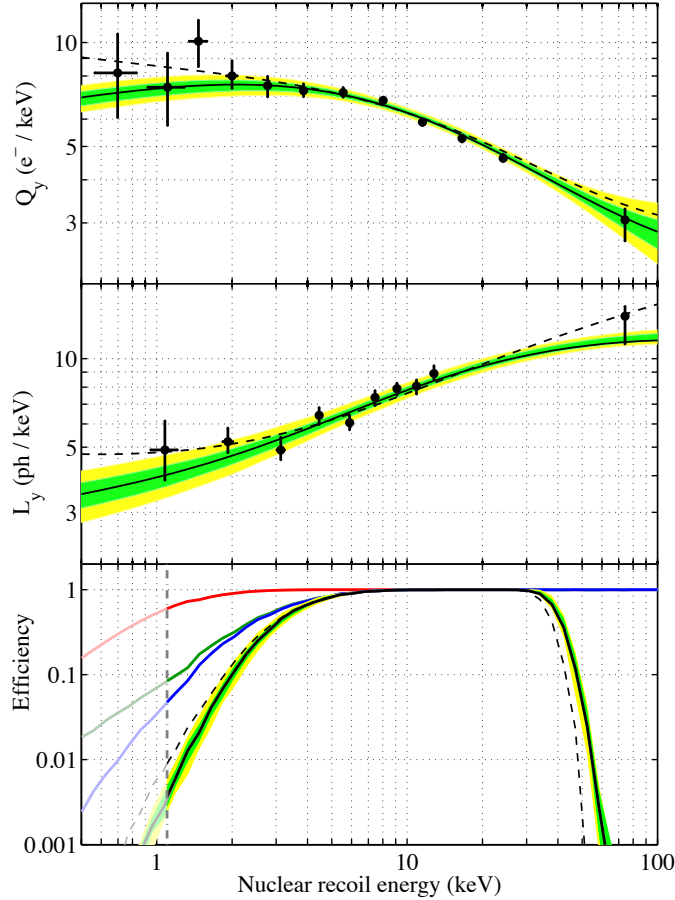


Figure 5.4: Signal yields and detection efficiency for NRs, as a function of recoil energy (taken from Ref. [17]). In all three panels, the simulation results are shown as a solid black curve (best-fit Lindhard), green and yellow bands ( $\pm 1\sigma$  and  $\pm 2\sigma$  Lindhard) and dashed curve (Bezrukov). In the top two panels, the DD measurements of charge and light yield are shown as black circular markers with error bars—these measurements determine the model parameters used in the simulations. In the bottom panel, the NR detection efficiency is calculated as described in the main text. The other curves show the efficiencies of individual selection criteria (for the nominal Lindhard model): in red, S2 detection efficiency; in green, S1 detection efficiency (including the two-PMT coincidence requirement); in blue, combined S1 and S2 detection efficiency. The final efficiency curves account for the additional thresholds on  $S1$  and  $S2_{\text{raw}}$ . In the WIMP signal models, LUX is assumed to be 0% efficient at detecting signals below  $1.1 \text{ keV}_{\text{nr}}$ , the lowest energy probed by the DD light yield measurement—this region is therefore grayed out in the bottom panel.

As can be seen,  $S1$  detection and the imposed thresholds drive the total efficiency, which falls to 10% at 2 keV. Above  $\sim 7$  keV, efficiency is 100%, until the  $S1 < 50$  phd upper bound kicks in at roughly 30 keV. Not included in this efficiency estimation is the probability for a valid single-scatter NR to fail the golden selection, due to effects not reproduced in the waveform simulation. To estimate this extra loss of acceptance, thousands of waveforms from calibration datasets were visually inspected in a “hand-scanning” effort to search for golden events missed by the DPF classification. This resulted in an additional  $(97.5 \pm 1.7)\%$  efficiency, taken to affect all energies equally.

#### 5.2.4 Limits

The 591 events of the final WS2013 data sample are shown in the top panel of Fig. 5.5, in the traditional ER/NR discrimination space of  $S1 - \log_{10} S2$ . The majority of events clearly populate the ER band, with a handful falling below the NR mean. The latter group are most likely due to the wall background, as evidenced by their high radius. A profile likelihood ratio statistic is used for hypothesis testing to produce the upper limits shown in the bottom panel, which will be discussed in great detail in the next chapter. Essentially, probability models are calculated in the space of observed quantities that allow discrimination between background and signal: position ( $r$  and  $z$ ) and energy ( $S1$  and  $S2$ ). From these signal and background models, the likelihood of the data under the hypothesis of the presence of a WIMP signal can be assessed, allowing for the construction of confidence intervals. These tests are performed independently at a range of WIMP

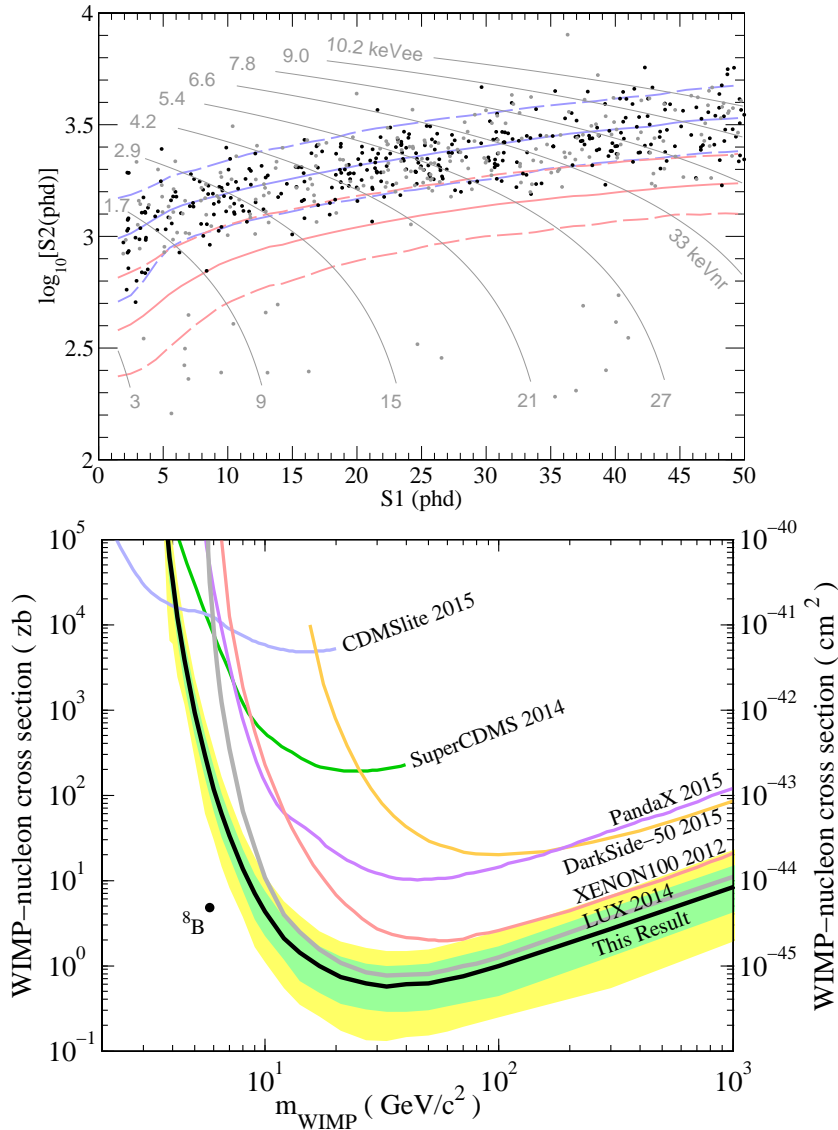


Figure 5.5: Top: final data from the WS2013 analysis, plotted in  $S1$ – $\log_{10}S2$  space. Data points with gray markers fall at the edge of the fiducial volume ( $r > 18$  cm), whereas solid black points are located more radially inward. The blue lines indicate the mean (solid), 10th and 90th percentile (dashed) contours of the ER band. The red contours show the same quantities for the NR model. Grey curves show the combined energy scale. Bottom: 90% confidence level upper limits on SI WIMP-nucleon cross section. The black curve shows the WS2013 result (expected sensitivity bands in green and yellow), whereas the gray curve shows the result from the first analysis [18]. Both figures taken from Ref. [17], which also contains the references for the other experimental limits shown.

masses, generating the curves shown Fig. 5.5.

Note that the strongest limits on cross section are obtained for intermediate WIMP masses (20–100 GeV), with a sharp drop in sensitivity at lower masses, and a gradual decrease at higher masses. This can be understood from the calculations shown in Chap. 2, in particular Figures 2.6 and 2.7. As WIMP mass decreases, the recoil spectrum falls off at smaller energies. Comparing to Fig. 5.4, it is clear that the spectra of small WIMPs ( $< 10$  GeV) are limited to energies in the low-efficiency regime of LUX. On the other hand, since the local WIMP mass density  $\rho_\chi$  is fixed in the signal model, increasing  $m_\chi$  necessarily decreases the number density  $n_\chi$  (i.e. heavier WIMPs means fewer WIMPs). So although the NR spectrum remains fairly constant at higher WIMP mass, sensitivity falls linearly due to decreasing flux of particles through the detector.

### 5.3 WS2014–2016

In an ideal world, the techniques developed and refined for the WS2013 analysis would have been directly transferrable to the WS2014–16 data. In reality, producing the SI cross section upper limits was not as simple as pressing “go” on the established machinery—many areas of the analysis required substantial reworking. In some cases, this was due to desirable improvements in the calibrations, data pipeline, and processing algorithms. For example, a blinding protocol was introduced to prevent bias when analyzing this unprecedentedly large dataset (which *a priori* could well have contained WIMP events). On the other hand, the complications arising from the distorted electric drift field geometry

	WS2013 analysis	WS2014–16 analysis
Livetime	95 days	332 days
Fiducial mass	145 kg	101 kg
Fiducial drift range	[38, 305] $\mu\text{s}$	[40, 300] $\mu\text{s}$
Fiducial radius range	$r < 20$ cm	$r_{\text{S2, wall}}(\phi_{\text{S2}}, z_{\text{S2}}) - r_{\text{S2}} > 3$ cm
$S1$ thresholds	[1,50] phd	[1,50] phd
$S2_{\text{raw}}$ threshold	$> 165$ phd	$> 200$ phd
Blinding scheme	–	salting
Observed counts (after cuts)	591	1221
Model PDF observables	$\{r, z, S1, \log_{10} S2\}$	$\{r_{\text{S2}}, \phi_{\text{S2}}, z_{\text{S2}}, S1, \log_{10} S2\}$
Background model components	$^{127}\text{Xe}$ , $^{37}\text{Ar}$ , $\gamma$ Comptons (low- $z$ , other), $\beta$ decays, Wall	Accidental coincidences, $^8\text{B}$ $\nu\text{s}$ , $\gamma$ Comptons (low- $z$ , other), $\beta$ decays, Wall

Table 5.2: Key quantities and features of the two WIMP search analyses. Note that the WS2014–16 fiducial mass is averaged over the exposure (since the mapping of S2 coordinates to real space coordinates was time varying, but the fiducial volume definition was fixed in S2 coordinates, the true fiducial volume changed over time as well).

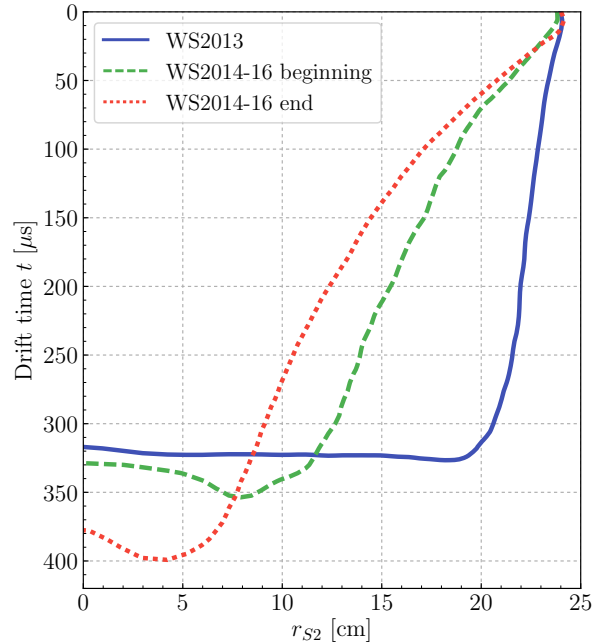


Figure 5.6: Edges of the LUX TPC active volume in the S2 coordinate system, as deduced from  $^{83\text{m}}\text{Kr}$  calibration data. Taken from Ref. [19]. Recall from Sec. 3.3.3 that reconstructed  $(x, y)$  position measures the point of electron emission at the liquid surface.

necessitated a wide-ranging “fix it in software” effort. An overview of the differences between the WS2013 and WS2014–16 analyses is shown in Table 5.2, with details elucidated in this section.

### 5.3.1 Electric drift field

As has been alluded to already, the LUX drift field in WS2013 was not perfectly uniform, exhibiting a nonzero radially inward component. This is thought to be a result of geometrical effects alone, as seen in XENON100 [135]. In contrast, a much stronger and more variable radial component was observed in WS2014–16. A new LUX publication [19] delves into this topic in detail, the main points of which will be discussed here.

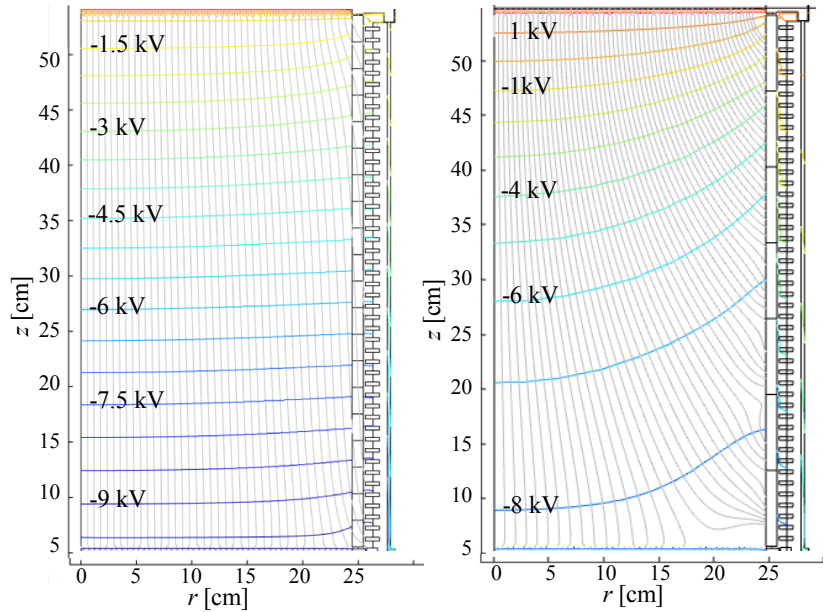


Figure 5.7: Field lines and equipotential contours calculated from a 2D electrostatic model of the LUX detector, for WS2013 (left) and WS2014–16 (right). Taken from Ref. [19].

The change in the LUX drift field was discovered following the grid conditioning campaign, via inspection of the reconstructed spatial distribution of the homogeneous  $^{83\text{m}}\text{Kr}$  calibration data. Figure 5.6 illustrates the difference between the WS2013 and WS2014–16 fields, as mapped out by the observed edges of the detector. Whereas, in WS2013, an ionization electron created at low- $z$  would drift by at most a few centimeters inward, the same electron could be forced  $\sim 10$  cm away from the wall before reaching the liquid level. Figure 5.7 illustrates how such a phenomenon might occur, showing the field lines calculated from a 2D electrostatic model of the WS2013 and WS2014–16 detector. The WS2013 results show the small “fringing” effect, caused entirely by geometric effects. The WS2014–16 model, however, includes patches of negative charge density distributed on the PTFE reflectors (the TPC walls), resulting in the more extreme distortion.

As described in Ref. [19], charge accumulation on the PTFE panels is the leading hypothesis explaining the observed electron drift trajectories. During the grid conditioning campaign, frequent electrical discharges in the GXe (an intended effect of the burn-in process) produced high energy VUV light, inducing the creation of electron-hole pairs in the PTFE (an unintended consequence). These charges would migrate under the influence of the applied field, with holes being removed faster than electrons [136, 137]. This would explain the negative charge build-up, as well as the observed gradual evolution of the field over time.

### 5.3.2 Position reconstruction implications

Since position reconstruction is a key element of background reduction and discrimination, the deformed geometry of the field lines created a corresponding wrinkle in the data analysis. To review: the  $(x, y)$  position of events is determined from the observed distribution of S2 light in the top PMT array (see Sec. 3.3.3 and Ref. [12]). This calculation identifies the location of electrons as they are extracted from the liquid, which in WS2014–16 might differ substantially from the  $(x, y)$  position of the actual energy deposition. The simple correction used on the WS2013 data [11] is not sufficient to account for the magnitude and variability of the distortion—azimuth-, depth-, and time-dependent as it was. Instead, a full 3D electrostatic model of the detector was constructed using the COMSOL MULTIPHYSICS software package [138], replete with tiles of tunable charge density on the PTFE panels.  $^{83\text{m}}\text{Kr}$  calibration data were compared to the simulated

trajectories of electrons in the field model, enabling the inference of the charge distribution on the PTFE walls. A Metropolis-Hastings algorithm was implemented to perform these fits.  $^{83\text{m}}\text{Kr}$  calibrations were therefore carried out frequently over the course of the WS2014–16 exposure, from which the time evolution of the charge density distribution was estimated.

Field maps were generated from the  $^{83\text{m}}\text{Kr}$ -based fits of the PTFE charge density. Electron trajectories were simulated from a 3D grid of starting points in the active volume, for which a number of quantities were calculated and recorded. Most importantly, the  $(x, y)$  position of the drifted electron upon reaching the liquid surface was saved, as well as the time of travel. These simulated quantities are precisely the observable S2 position coordinates; thus, the field maps provide a means of converting  $\{r, \phi, z\} \leftrightarrow \{r_{\text{S2}}, \phi_{\text{S2}}, z_{\text{S2}}\}$ . Additionally, the simulated electric field strength was calculated at each grid point. Figure 5.8 visualizes the data stored in the field maps, where for each grid point in real space, a corresponding  $\mathbf{r}_{\text{S2}}$  coordinate and field value is stored.

Originally, a variety of approaches were considered for dealing with the issue of the WS2014–16 fields in analysis. One choice concerned the position reconstruction: should a field map-based correction be applied to the data, in an attempt to map observed events from S2 space to their true positions? Or, conversely, should the data be left alone, and compared against models that have been transformed into the S2 coordinate space? In the end, the latter approach was settled on. It was decided that there was too great a danger of accepting spurious high radius events if an un-squishing procedure were applied

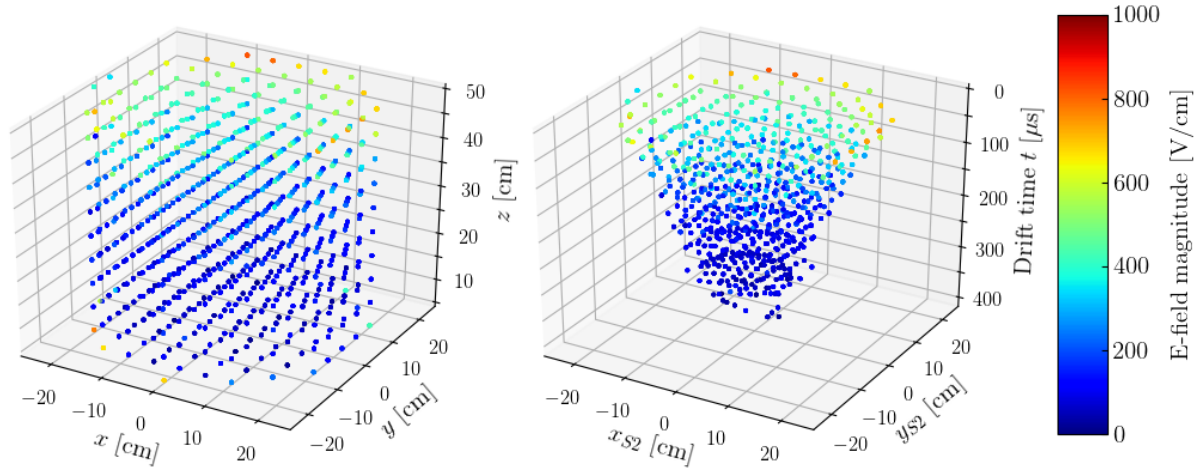


Figure 5.8: An example of field map data: the regular grid of points in real space (at left) is transformed into S2 space (at right), with field strength values indicated. Taken from Ref. [19].

to the raw reconstructed positions of the data. Thus, the fiducial volume was defined in the S2 coordinate space, with a drift time cut (as in WS2013) and a radial cut (harsher, including only 101 kg of LXe, while WS2013 contained 145 kg; see Table 5.2). There is a steep rise in  $^{210}\text{Pb}$  related backgrounds near the PTFE wall. The field distortions in WS2014–6 allow more of this background to be reconstructed in the central LXe volume, necessitating a harsher cut. An analysis tagging  $^{210}\text{Pb}$  chain events identified the position of the wall in S2 space:  $r_{\text{S2, wall}}(\phi_{\text{S2}}, z_{\text{S2}})$ , a function of azimuth and depth. Events passing the fiducial cut were required to occur at least 3 cm radially inward (as measured in S2 space) from the wall. Note that this translates to a more stringent cut towards the bottom of the detector, where 3 cm in S2 space might correspond to double that length in true coordinates.

In order to construct the probability models used to test background and signal hypotheses against the WIMP search data, an interpolation of the field map data was imple-

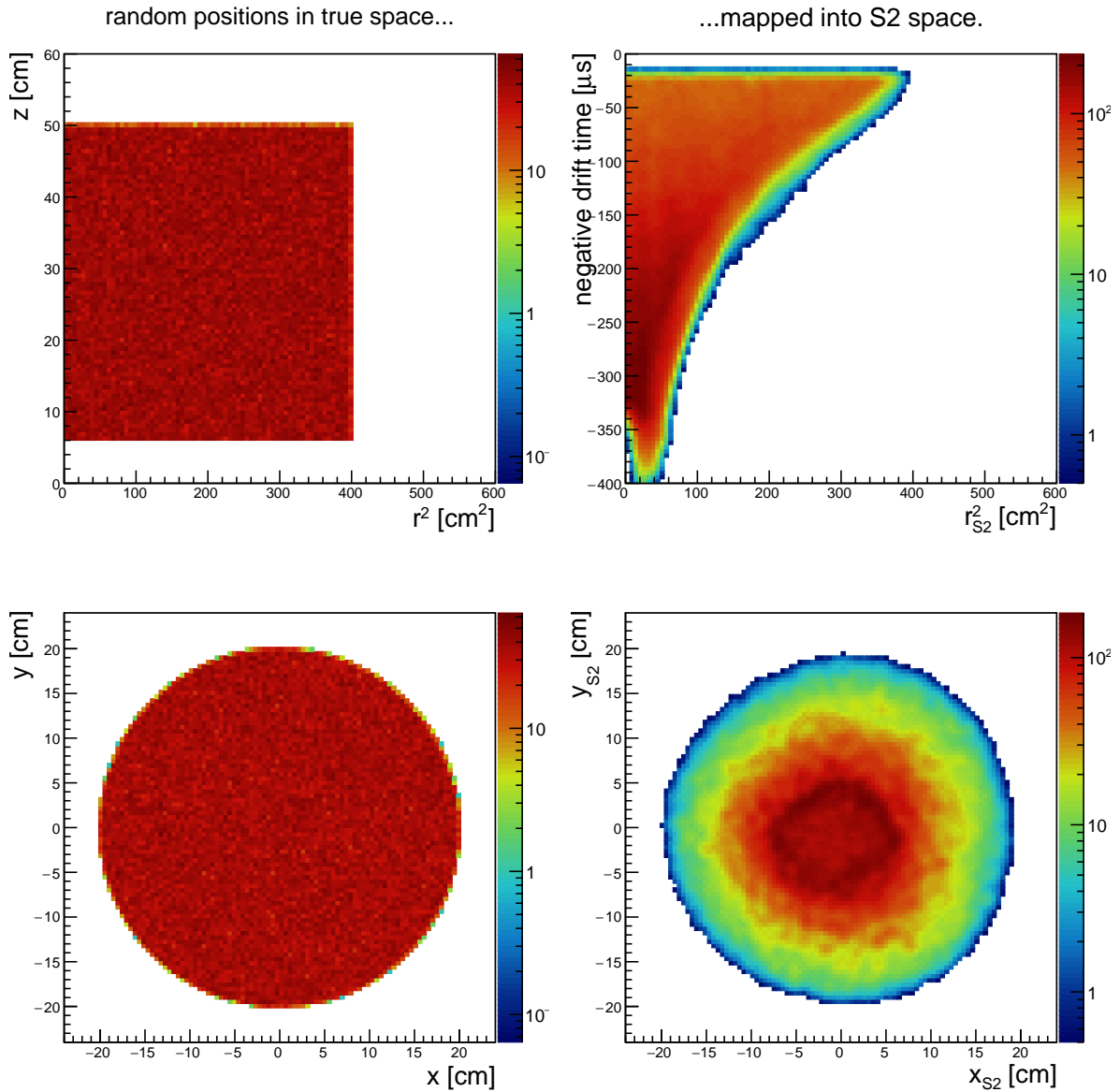


Figure 5.9: Demonstration of the C3PO field map interpolation algorithm. At left,  $r^2$ - $z$  (top) and  $x$ - $y$  (bottom) histograms of the uniformly distributed positions fed as inputs into the program. At right, the calculated S2-space position distributions are shown, based on an August, 2016 field map.

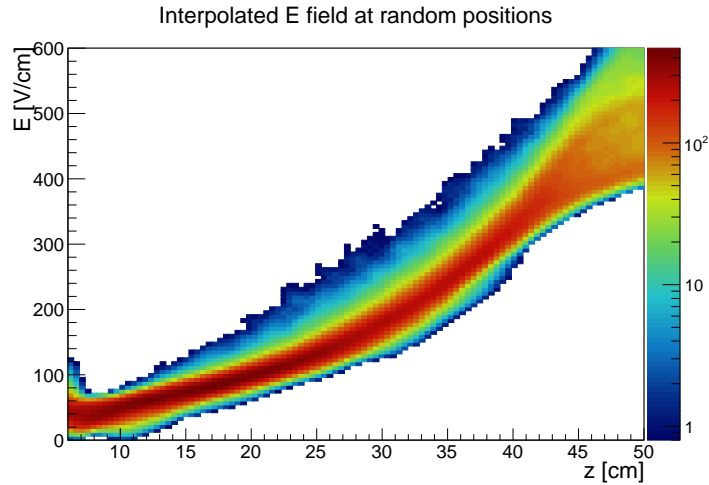


Figure 5.10: The electric field strength, calculated for each point sampled in Fig. 5.9, is plotted against the true  $z$  position, projecting all values of radius and azimuth. The scale of the variation in  $z$  is large, with the breadth of the correlation showing subdominant dependence of  $E_{\text{drift}}$  on  $(x, y)$  position.

mented capable of mapping arbitrary points in real space to S2 space. A fast interpolation program was written in C++, using trilinear interpolation as the core algorithm. However, since some grid points in the field map contain undefined values<sup>2</sup>, a backup weighted average algorithm was implemented (since trilinear interpolation requires 8 surrounding grid points to be defined). This failsafe approach uses inverse distance as a weighting function, averaging the values of only those grid points within a small sphere centered on the point of interest. The interpolation algorithm gained the moniker C3PO, short for “Curt’s Post-Processing Position Offset Corrections”.<sup>3</sup> Figure 5.9 shows the results of C3PO, where points have been sampled uniformly from within the WS2013 fiducial volume ( $r < 20$  cm) and transformed into S2 space using one of the WS2014–16 field

<sup>2</sup>This was a result of the simulated test charge failing to reach the liquid surface, often due to being trapped in a pocket of field line loops close to the TPC edges.

<sup>3</sup>Credit goes to E. Pease for the software branding.

maps. The same algorithm can be also used to interpolate the electric field strength at these positions in the detector (using the values calculated from the COMSOL model), as shown in Fig. 5.10. As can be seen, the field strength correlates strongly with  $z$ -position, with limited  $(x, y)$  dependence.

### 5.3.3 Addressing field variation effects on electron-ion recombination

The charge and light yields of LXe depend on electric field strength, particularly in the case of ER energy depositions. Thus, a further complication of the spatially varying fields in WS2014–16 is position dependence of the energy response, throwing a wrench in the calculation of the area corrections described in Sec. 3.3.3. Disentangling the effects of the field variation and the usual geometric inefficiencies proved to be a great challenge. The technique developed to address this, leveraging information from both  $^{83\text{m}}\text{Kr}$  and  $^3\text{H}$  calibration datasets, is summarized in Ref. [20] and thoroughly documented in Ref. [139]. Essentially, the strategy exploits the differences in field effects on electron-ion recombination at different scales of energy deposition: the low-energy tritium  $\beta$  decays and the smaller of the two  $^{83\text{m}}\text{Kr}$  transitions are less affected than the higher energy  $^{83\text{m}}\text{Kr}$  transition, which varies significantly with field (the ratio of charge to light yields changes by a factor of  $\sim 3$  for a 30 keV ER deposition occurring in either extreme of the WS2014–16 field; see e.g. Fig. 1 of Ref. [140]). The resulting area corrections successfully accounted for the geometric effects alone, leaving the field effects intact.

(Because the field effects are a function of not only position, but also interaction type and energy, no universally applied correction could accurately counteract them.) The importance of this pillar of the WS2014–16 analysis is difficult to overstate; without it, the energy resolution of the detector would be unacceptably degraded.

The ER band reckoned over the entire fiducial volume is substantially smeared out, and the NR band slightly smeared out, due to the electric field variations of 50–600 V/cm in WS2014–16. Unaddressed, this smearing would cause a reduction in the discrimination power of the  $S1$  and  $S2$  observables. To address this smearing, the TPC was not treated as a single homogenous volume as it had been in WS2013, but was segmented into chunks, within which the field variation was less drastic. Boundaries in the data were thus defined in drift time (4 “ $z$ -slices”) as well as calendar date (4 “date bins”), with unique ER and NR models defined for each (16 chunks, in total). The choice of these divisions was driven by the  $^{83\text{m}}\text{Kr}$ -based monitoring of the fields and by the timing of calibration runs (see Refs. [19, 103] for details). Figure 5.11 shows the time evolution of the modeled charge density and field strength in each  $z$ -slice.

For each date bin, a unique  $^3\text{H}$  dataset was used to tune the empirical NEST ER models for each  $z$ -slice. In practice, this meant varying detector gains as well as Xe response parameters in order to reproduce the observed bands in  $S1$ – $S2$  space. As can be seen in Table 5.3, the fit parameters included global detector quantities allowed to change between date bins but fixed for all  $z$ -slices within a date bin:  $g_1$  ( $S1$  gain),  $\epsilon_{\text{ee}}$  (electron extraction efficiency),  $\tau_e$  (electron lifetime, a measure of Xe purity), and the

<b>Date Bin 1 (9/11/2014 – 1/1/2015)</b>				
	[40, 105] $\mu\text{s}$	[105, 170] $\mu\text{s}$	[170, 235] $\mu\text{s}$	[235, 300] $\mu\text{s}$
$E_{\text{drift}}$ [V/cm]	$322 \pm 37$	$233 \pm 28$	$170 \pm 21$	$121 \pm 14$
$F_r \times 10^3$	$9.3 \pm 1.5$	$8.6 \pm 1.1$	$7.8 \pm 1.0$	$7.5 \pm 0.7$
$g_1$ [phd/ $n_\gamma$ ]			0.103	
$\epsilon_{\text{ee}}$			$0.67 \pm 0.01$	
$\tau_e$ [ $\mu\text{s}$ ]			735	
SE (mean) [phd]			26.4	
SE (width) [phd]			5	
<b>Date Bin 2 (1/1/2015 – 4/1/2015)</b>				
	[40, 105] $\mu\text{s}$	[105, 170] $\mu\text{s}$	[170, 235] $\mu\text{s}$	[235, 300] $\mu\text{s}$
$E_{\text{drift}}$ [V/cm]	$347 \pm 62$	$207 \pm 44$	$124 \pm 26$	$78 \pm 14$
$F_r \times 10^3$	10.0	10.0	10.0	10.0
$g_1$ [phd/ $n_\gamma$ ]			0.099	
$\epsilon_{\text{ee}}$			0.70	
$\tau_e$ [ $\mu\text{s}$ ]			947	
SE (mean) [phd]			26	
SE (width) [phd]			5.4	
<b>Date Bin 3 (4/1/2015 – 10/1/2015)</b>				
	[40, 105] $\mu\text{s}$	[105, 170] $\mu\text{s}$	[170, 235] $\mu\text{s}$	[235, 300] $\mu\text{s}$
$E_{\text{drift}}$ [V/cm]	$332 \pm 17$	$256 \pm 14$	$152 \pm 9$	$97 \pm 6$
$F_r \times 10^3$	$10.5 \pm 0.7$	$9.6 \pm 0.6$	$9.0 \pm 0.6$	$8.1 \pm 0.6$
$g_1$ [phd/ $n_\gamma$ ]			0.097	
$\epsilon_{\text{ee}}$			$0.708 \pm 0.004$	
$\tau_e$ [ $\mu\text{s}$ ]			871	
SE (mean) [phd]			25.8	
SE (width) [phd]			5.6	
<b>Date Bin 4 (10/1/2015 – 5/2/2016)</b>				
	[40, 105] $\mu\text{s}$	[105, 170] $\mu\text{s}$	[170, 235] $\mu\text{s}$	[235, 300] $\mu\text{s}$
$E_{\text{drift}}$ [V/cm]	$382 \pm 47$	$286 \pm 34$	$156 \pm 19$	$86 \pm 12$
$F_r \times 10^3$	$10.7 \pm 1.4$	$9.6 \pm 1.3$	$8.9 \pm 1.2$	$8.7 \pm 1.3$
$g_1$ [phd/ $n_\gamma$ ]			0.097	
$\epsilon_{\text{ee}}$			$0.703 \pm 0.010$	
$\tau_e$ [ $\mu\text{s}$ ]			1635	
SE (mean) [phd]			25.3	
SE (width) [phd]			5.6	

Table 5.3: NEST parameters for the WS2014–16 ER and NR models. Data transcribed from Ref. [41]. Where shown, error bars do not represent formal uncertainties, but rather heuristic ranges of values yielding good agreement between model and calibration data; these parameters do not enter into the profile likelihood as constrained nuisance parameters.

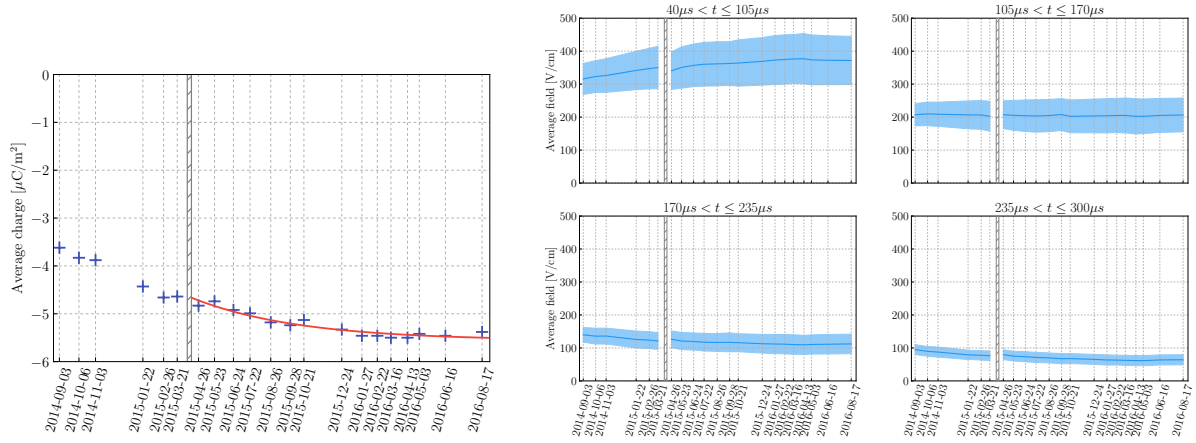


Figure 5.11: Time evolution of the modeled electric charge density and field. At left, the average charge density on the PTFE walls, with an exponential fit shown in red. The indicated discontinuity marks the time of a test where the cathode grid was grounded. At right, the drift field strength in each  $z$ -slice over time. Both figures taken from Ref. [19].

mean and width of SE (single electron size). Furthermore, two NEST parameters were allowed to vary between  $z$ -slices: the field strength  $E_{\text{drift}}$  and the “Fano-like prefactor”  $F_r$  [99]. The first of these is easily understood: since the electric field strength governs the average recombination fraction, this NEST parameter affects the mean of the ER band (greater field  $\rightarrow$  more electrons  $\rightarrow$  bigger  $S2$  for a given  $S1$ , on average). Though  $E_{\text{drift}}$  is also the physical quantity thought to cause the behavior of the observed ER bands, the NEST fits were not originally intended to give a valid estimate of the true field strengths; rather,  $E_{\text{drift}}$  was treated as an arbitrary knob to tune in order to create an accurate empirical model. However, it was found that the best fit  $E_{\text{drift}}$  values from the  $^3\text{H}$  NEST modeling were in good agreement with the entirely independent estimates of the  $^{83\text{m}}\text{Kr}$ -based COMSOL models [19]. This is seen as a validation of both simulation models, and of the description of the WS2014–16 fields in general.

In contrast, the fit values of  $F_r$  (the other NEST parameter in Table 5.3) are not

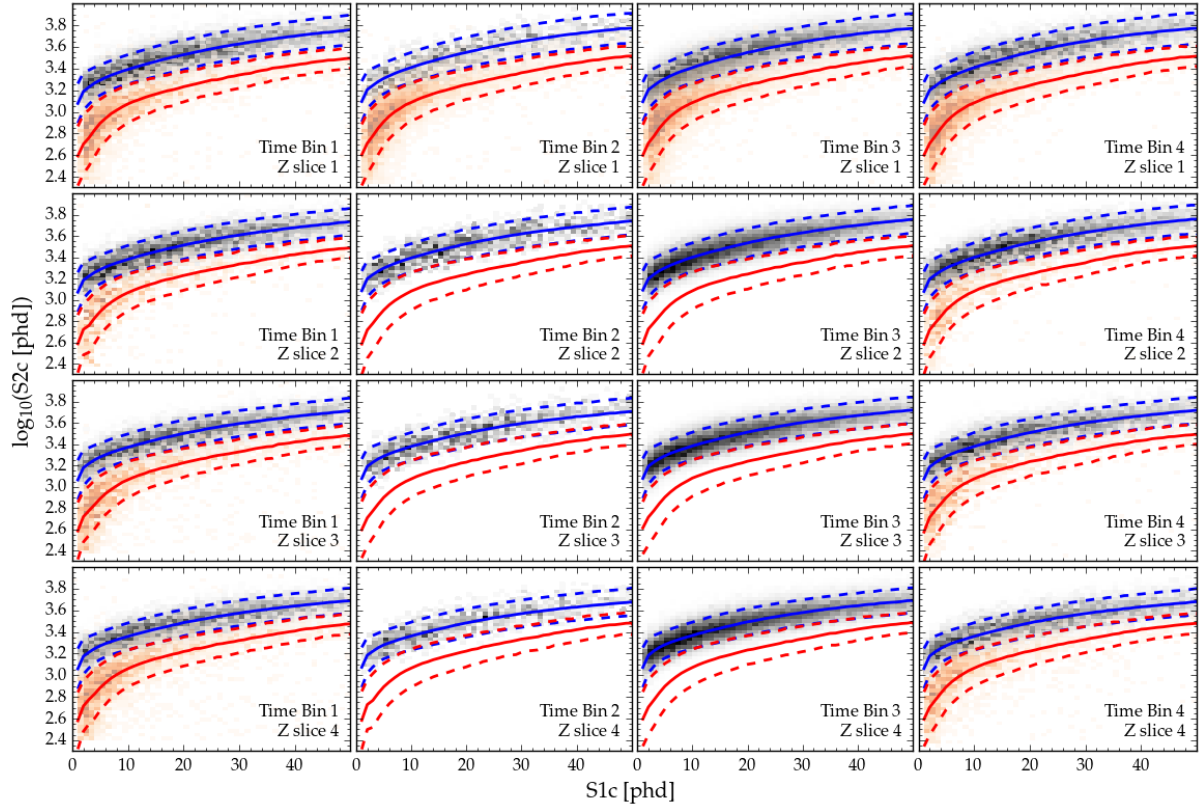


Figure 5.12: ER (blue) and NR (red) bands, shown as the mean and 10th/90th percentile  $S2$  values for a given  $S1$ , calculated from NEST models of each WS2014–16 exposure segment. The calibration data ( $^3\text{H}$  for ER, DD for NR) is shown as histograms in each panel. Note that the NEST fitting procedure was performed with ER calibration data only; the resulting parameters were used in the NR model, and found to be in good agreement with the DD calibration data (of which multiple  $z$ -positions were available only in the first and final DD datasets).

interpreted as having physical significance. This parameter is tuned to adjust the simulated *width* of the ER band, as a proxy for the actual variation of  $E_{\text{drift}}$  within a  $z$ -slice.<sup>4</sup>

Figure 5.12 shows the simulated ER and NR bands, for each of the date and  $z$ -slice bins, along with the calibration data used to create the models.

<sup>4</sup>The Fano-like factor in the NEST model accounts for non-Poissonian fluctuations in the recombination fraction  $r$ , and depends proportionally on the number of electron-ion pairs initially produced. The constant of proportionality is the prefactor notated here and in Ref. [20] as  $F_r$ . Note that in Ref. [99], where this model is specified, the prefactor is given by  $\mathcal{C}$ , and  $\mathcal{F}_r$  refers to the factor itself.

### 5.3.4 Additional selection cuts

The WS2014–16 analysis employed many of the same selection cuts as in WS2013: the golden event filter and the  $S1$  thresholds were unchanged (see Table 5.2), and the cleanliness cut weeding out electron train events was tweaked only slightly. The  $S2_{\text{raw}}$  threshold was raised to 200 phd to mitigate the wall background, now a more threatening background than in WS2013 because of the position reconstruction issues. The fiducial volume definition was discussed in Sec. 5.3.2. Additional cuts on S2 pulse shape were developed to eliminate pathological events arising from misreconstructed gas events and merged multiple scatters [20, 103]. Unlike the NR efficiencies of WS2013, the efficiencies of these pulse shape cuts were assessed empirically using  $^3\text{H}$  calibration data, and included in the signal and background models as a scaling of the simulated event weights. Finally, events were rejected if they had  $S2 > 10^4$  phd, or if they fell significantly higher than the ER band mean or below the NR band, as these events are not easily modeled, and are considered far from the WIMP region of interest.

### 5.3.5 Blinding scheme

To prevent bias in the development of selection cuts, the LUX data was “salted” with fake NR events. As opposed to a more traditional blinding scheme, this approach allows for the data to be inspected throughout the exposure. The knowledge that a WIMP-like signal *should* be present in the search data is intended to counteract the tendency (subconscious or not) of analysts to “sculpt” the data to match a prior expectation. In

principle, the advantage of salting lies in the ability to identify background populations throughout the run, avoiding a nasty surprise when one “opens the box.” Great care was taken to make the salt indistinguishable from real events, as documented in Refs. [20, 103]. In summary: a salt generation program paired real S1 and S2 waveforms from different  $^3\text{H}$  calibration events such that the resulting hybrid event mimicked an NR interaction. These waveforms were periodically injected into the `.evt` files before data processing (the `.dat` files were therefore salt-free, and were stored under lock and key). A database of salt events was maintained and accessible by a non-LUX secret keeper. Once the selection cuts were finalized, a list of events was passed on to the secret keeper, who revealed which of the events were salt.

The final dataset of 1221 events observed in WS2014–16 is shown in Fig. 5.13. All cuts have been applied, and 54 salt events have been removed. However, the unsalting procedure did not go exactly as planned—following the removal of the salt events, a number of events remained obstinately in the NR band. The waveforms of these events were given extra scrutiny, and two pathological populations were discovered as a result. These included spurious events likely due to light occurring external to the TPC, as well as events with a gas-like S1. Knowing of the existence of salting inhibited intense scrutiny of the candidates, which could have been undertaken prior to unmasking the salt. New cuts on S1 pulse shape were developed to exclude these populations (which were clearly inconsistent with energy depositions in the LXe); both cuts were found to have  $> 99\%$  acceptance of valid ER and NR calibration events, irrespective of energy. These cuts

removed a further 19 events from the dataset [103], leaving the final 1221 events shown in Fig. 5.13.

### 5.3.6 Limits

The likelihood models constructed for the WS2014–16 limit-setting were necessarily more complex than the WS2013 versions, owing to the segmented structure of the data ( $z$ -slices and date bins). This topic is discussed in detail in the next chapter. The background sources considered in the hypothesis testing were the same as WS2013, with a few exceptions:  $^{127}\text{Xe}$  was neglected (owing to its short half-life, it had decayed away before the start of the exposure) as was  $^{37}\text{Ar}$  (no evidence for it was observed);  $^8\text{B}$  solar neutrinos and accidental coincidences were added to the models. The WIMP search data was found to be consistent with the background-only hypothesis (with some small tension at low WIMP masses, discussed in Sec. 6.3), and 90% confidence level upper limits were placed on the SI cross section as in WS2013. Additionally, the WS2013 and WS2014–16 datasets were considered in a unified analysis, with their combined statistical power shown in Fig. 5.14.

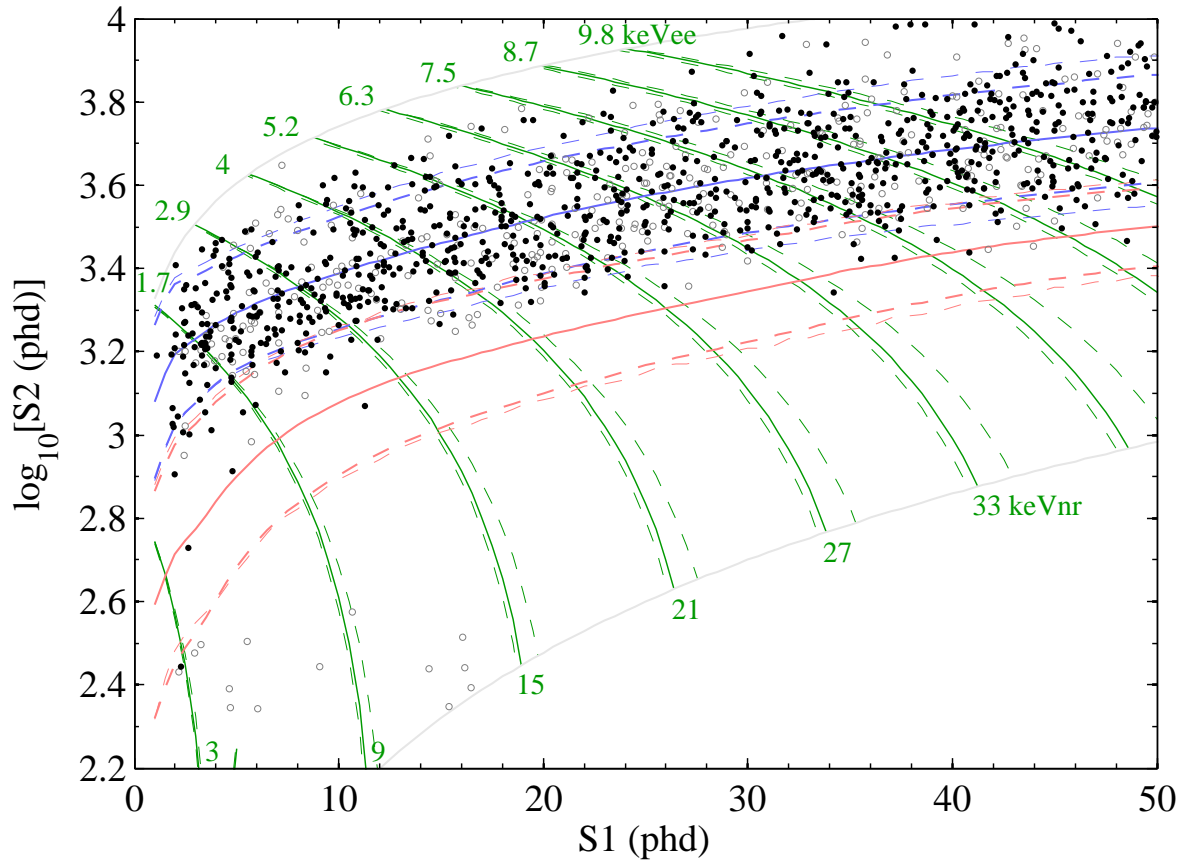


Figure 5.13: Final data from the WS2014–16 analysis, plotted in  $S1$ – $\log_{10}S2$  space. Data points with hollow markers fall at the edge of the fiducial volume ( $r_{S2,\text{fid.}} - r_{S2} < 1$  cm), whereas solid black points are located more radially inward. The blue lines indicate the mean (solid), 10th and 90th percentile (dashed) contours of the ER band. The red contours show the same quantities for the NR model. Green curves show the combined energy scale. Multiple instances of the dashed curves indicate the deviation of the ER and NR models over the 16 exposure bins. The salt has been removed from this data, as have pathological events discovered after the unblinding. Taken from Ref. [20].

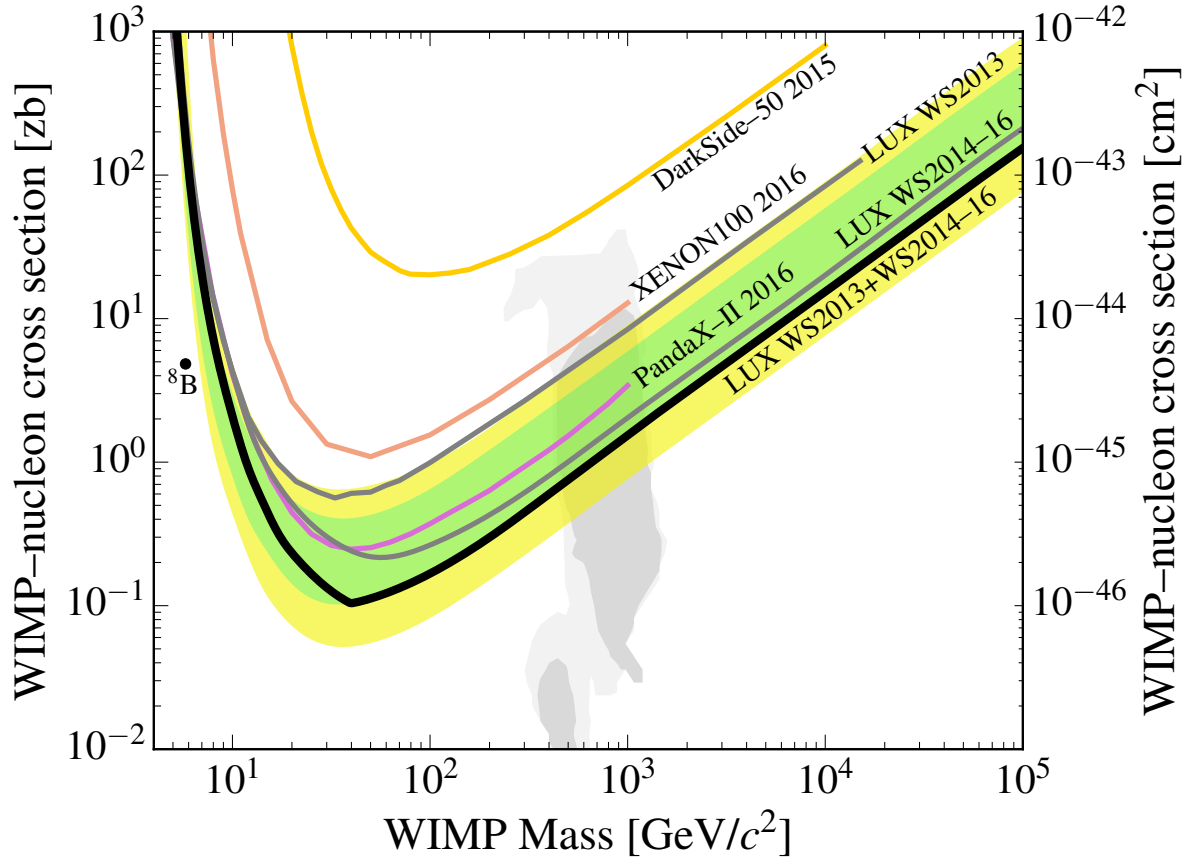


Figure 5.14: Upper limits on SI WIMP-nucleon cross section, derived from the WS2014–16 and WS2013 datasets (thick black line, with expected sensitivity shown as green and yellow bands). The kink at  $\sim 40$  GeV arises from the power constraint applied at  $-1\sigma$ . The WS2014–16 result (before combination with WS2013) is also shown, as a gray line. Note that WS2014–16 outperforms the earlier result for higher masses (due to the greater exposure), but because of background events at small  $S1$ , WS2014–16 is less constraining of light WIMPs than WS2013. The grey shaded areas show regions of favored CMSSM parameter space [21]. Taken from Ref. [20], which contains references to the other experimental results shown.

# Chapter 6

## Profile Likelihood Statistics

The constraints placed on WIMP-nucleon scattering cross sections shown in Chapters 5 and 7 are calculated using a frequentist limit-setting procedure. This chapter explores the details of this statistical analysis, including the construction of the LUX likelihood models.

### 6.1 Introduction

In the field of particle physics, frequentist confidence intervals are the quantities customarily used when presenting results. A detection claim is often accompanied by a calculated allowed region in the signal model parameter space; for a null result, a corresponding excluded region is shown. Frequentist (or “classical”) confidence intervals are calculated according to the Neyman construction [141], possessing different properties than their more intuitive Bayesian counterparts: credible intervals. Feldman and

Cousins discuss these techniques in their seminal paper [22]. As in that reference, we review both procedures, as it is perhaps easiest to understand the frequentist interval by identifying its differences from the Bayesian interval.

### 6.1.1 Frequentist and Bayesian intervals

Following the notation of Ref. [22], we consider an experiment that measures a random variable  $x$  (the “observable”) distributed according to a model parametrized by  $\mu$ , an unknown. In the case of continuous  $x$ , this model is mathematically expressed as a probability density function (PDF)  $f(x|\mu)$ , such that the probability of measuring a value of  $x$  in the range  $[x_1, x_2]$  is

$$P(x \in [x_1, x_2]) = \int_{x_1}^{x_2} f(x|\mu) dx \quad . \quad (6.1)$$

The parameter of interest (POI)  $\mu$  in our physics model could in principle take any value, but we expect there to exist a single true value  $\mu_t$  that describes our universe.

Now suppose that we conclude our data-taking run, perform an analysis, and measure a value  $x_0$  for  $x$ . We would like to use this information to make a statistical inference of  $\mu_t$ . In both the frequentist and Bayesian prescriptions, the probability density of observing  $x = x_0$  is

$$\mathcal{L}(x_0|\mu) \equiv f(x_0|\mu) \quad , \quad (6.2)$$

called the *likelihood function*. At this point, the Bayesian and frequentist approaches diverge: whereas frequentists bristle at the notion of defining a PDF for  $\mu_t$  (which in their philosophy is a fixed constant of nature, not a random variable), this is precisely

what Bayesians do.<sup>1</sup> Indeed, a simple application of Bayes' Theorem gives the posterior PDF

$$f(\mu_t|x_0) = \frac{\mathcal{L}(x_0|\mu_t)f(\mu_t)}{f(x_0)} \quad , \quad (6.3)$$

where  $f(x_0)$  is a constant of normalization (i.e., the integral of the numerator over the domain of  $\mu_t$ ). With a suitable assumption for a prior PDF  $f(\mu_t)$ , the Bayesian credible interval  $[\mu_1, \mu_2]$  for a given confidence level  $\alpha$  must satisfy

$$P(\mu_t \in [\mu_1, \mu_2]) = \int_{\mu_1}^{\mu_2} f(\mu_t|x_0) = \alpha \quad . \quad (6.4)$$

For example, we might choose  $\alpha = 0.9$  and opt to set an upper limit  $\mu_{UL} \equiv \mu_2$  (with  $\mu_1 = 0$ ); we would report that there is a 90% probability that  $\mu_t < \mu_{UL}$  given our dataset and assuming some prior PDF.

To reiterate, the concept of associating a probability with a model parameter's true value is strictly Bayesian. Feldman and Cousins take issue with this approach in rare event searches primarily because of the ambiguity and subjectivity inherent in choosing a “non-informative” prior PDF. In the Neyman construction, this issue is sidestepped by considering the probability of the derived interval *covering* a fixed parameter value.

Switching to the frequentist framework, we now consider the same experiment measuring  $x$  and making inferences on  $\mu$ . The frequentist interval  $[\mu_1, \mu_2]$  that we calculate must satisfy, for a *fixed*  $\mu$ , the property

$$P(\mu \in [\mu_1, \mu_2]) = \alpha \quad , \quad (6.5)$$

where the interval bounds  $\mu_1$  and  $\mu_2$  are the random variables (derived from the observed

---

<sup>1</sup>The author declines to take sides in this ideological debate.

value  $x_0$ ). In other words:

1. Suppose our universe is described by  $\mu_0$ . Thus, an ensemble of experiments (identical to ours) will observe different  $x_0$  (values of  $x$ ) distributed with probabilities  $f(x_0|\mu_0)$ .
2. Each experiment in the ensemble will calculate an interval  $[\mu_1, \mu_2]$  using their respective measured values  $x_0$ , with confidence level  $\alpha$ . In this sense, the bounds  $\mu_1$  and  $\mu_2$  are random variables that vary with  $x_0$ .
3. If the intervals are calculated according to the Neyman construction, then a fraction  $\alpha$  of the experiments in the ensemble will produce intervals for which  $\mu_0 \in [\mu_1, \mu_2]$ . This is the frequentist definition of the probability statement  $P(\mu_0 \in [\mu_1, \mu_2]) = \alpha$ .
4. Other techniques might yield intervals that, for some values of  $\mu_0$ , “undercover” ( $P(\mu_0 \in [\mu_1, \mu_2]) < \alpha$ ) or “overcover” ( $P(\mu_0 \in [\mu_1, \mu_2]) > \alpha$ ).

Figure 6.1 shows illustrations of the Neyman technique, which guarantees (by construction) correct coverage. In this procedure, for all possible values of  $\mu$ , bounds of  $x$  are chosen such that:

$$\int_{x_1(\mu)}^{x_2(\mu)} f(x|\mu)dx = \alpha \quad . \quad (6.6)$$

Then, for an observed value  $x_0$ , the confidence interval is given by the union of values of  $\mu$  for which  $x_0 \in [x_1(\mu), x_2(\mu)]$ . The visualizations make this much more intuitive.

The range  $[x_1(\mu), x_2(\mu)]$  is called the “acceptance region” because if it contains  $x_0$ , then we accept the hypothesis  $\mu$  (with confidence level  $\alpha$ ). Note that  $x_1(\mu)$  and  $x_2(\mu)$

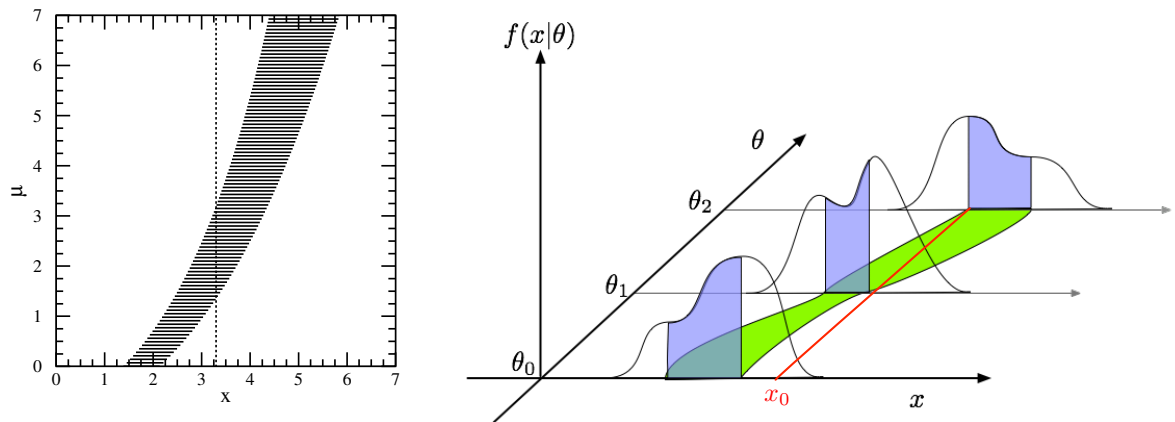


Figure 6.1: At left: illustration of a confidence belt, taken from Ref. [22]. The interceptions of the  $x = x_0$  line with the edges of the belt determine the confidence interval bounds. At right: 3D visualization of a confidence belt, taken from Ref. [23]. Note that Cranmer uses  $\theta$  instead of  $\mu$  to represent the model parameter, so that the green band in the  $x$ - $\theta$  plane represents the confidence belt (as shown in the left plot). Blue regions under the PDF curves indicate the integrated areas that equal  $\alpha$ , the bounds of which determine the edges of the belt.

are not uniquely determined by eq. 6.6, though choosing a value for one fixes the value of the other. As Feldman and Cousins put it [22], “one has total freedom to make this choice, *if the choice is not influenced by the data  $x_0$* ” (emphasis theirs). The key insight of their work was identifying an ordering principle by which to construct acceptance intervals using likelihood ratios. Namely, for a given  $\mu_0$ , values of  $x$  are ranked by  $\lambda = \mathcal{L}(x|\mu_0)/\mathcal{L}(x|\hat{\mu}(x))$ , where  $\hat{\mu}(x)$  maximizes the likelihood function. Values of  $x$  are incrementally added in order of decreasing  $\lambda$  to the acceptance region until the integrated probability reaches  $\alpha$ . This prescription has a number of attractive properties (detailed in [22]), and is closely related to the profile likelihood ratio (PLR) used in more complex analyses.

### 6.1.2 Profile likelihood ratio test statistic

Our trusty experiment with one observable and one model parameter, an apt characterization of counting experiments with well-defined backgrounds, falls short of describing complex datasets of multiple observables. In LUX, we consider energy ( $S_1, S_2$ ) as well as position ( $r, \phi, z$ ) observables for hundreds of events passing selection cuts, resulting in a high-dimensional data space. In principle, we could define a restrictive signal region, count the number of events, and calculate a Feldman-Cousins (FC) style limit. One limitation of this approach is that it does not account for uncertainties in our model (though see Ref. [142] for a technique allowing for this). Another is that we would be throwing out information that might enable better discrimination between signal and background events. Using the profile likelihood ratio addresses both of these issues, allowing for the construction of powerful confidence intervals with good coverage properties in reasonable computation time.

Before going into detail about the PLR, it's time for a notation update! Table 6.1 summarizes the terminology used in the following section. Note in particular that instead of  $\mu$ , our model parameters are now denoted by  $\sigma$ , the “parameter of interest” (POI), and a number of other “nuisance parameters” (NPs)  $\theta$ , whose values are also unknown but not of primary concern. In LUX analyses, the POI is often a WIMP-nucleon cross section, so  $\sigma$  is a convenient choice. The NPs are typically the expected event rates of various background sources, which are estimated from auxiliary measurements but have associated uncertainties. The likelihood of a dataset  $\mathcal{D}$  as a function of these model

Symbol	Description	Acronym	LUX example
$\sigma$	Parameter of interest	POI	WIMP-nucleon cross section
$\boldsymbol{\theta}$	Nuisance parameters	NPs	Background rates
$\mathbf{x}$	Observables: quantities measured for each event	–	S1, S2, position
$f(\mathbf{x})$	Probability density function (sometimes referred to simply as “model”)	PDF	S1–S2 distribution of ERs from Compton scattering
$\mathcal{D} = \{\mathbf{x}_e\}$	Dataset: collection of observables for each event $e$	–	WS2013, or an MC pseudo-experiment thereof
$\mathcal{L}(\mathcal{D}   \sigma, \boldsymbol{\theta})$	Likelihood function (the $\mathcal{D}$ is often dropped, as in the below definitions, with dataset dependency implied)	–	Extended unbinned likelihood (product of PDFs evaluated at each event, with a Poisson factor)
$\hat{\sigma}, \hat{\boldsymbol{\theta}}$	Maximum likelihood estimators: values of model parameters that maximize $\mathcal{L}$	MLEs	Best-fit rate of Rn and Kr beta decays in WS2014–16
$\hat{\boldsymbol{\theta}}(\sigma)$	Conditional maximum likelihood estimators: values of NPs that maximize $\mathcal{L}$ with $\sigma$ fixed	CMLEs	Best-fit rate of wall events in WS2014–16, assuming presence of 10 GeV WIMP signal
$\lambda(\sigma) \equiv \mathcal{L}(\sigma, \hat{\boldsymbol{\theta}}) / \mathcal{L}(\hat{\sigma}, \hat{\boldsymbol{\theta}})$	Profile likelihood ratio for test hypothesis $\sigma$	PLR	–
$q_\sigma \equiv -2 \ln(\lambda(\sigma))$	PLR test statistic: asymptotic behavior like chi-squared test	TS	–
$\alpha$	Confidence level	CL	Traditionally 90% for direct detection upper limits

Table 6.1: Notation used in this chapter pertaining to the statistical modeling of LUX data.

parameters is expressed as  $\mathcal{L}(\mathcal{D} | \sigma, \boldsymbol{\theta})$ . The structure of the LUX likelihood functions will be discussed in the following sections, but the definition remains the same as before: the likelihood of a dataset is its probability given certain values of the model parameters. For a given dataset, the likelihood can be maximized by scanning over the space spanned by  $\sigma$  and  $\boldsymbol{\theta}$ ; the resulting maximum likelihood estimators (MLEs) for the model parameters are called  $\hat{\sigma}$ ,  $\hat{\boldsymbol{\theta}}$ . Holding  $\sigma$  fixed to a test hypothesis value and varying the  $\boldsymbol{\theta}$  to maximize  $\mathcal{L}$  yields the conditional maximum likelihood estimators (CMLEs)  $\hat{\hat{\boldsymbol{\theta}}}$ .

The PLR test statistic  $q$  is defined as

$$q_\sigma \equiv -2 \ln(\lambda(\sigma)) \quad , \quad (6.7)$$

where  $\lambda$  is the PLR itself:

$$\lambda(\sigma) = \frac{\mathcal{L}(H_0)}{\mathcal{L}(H_1)} = \frac{\mathcal{L}(\sigma, \hat{\hat{\boldsymbol{\theta}}})}{\mathcal{L}(\hat{\sigma}, \hat{\boldsymbol{\theta}})} \quad . \quad (6.8)$$

In general, a test statistic (TS) maps a dataset to a single real number that, when compared against a reference TS distribution, indicates the compatibility between the data and a hypothesis. This enables us to go about setting acceptance regions as in Sec. 6.1.1, where our single observable served as our effective TS. The PLR is the optimal quantity from which to construct a TS for the same reason the FC ordering principle is ideal (see Neyman-Pearson Lemma [143]). In 6.8, the numerator represents the likelihood of the null hypothesis ( $H_0$ ) specified by  $\sigma$ , while the denominator corresponds to the alternative hypothesis ( $H_1$ ) defined by the unconditional MLEs, i.e. the “best-fit” hypothesis. Note that the nuisance parameters are “profiled” out:  $\lambda$  is independent of  $\boldsymbol{\theta}$ . In other words,

the value of the TS depends only on the dataset and the test hypothesis  $\sigma$ :

$$\lambda : \{\mathcal{D}, \sigma\} \rightarrow [0, 1] \quad (6.9)$$

$$\implies q : \{\mathcal{D}, \sigma\} \rightarrow [0, \infty] \quad . \quad (6.10)$$

As the test  $\sigma$  approaches  $\hat{\sigma}$ ,  $q$  approaches zero ( $\lambda \rightarrow 1$ ), indicating good agreement between the data and the test hypothesis. On the other hand, high  $q$  (i.e.  $\lambda \ll 1$ ) implies a poor fit of the test hypothesis to the data. In isolation, however, these statements are not very helpful; we need a distribution  $f(q_\sigma|\sigma)$  in order to quantify the compatibility of  $\sigma$  with  $\mathcal{D}$ . Here,  $f(q_\sigma|\sigma)$  is the distribution of the TS for datasets where  $\sigma$  is true.

Equipped with such a PDF (sometimes called a “sampling distribution”), we could calculate the  $p$  value of our observed data  $\mathcal{D}_{\text{obs}}$  under a test hypothesis  $\sigma$ :

$$p(\sigma) = \int_{q_{\sigma,\text{obs}}}^{\infty} f(q_\sigma|\sigma) dq \quad , \quad (6.11)$$

where  $q_{\sigma,\text{obs}}$  is the observed value of the TS, and  $p(\sigma)$  is the probability of observing a dataset at least as “extreme” as ours, if the test hypothesis is true.<sup>2</sup> In the case of the PLR, “more extreme” means yielding a worse fit of the test hypothesis. Figure 6.2 shows a cartoon of how this calculation is performed. The red distribution is integrated to find the  $p$  value for the observed data under the test hypothesis  $\sigma$ . One might also be interested in how a typical dataset corresponding to an alternate hypothesis compares to

<sup>2</sup>A common source of confusion arises when referring to  $\sigma$  as the “null hypothesis.” In hypothesis testing, “null” does not necessarily mean “no signal” (as it often does in the discussion of “null results” for direct detection experiments). In fact, when setting upper limits, it means the opposite: the null hypothesis is the presence of signal (with strength parameterized by  $\sigma$ ), which we are trying to reject at a certain CL. Since “test” seems more intuitive than “null” anyway, the former will continue to be used instead.

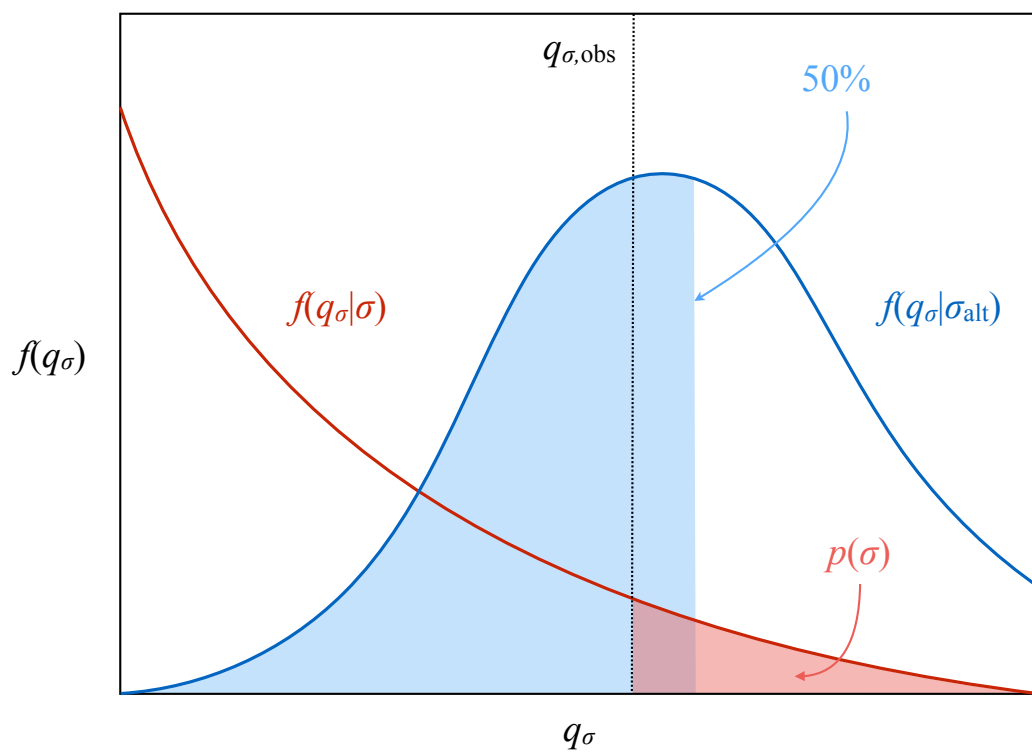


Figure 6.2: Illustration of a test statistic PDF. For the PLR test statistic, higher  $q$  indicates greater disagreement between the data and test hypothesis.

the test hypothesis and to the data. For example, when setting upper limits, it is desirable to know the *expected* limits; i.e., the confidence interval generated by the typical signal-free dataset. To this end, the blue distribution shows  $f(q_\sigma)$  for an ensemble of datasets where the true POI is not  $\sigma$ , but some alternative value  $\sigma_{\text{alt}}$  (but  $q_\sigma$  is still calculating by fixing the POI to  $\sigma$  in the numerator of  $\lambda$ ). The blue shaded region shows where 50% of the distribution is contained, so its rightmost edge denotes the median  $q_\sigma$  value for datasets drawn from the  $\sigma_{\text{alt}}$  model. The integral of  $f(q_\sigma|\sigma)$  can also be performed from this median  $q_\sigma$  to calculate the typical  $p(\sigma)$  value for datasets where  $\sigma_{\text{alt}}$  is true. More generally, other quantiles of  $f(q_\sigma|\sigma_{\text{alt}})$  can be used to determine the range of “expected”  $p(\sigma)$  values (assuming  $\sigma_{\text{alt}}$  is true).

Now that we can calculate  $p$  values for different  $\sigma$  hypotheses, we can “invert” these tests to find a confidence interval using the Neyman construction. Figure 6.3 illustrates this procedure, wherein  $p(\sigma)$  for the observed data is calculated over a range of test hypotheses. Values of  $\sigma$  are rejected when  $p(\sigma) < 1 - \alpha$ , which in this example corresponds to the range  $[\sigma_{\text{UL}}, \infty]$ .

A potential pitfall of naively reporting confidence intervals calculated from the raw PLR TS is that a lucky downward fluctuation in the background rate might result in a confidence interval which is *too* good; that is, we might exclude cross sections to which we are insensitive. Figure 6.4 shows an example of this, where the observed  $p$ -value reaches 10% at nearly the same cross section as the  $-2$  standard deviation quantile of background-only trials. For this reason, some experimentalists modify the definition

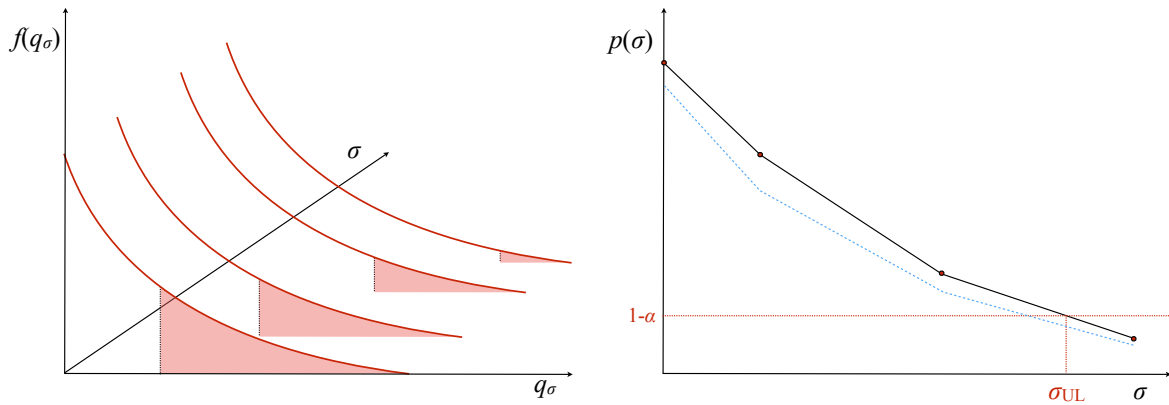


Figure 6.3: Inverted hypothesis testing for confidence interval construction. In the left panel, calculations of  $p(\sigma)$  are performed as in Fig. 6.2, at multiple values of  $\sigma$ . This information is condensed in the  $p$  value curve in the right panel, from which  $\sigma_{UL}$  may be found by solving  $p(\sigma) = 1 - \alpha$ . In addition to the  $p$  value curve obtained from the observed dataset, a blue curve is shown representing the median  $p(\sigma)$  values of an ensemble of datasets drawn from a fixed alternate hypothesis. For example, when setting an upper limit, this alternate hypothesis would be that the signal cross section is zero.

of the acceptance region by dividing the  $p$  value under the null hypothesis by the  $p$  corresponding to the alternate hypothesis (CLs method [144]). LUX results do not follow this approach; instead, we “power constrain” [145] the limits to some quantile of the expected distribution. Unlike CLs, this method has well defined coverage properties. Instead of modifying the confidence interval, a pre-decided floor is enforced such that the reported limit can be no smaller than this.

### 6.1.3 Applying the PLR to LUX

The asymptotic properties (in the limit of many events per dataset) of  $q_\sigma$  mimic a chi-square distribution [146], but in the intermediate regime of LUX data, no convenient analytic form for  $f(q_\sigma|\sigma)$  is available. As such, the distributions  $f(q_\sigma|\sigma)$  and  $f(q_\sigma|\sigma_{alt})$

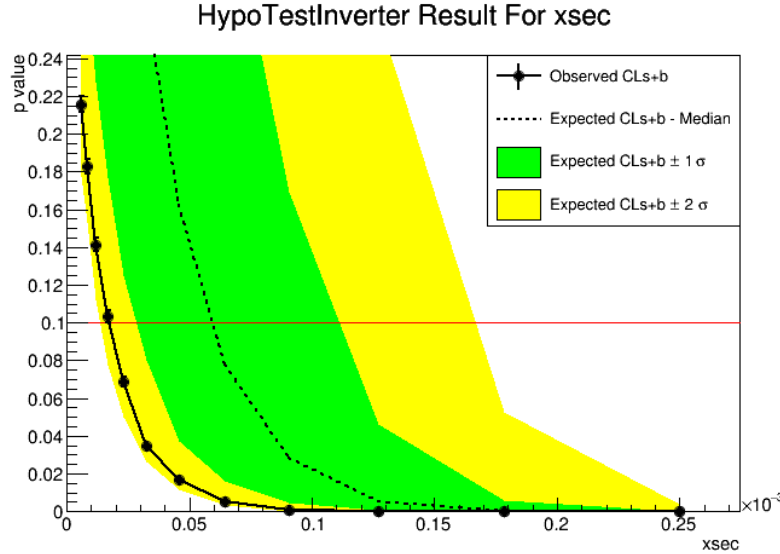


Figure 6.4:  $p$ -value curve for 100 GeV WIMP, neutron-only spin-dependent coupling. The solid black line shows  $p_{\text{obs}}$  as a function of the POI (here abbreviated “xsec”). The dashed black line shows  $p$  for a median dataset drawn from the background-only model, and the green and yellow bands show the  $\pm 1$ - and  $\pm 2$ - s.d. quantiles.

must be assembled via Monte Carlo (MC) simulation. The pseudocode in Algorithm 1 explicitly walks through the computational steps necessary to calculate the LUX upper limits on WIMP-nucleon cross section  $\sigma$ . The procedure is repeated in a scan over potential masses; the  $m_\chi$ -dependent limits are often interpolated to produce a smooth curve. Note (e.g. line 7 of code) that in the simulations performed to build the PDFs for  $q_\sigma$ , the NPs are set to the CMLE values calculated for the observed data under the test hypothesis. This is a short-cut: the truly frequentist thing to do would be to generate data from models defined by *all*  $\theta$ , not just  $\hat{\theta}(\sigma)$ ; however the curse of dimensionality usually renders this approach computationally impossible. Using  $\hat{\theta}(\sigma)$  to generate pseudo-experiments is known to statisticians as “hybrid resampling” [147, 148] and to physicists as the “profile construction” [23, 149], and turns out to be a good

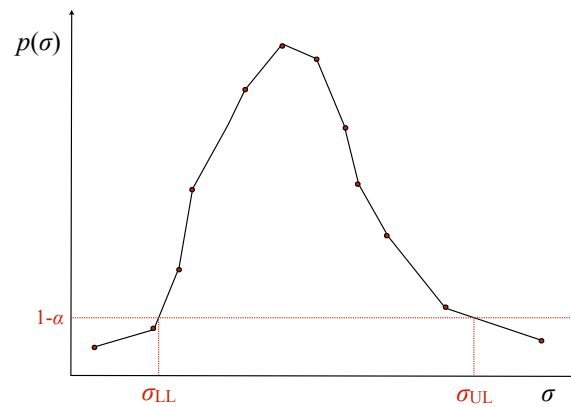


Figure 6.5:  $p(\sigma)$  values for a two-sided PLR TS. The best-fit  $\hat{\sigma}$  falls near the peak of the curve.

approximation of the full Neyman construction.

Another subtlety not yet considered concerns the range of values one allows  $\hat{\sigma}$  to take in the ML fits. This actually relates to the freedom to choose a one-sided upper limit or two-sided confidence interval, mentioned in Sec. 6.1.1. One advantage of the FC technique is that this transition between limits and allowed regions is handled seamlessly. The analogous approach using the PLR is to allow  $\hat{\sigma} > \sigma$  when calculating  $q_\sigma$ . This effectively yields a two-sided limit, since we are comparing the test hypothesis ( $\sigma$ ) to an alternative hypothesis ( $\hat{\sigma}$ ) that can have either more or less signal strength; both scenarios are considered “extreme”. A one-sided PLR test, on the other hand, restricts the definition of incompatibility to mean  $\hat{\sigma} < \sigma$ . This is discussed in detail in Ref. [146]. Two-sided PLR intervals have become the default choice for presenting results, because like the FC approach, they will return upper limits for small  $\hat{\sigma}$  but then transition to allowed regions when  $\hat{\sigma}$  is large. Figure 6.5 shows how  $p(\sigma)$  behaves in the latter scenario.

So far, we have described the PLR limit-setting procedure with only an abstract

---

**Algorithm 1:** PLR procedure for setting upper limits.

---

**Data:** WS dataset  $\mathcal{D}_{\text{obs}} = \{\mathbf{x}_e\}$   
**Result:** 90% CL upper limit on WIMP–nucleon cross section  $\sigma(m_\chi)$

```

// iterate over WIMP masses
1 for  $m_\chi \in [5, 10^5]$  GeV do
2   Calculate MLEs  $(\hat{\sigma}_{\text{obs}}, \hat{\boldsymbol{\theta}}_{\text{obs}})$  from  $\mathcal{L}(\mathcal{D}_{\text{obs}}|\sigma, \boldsymbol{\theta})$ ;
   // iterate over test hypotheses
3   for  $\sigma \in [\sigma_{\text{min}}, \sigma_{\text{max}}]$  do
4     Calculate CMLEs  $\hat{\boldsymbol{\theta}}_{\text{obs}}(\sigma)$ ;
5      $q_{\sigma, \text{obs}} = \mathcal{L}(\sigma, \hat{\boldsymbol{\theta}}_{\text{obs}}(\sigma)) / \mathcal{L}(\hat{\sigma}_{\text{obs}}, \hat{\boldsymbol{\theta}}_{\text{obs}})$ ;
     // build pdf for test statistic with MC trials
6     for  $i = 1$  to  $N_{MC}$  do
7       Generate dataset  $\mathcal{D}_i$  from  $\mathcal{L}(\sigma, \hat{\boldsymbol{\theta}}_{\text{obs}}(\sigma))$ ;
8       Calculate MLEs and CMLEs from  $\mathcal{L}(\mathcal{D}_i|\sigma, \boldsymbol{\theta})$ ;
9        $q_{\sigma, i} = \mathcal{L}(\sigma, \hat{\boldsymbol{\theta}}_i(\sigma)) / \mathcal{L}(\hat{\sigma}_i, \hat{\boldsymbol{\theta}}_i)$ ;
10      Update  $q_\sigma$  histogram to build  $f(q_\sigma|\sigma)$ ;
11    end
     // repeat for alternative (background-only) hypothesis
12    for  $i = 1$  to  $N_{MC}$  do
13      Generate dataset  $\mathcal{D}_i^{\text{alt}}$  from  $\mathcal{L}(0, \hat{\boldsymbol{\theta}}_{\text{obs}}(0))$ ;
14      Calculate MLEs and CMLEs from  $\mathcal{L}(\mathcal{D}_i^{\text{alt}}|\sigma, \boldsymbol{\theta})$ ;
15       $q_{\sigma, i} = \mathcal{L}(\sigma, \hat{\boldsymbol{\theta}}_i(\sigma)) / \mathcal{L}(\hat{\sigma}_i, \hat{\boldsymbol{\theta}}_i)$ ;
16      Update  $q_\sigma$  histogram to build  $f(q_\sigma|0)$ ;
17    end
18     $p_{\text{obs}}(\sigma) = \int_{q_{\sigma, \text{obs}}}^{\infty} f(q_\sigma|\sigma) dq_\sigma$ ;
19    Calculate  $p_{\text{exp}}(\sigma)$  using quantiles of  $f(q_\sigma|0)$  as lower integration bounds;
20  end
21  Interpolate  $p_{\text{obs}}$  vs.  $\sigma$  curve to solve  $p_{\text{obs}}(\sigma_{\text{UL}}) = 0.1$  (i.e.  $1 - \alpha$ );
22  Repeat with  $p_{\text{exp}}$  to find expected upper limits;
23 end
24 Plot  $m_\chi$  vs.  $\sigma_{\text{UL}}$ , showing both observed and expected limits;

```

---

notion of what the LUX likelihood function actually is. The exact structure will be examined in the following sections, but this equation serves as a helpful introduction:

$$\mathcal{L}(\mathcal{D}_{\text{obs}}|\sigma, \boldsymbol{\theta}) = e^{-n_{\text{exp}}(\sigma, \boldsymbol{\theta})} \left( \frac{n_{\text{exp}}(\sigma, \boldsymbol{\theta})^{n_{\text{obs}}}}{n_{\text{obs}}!} \right) \prod_{e=1}^{n_{\text{obs}}} f_{\text{tot}}(\mathbf{x}_e|\sigma, \boldsymbol{\theta}) \quad , \quad (6.12)$$

where the observed dataset  $\mathcal{D}_{\text{obs}}$  consists of  $n_{\text{obs}}$  events, with observables  $\mathbf{x}_e$ . This is the generic form of an extended unbinned likelihood function. The factor before the product is just the Poisson probability of observing  $n_{\text{obs}}$  events when expecting  $n_{\text{exp}}$ , hereafter expressed simply as  $\text{Pois}(n_{\text{obs}}|n_{\text{exp}})$ . (This factor is what “extended” refers to). Note that  $n_{\text{exp}}$  is determined by the model parameters; this dependence is shown explicitly in eq. 6.12, but will be omitted in future equations to preserve clarity.

The product over events constitutes the “unbinned” nature of the likelihood: the probability density of each event is considered via the total PDF  $f_{\text{tot}}$ , which depends parametrically on  $\sigma$  and  $\boldsymbol{\theta}$ . Typically, in rare event searches, this PDF is the weighted sum of various contributions, including the signal model  $f_s$  and various background model components  $f_b$  (recall that all PDFs  $f_i(\mathbf{x})$  are normalized to unity, by definition):

$$f_{\text{tot}}(\mathbf{x}) = \frac{1}{n_s + \sum_b n_b} \left[ n_s f_s(\mathbf{x}) + \sum_b n_b f_b(\mathbf{x}) \right] \quad . \quad (6.13)$$

Here, again, everything implicitly depends on  $\sigma$  and  $\boldsymbol{\theta}$ . In fact, in many analyses, one can take the POI  $\sigma$  to be the average number of signal events ( $n_s$ ), and the NPs to be the average number of background events of each type:  $\boldsymbol{\theta} = \{n_b\}$ . This is essentially the approach taken in the LUX analyses.

## 6.2 LUX WS2013 Likelihood

In the analysis of the WS2013 dataset, the extended unbinned likelihood takes the following form:

$$\begin{aligned} \mathcal{L}_{\text{WS2013}}(\mathcal{D}_{\text{obs}} | \sigma, \boldsymbol{\theta}) &= \text{PoiSS}(n_{\text{obs}} | n_{\text{exp}}) \\ &\times \prod_{e=1}^{n_{\text{obs}}} \frac{1}{n_{\text{exp}}} \left[ n_s(\sigma, k_{\text{Lind.}}) f_s(\mathbf{x}_e | g_{2,\text{DD}}) + \sum_b n_b f_b(\mathbf{x}_e) \right] \\ &\times \prod_{i \in \text{constr.}} \text{Gauss}(\theta_i | \theta_i^{\text{exp}}, \Delta\theta_i) \quad . \end{aligned} \quad (6.14)$$

Here, the POI  $\sigma$  is the WIMP-nucleon cross section, and  $\boldsymbol{\theta}$  are the nuisance parameters. As before,  $n_{\text{obs}}$  is the number of events (each with observables  $\mathbf{x}$ ) in the dataset  $\mathcal{D}_{\text{obs}}$ , the  $n_b$  are the NPs for expected counts in each background population, and  $n_s$  is the expected number of signal events, a function of POI  $\sigma$  and NP  $k_{\text{Lind.}}$  (Lindhard  $k$  [97]). We therefore define  $n_{\text{exp}} = n_s + \sum n_b$ , and the first factor in the likelihood becomes the familiar “extended” Poisson term. The subsequent product over events represents the probability of the dataset under the full model: a weighted sum of background PDFs  $f_b(\mathbf{x})$  and signal PDF  $f_s(\mathbf{x}_e | g_{2,\text{DD}})$ , where the latter is conditional on the NP for S2 gain during the DD calibration. Finally, the second product enforces Gaussian constraints on a subset of the NPs, encoding knowledge from auxiliary analyses into the likelihood.<sup>3</sup> A summary of NPs from WS2013, including their constraints and MLEs, can be found in Tab. 6.2, adapted from Ref. [17].

As shown in the table, the WS2013 backgrounds were grouped into six broad cate-

---

<sup>3</sup>These constraints on model parameters might smack of Bayesian priors, but a frequentist interpretation of them can be found in [23].

Parameter ( $\theta_i$ )	Constraint ( $\theta_i^{\text{exp}} \pm \Delta\theta_i$ )	Fit value ( $\hat{\theta}_i$ )
Lindhard $k$	$0.174 \pm 0.006$	...
S2 gain ratio: $g_{2,\text{DD}}/g_{2,\text{WS}}$	$0.94 \pm 0.04$	...
Low- $z$ -origin $\gamma$ counts: $n_{\gamma,\text{bottom}}$	$172 \pm 74$	$165 \pm 16$
Other $\gamma$ counts: $n_{\gamma,\text{rest}}$	$247 \pm 106$	$228 \pm 19$
$\beta$ counts: $n_{\beta}$	$55 \pm 22$	$84 \pm 15$
$^{127}\text{Xe}$ counts: $n_{\text{Xe-127}}$	$91 \pm 27$	$78 \pm 12$
$^{37}\text{Ar}$ counts: $n_{\text{Ar-37}}$	...	$12 \pm 8$
Wall counts: $n_{\text{wall}}$	$24 \pm 7$	$22 \pm 4$

Table 6.2: Nuisance parameters in the WS2013 likelihood model. Constraints are Gaussian with means and standard deviations indicated. Event counts are after cuts and analysis thresholds. The best-fit model has zero contribution from the signal PDF. In this case the signal-model parameters simply float to the central values of their constraints, and so are not listed.

gories: Compton scattering caused by gammas originating from beneath the LXe ( $n_{\gamma,\text{bottom}}$ ), other Comptons ( $n_{\gamma,\text{rest}}$ ), beta decays from Rn and Kr contamination in the LXe itself ( $n_{\beta}$ ), residual cosmogenic  $^{127}\text{Xe}$  ( $n_{\text{Xe-127}}$ ),  $^{37}\text{Ar}$  ( $n_{\text{Ar-37}}$ ), and misreconstructed events occurring near the walls of the detector ( $n_{\text{wall}}$ ). In principle, though, a much more detailed background model could be constructed. For example, the contribution from each bolt and screw in the detector could be modeled individually and added to the likelihood model with an associated NP weight. However, doing so would not only drastically slow down the ML fitting algorithm, it would not considerably improve discrimination. Besides, the WS data is not sensitive to small shifts in the radioactivity of individual detector components. Backgrounds *are* simulated in this way (piece by piece) to estimate their strength and PDFs, but similar ones are grouped together to simplify the final model. In fact, all Compton backgrounds were originally modeled with a single normalization NP,

since they have the same recoil distribution. However, this approach failed to yield a good fit to the data. It was discovered that a higher than expected rate of Compton events were occurring in the lower portion of the detector [17]. As such, the Compton model was broken in two to account for this uncertainty; one population describes the low- $z$  gammas, the other describes the rest.

Apart from the constraint factors, the main departures of eq. 6.14 from the simplest case analysis discussed in Sec. 6.1.3 are the NPs affecting the signal model. Varying the  $k_{\text{Lind.}}$  parameter in the NR model within its uncertainties was found to affect the WIMP detection rate (i.e. events per unit cross section) by shifting the S1–S2 distribution into or out of the region of interest determined by the selection cuts. This effect was parameterized and included in the model (see Fig. 6.6). Note that the *shape* of the signal model  $f_s(S1, \log_{10} S2)$  is assumed to be unaffected by  $k_{\text{Lind.}}$ , though this is an approximation. On the other hand, the  $g_2$  value (S2 gain) is allowed to float as a NP, as this detector parameter is thought to have drifted during the time between the WIMP search exposure and the NR calibration (DD neutron beam). Since this systematic effect represents an uncertainty in the shape of the signal S1–S2 PDF (and not simply the normalization), allowing it to float in the ML fits introduces a grave computation slowdown. A new PDF  $f_s$  must be built (via MC generation) every time the NP is incremented beyond a certain step size. With that said, the uncertainty on this model parameter is constrained with a standard deviation of just  $\sim 4\%$ , and its inclusion as a NP has a negligible effect on the calculated limit. It is therefore frozen at its nominal value in the

combined WS2013+WS2014–16 analysis to save CPU cycles (discussed in Sec. 6.4).<sup>4</sup>

In WS2013, the PDFs and events are defined in four observables:

$$\mathbf{x} = \{r, z, S1, \log_{10} S2\} \quad , \quad (6.15)$$

where the position variables  $r$  and  $z$  have been corrected (via a transformation of the raw reconstructed coordinates that accounts for E-field fringing). Adopting the notation of Ref. [20], the italicized pulse areas  $S1$  and  $S2$  have also been corrected for geometry dependent efficiencies (i.e. light collection and electron lifetime). Signal events (NRs from WIMP scattering) populate different regions in observable space than background events. The choice of which observables to include in an analysis is guided by maximizing this discrimination. We could, for example, elect to consider only  $S1$  and  $S2$  in our analysis, since after all, ERs and NRs are distinguished via these variables. On the other hand, some background events originate from radiation sources external to the LXe, and are concentrated near the edges of the fiducial volume. This spatial information can be used to further discriminate between signal and background events, which is why  $r$  and  $z$  are included in the likelihood models. See Appendix B for a brief study on the discriminating power of just the S1 and S2 observables.

Most of the PDFs are decomposed into lower-dimensional functions:

$$f(\mathbf{x}) = f(r, z) \times f(S1, \log_{10} S2) \quad , \quad (6.16)$$

since the position observables are typically uncorrelated with the energy response ob-

---

<sup>4</sup>In general, including more NPs in an analysis or relaxing the constraints on them tends to weaken the resultant PLR limits. As Cowan *et al.* explain [146]: “This reflects the loss of information about [the POI] due to the systematic uncertainties.” Thus, since  $g_{2,DD}$  is constrained so tightly, fixing it to its nominal value does not result in a substantial (unfair) gain in sensitivity. Specifically, the expected WS2013 limit for 50 GeV WIMPs improves by less than 2% when this NP is fixed.

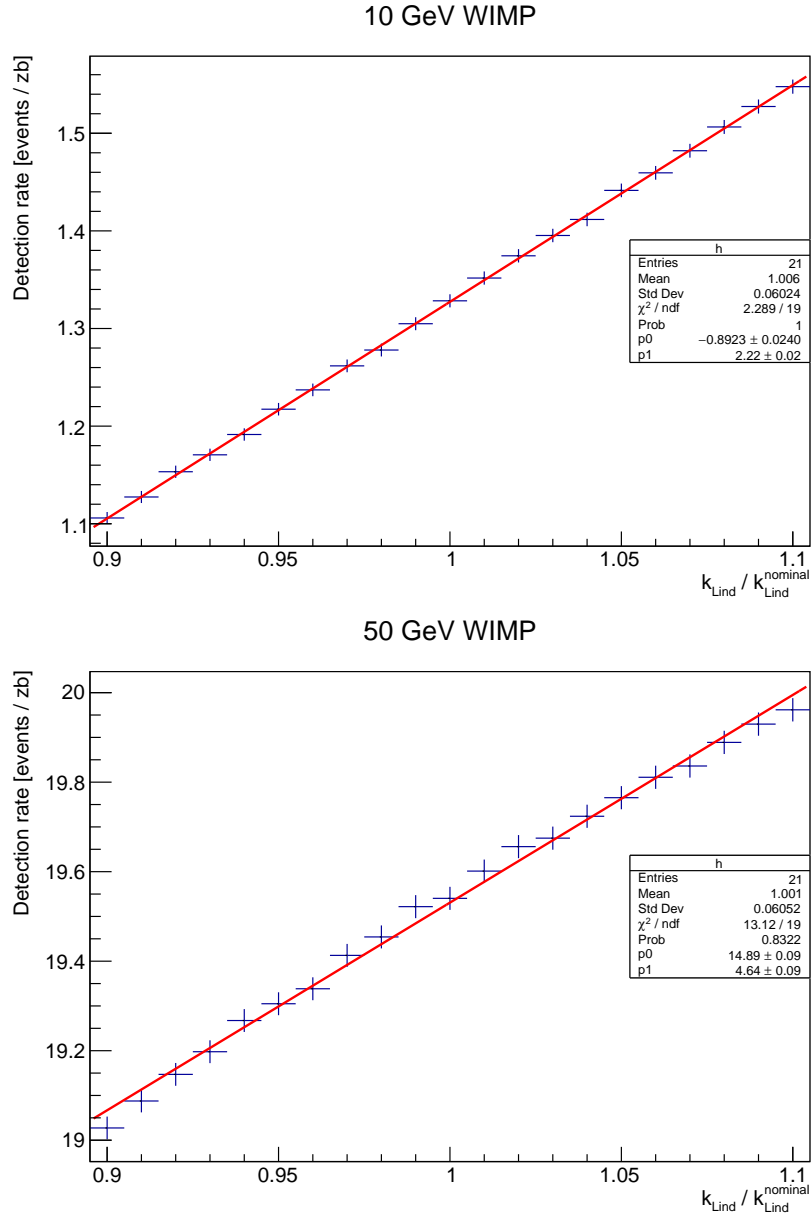


Figure 6.6: WS2014–16 dependence of  $n_s$  on  $k_{\text{Lind.}}$ , shown for two WIMP masses. This introduces uncertainty on the WIMP detection rate at a given signal cross section in the likelihood model. Note that the small uncertainty on  $k_{\text{Lind.}}$  (see Tab. 6.2) means that the NP is effectively constrained to within  $\sim 4\%$  of the nominal value. Even for small WIMP masses, where the effect is most prominent, this translates to only  $\sim 20\%$  uncertainty in the detection rate.

servables. In particular, we have:

$$f_s(\mathbf{x}|g_{2,DD}) = \text{unif}(r^2) \times \text{unif}(z) \times f_\chi(S1, \log_{10} S2 | g_{2,DD}) \quad (6.17)$$

$$f_{\gamma,\text{bottom}}(\mathbf{x}) = f_{\gamma,\text{bottom}}(r, z) \times f_{\text{ER}}(S1, \log_{10} S2) \quad (6.18)$$

$$f_{\gamma,\text{rest}}(\mathbf{x}) = f_{\gamma,\text{rest}}(r, z) \times f_{\text{ER}}(S1, \log_{10} S2) \quad (6.19)$$

$$f_\beta(\mathbf{x}) = \text{unif}(r^2) \times \text{unif}(z) \times f_{\text{ER}}(S1, \log_{10} S2) \quad (6.20)$$

$$f_{\text{Xe-127}}(\mathbf{x}) = f_{\text{Xe-127}}(r, z) \times f_{\text{Xe-127}}(S1, \log_{10} S2) \quad (6.21)$$

$$f_{\text{Ar-37}}(\mathbf{x}) = \text{unif}(r^2) \times \text{unif}(z) \times f_{\text{Ar-37}}(S1, \log_{10} S2) \quad (6.22)$$

Because our position coordinates are corrected, some of the event populations have spatial PDFs that are conveniently uniform in the fiducial volume. This includes the WIMP signal model as well as background contaminants that are dissolved within the LXe (i.e. other nobles elements: Ar, Kr, and Rn). Other spatial PDFs are non-trivial, and have been estimated with MC simulations generated with the GEANT4-based [118] LUXSIM [119] software. These nonuniform PDFs are implemented as 2D histograms with 20 bins in radius ( $r \in [0, 20]$  cm) and 40 bins in height ( $z \in [6.54, 48.6]$  cm).

The energy response PDFs are calculated using MC data from the Noble Element Simulation Technique (NEST) [99] package. Here,  $f_{\text{ER}}$  denotes the distribution generated from seeding NEST with electron recoils uniform in energy ( $E \in [0, 20]$  keV). In our low-energy region of interest, this is a reasonable approximation for Compton and radon/krypton beta spectra.  $f_{\text{Xe-127}}(S1, \log_{10} S2)$  and  $f_{\text{Ar-37}}(S1, \log_{10} S2)$  are also gen-

erated from NEST-simulated ERs, but each have specific recoil spectra. Similarly, the WIMP NR model  $f_{\chi}(S1, \log_{10} S2 | g_{2,DD})$  is generated from NEST trials, using the recoil spectrum relevant to the WIMP mass being tested and interaction type (SI or SD).

The final background PDF implemented for WS2013 describes “wall” events: interactions occurring on the PTFE panels with suppressed charge yield (i.e. small S2). Since the statistical uncertainty of position reconstruction scales as  $S2^{-1/2}$ , the (reconstructed) low-radius tail of this population can leak into the fiducial volume. Unlike the other models, the wall model was empirically constructed using sideband samples of the WIMP-search data. The final PDF is defined as:

$$f_{\text{wall}}(\mathbf{x}) = f_{\text{wall}}(r | \log_{10} S2) \times f_{\text{wall}}(S1, \log_{10} S2) \times f_{\text{wall}}(z) \quad . \quad (6.23)$$

The radial model  $f_{\text{wall}}(r | \log_{10} S2)$  is actually implemented analytically as a Gaussian centered at the wall radius ( $r = 23.65$  cm) with sigma given by a fitted function of  $S2$ :  $\sigma = (a \log_{10} S2 + b)^{-1}$ . The remaining PDFs are inferred from the sideband data (smoothed with a kernel density estimation technique) and implemented as histograms (Ref. [120] has more details).

### 6.3 LUX WS2014–16 Likelihood

The structure of the WS2014–16 likelihood function differs from that of WS2013 in that it consists of multiple channels:

$$\begin{aligned}
 \mathcal{L}_{\text{WS2014–16}}(\mathcal{D}_{\text{obs}} | \sigma, \boldsymbol{\theta}) &= \prod_{t \in \text{d.b.}} \text{Poiss}(n_{\text{obs}}^t | n_{\text{exp}}^t) \\
 &\times \prod_{e=1}^{n_{\text{obs}}^t} \frac{1}{n_{\text{exp}}^t} \left[ n_s^t(\sigma, k_{\text{Lind.}}) f_s^t(\mathbf{x}_e) + \sum_b n_b^t f_b^t(\mathbf{x}_e) \right] \\
 &\times \prod_{i \in \text{constr.}} \text{Gauss}(\theta_i | \theta_i^{\text{exp}}, \Delta\theta_i) \quad .
 \end{aligned} \tag{6.24}$$

The WS2014–16 exposure is segmented into four discrete time periods (or “date bins”) within which detector conditions were reasonably stable. The index  $t$  refers to these date bins. Each date bin is modeled separately with unique signal and background PDFs (now labeled by  $t$ ), though the NPs were kept as global quantities. That is, the total expected counts  $n_{s,b} = \sum_t n_{s,b}^t$  are allowed to float, but the ratios  $n_{s,b}^t/n_{s,b}$  are fixed. As such, there are no date bin-specific NPs or constraints. NP values and constraints are reproduced from Ref. [20] in Tab. 6.3.

As a result of the challenges posed by the distorted field geometry in WS2014–16, the models describing signal and background distributions become necessarily more complex. Most strikingly, the spatial distributions must mimic the warped detector shape as it appears in uncorrected S2 coordinate space. A decision was made early in the analysis to use the raw reconstructed position variables for the data (as opposed to attempting a correction, as in WS2013), and transform the models into this coordinate space. In the notation of Ref. [20],  $\mathbf{r}_{\text{S2}} = \{r_{\text{S2}}, \phi_{\text{S2}}, z_{\text{S2}}\}$  are the spatial observables: reconstructed S2

Parameter ( $\theta_i$ )	Constraint ( $\theta_i^{exp} \pm \Delta\theta_i$ )	Fit Value ( $\hat{\theta}_i$ )
Lindhard $k$ [15]	$0.174 \pm 0.006$	-
Low- $z$ -origin $\gamma$ counts	$94 \pm 19$	$99 \pm 14$
Other $\gamma$ counts	$511 \pm 77$	$590 \pm 34$
$\beta$ counts	$468 \pm 140$	$499 \pm 39$
$^8\text{B}$ counts	$0.16 \pm 0.03$	$0.16 \pm 0.03$
PTFE surface counts	$14 \pm 5$	$12 \pm 3$
Random coincidence counts	$1.3 \pm 0.4$	$1.6 \pm 0.3$

Table 6.3: Model parameters in the best fit to WS2014–16 data for an example 50 GeV  $c^{-2}$  WIMP mass. Constraints are Gaussian with means and standard deviations indicated. Fitted event counts are after cuts and analysis thresholds.

radius, azimuth, and event drift time. (The introduction of the third spatial dimension is necessary, owing to the axial asymmetry of the field deformation). Thus, simulations from LUXSIM are transformed into S2-space (using a mapping derived from  $^{83\text{m}}\text{Kr}$  calibration data) before being binned and smoothed into histogram PDFs.

The electric field strength varied significantly within the fiducial volume, resulting in position-varying light and charge yield. This field variation is primarily correlated to  $z$ -position. So, in addition to the segmentation by calendar date, the data are further divided into four bins corresponding to interaction height in the detector (these bins are termed “ $z$ -slices”). Within a  $z$ -slice of a given date bin, electric field variation is small enough that good separation between  $f_{\text{ER}}$  and  $f_{\text{NR}}$  is achieved. Therefore, instead of a single PDF describing the energy response of the detector to a given population (as in WS2013), there are now  $4[\text{date bins}] \times 4[\text{z-slices}] = 16$ .

Bringing all of this together, we have our observables:

$$\mathbf{x} = \{r_{S2}, \phi_{S2}, z_{S2}, S1, \log_{10} S2\} \quad , \quad (6.25)$$

and, for most models,

$$f^t(\mathbf{x}) = f^t(\mathbf{r}_{S2}) \times f^t(S1, \log_{10} S2 | z_{S2}) \quad , \quad (6.26)$$

where

$$f^t(S1, \log_{10} S2 | z_{S2}) \equiv f^{t,z}(S1, \log_{10} S2) = \begin{cases} f^{t,1}(S1, \log_{10} S2) & z_{S2} \in \text{z-slice 1} \\ f^{t,2}(S1, \log_{10} S2) & z_{S2} \in \text{z-slice 2} \\ f^{t,3}(S1, \log_{10} S2) & z_{S2} \in \text{z-slice 3} \\ f^{t,4}(S1, \log_{10} S2) & z_{S2} \in \text{z-slice 4} \end{cases} \quad . \quad (6.27)$$

The NR signal model is implemented in this way, as are the ER background distributions (for  $\gamma$ s and  $\beta$ s). In WS2014–16,  $^{127}\text{Xe}$  is not included in the background model (this cosmogenic isotope had decayed away), and  $^{37}\text{Ar}$  is also omitted (no evidence for it was seen in the data). However, an NR background from coherent nuclear scattering from  $^8\text{B}$  solar neutrinos is included (using this same PDF structure), even though the expected rate was calculated to be only 0.16 events for the entire exposure.<sup>5</sup>

Another new model was introduced in WS2014–16 to describe accidental coincidences of random, uncorrelated S1 and S2 pulses. This model is constructed empirically, using the distributions of isolated S1 and S2 pulses, and assuming a uniform spatial distribution:

$$f_{\text{acc.}}^t(\mathbf{x}) = f_{\text{unif.}}^t(\mathbf{r}_{S2}) \times f_{\text{acc.}}(S1, \log_{10} S2) \quad . \quad (6.28)$$

Note that  $f_{\text{unif.}}^t(\mathbf{r}_{S2})$  describes a uniform (in “true” coordinates) 3D spatial distribution

---

<sup>5</sup>In retrospect, it would have been more prudent to model the NR background contribution of neutrons (originating from  $(\alpha, n)$  reactions in detector components, or from cosmic muon spallation). A moderately higher rate (on the order of  $\sim 0.5$  total events) is expected from these sources [16].

that has been mapped into the  $t$ -specific S2 coordinate system. This PDF is also used for the signal,  $^8\text{B}$ , and  $\beta$  models.

Finally, the most cumbersome background model implemented in the WS2014–16 likelihood again describes the population of wall events. The PDF formulation is similar to Eqn. 6.23, though now that we are in S2 coordinate space, the correlations are more intricate. For example, in S2 space, the position of the wall (and thus the center of the radial distribution) is not at a constant  $r_{\text{S2}}$ . Rather, wall position depends strongly on  $\{\phi_{\text{S2}}, z_{\text{S2}}\}$  and evolves in time. The wall model is constructed according to:

$$f_{\text{wall}}^t(\mathbf{x}) = f_{\text{wall}}^t(r_{\text{S2}} | \log_{10} S2, \phi_{\text{S2}}, z_{\text{S2}}) \times f_{\text{wall}}^t(S1, \log_{10} S2) \times f_{\text{wall}}^t(\phi_{\text{S2}}, z_{\text{S2}}) \quad . \quad (6.29)$$

Because of technical issues, the PDF was not actually implemented in this separable, conditional format. Instead, it was evaluated on a 5D grid and stored as a finely binned histogram object. This technique was shown to be reliable, albeit inelegant: each date bin required its own 5D histogram (with  $\sim 10^7$  total bins) to describe the wall model, adding  $\sim 4$  GB to the RAM budget of the PLR calculation code.

Unlike in WS2013, the WS2014–16 was “salted,” so the likelihood model was tested against a sideband region to assess goodness of fit. Namely, events above the ER band mean in  $S1$ – $\log_{10} S2$  space (i.e. far from the signal region and the salt events) were compared against the model. This fit informed the nominal values of some of the NPs. Following unblinding, the best-fit model projections and data show very good agreement, as seen in Fig. 6.7 through 6.13. Given the electric field complications, the compatibility of the projected spatial distributions with the data is almost miraculous, though the last

bin of the  $r_{S2}$  histogram might indicate the limitations of the field mapping algorithms. Another discrepancy can be seen in the first  $S1$  bin (see Fig 6.7), where the model strongly over-predicts events. This effect was traced to a difference between the MC simulations and the processing of real waveforms, and was found not to significantly affect the overall quality of the fit or the PLR results. In the  $\log_{10} S2$  spectrum (Fig. 6.8), low area pulses are more abundant in the data than predicted by the model. Below 1000 phd, we expect 13 events but see 20 (Poisson  $p = 4.2\%$ , though the discrepancy is more pronounced if one cuts at lower  $S2$ ). This can be seen as well in Fig. 6.9, where these events appear at  $S1 < 17$  phd, perhaps pointing to an inadequacy in the wall or accidentals model. In fact, two of these events occur at low enough radius that they are not well-described by the wall model at all, and are singlehandedly responsible for the weakness of the LUX limits for low WIMP masses. A PLR discovery test performed for 5 GeV WIMPs yields  $p \sim 2\%$ ; certainly not enough to claim anything interesting, other than maybe an overlooked or misunderstood background population.

## 6.4 Combined Analysis

The combined WS2013 and WS2014–16 likelihood is essentially the product of the two run-specific likelihoods. In this way, WS2013 can be thought of as a fifth date bin in the multi-channel likelihood describing WS2014–16 (indeed, this is how it was implemented in ROOFIT). Nuisance parameters were taken to be 100% uncorrelated between WS2013 and WS2014–16, with the exception of Lindhard  $k$ , which is assumed to be 100%. This

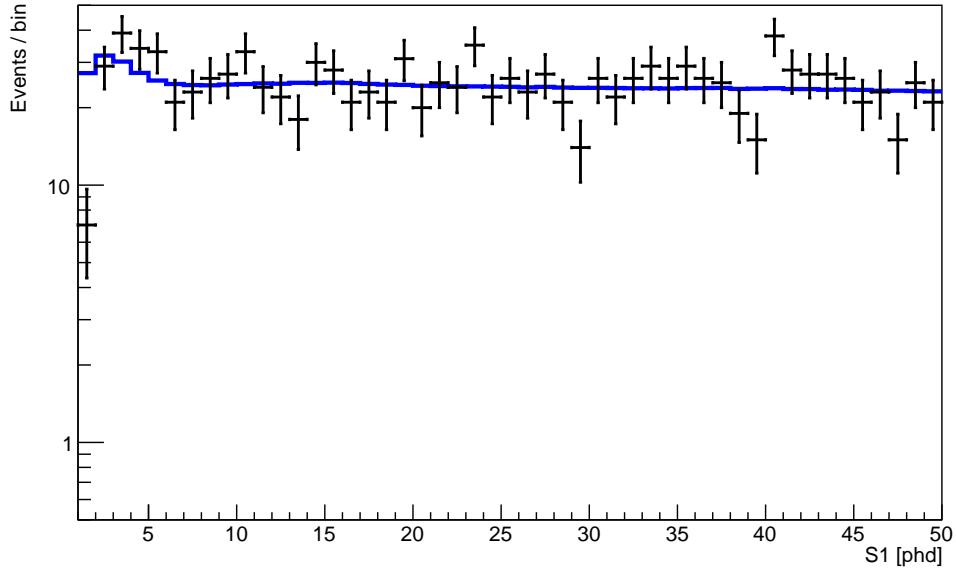


Figure 6.7: Projection of the background onto the  $S1$  axis (blue), with the WS2014–16 data shown in black.

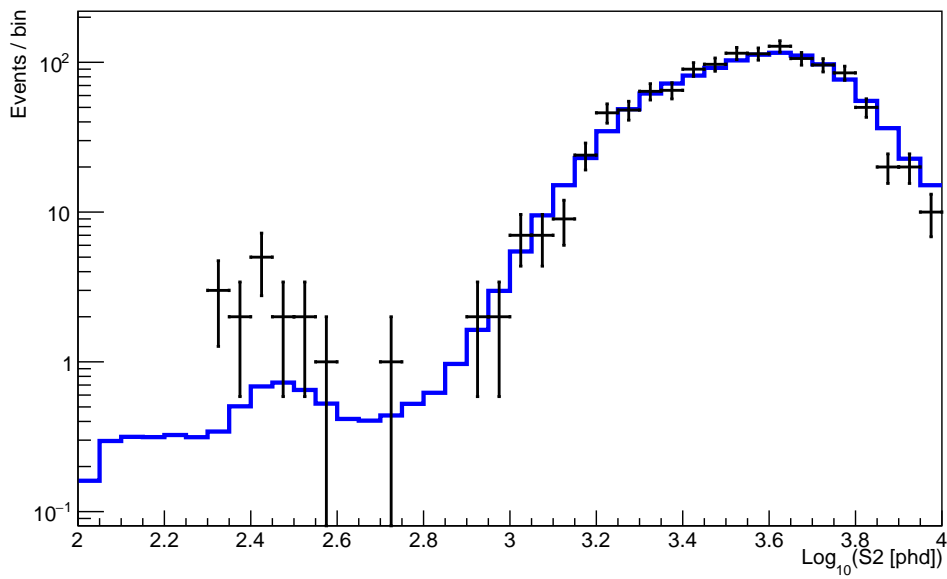


Figure 6.8: Projection of the background model onto the  $\log_{10} S2$  axis (blue), with the WS2014–16 data shown in black.

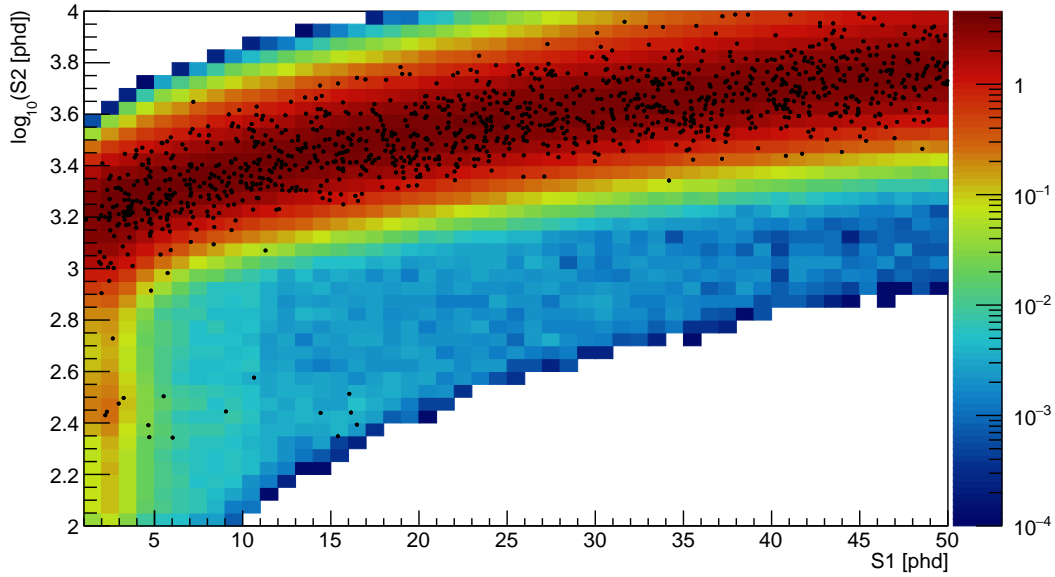


Figure 6.9: Projection of the background model onto the  $S1$ - $\log_{10} S2$  plane (blue), with the WS2014–16 data shown in black.

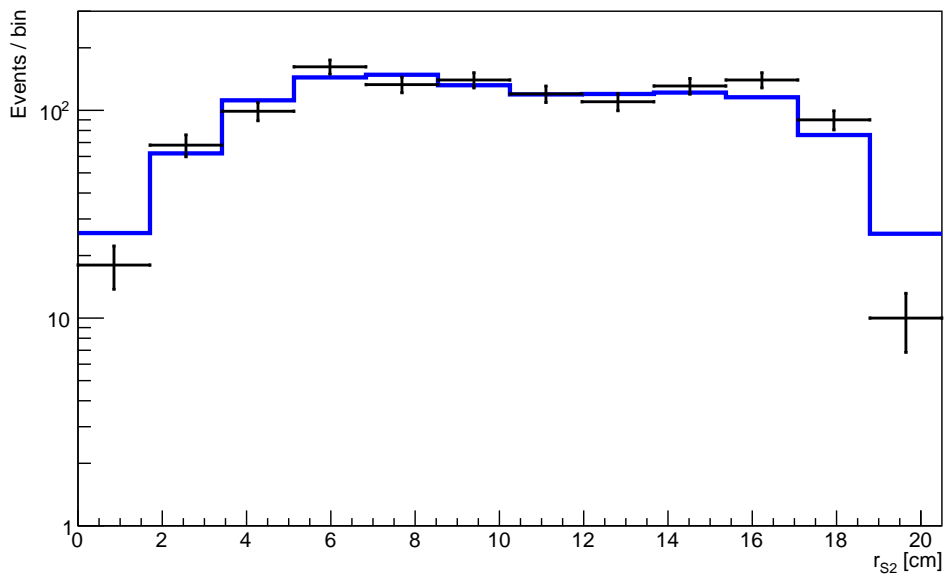


Figure 6.10: Projection of the background model onto the  $r_{S2}$  axis (blue), with the WS2014–16 data shown in black.

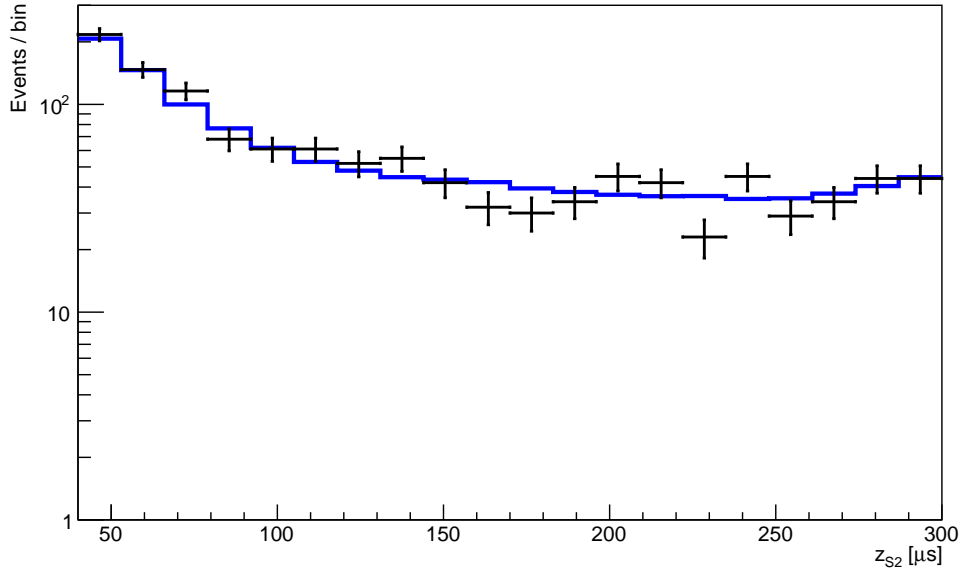


Figure 6.11: Projection of the background model onto the  $z_{S2}$  axis (blue), with the WS2014–16 data shown in black.

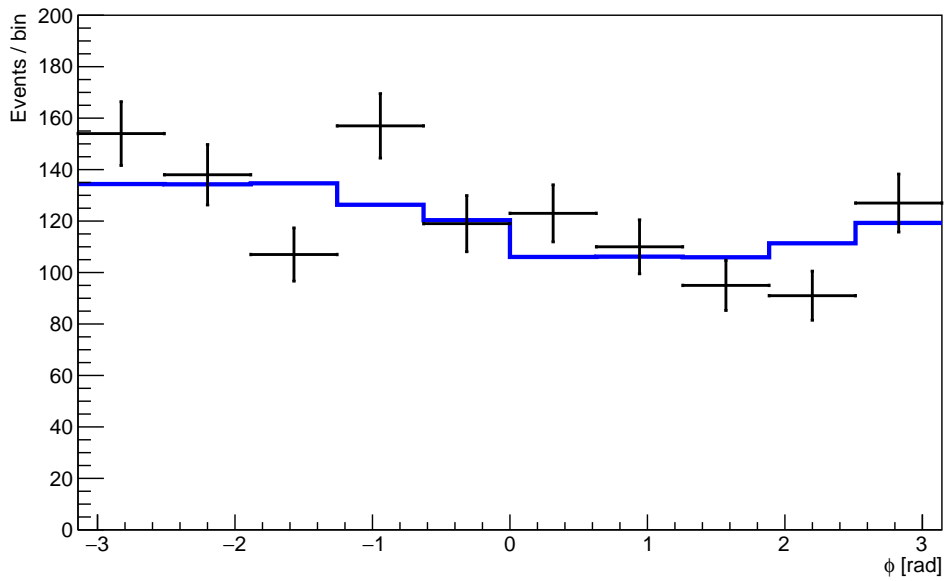


Figure 6.12: Projection of the background model onto the  $\phi_{S2}$  axis (blue), with the WS2014–16 data shown in black.

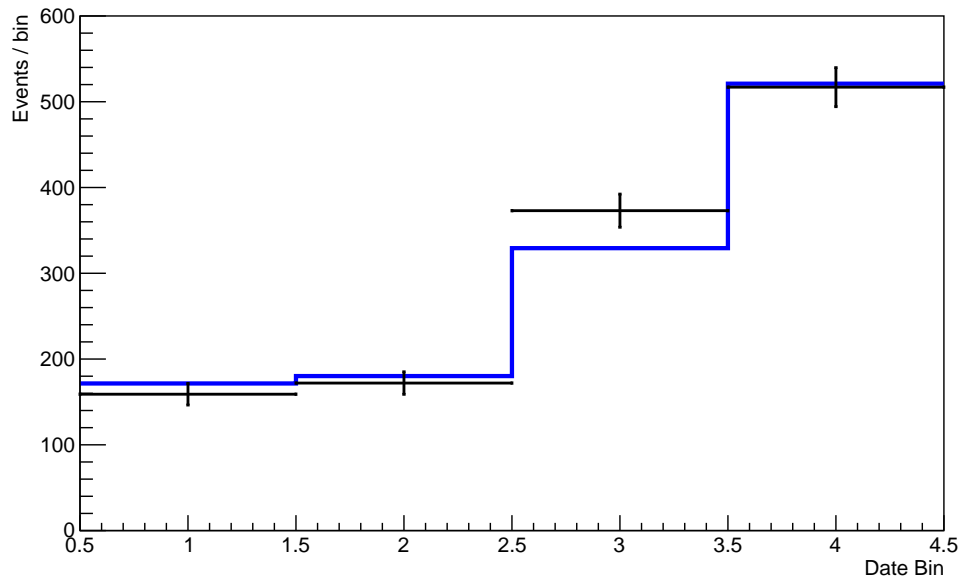


Figure 6.13: Projection of the background model onto the date bin axis (blue), with the WS2014–16 data shown in black. Note that the date bins do not each have equal live time: date bins 1 and 2 each contain  $\sim 47$  livedays, whereas date bins 3 and 4 contain double and triple that exposure time, respectively. The background rate is thus roughly constant.

approach is justifiable from purely physical considerations: true background levels, especially from Kr/Rn contamination in the LXe, could easily have changed between runs; furthermore, since the simulation and calculation of expected background rates differed substantially in WS2014–16 (different fiducial volume, spatial coordinate mapping, etc.), we do not expect systematic uncertainty on these rates to be correlated with those of WS2013. Symbolically, then,

$$\mathcal{L}_{\text{LUX}}(\sigma, \boldsymbol{\theta}) = \mathcal{L}'_{\text{WS2013}}(\sigma, \boldsymbol{\theta}'_{\text{WS2013}}) \times \mathcal{L}_{\text{WS2014–16}}(\sigma, \boldsymbol{\theta}_{\text{WS2014–16}}) \quad , \quad (6.30)$$

where  $\mathcal{L}'_{\text{WS2013}}(\sigma, \boldsymbol{\theta}'_{\text{WS2013}})$  differs from Eqn. 6.14 in the omission of  $g_{2,DD}$  as a nuisance parameter. Note also that the NP  $k_{\text{Lind}}$  appears in both  $\boldsymbol{\theta}'_{\text{WS2013}}$  and  $\boldsymbol{\theta}_{\text{WS2014–16}}$  (whereas all other NPs are unique), and the corresponding Gaussian constraint is applied only once.

## 6.5 Review of LUX PDFs

Here, we recapitulate the format of the LUX model PDFs. Visualizations are provided at the end of the chapter for projections of the WS2014–16 models.

### 6.5.1 WS2013

**1D histogram PDFs**  $f_{\text{wall}}(z)$

**2D histogram PDFs**  $f_{\gamma, \text{bottom}}(r, z), f_{\gamma, \text{rest}}(r, z), f_{\text{Xe-127}}(r, z), f_{\chi}(S1, \log_{10} S2),$

$f_{\text{ER}}(S1, \log_{10} S2), f_{\text{Xe-127}}(S1, \log_{10} S2), f_{\text{Ar-37}}(S1, \log_{10} S2), f_{\text{wall}}(S1, \log_{10} S2)$

**Conditional analytic PDFs**  $f_{\text{wall}}(r | \log_{10} S2)$

Note that the wall PDF must be implemented with the conditional radial distribution for the use of  $f_{\text{wall}}(S1, \log_{10} S2)$  to be valid. If this is impractical, the model would need to be handled in a way similar to WS2014–16, and evaluated on a 3D grid to obtain a joint histogram PDF for  $f_{\text{wall}}(r, S1, \log_{10} S2)$ .

### 6.5.2 WS2014–16

**2D histogram PDFs**  $f_{\chi}^{t,z}(S1, \log_{10} S2)$ ,  $f_{\text{ER}}^{t,z}(S1, \log_{10} S2)$ ,  $f_{\text{sB}}^{t,z}(S1, \log_{10} S2)$ ,  
 $f_{\text{acc.}}(S1, \log_{10} S2)$

**3D histogram PDFs**  $f_{\text{unif.}}^t(\mathbf{r}_{\text{S2}})$ ,  $f_{\gamma, \text{bottom}}^t(\mathbf{r}_{\text{S2}})$ ,  $f_{\gamma, \text{rest}}^t(\mathbf{r}_{\text{S2}})$

**5D histogram PDFs**  $f_{\text{wall}}^t(\mathbf{r}_{\text{S2}}, S1, \log_{10} S2)$

Recall that the  $t$  and  $z$  indices run from 1 to 4, implying a multiplicity of 4 or 16 for some of the PDFs. Note also that the NR and ER models are not completely separable into 2D and 3D: the energy response PDF is conditional on position (as described in Eqn. 6.27).

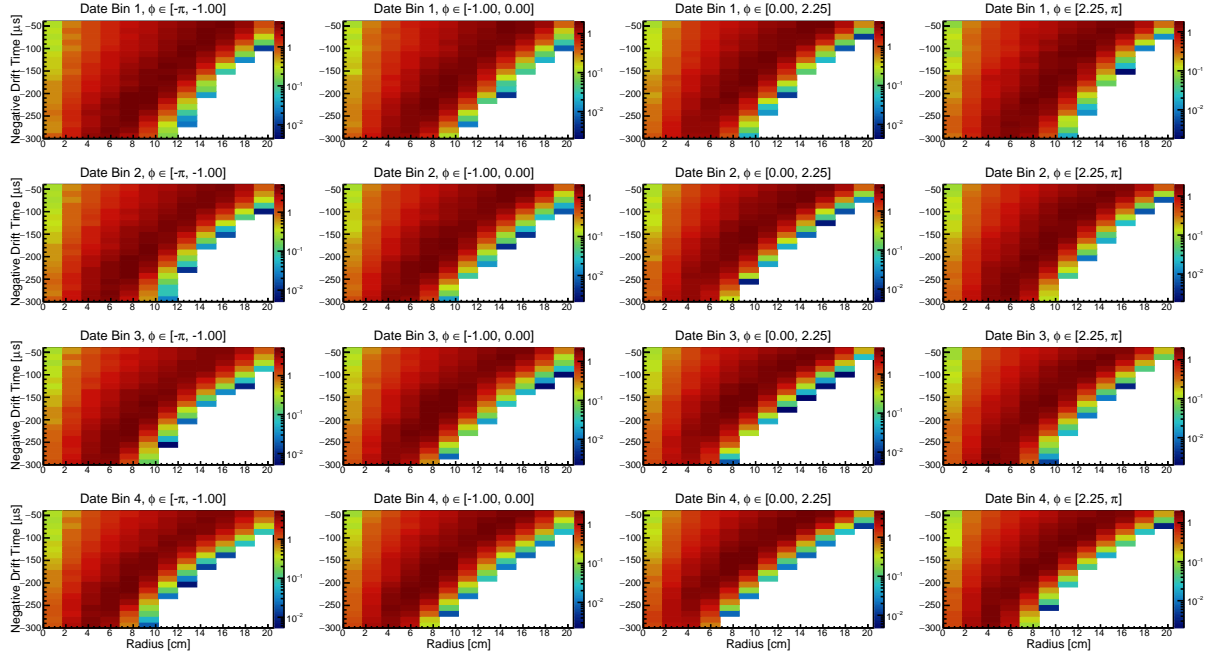


Figure 6.14: Uniform spatial distribution (in real space) converted into S2 coordinates:  $f_{\text{unif}}^t(\mathbf{r}_{S2})$ , radius vs. drift time in slices of azimuth and date. Describes WIMP,  $^8\text{B}$ ,  $\beta$ , and accidental coincidence populations.

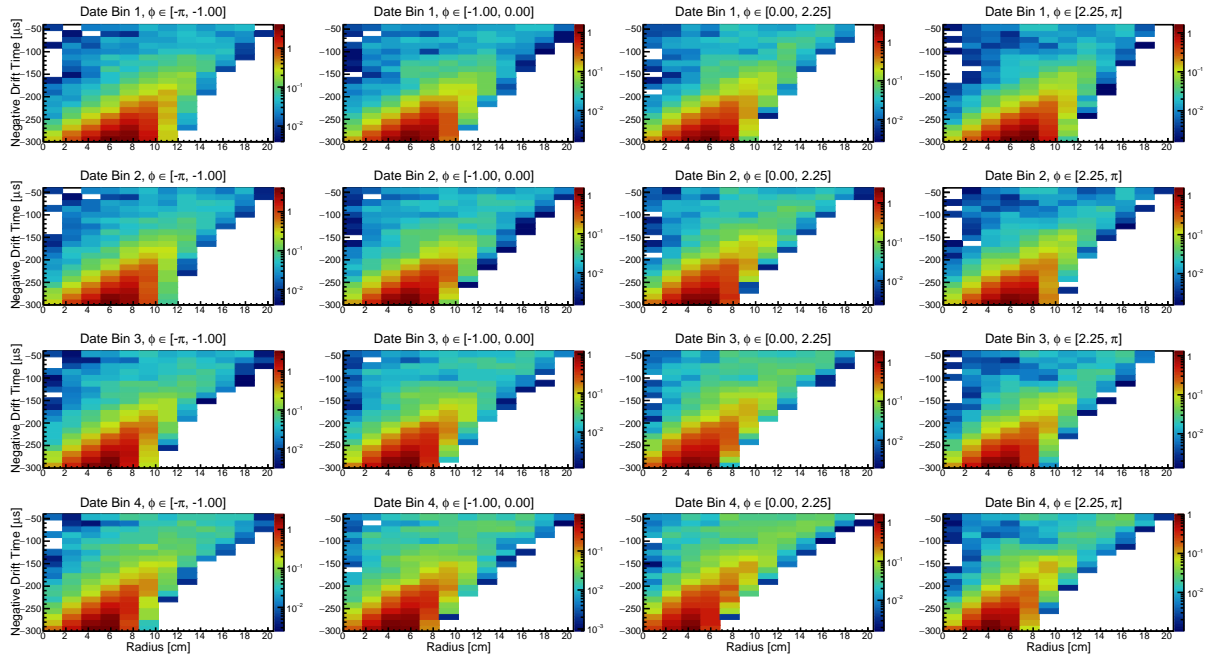


Figure 6.15: Low- $z$  Compton scatters:  $f_{\gamma, \text{bottom}}^t(\mathbf{r}_{S2})$ , radius vs. drift time in slices of azimuth and date.

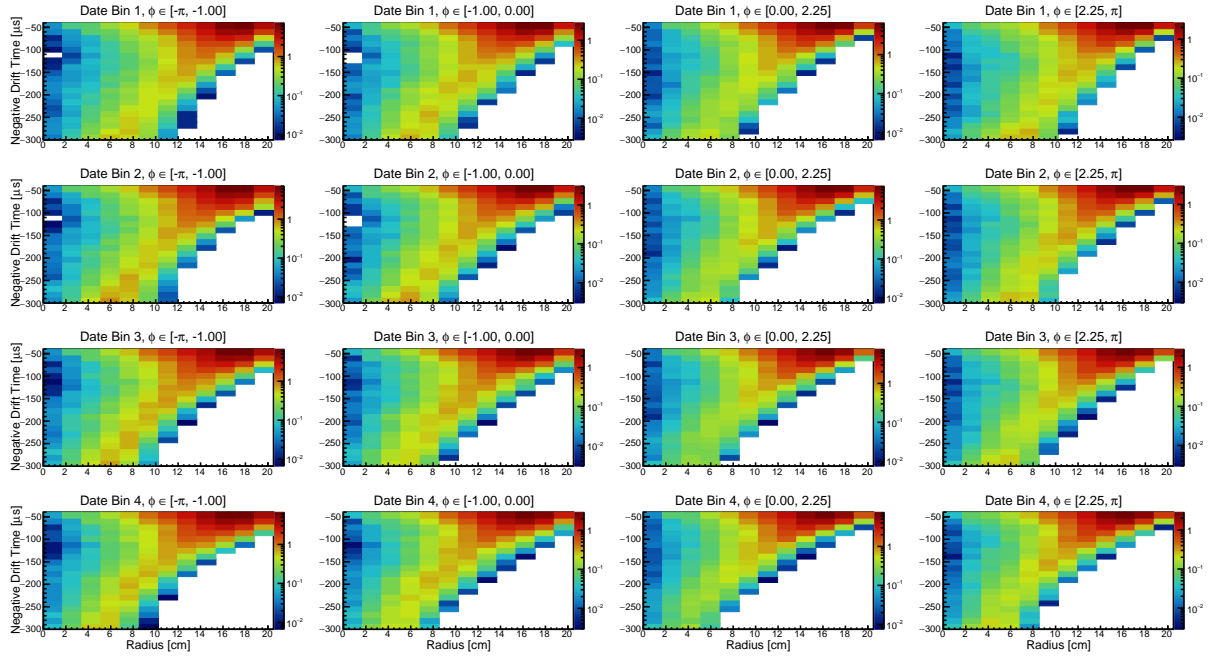


Figure 6.16: Other Compton scatters:  $f_{\gamma, \text{rest}}^t(\mathbf{r}_{S2})$ , radius vs. drift time in slices of azimuth and date.

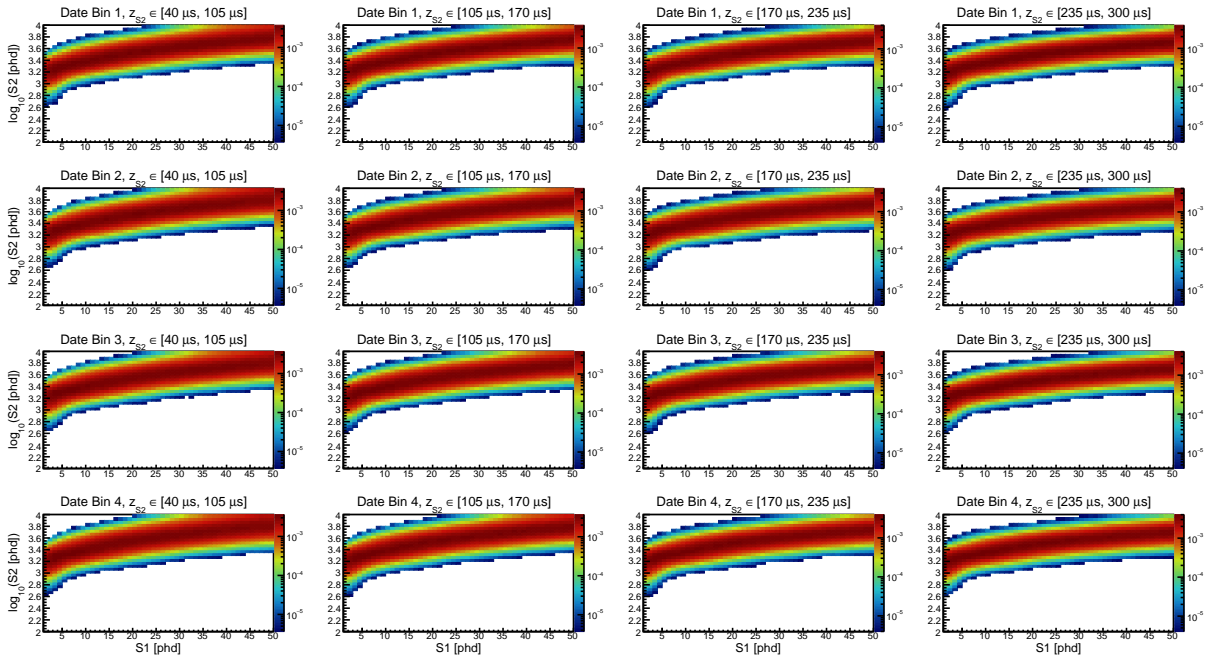


Figure 6.17: ER distribution  $f_{\text{ER}}^{t,z}(S1, \log_{10} S2)$  for Comptons and betas. Note that the band is pushed up at lower drift times (higher  $z$ ), where the drift field is stronger.

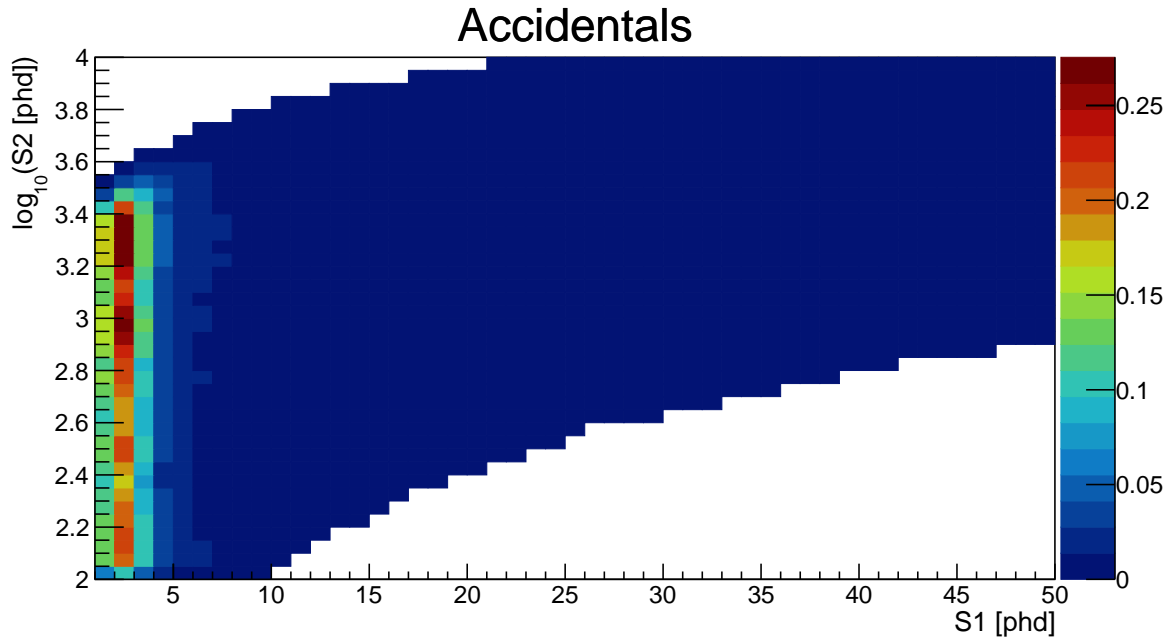


Figure 6.18:  $f_{acc.}(S1, \log_{10} S2)$ , which is taken to be independent of drift and date.

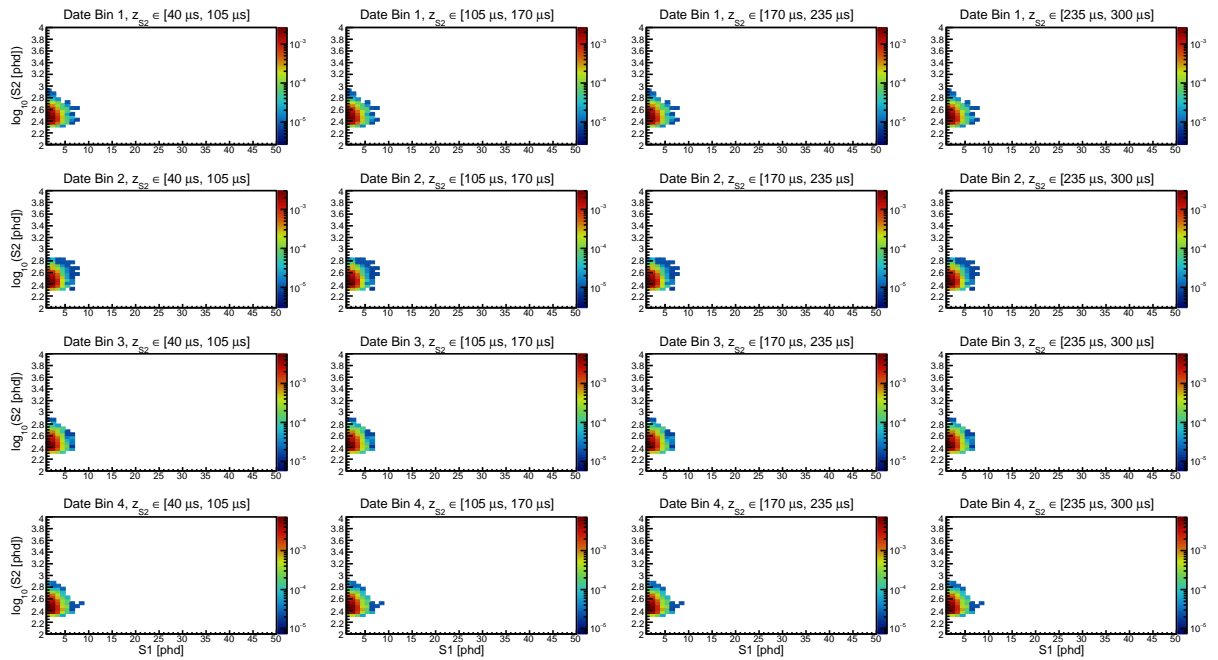


Figure 6.19: NR distribution  $f_{8B}^{t,z}(S1, \log_{10} S2)$  for  $^8B$  neutrinos. Variation with electric field is expected to be small.

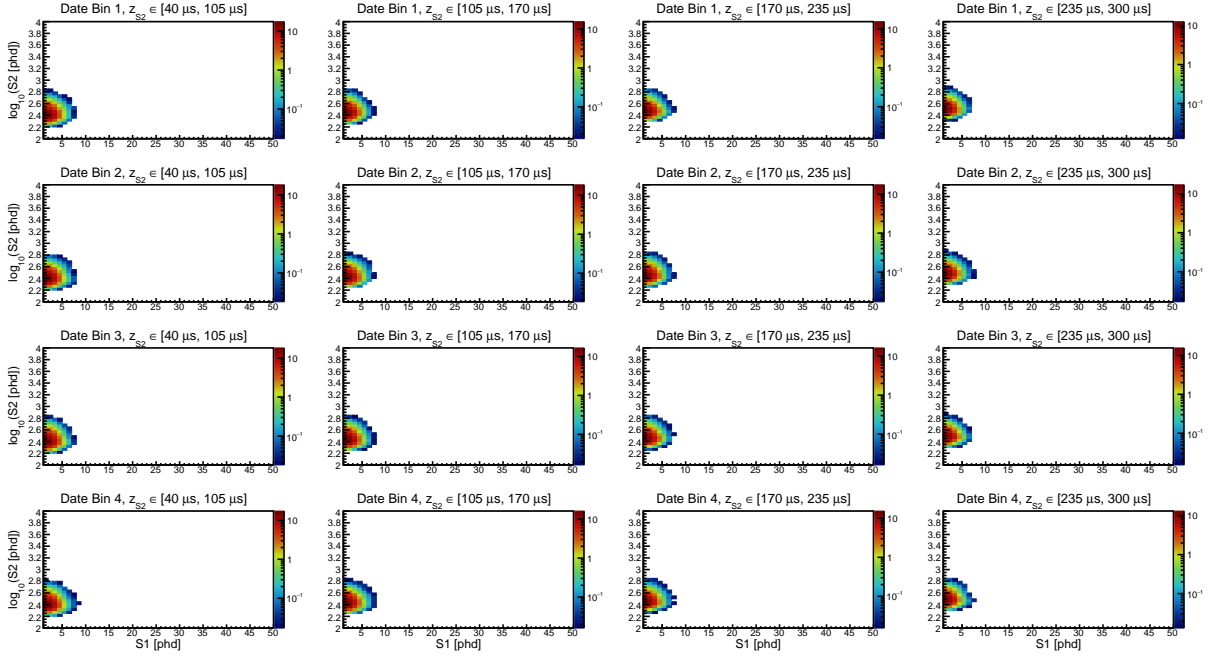


Figure 6.20: NR distribution  $f_{\chi}^{t,z}(S1, \log_{10} S2)$  for 5 GeV WIMPs. Plots normalized to expected events per bin per zb per day per kg.

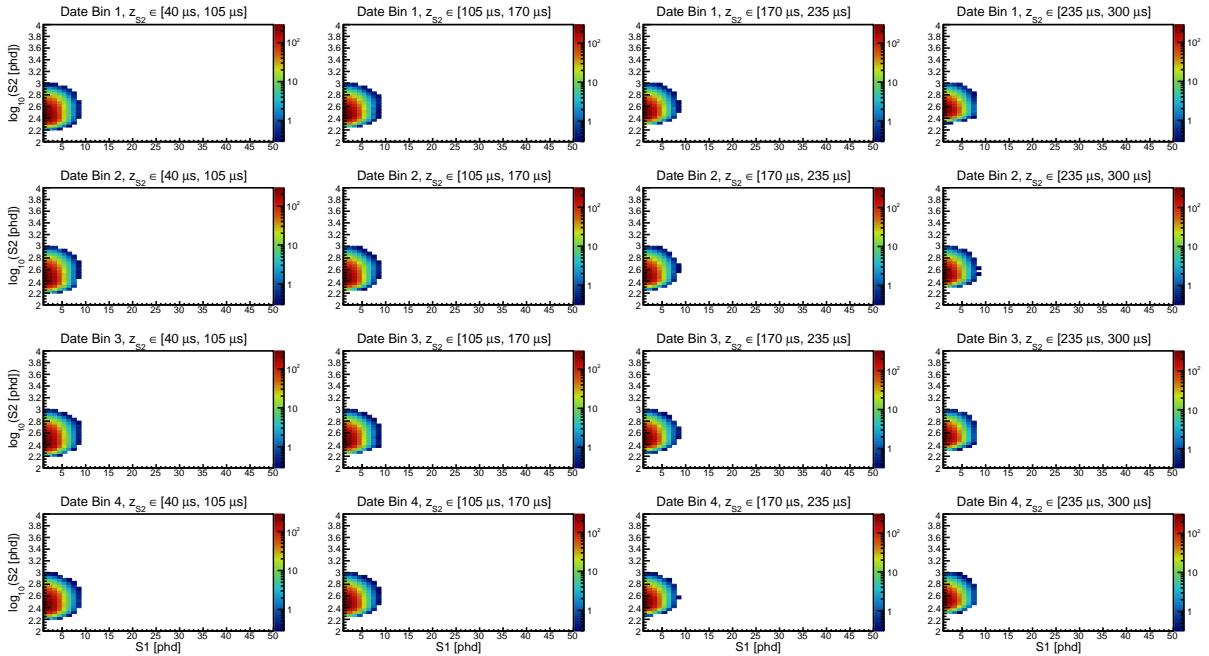


Figure 6.21: NR distribution  $f_{\chi}^{t,z}(S1, \log_{10} S2)$  for 7 GeV WIMPs.

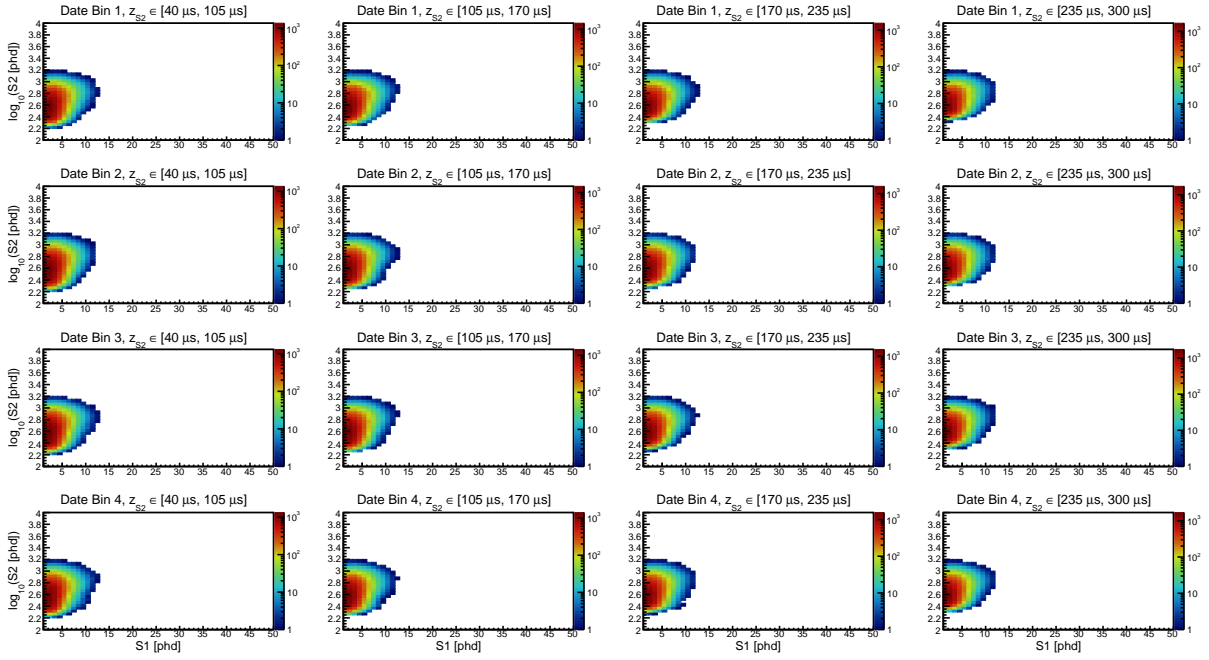


Figure 6.22: NR distribution  $f_{\chi}^{t,z}(S1, \log_{10} S2)$  for 10 GeV WIMPs.

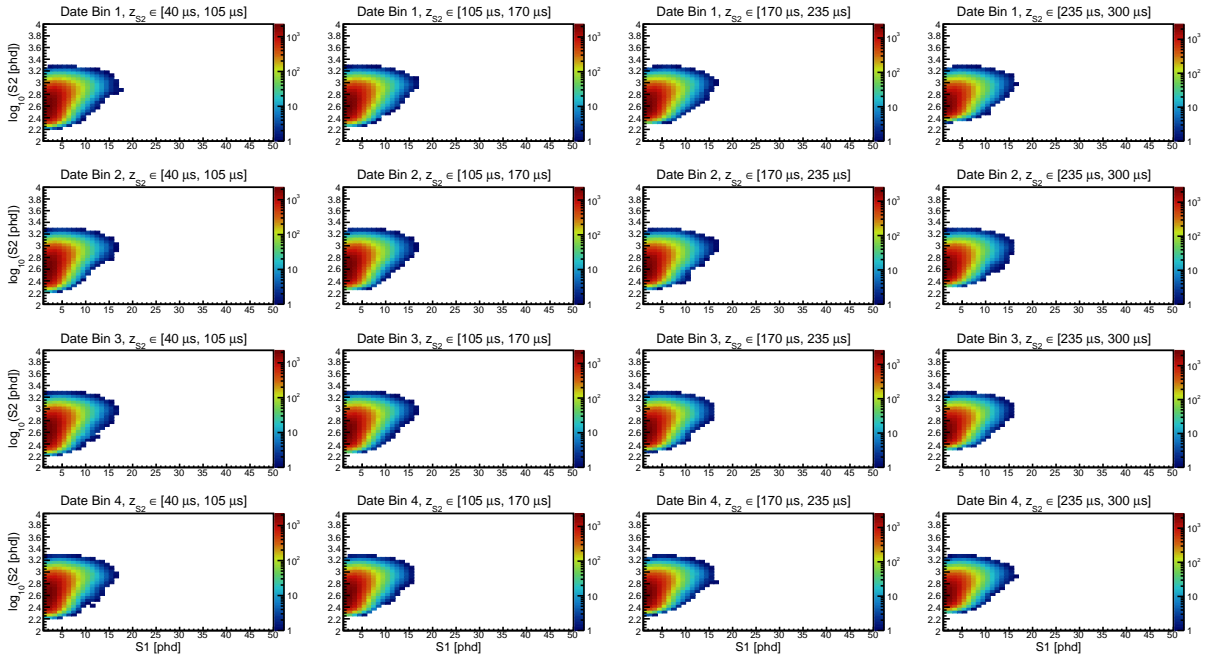


Figure 6.23: NR distribution  $f_{\chi}^{t,z}(S1, \log_{10} S2)$  for 12 GeV WIMPs.

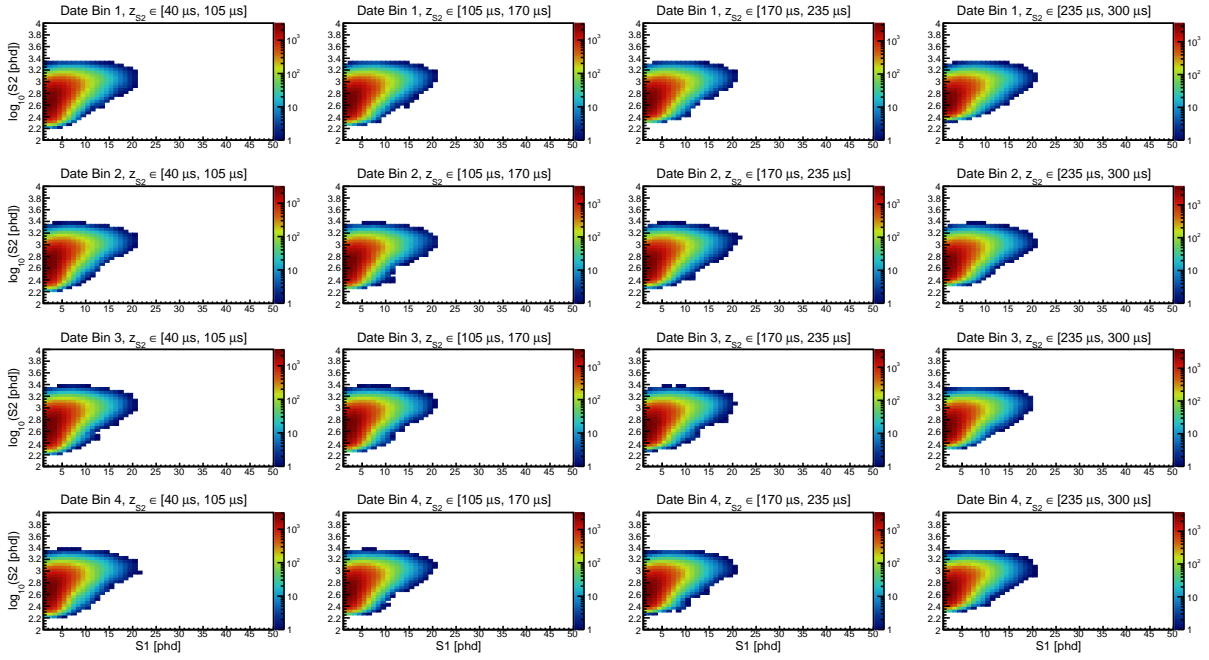


Figure 6.24: NR distribution  $f_{\chi}^{t,z}(S1, \log_{10} S2)$  for 14 GeV WIMPs.

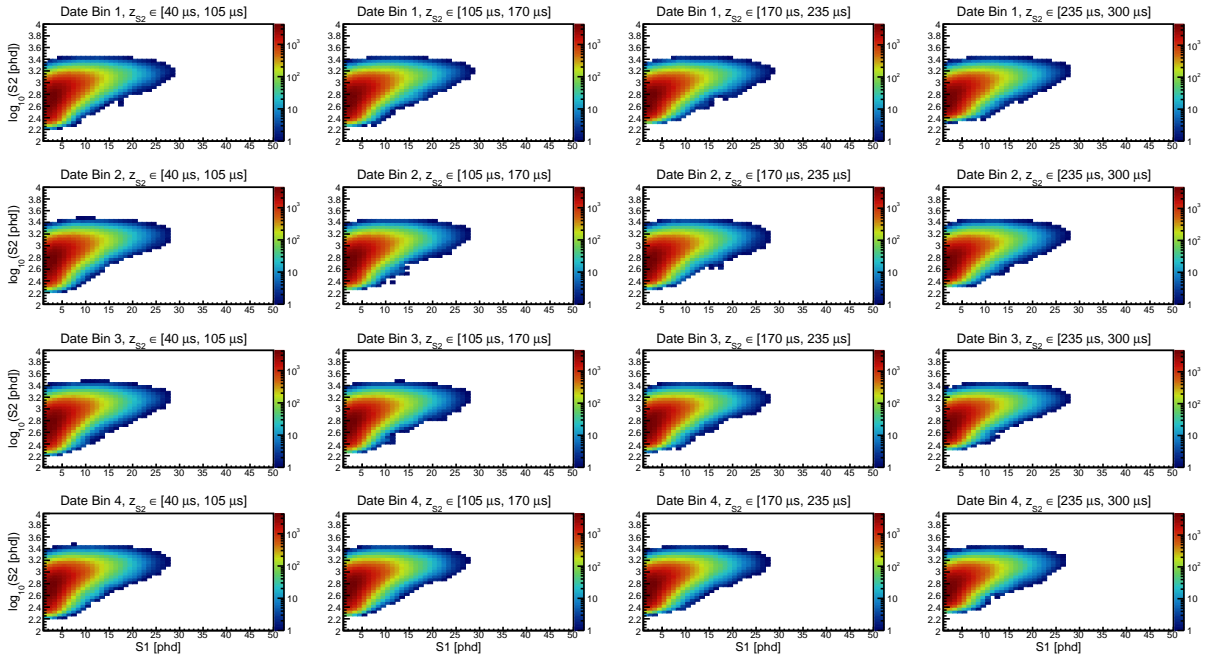


Figure 6.25: NR distribution  $f_{\chi}^{t,z}(S1, \log_{10} S2)$  for 17 GeV WIMPs.

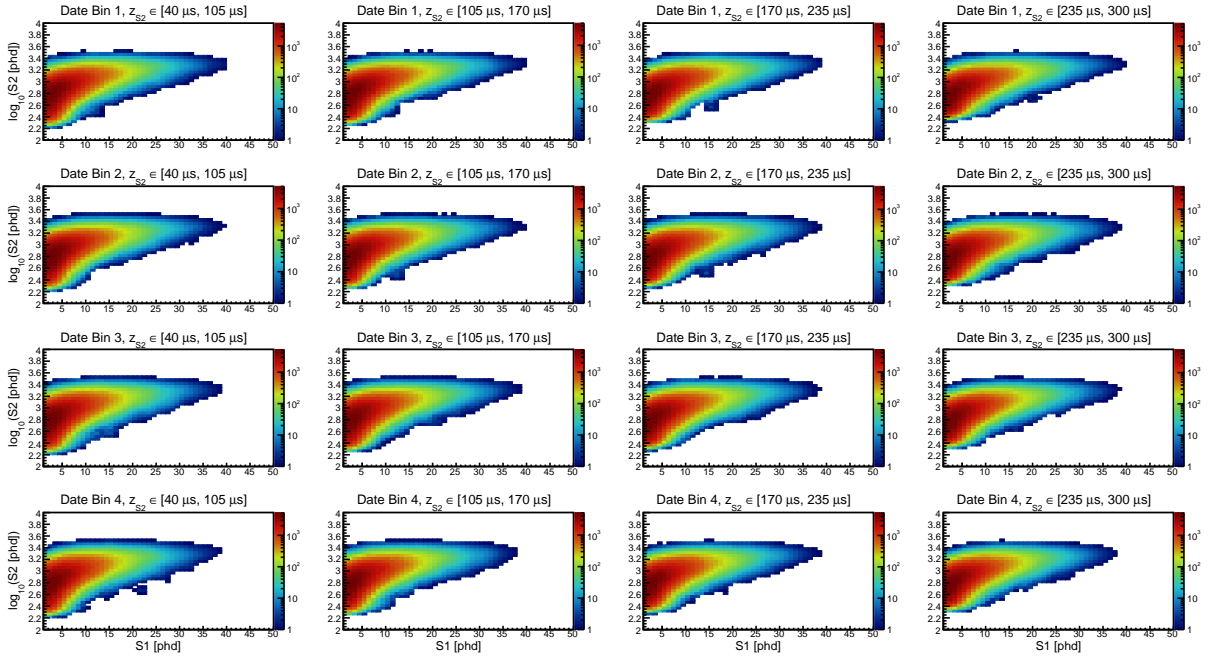


Figure 6.26: NR distribution  $f_{\chi}^{t,z}(S1, \log_{10} S2)$  for 21 GeV WIMPs.

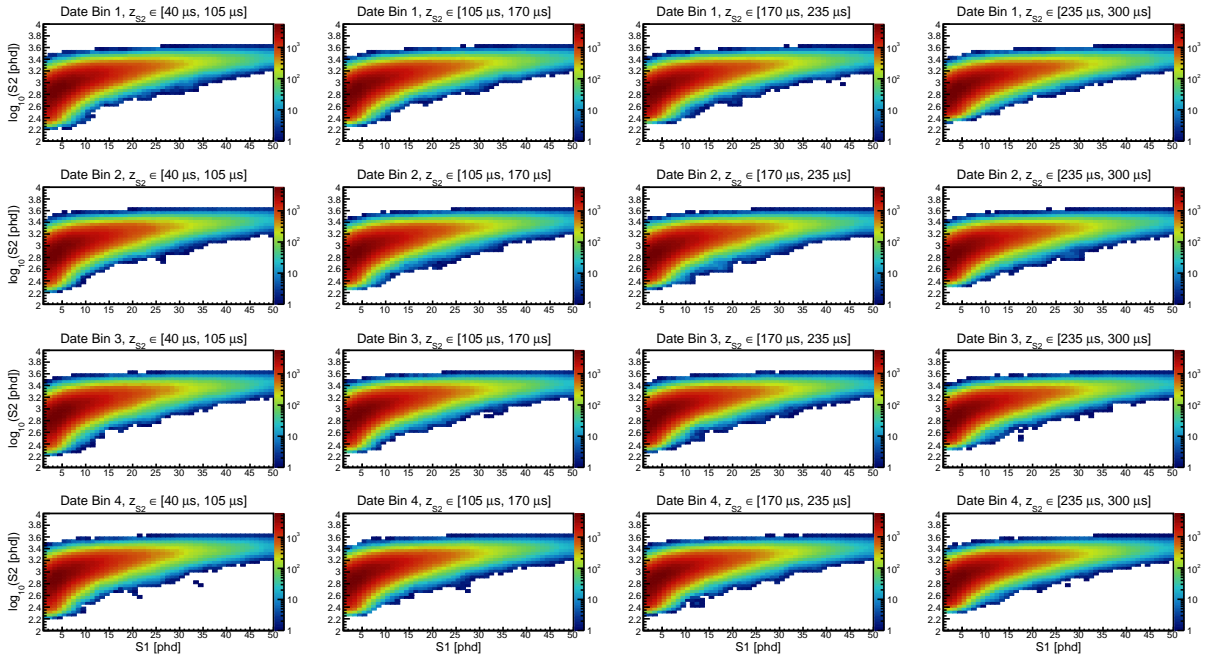


Figure 6.27: NR distribution  $f_{\chi}^{t,z}(S1, \log_{10} S2)$  for 33 GeV WIMPs.

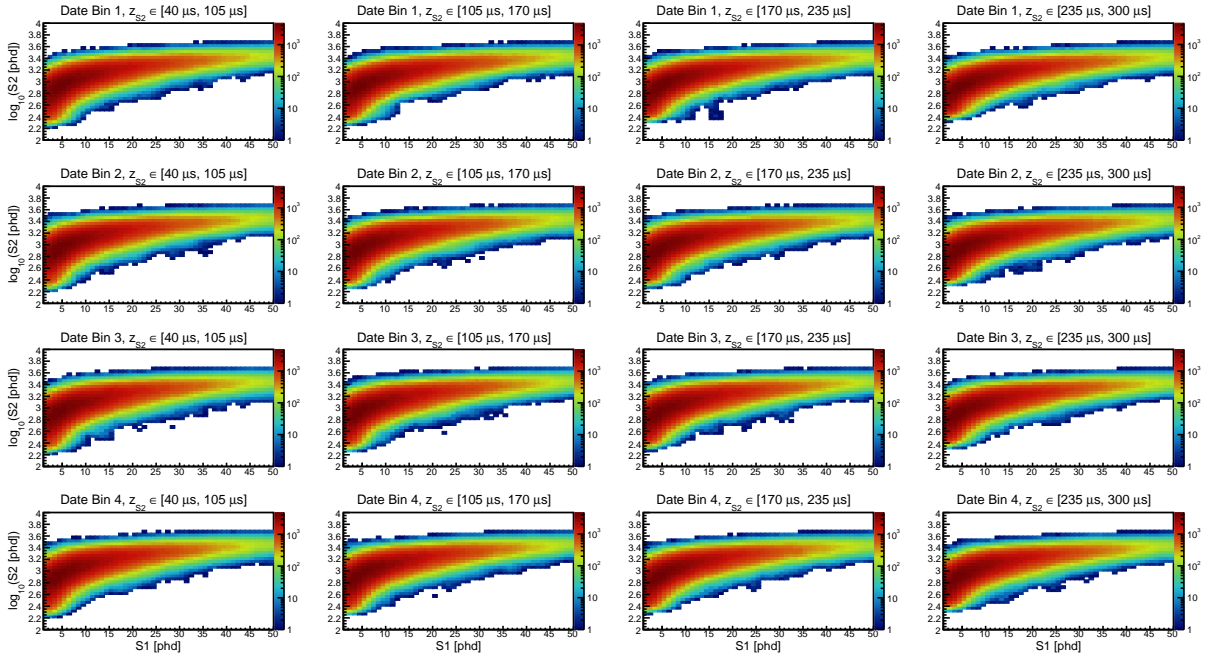


Figure 6.28: NR distribution  $f_{\chi}^{t,z}(S1, \log_{10} S2)$  for 50 GeV WIMPs.

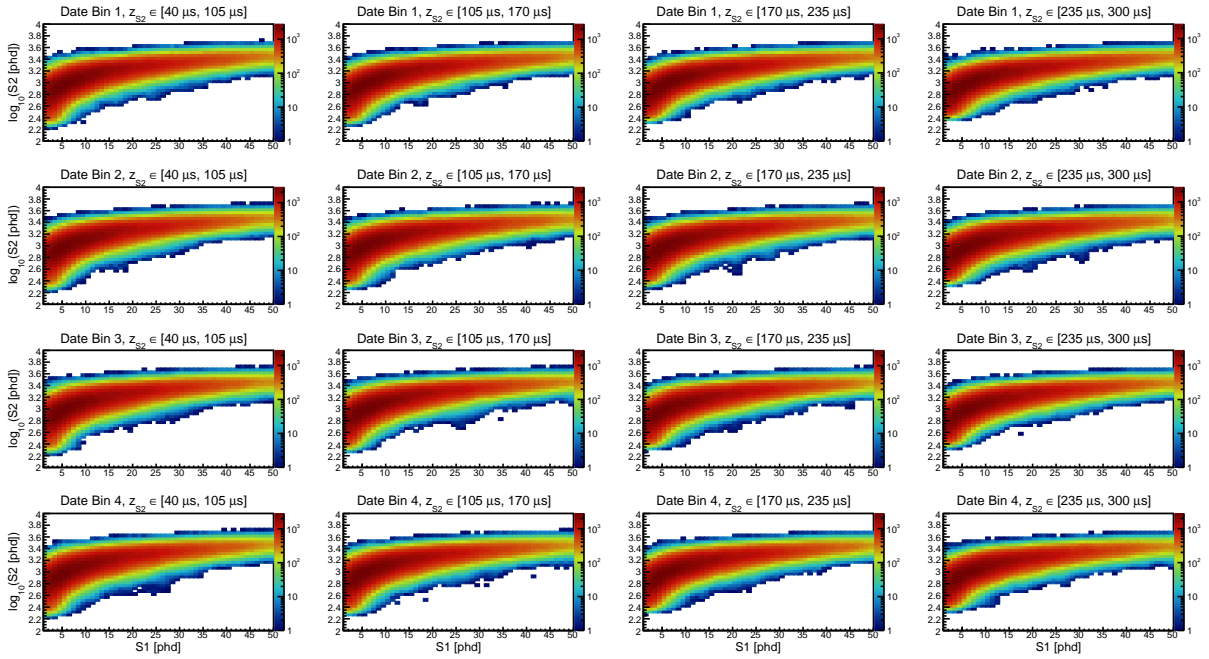


Figure 6.29: NR distribution  $f_{\chi}^{t,z}(S1, \log_{10} S2)$  for 100 GeV WIMPs.

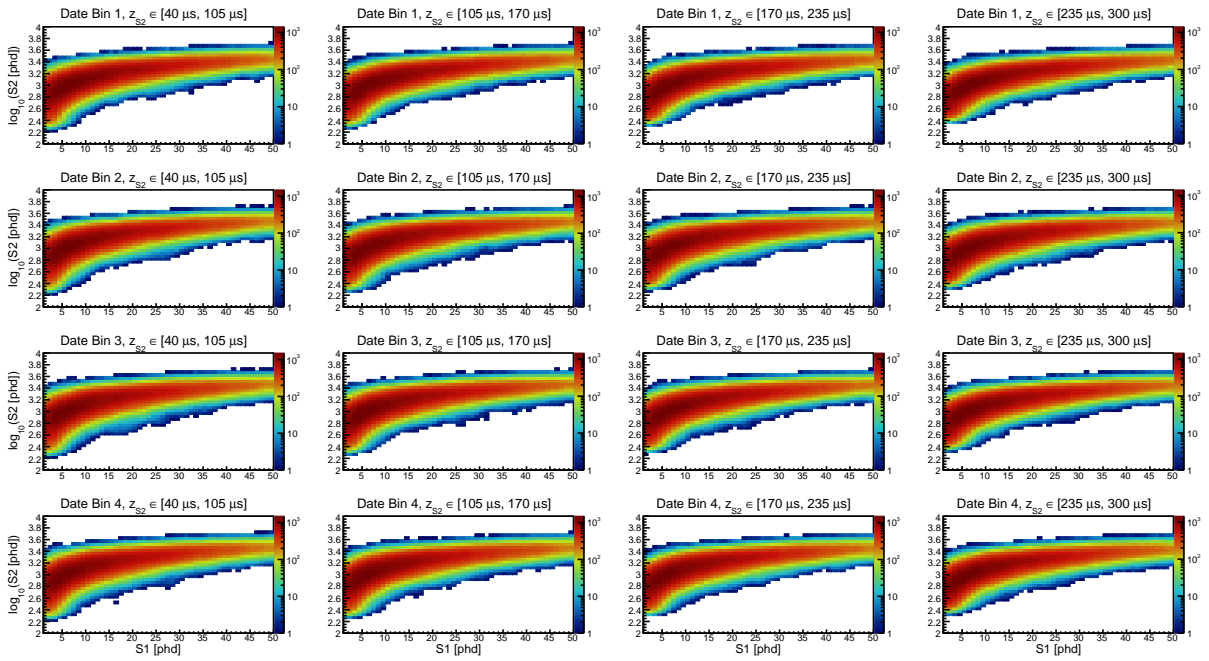


Figure 6.30: NR distribution  $f_{\chi}^{t,z}(S1, \log_{10} S2)$  for 200 GeV WIMPs. At higher WIMP masses, the spectrum is essentially the same.

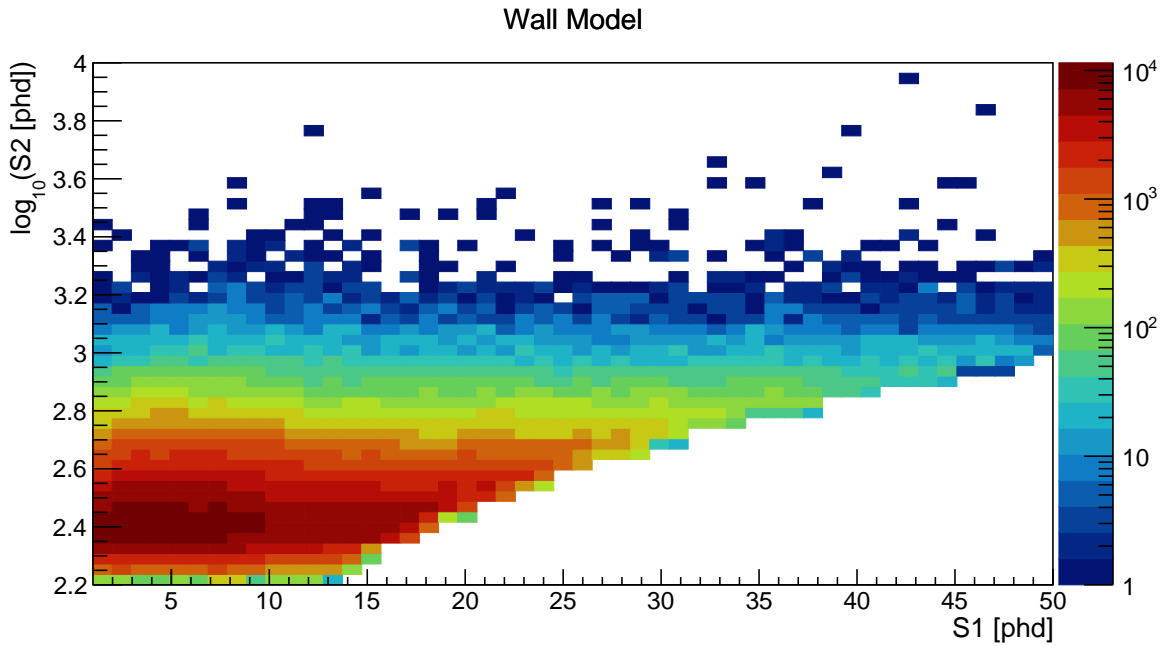


Figure 6.31: Wall model: projection of  $f_{\text{wall}}^{t=1}(\mathbf{r}_{S2}, S1, \log_{10} S2)$  onto  $S1$ - $\log_{10} S2$  plane.

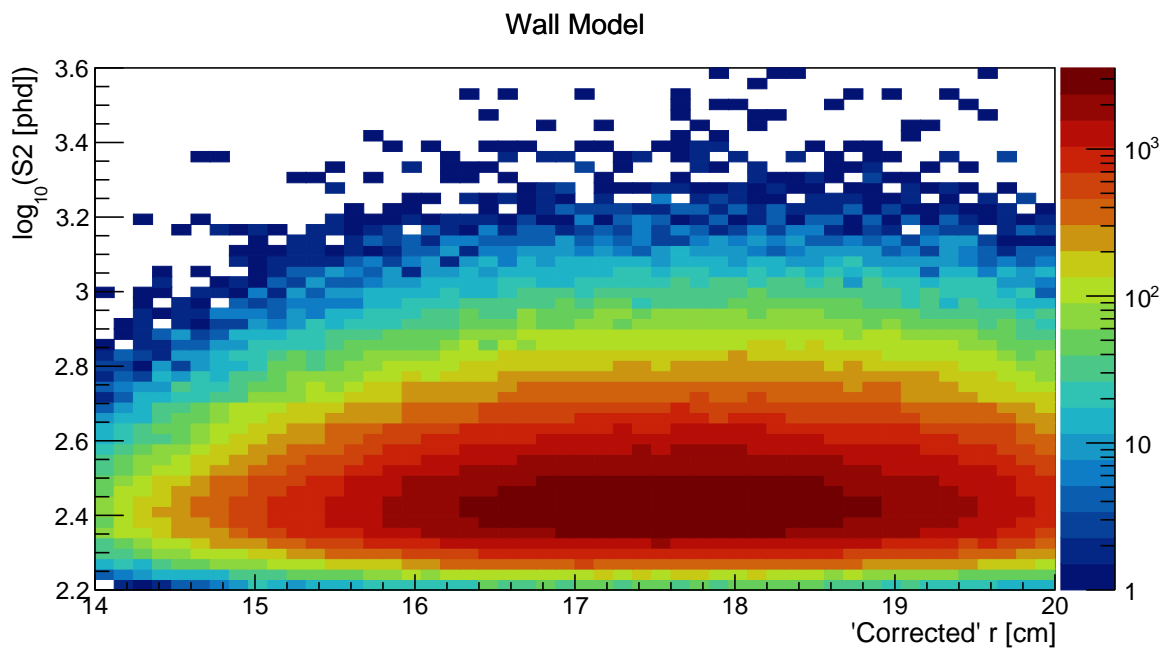


Figure 6.32: Wall model: projection of  $f_{\text{wall}}^{t=1}(\mathbf{r}_{S2}, S1, \log_{10} S2)$  onto  $R$ - $\log_{10} S2$  plane, where  $R$  is a crude correction of radius that approximates true position. This shows how smaller  $S2$  area leads to greater radial uncertainty (and therefore greater penetration into the fiducial volume).

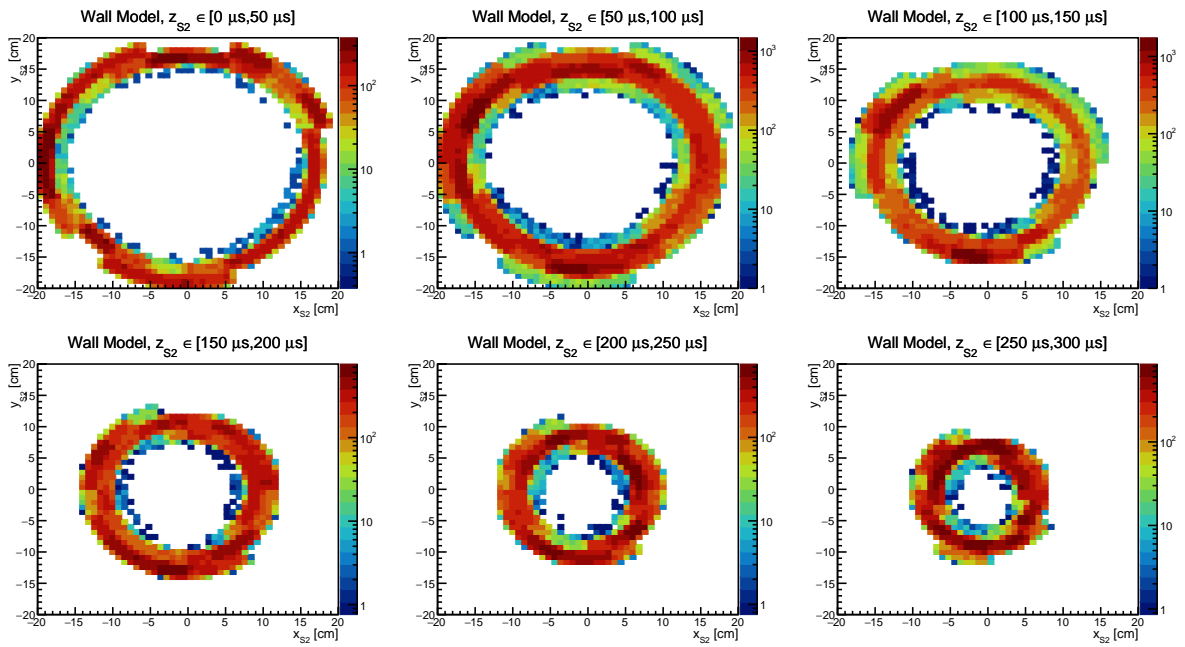


Figure 6.33: Wall model: projection of  $f_{\text{wall}}^{t=1}(\mathbf{r}_{S2}, S1, \log_{10} S2)$  onto  $x_{S2}$ - $y_{S2}$  plane, in slices of drift time. Note the azimuthal asymmetry, and the shrinking of the detector at greater drift times.

# Chapter 7

## Limits on spin-dependent WIMP scattering from full LUX dataset

This chapter was published in an abbreviated form as Ref. [38] in Physical Review Letters. The text and figures are reproduced here largely unchanged, though some sections have been added or expanded; such additions are typically in the form of subsections “7.X.X”. In particular, the summary of the theory behind the signal model has been replaced by a much more thorough derivation. The discussion of results now includes a detailed look at complementarity with LHC searches, featuring a new presentation of LUX spin-dependent limits. In order to preserve the flow and clarity of the writing, sections which repeat information conveyed elsewhere in this dissertation are retained. As such, this chapter should stand as a self-contained document.

## 7.1 Introduction

The existence of dark matter is now supported by a wide array of astrophysical evidence, though the nature of its composition remains a mystery. The hypothetical WIMP (Weakly Interacting Massive Particle) is a compelling candidate, addressing both the observed astronomical phenomena as well as shortcomings of the Standard Model of particle physics (SM). The WIMP appears in many extensions of the SM, including supersymmetry [3], extra dimensions [150], and little Higgs theories [151]. In these models, WIMPs may couple to SM particles mainly via scalar, vector (both spin-independent), and axial-vector (spin-dependent) interactions. The Large Underground Xenon (LUX) experiment, operating at the Sanford Underground Research Facility in Lead, South Dakota, is designed to detect such interactions through the scattering of galactic WIMPs with Xe nuclei. The LUX WIMP search program comprises two distinct exposures, termed WS2013 and WS2014–16. The combined dataset of both runs has been analyzed to produce world-leading limits on the spin-independent (SI) WIMP-nucleon cross section [20]. Here, we present the results for the spin-dependent (SD) coupling of WIMPs to protons and neutrons.

## 7.2 The LUX detector and WS2014–16 run

LUX searches for WIMPs with a dual phase time projection chamber (TPC), detecting energy depositions through the resulting ionization and scintillation in the target mate-

rial. The active detector volume, containing 250 kg of liquid xenon (LXe), is monitored by two horizontal arrays of 61 photomultiplier tubes (PMTs) each. The bottom array sits underneath a cathode grid in the LXe, while the top array looks on from above, in the gas phase. An energy deposition in the active region generates prompt scintillation photons as well as ionization electrons, which drift upwards under the influence of an applied electric field. The scintillation light is the first signal observed in the PMTs (S1). The second signal (S2) corresponds to the liberated charge: ionized electrons travel vertically to the liquid surface, where they are extracted into the gas phase and accelerated by a strong electric field. This produces additional vacuum ultraviolet (VUV) photons via electroluminescence. The S2 signal, originating close to the top PMT array, localizes the interaction in the  $(x, y)$  plane. Additionally, the time delay between S1 and S2 gives the depth below the liquid surface, thereby allowing for full 3D position reconstruction. Position information is crucial for defining a fiducial volume, excluding background events that occur near the TPC walls. Further discrimination between WIMP signals (nuclear recoils, or NRs) and Compton or beta backgrounds (electron recoils, or ERs) is achieved using the S2 to S1 ratio.

As discussed in [20], the recent WS2014–16 dataset was collected under substantially different detector conditions than WS2013: the electric drift field in the active volume featured spatial non-uniformities that evolved slowly over the course of the exposure. In particular, a significant radial component of the field was observed, as well as a vertical gradient in field magnitude. As a consequence of this field symmetry deformation, elec-

tron drift trajectories were bent radially inward, complicating the position reconstruction process. Though a similar phenomenon was seen in WS2013, the effects in WS2014–16 were more severe in magnitude, azimuthal distortion, and time-dependence. For example, in WS2014–16, an ionized electron originating near the edge of the cathode at a radius of  $\sim 24$  cm would reach the liquid surface at a radius of  $\sim 10$  cm (as opposed to  $\sim 20$  cm in WS2013). In addition to affecting electron drift paths, the field asymmetry introduced spatially-varying charge and light yields in the LXe. This is a result of the recombination physics of electron-ion pairs—more electrons (and thus fewer photons) will escape an interaction taking place in a region of greater field strength. As such, the boundaries of the bands populated by ERs and NRs in S1–S2 space vary slightly as a function of event position (and, to a lesser extent, calendar date).

A rigorous calibration regimen was established to address the challenges presented by the unique field geometry in the WS2014–16 analysis. Weekly  $^{83\text{m}}\text{Kr}$  injections [152–154], in conjunction with periodic injections of tritiated methane [14], enabled the separation of electric field effects from the usual geometric effects typical of TPC detectors (i.e. spatial light collection efficiency and electron lifetime). Furthermore,  $^{83\text{m}}\text{Kr}$  data were used to tune a 3-D electrostatic model of the detector, built with the COMSOL MULTIPHYSICS package [138]. The electric field maps produced from this effort allowed for the time-dependent translation between true event position and the position inferred from the observed S2.

NR calibrations were performed with neutrons from a deuterium-deuterium (DD) fu-

sion generator [15, 155]. This technique, pioneered by LUX following the WS2013 run, was employed throughout the WS2014–16 exposure to monitor the detector’s expected response to signal events. ER calibrations were obtained with tritiated methane, where the beta decays of tritium (endpoint 18.6 keV) give an excellent high statistics characterization of ER background events [14].

### 7.3 The Dataset and Selection

This analysis combines the WS2013 and WS2014–16 datasets in search of spin-dependent scattering between WIMPs and Xe nuclei. The WS2013 exposure was taken between April and August of 2013, totaling 95 live-days with a fiducial mass of 145 kg [17]. A simple set of selection cuts were applied to the data, leaving 591 events in the region of interest. This dataset was previously analyzed to set SD WIMP-nucleon cross section limits [25]. The WS2014–16 dataset was subjected to similar cuts, and furthermore featured a blinding protocol wherein fake WIMP events (“salt”) were injected into the data-stream. A full discussion of these data quality and selection cuts as well as the salting scheme can be found in Ref. [20]. In both runs, cuts were designed to select low-energy events with a single S1 followed by a single S2. The net effect on NR detection efficiency is illustrated in Fig. 7.1, which shows the exposure-weighted efficiency of both WS2013 and WS2014–16 (black line, left axis scale). Efficiencies are calculated by applying analysis cuts to simulated NR events. Also plotted on the same energy scale are sample recoil spectra from SD WIMP-nucleon elastic scattering (right axis scale).

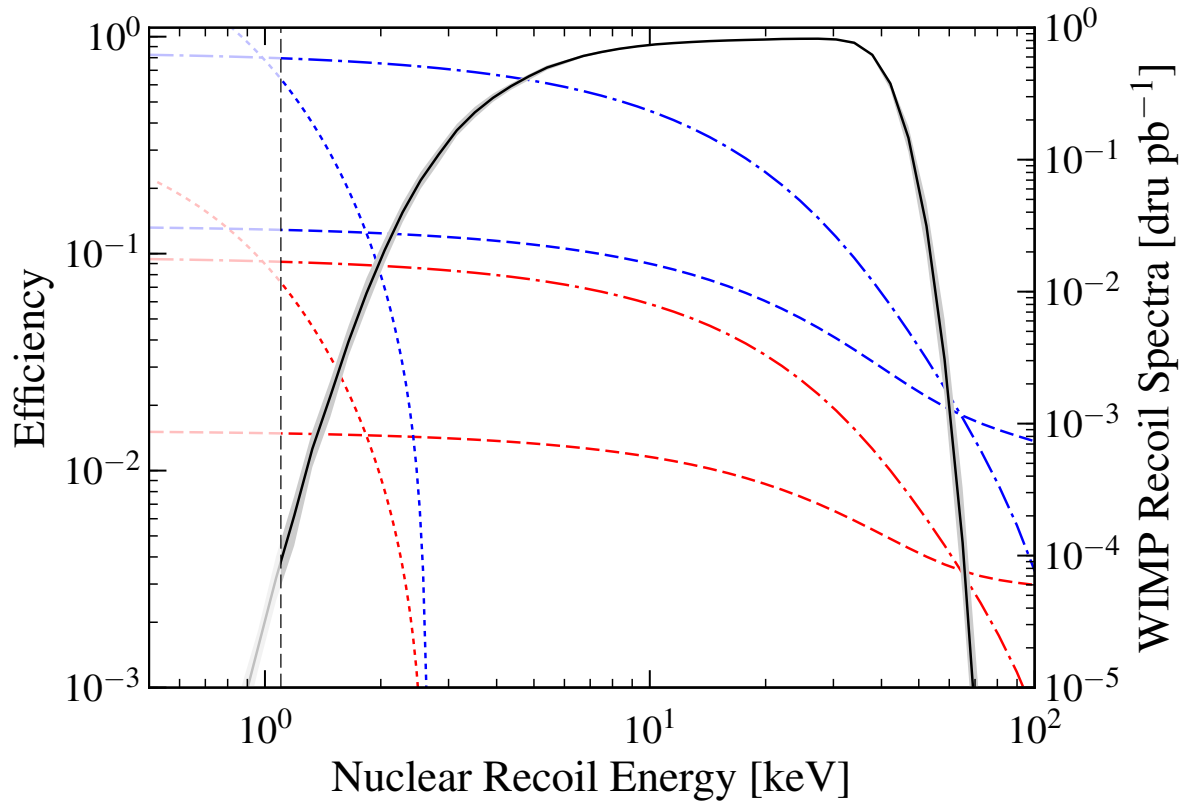


Figure 7.1: LUX total efficiency (black), averaged over the entire exposure. NR model uncertainties are illustrated by the gray band, indicating  $\pm 1\sigma$  variation. The vertical dashed line represents the analysis threshold of 1.1 keV (the lowest DD calibration point), below which we conservatively take the LUX efficiency to be zero. Sample WIMP spectra are plotted in color, with values corresponding to the right-hand y-axis. dru is the differential rate unit ( $\text{events kg}^{-1}\text{d}^{-1}\text{keV}^{-1}$ ), and the spectra have each been calculated with WIMP-nucleon cross section = 1 pb. Spectra for WIMP-proton and -neutron scattering are given by the red and blue curves, respectively, for three WIMP masses:  $5 \text{ GeV } c^{-2}$  (dotted),  $50 \text{ GeV } c^{-2}$  (dash-dotted), and  $1000 \text{ GeV } c^{-2}$  (dashed). Structure functions from [24] are used for this calculation.

## 7.4 Signal model construction

The recoil spectra shown in Fig. 7.1, essential ingredients of the signal model for this analysis, are calculated from the differential WIMP-nucleus cross section and integration over the local WIMP velocity distribution. We focus first on the former quantity,  $d\sigma/dq^2$ , where  $\sigma$  is the WIMP-nucleus cross section and  $q$  is the momentum exchange. Chiral effective field theory (EFT) is used to generically derive the axial-vector WIMP-nucleus cross section as a multipole expansion, which requires detailed nuclear calculations to evaluate. As in Ref. [25], we use the calculations by Klos *et al.* [24], which include 2-body currents in the EFT calculation (i.e. WIMPs may effectively couple to two nucleons) and employ state-of-the-art nuclear shell-models to obtain the final spectra.

### 7.4.1 Spin-dependent coupling between WIMPs and Xe nuclei

The following calculations will be analogous to those laid out in Sec. 2.2, but in the SD instead of SI case. As derived in [83], we can express the differential WIMP-nucleus cross section as:

$$\frac{d\sigma}{dq^2} = \frac{8 G_F^2}{(2J + 1)v^2} S_A(q) \quad , \quad (7.1)$$

where  $G_F$  is the Fermi constant,  $J$  is the ground state angular momentum of the nucleus,  $v$  is the WIMP velocity, and  $S_A(q)$  is the non-trivial momentum dependent axial-vector structure factor. Analogous to the form factor used in SI calculations,  $S(q)$  can be thought of as the Fourier transform of the nuclear spin distribution. We would like to have an expression in terms of a single-valued parameter of interest for hypothesis testing,

rather than a momentum-dependent function. To this end, it is standard to define the total cross section in the zero momentum transfer limit [3, 156]:

$$\sigma_A \equiv \int_0^{4\mu_A^2 v^2} \frac{d\sigma(q=0)}{dq^2} dq^2 \quad (7.2)$$

$$= \frac{32 G_F^2 \mu_A^2}{2J+1} S_A(0) \quad . \quad (7.3)$$

Here, we have introduced the WIMP-nucleus reduced mass  $\mu_A$ , with the subscript  $A$  referring to the mass number of the nucleus being considered (and likewise for  $\sigma_A$ ). We will abuse notation slightly and similarly take  $S_A(q)$  to be the spin structure function for nuclei of isotope  $A$ . In eq. 7.2, we are integrating the differential cross-section (in the  $q=0$  limit) over the full range of possible  $q^2$ , with the upper bound  $4\mu_A^2 v^2$  given by the kinematic maximum of elastic scattering. Eq. 7.3 is then trivially found by plugging in eq. 7.1. With this definition, we can now express the differential cross section as:

$$\frac{d\sigma}{dq^2} = \frac{\sigma_A}{4\mu_A^2 v^2} \frac{S_A(q)}{S_A(0)} \quad , \quad (7.4)$$

achieving the goal of parameterizing the signal response in a single variable  $\sigma_A$ . Some authors opt to define a dimensionless constant  $C_A$ , the “enhancement factor,” for notational convenience [3, 156]:

$$C_A \equiv \frac{8}{2J+1} S_A(0) \quad , \quad (7.5)$$

in which case (from eq. 7.3):

$$\sigma_A = 4 G_F^2 \mu_A^2 C_A \quad , \quad (7.6)$$

and:

$$\frac{d\sigma}{dq^2} = \frac{G_F^2 C_A}{v^2} \frac{S_A(q)}{S_A(0)} \quad , \quad (7.7)$$

which matches eq. 2.1 by identifying the normalized form factor  $F^2(q)$  with  $S_A(q)/S_A(0)$ .

Though we could now proceed with these formulae and set observational limits on  $\sigma_A$ , it would be preferable to consider a more fundamental quantity. Instead of the WIMP-nucleus total cross section, we could focus on the WIMP-proton(neutron) total cross section  $\sigma_{p,n}$ . This affords the advantage of allowing comparison of results with experiments that use target materials other than xenon, as well as results from indirect detection and collider experiments. From 7.6, we can see that:

$$\sigma_A = \sigma_{p,n} \frac{\mu_A^2}{\mu_{p,n}^2} \frac{C_A}{C_{p,n}} \quad . \quad (7.8)$$

In order to make progress in evaluating this relationship, we must digress into a discussion on the structure factors.

In general, the structure functions may be decomposed in the isospin basis as [3, 24]:

$$S_A(q) = a_0^2 S_{00}(q) + a_0 a_1 S_{01}(q) + a_1^2 S_{11}(q) \quad , \quad (7.9)$$

where  $a_0$  and  $a_1$  are the isoscalar and isovector couplings to WIMPs, and  $S_{ij}(q)$  are the respective components of the structure function. In this basis, we can also explicitly express the  $q = 0$  limiting case as [24]:

$$S_A(0) = \frac{(2J+1)(J+1)}{4\pi J} |(a_0 + a'_1)\langle \mathbf{S}_p \rangle + (a_0 - a'_1)\langle \mathbf{S}_n \rangle|^2 \quad , \quad (7.10)$$

where  $a'_1 = a_1(1 + \delta a_1(0))$  includes the correction that arises from considering 2-body currents, and  $\langle \mathbf{S}_{p,n} \rangle$  are the spin expectation values of the proton and neutron groups

in the nucleus. An important consequence of this equation that holds not just in the  $q = 0$  limit is that even- $A$  nuclei (for which  $\langle \mathbf{S}_p \rangle = \langle \mathbf{S}_n \rangle = 0$ ) do not participate in SD interactions. Thus, for xenon, only  $^{129}\text{Xe}$  and  $^{131}\text{Xe}$  (with respective isotopic abundances of 29.5% and 23.7%) contribute to the SD cross section.

In the literature, it is also common to see expressions in the proton-neutron basis:

$$\begin{aligned} a_p &= \frac{1}{2}(a_0 + a_1) \\ a_n &= \frac{1}{2}(a_0 - a_1) \quad , \end{aligned} \quad (7.11)$$

where  $a_{p,n}$  are the WIMP-proton(neutron) coupling constants. Eq. 7.9 therefore becomes:

$$S_A(q) = (a_p + a_n)^2 S_{00}(q) + (a_p^2 - a_n^2) S_{01}(q) + (a_p - a_n)^2 S_{11}(q) \quad . \quad (7.12)$$

Returning to the task of evaluating  $C_{p,n}$ , we must consider the zero momentum transfer structure factor associated with a WIMP scattering off a single, free nucleon. In this case, there are no 2-body currents by construction, so  $a'_1 \rightarrow a_1$ , and eq. 7.10 becomes:

$$S_A(0) = \frac{(2J+1)(J+1)}{4\pi J} \left| (a_0 + a_1) \langle \mathbf{S}_p \rangle + (a_0 - a_1) \langle \mathbf{S}_n \rangle \right|^2 \quad (7.13)$$

$$= \frac{(2J+1)(J+1)}{\pi J} \left| a_p \langle \mathbf{S}_p \rangle + a_n \langle \mathbf{S}_n \rangle \right|^2 \quad (7.14)$$

$$= \frac{(2(\frac{1}{2})+1)(\frac{1}{2}+1)}{\pi (\frac{1}{2})} \left| a_{p,n} \left( \frac{1}{2} \right) \right|^2 \quad (7.15)$$

$$= \frac{3}{2\pi} a_{p,n}^2 \quad . \quad (7.16)$$

In 7.14, we have applied 7.11 to change basis (note the factor of 4), and the equation holds generally for 1-body currents. We specify the case of a single proton (neutron) in

eq. 7.15, using  $J = 1/2$ ,  $\langle \mathbf{S}_{p,n} \rangle = 1/2$ , and also  $\langle \mathbf{S}_{n,p} \rangle = 0$ . This result matches eq. 5.16 in the otherwise superlative Ref. [157], though slightly flawed reasoning is employed there: the  $a'_1$  term disappears not because of cancellation, but by definition. Furthermore, only one of  $\langle \mathbf{S}_{p,n} \rangle = 1/2$ ; the other must be set to 0. Thus, according to definition 7.5,

$$C_{p,n} = \frac{8}{2(\frac{1}{2}) + 1} \left( \frac{3}{2\pi} a_{p,n}^2 \right) \quad (7.17)$$

$$= \frac{6}{\pi} a_{p,n}^2 \quad , \quad (7.18)$$

which agrees with Ref. [156]. Using this result in eq. 7.8, we obtain the total cross section for a nucleus in terms of the corresponding quantity for a single nucleon:

$$\sigma_A = \frac{4\pi}{3} \frac{\mu_A^2}{\mu_{p,n}^2} \frac{1}{2J + 1} \frac{S_A(0)}{a_{p,n}^2} \sigma_{p,n} \quad . \quad (7.19)$$

Finally, returning to the differential cross section as expressed in eq. 7.4, it follows that

$$\frac{d\sigma}{dq^2} = \frac{\pi}{3\mu_{p,n}^2 v^2 (2J + 1)} \frac{S_A(q)}{a_{p,n}^2} \sigma_{p,n} \quad . \quad (7.20)$$

At this point, it becomes useful to introduce the cases of “proton-only” ( $a_n = 0$ ) and “neutron-only” ( $a_p = 0$ ) coupling, which can be thought of as orthogonal vectors in the  $a_n$ - $a_p$  parameter space. The nomenclature can be understood by considering eq. 7.14, where in the proton-only scenario, the neutrons make no contribution to the total cross section (and vice versa for neutron-only). However, it is important to note that in the 2-body calculation (eq. 7.10) of Klos *et al.* [24], the spin averages of both nucleons can contribute in either scenario. Thus, for target nuclei with unpaired neutrons such as

$^{129}\text{Xe}$  and  $^{131}\text{Xe}$ , sensitivity is much greater in the neutron-only case (since  $\langle \mathbf{S}_n \rangle \gg \langle \mathbf{S}_p \rangle$ ), though 2b currents allow for non-zero sensitivity to a proton coupling.

If we rewrite eq. 7.12 in the proton(neutron)-only cases, we find:

$$S_A(q) = a_{p,n}^2 (S_{00}(q) \pm S_{01}(q) + S_{11}(q)) \quad . \quad (7.21)$$

Klos *et al.* define a normalized version [24]:

$$S_{p,n}^{\text{Klos}}(q) \equiv S_{00}(q) \pm S_{01}(q) + S_{11}(q) = \frac{S_A(q)}{a_{p,n}^2} \quad . \quad (7.22)$$

Parametrizations of these functions, calculated for a number of isotopes, are provided in Ref. [24] (Table IV of that paper contains the data for  $^{129}\text{Xe}$  and  $^{131}\text{Xe}$ ). For the practical purpose of signal model implementation, we can re-express the differential cross section in the case of proton(neutron)-only coupling:

$$\frac{d\sigma}{dq^2} = \frac{\pi S_{p,n}^{\text{Klos}}(q)}{3\mu_{p,n}^2 v^2 (2J+1)} \sigma_{p,n} \quad . \quad (7.23)$$

In this equation, we see that the only unknown variables are  $\sigma_{p,n}$ , which act as a simple scaling of the overall spectrum.

## 7.4.2 Nuclear recoil spectra

Relying on the machinery developed in Sec. 2.2, we can now fold in the WIMP velocity integral to the differential cross section in order to generate the expected nuclear recoil

spectrum. First, we move into energy space (see eq. 2.4):

$$\frac{d\sigma}{dE_R} = \frac{d\sigma}{dq^2} \frac{dq^2}{dE_R} \quad (7.24)$$

$$= \frac{2\pi}{3} \frac{m_A S_{p,n}^{\text{Klos}}(q)}{\mu_{p,n}^2 v^2 (2J+1)} \sigma_{p,n} \quad . \quad (7.25)$$

Next, we can use eq. 2.11 to express the SD equivalent of the SI differential rate (eq. 2.37):

$$\frac{dR}{dE_R} = \sigma_{p,n}^{\text{SD}} \frac{2\pi m_A N_T \rho_\chi}{3m_\chi \mu_{p,n}^2 (2J+1)} S_{p,n}^{\text{Klos}}(E_R) \int_{v_{\min}(E_R)}^{\infty} \frac{d^3\vec{v}}{v} f_{\oplus}(\vec{v}, \vec{v}_{\text{obs}}) \quad . \quad (7.26)$$

Using the SHM parameters discussed in Sec. 2.2.4 (see Table 2.1), and calculating exposure-averaged Earth velocities  $\langle v_{\text{obs}} \rangle_{\text{WS2013}} = 245$  km/s and  $\langle v_{\text{obs}} \rangle_{\text{WS2014–16}} = 230$  km/s (see Appendix A for details), we produce the recoil spectra shown in Fig. 7.1 and used in the signal model. Note that eq. 7.26 must be evaluated separately for  $^{129}\text{Xe}$  and  $^{131}\text{Xe}$ , using the isotopic abundances to weight the sum.

## 7.5 Statistical Analysis

A two-sided profile likelihood ratio (PLR) statistic is used to test signal hypotheses [146], whereby the complete LUX dataset is compared against a multi-channel, extended, unbinned likelihood function [23, 158]. LUX data are categorized into five “channels”: one corresponds to the WS2013 exposure, and the remaining four represent discrete time periods of relatively constant detector conditions in the WS2014–2016 dataset, termed “date bins.” The simultaneous model is thus the product of each channel’s likelihood, along with the nuisance parameter constraints. Nuisance parameters, representing sys-

tematic uncertainties in the model, are described in [20], as are the components of the background model. Here, we review some details of the model construction.

The signal and background probability distribution functions (PDFs) for WS2013 are defined in four observables: corrected interaction radius and height,  $S1$ , and  $\log_{10}(S2)$  [17]. Uncorrected S2 position coordinates  $\{r_{S2}, \phi_{S2}, z_{S2}\}$  are used in WS2014–16, with the loss of axial symmetry necessitating the introduction of the third spatial dimension. ER backgrounds as well as the NR signal are modeled by further subdividing the data into segments of drift time.<sup>1</sup> For each date bin of WS2014–16, calibration data is used to tune  $\{S1, S2\}$  response models in four horizontal slices of the detector (within which the field strength variation is acceptably low). From these date- and depth-specific models, implemented with the Noble Element Simulation Technique (NEST) [99], Monte Carlo (MC) data are generated to produce 16 ER and NR PDFs. Spatial PDFs are built separately using MC from the GEANT4-based [118] LUXSIM [119] software: simulated event positions are transformed into the observed S2 coordinate space via the  $^{83\text{m}}\text{Kr}$ -derived field maps, once for each date bin.

As in WS2013, the WS2014–16 data contains a background population that defies the ER and NR description. Interactions occurring very near the TPC walls suffer charge loss to the PTFE panels, suppressing the S2 signal. Since position reconstruction statistical uncertainty scales as  $S2^{-1/2}$ , these low charge yield events are more likely to be misreconstructed as taking place within the fiducial volume (because of the long tail in

---

<sup>1</sup>A small NR background from  $^8\text{B}$  solar neutrinos is also modeled with this technique. Neutrons (muon-induced or from detector components) can also produce NR background events, though the estimated rate is negligible [16, 20].

their radial distribution). An empirical model is constructed to describe this population using control samples of the dataset outside the region of interest. More so than the other models, this “wall” model features strong correlations between position and pulse area observables. For example, the width of the radial distribution is dependent on uncorrected S2, which is itself a function of the corrected  $S2$  and  $z_{S2}$  observables used in the PLR. Furthermore, in observed S2 position coordinates, the radial position of the wall varies with  $\{\phi_{S2}, z_{S2}\}$ . The final PDF is implemented as a finely binned 5-dimensional histogram in each date bin, via an extension of the technique described in Ref. [120]. Specifics of the model construction will be detailed in a forthcoming publication.

The full background model is found to be a good fit to the combined dataset. The data are consistent with the background-only hypothesis (PLR  $p = 0.35$ ) when testing a 50 GeV  $c^{-2}$  signal. As a further cross-check, the WS2013 and WS2014–16 PDFs are separately projected into 1-dimensional spectra for each observable. These are compared to data with a Kolmogorov-Smirnov test, demonstrating acceptable goodness of fit ( $p \geq .05$  and  $p \geq .6$  in WS2013 and WS2014–16, respectively) [17, 20]. Finding no evidence for WIMP signals in the data, we proceed in setting 90% confidence level (CL) limits on the WIMP-nucleon cross section, in the case of spin-dependent coupling.

## 7.6 Results

For a given WIMP mass and choice of coupling type, the PLR test statistic distribution is constructed at a range of signal cross sections from MC pseudo-experiments generated

with the ROOSTATS package [159]. The  $p$ -value of the observed data is then calculated over this range, where by definition the 90% CL upper limit is given by the cross section at which  $p = 0.1$ . In using the raw PLR test statistic, however, an experiment may benefit unreasonably from background under-fluctuations. To safeguard against setting an upper limit at a cross section to which LUX is insensitive, a power constraint [145] is imposed at  $-1\sigma$  of the expected sensitivity calculated from background-only trials (as in [20]). Since the WS2013 limits were reported with an overly conservative power constraint at the median expected sensitivity, this combined result exhibits a stronger improvement than suggested simply by the increase in exposure.

The advance in sensitivity can be seen in Fig. 7.2, which shows cross section limits as a function of WIMP mass in the cases of neutron- and proton-only coupling. The limits from the combined LUX data are plotted as a thick black line, labeled “LUX WS2013+WS2014–16”. LUX is more sensitive to the neutron-only scenario, owing to the unpaired neutron in  $^{129}\text{Xe}$  and  $^{131}\text{Xe}$  nuclei, and sets a minimum upper limit of  $1.6 \times 10^{-41} \text{ cm}^2$  at  $35 \text{ GeV } c^{-2}$ , a nearly sixfold improvement over the previous WS2013 result. Indeed, among direct detection experiments, LUX is world-leading in sensitivity to WIMP-neutron interactions. Also shown are sample results from LHC searches, interpreted as exclusions in the WIMP mass vs. cross section plane by assuming mediator coupling parameters in a  $Z'$ -like simplified model[86, 160]. Though strictly model-dependent, these limits present strong constraints below  $\sim 500 \text{ GeV}$ , whereas the sensitivity of LXe TPCs extends to much higher WIMP masses.

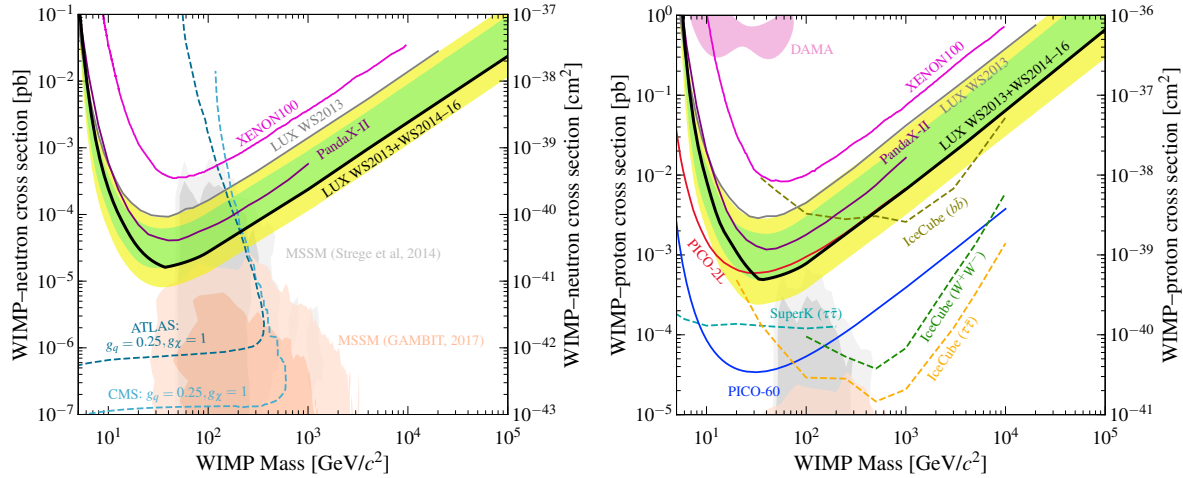


Figure 7.2: 90% CL upper limits on WIMP-neutron (left) and WIMP-proton (right) cross section. Results from this analysis are shown in thick black (“LUX WS2013+WS2014–16”), with the range of expected sensitivity indicated by the green (1- $\sigma$ ) and yellow (2- $\sigma$ ) bands. Solid gray curves show the previously published LUX WS2013 limits [25]. Constraints from other LXe TPC experiments are also shown, including XENON100 [26] and PandaX-II [27]. In the left panel, model-dependent (axial-vector mediator with indicated couplings) LHC search results are represented by dashed lines, with CMS [28] in light blue, and ATLAS [29] in dark blue. As calculated by a new profile likelihood scan of the MSSM7 [30], favored parameter space is shown as dark (1- $\sigma$ ) and light (2- $\sigma$ ) peach regions; an earlier calculation using the MSSM-15 [31] is shown in gray, with analogous shading of confidence levels. In the right panel, the DAMA allowed region (as interpreted in [32]) is shown in pink (the analogous neutron-only region is above the bounds of the plot). Such an interpretation is in severe tension with this result, as well as the PICO-2L [33] and PICO-60 [34] constraints. Selected limits from indirect searches at neutrino observatories (Super-Kamiokande [35] and IceCube [36]) are plotted as dashed lines.

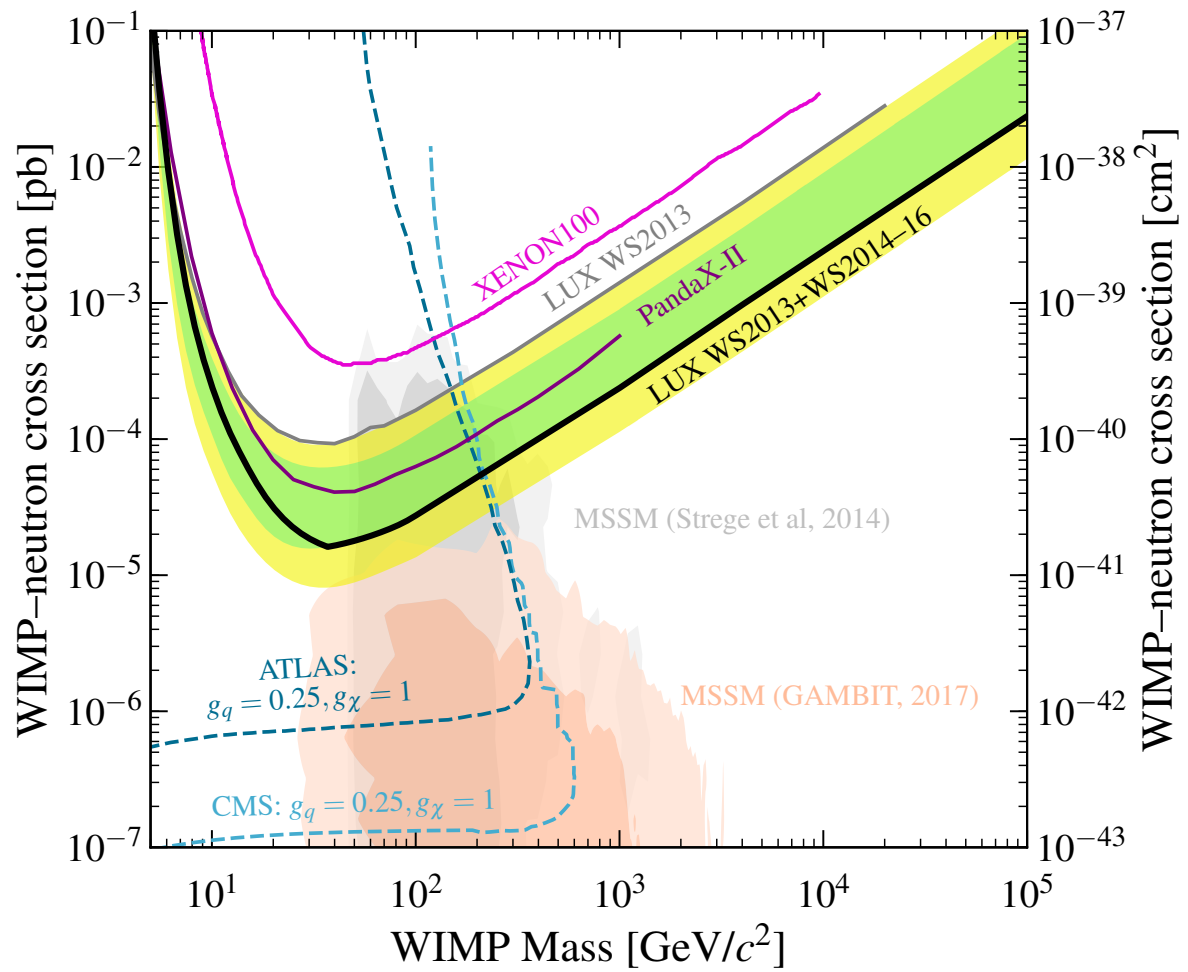


Figure 7.3: Fig. 7.2a, enlarged for visibility.

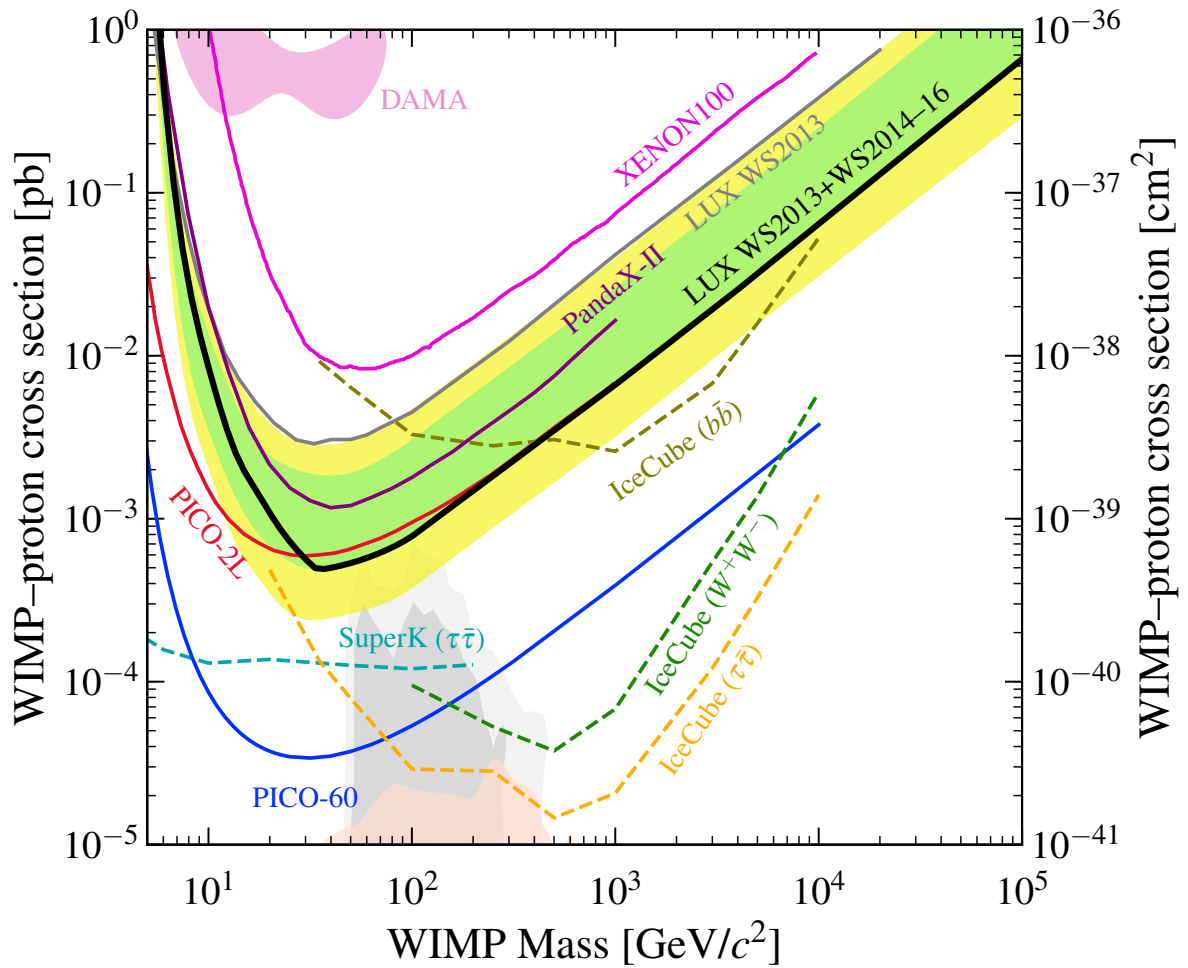


Figure 7.4: Fig. 7.2b, enlarged for visibility.

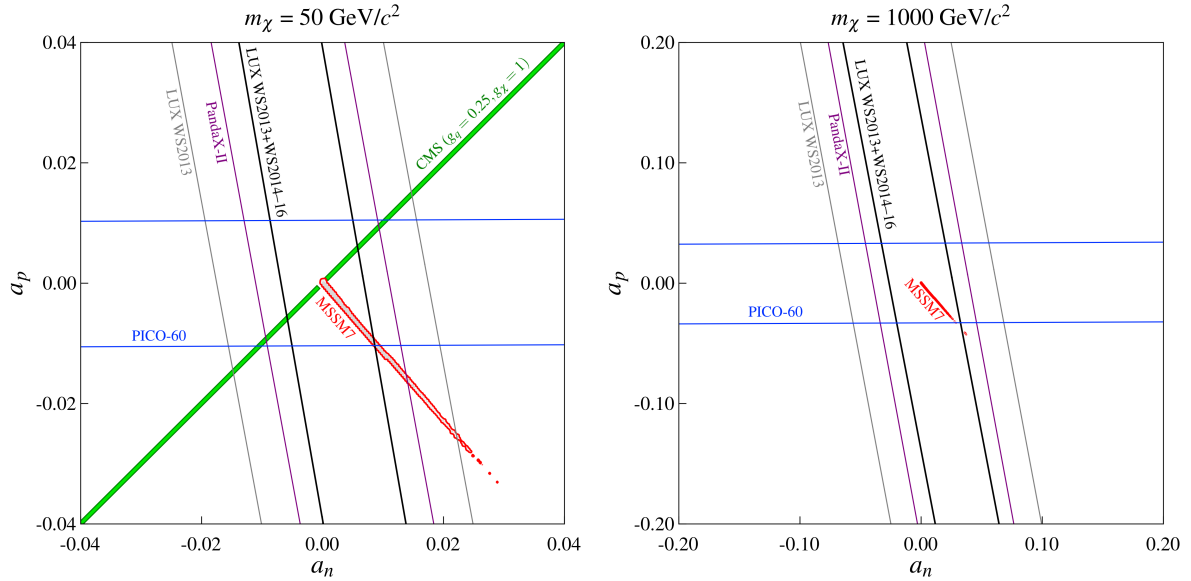


Figure 7.5: 90% CL exclusions on coupling parameters  $a_n$  and  $a_p$  for  $50 \text{ GeV } c^{-2}$  and  $1000 \text{ GeV } c^{-2}$  WIMPs. Ellipse boundaries are colored as in Fig. 7.2: this result (thick black), LUX WS2013 (gray), PandaX-II (purple), and PICO-60 (blue). Geometrically, Eq. 7.27 describes a rotated ellipse when the sum is performed over multiple isotopes with distinct  $\sigma_p^A/\sigma_n^A$ , as is the case for LXe experiments. PICO-60 considers only  $^{19}\text{F}$  (for which  $\langle \mathbf{S}_n \rangle \sim 0$ ), and thus sets limits only on  $a_p$ . The innermost region (bounded by LUX and PICO-60) represents parameter space not in tension with experimental data. The model-dependency of the LHC results is apparent in this plane, as the CMS excluded region (shown as a green band) is restricted to the  $a_n = a_p$  line (see main text for important caveat). This line is absent from the lower panel since, in this treatment, CMS is insensitive to WIMPs at the TeV mass scale. MSSM7 favored regions from the GAMBIT scan are also shown, with a red contour at the  $2\text{-}\sigma$  level for visibility. The degeneracies assumed in the MSSM7 Lagrangian lead to the tight correlation between  $a_n$  and  $a_p$ . This scan includes a range of possible WIMP masses (unlike the mass-specific experimental exclusions), and thus appears identically in each panel, noting the change in axis scale. Additionally, the scans include models with sub-dominant relic densities, for which experimental limits are rescaled accordingly.

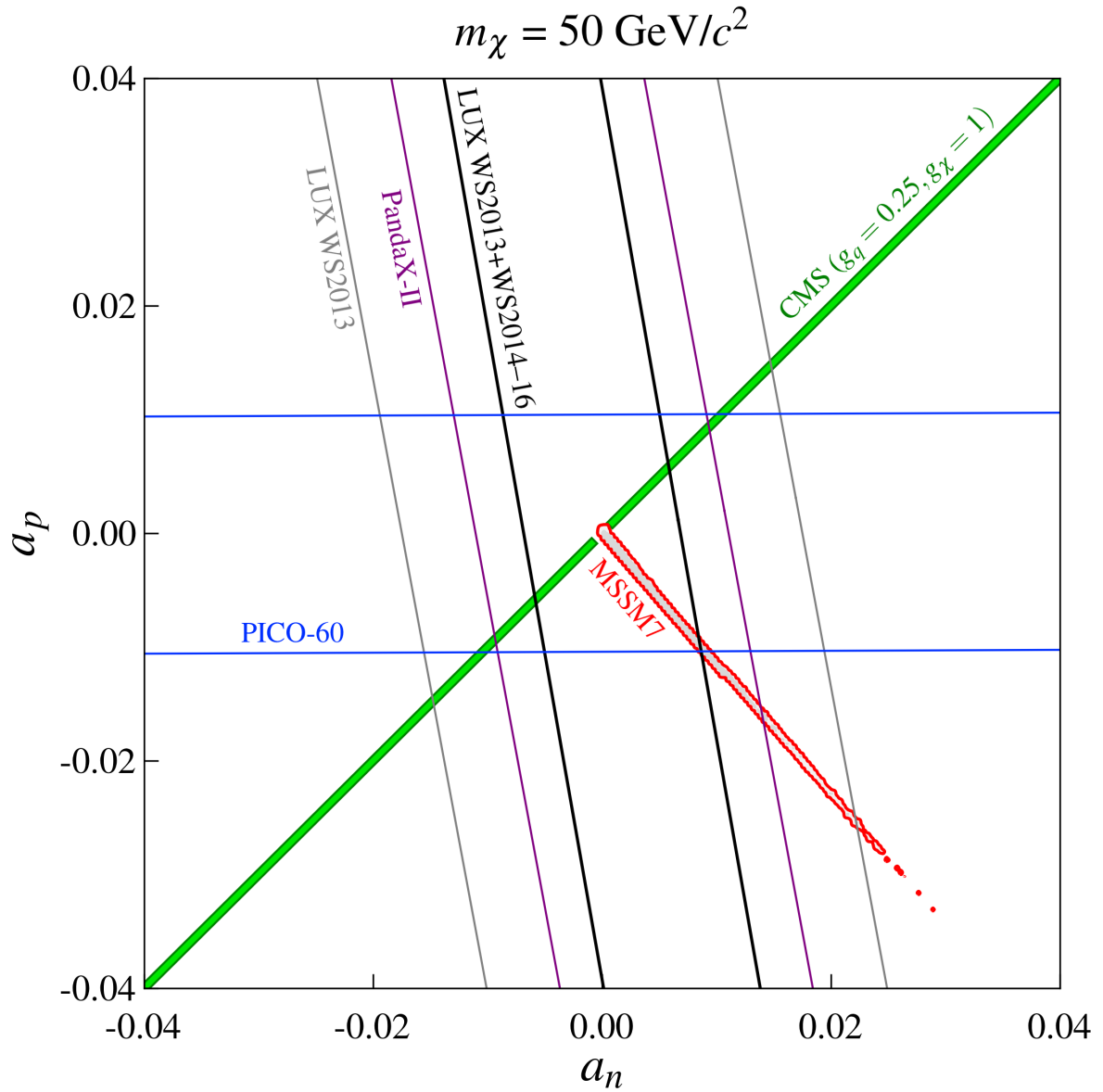


Figure 7.6: Fig. 7.5a, enlarged for visibility.

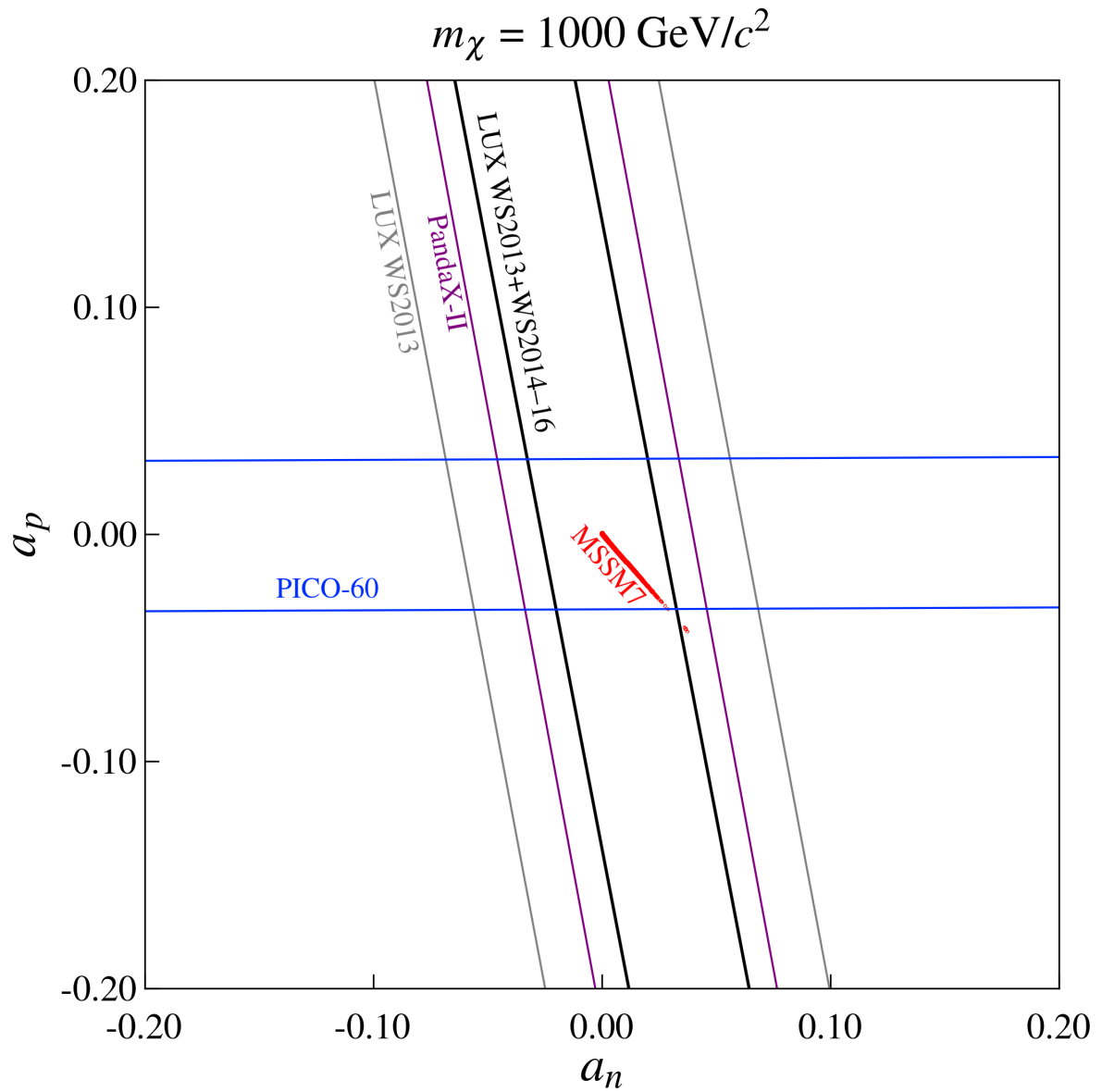


Figure 7.7: Fig. 7.5b, enlarged for visibility.

To contextualize these WIMP-neutron cross section limits, regions of favored parameter space derived from a 7-parameter Minimal Supersymmetric Standard Model (MSSM7 [161]) are also indicated. These regions, newly calculated [30] by the GAMBIT collaboration [162–165], are generated from scans of the MSSM7, where constraints from a suite of experimental results appear in the likelihood functions. In particular, recent results from LUX [20] and PandaX-II [166] are included. As such, the favored parameter space is appropriately just beyond the sensitivity of this work (since the dataset used here is the same as in the SI analysis of Ref. [20], which is already taken into account by the GAMBIT profile likelihood scan). Another region of favored parameter space from a 2014 scan of MSSM-15 [31] is shown for comparison, illustrating the rapid advance of the field and the contribution of direct detection searches such as LUX.

In the proton-only scenario, high mass limits from this result now coincide with those previously set by the PICO-2L experiment. The recent limit from PICO-60 sets the standard for proton-only sensitivity in direct detection, bolstering the constraints from indirect searches performed by the neutrino detectors IceCube and Super-Kamiokande. CMS and ATLAS take  $g_q$  (i.e. the coupling of quark type  $q \in \{u, d, s \dots\}$  to the axial-vector mediator) to be universal, and thus set equivalent limits on WIMP-neutron and -proton cross section (the curves are omitted in the right panel of Fig. 7.2 for clarity). However, we note that in a more careful treatment of the simplified model, renormalization group evolution of the couplings from the LHC to nuclear energy scale leads to significant isospin violation (see Ref. [39, 167, 168]).

The cases of neutron- and proton-only coupling fall on the axes of the more general parameter space spanned by  $a_n$  and  $a_p$ . By following the prescription laid out in [156], elliptical exclusions in this plane are made according to:

$$\sum_A \left( \frac{a_p}{\sqrt{\sigma_p^A}} \pm \frac{a_n}{\sqrt{\sigma_n^A}} \right)^2 > \frac{\pi}{24G_F^2 \mu_p^2} \quad , \quad (7.27)$$

where the sum is performed over target isotopes with mass numbers  $A$ , and  $\sigma_{p(n)}^A$  are the 90% CL upper limits on WIMP-proton(neutron) cross-section, calculated individually from these isotopes. For the PICO-60 results, where only the proton-only results are reported, limits are calculated according to [169]. Exclusions are shown in Fig. 7.5 for two choices of WIMP mass, highlighting the complementary experimental reach of LXe and fluorine-rich detectors. The CMS results are also shown in this plane as exclusions along the  $a_n = a_p$  line (since  $g_q$  is assumed to be the same for all quarks) [28, 170]. Results from the GAMBIT scans of the MSSM7 are also displayed.

### 7.6.1 Ramifications for particle physics models

As discussed in Sec. 2.2.6, it is customary for direct detection experiments to report results solely in terms of WIMP-nucleon couplings, without relating these to parameters in deeper particle physics models. This approach naturally has the advantage of model-independence; it is left to phenomenologists to convert LHC results and model predictions into the direct detection plane of WIMP mass vs. WIMP-nucleon cross section. The recent PICO publication [34], however, bucks tradition. In Fig. 6 of that paper, the procedures laid out in Ref. [86] are run in reverse, allowing the direct detection results to

be shown in the LHC plane. In this section, we apply this technique to the LUX results and follow with a discussion on the limitations of such a treatment.

As in Ref. [86], we assume a simplified model where the dark matter particle  $\chi$  (mass  $m_\chi$ ) couples to quarks via a spin-1 mediator  $Z'$  (mass  $M_{\text{med}}$ ):

$$\mathcal{L}_{\text{vector}} = g_\chi Z'_\mu \bar{\chi} \gamma^\mu \chi + \sum_q g_q Z'_\mu \bar{q} \gamma^\mu q \quad (7.28)$$

$$\mathcal{L}_{\text{axial-vector}} = g_\chi Z'_\mu \bar{\chi} \gamma^\mu \gamma^5 \chi + \sum_q g_q Z'_\mu \bar{q} \gamma^\mu \gamma^5 q \quad . \quad (7.29)$$

The mediator has coupling coefficients  $g_q$  to quarks and  $g_\chi$  to the DM particle. We assume that the vector coupling to  $\chi$  is zero, as in the case where  $\chi$  is a Majorana fermion. (Otherwise, an SI interaction would be allowed, to which direct detection experiments are far more sensitive than the LHC, owing to the  $A^2$  enhancement discussed in Sec. 2.2.6.) This leaves only the axial vector couplings, which we set to the recommended values  $g_q = 0.25$  (universal for all quarks) and  $g_\chi = 1$ . With these values fixed, the theory is now defined by only two parameters:  $M_{\text{med}}$  and  $m_\chi$ . This is the parameter space in which LHC constraints are presented.

To obtain the effective WIMP-nucleon axial-vector couplings  $f_{p,n}(g_q)$ , we simply take the sum of quark couplings weighted by the spin contribution  $\Delta_q^{(p,n)}$  of each quark to the

proton or neutron (see e.g. eq. 3.11-12 of [83] or eq. 7.3 of [3]):

$$f_{p,n}(g_q) = \Delta_u^{(p,n)} g_u + \Delta_d^{(p,n)} g_d + \Delta_s^{(p,n)} g_s \quad (7.30)$$

$$= g_q \sum_{q=u,d,s} \Delta_q^{(p,n)} \quad (7.31)$$

$$= 0.32 g_q \quad . \quad (7.32)$$

The first line is fully general, using quark-specific couplings  $g_q$ ; the next line invokes universal quark coupling, and the final line evaluates the expression using the following PDG values for the axial-vector current matrix elements of the nucleons [171]:

$$\begin{aligned} \Delta_u^{(p)} &= \Delta_d^{(n)} = 0.84 \pm 0.02 \\ \Delta_d^{(p)} &= \Delta_u^{(n)} = -0.43 \pm 0.02 \\ \Delta_s^{(p)} &= \Delta_s^{(n)} = -0.09 \pm 0.02 \end{aligned} \quad (7.33)$$

which are obtained from the COMPASS [172] and HERMES [173] deep inelastic scattering experiments.

Now we can express the zero-momentum transfer (or “standard”) SD WIMP-nucleon cross section in terms of the model parameters:

$$\sigma_{p,n}^{\text{SD}} = \frac{3 f_{p,n}^2(g_q) g_\chi^2 \mu_{p,n}^2}{\pi M_{\text{med}}^4} \quad . \quad (7.34)$$

This can be easily inverted to obtain  $M_{\text{med}}$  as a function of  $\sigma_{p,n}^{\text{SD}}$ , which allows for the conversion of limits on  $\sigma_{p,n}^{\text{SD}}$  into limits on  $M_{\text{med}}$  over a range of  $m_\chi$ . Note that in this

framework, the traditional WIMP-nucleon couplings  $a_{p,n}$  are determined by:

$$a_{p,n}^2 = \frac{f_{p,n}^2 (g_q) g_\chi^2}{8 G_F^2 M_{\text{med}}^4} . \quad (7.35)$$

With our assumption of universal quark coupling,  $f_n = f_p$  and  $a_n = a_p$  (though this comes with the same caveat raised in the discussion of Fig. 7.5). Thus, we are free to choose the more constraining LUX results for WIMP-neutron coupling when we convert to limits on  $M_{\text{med}}$ , just as PICO uses their WIMP-proton results.<sup>2</sup> The only remaining task is to obtain limits at the 95% CL (as opposed to 90% CL), the standard for LHC searches, which is easily done using the saved  $p$ -value vs. cross section curves from the hypothesis test pseudo-trials.

Figure 7.8 presents the LUX exclusions converted into the  $M_{\text{med}}-m_\chi$  plane, along with the PICO and CMS constraints for comparison. The plot is essentially a rotation of Fig. 7.2, with the cross section axis compressed due to the  $M_{\text{med}} \propto \sigma^{-1/4}$  mapping. Since this simplified model predicts equivalent coupling between WIMPs and protons and neutrons, the PICO and LUX results are essentially redundant, ruling out lower mass mediators over a wide swath of WIMP masses. The CMS constraints carve much deeper along the mediator axis, but are kinematically limited from accessing higher mass WIMPs. Though the red exclusion region is cut off near  $M_{\text{med}} = 50$  GeV, Ref. [28] points out that the region is expected to extend to smaller  $M_{\text{med}}$  and  $m_\chi$ , but the signal model was not constructed outside the shown range.

<sup>2</sup>Technically, the LUX results could be recalculated with a signal model allowing both WIMP-proton and WIMP-neutron coupling. But since sensitivity would be dominated by the WIMP-neutron interaction, this exercise is not worth the computing expense.

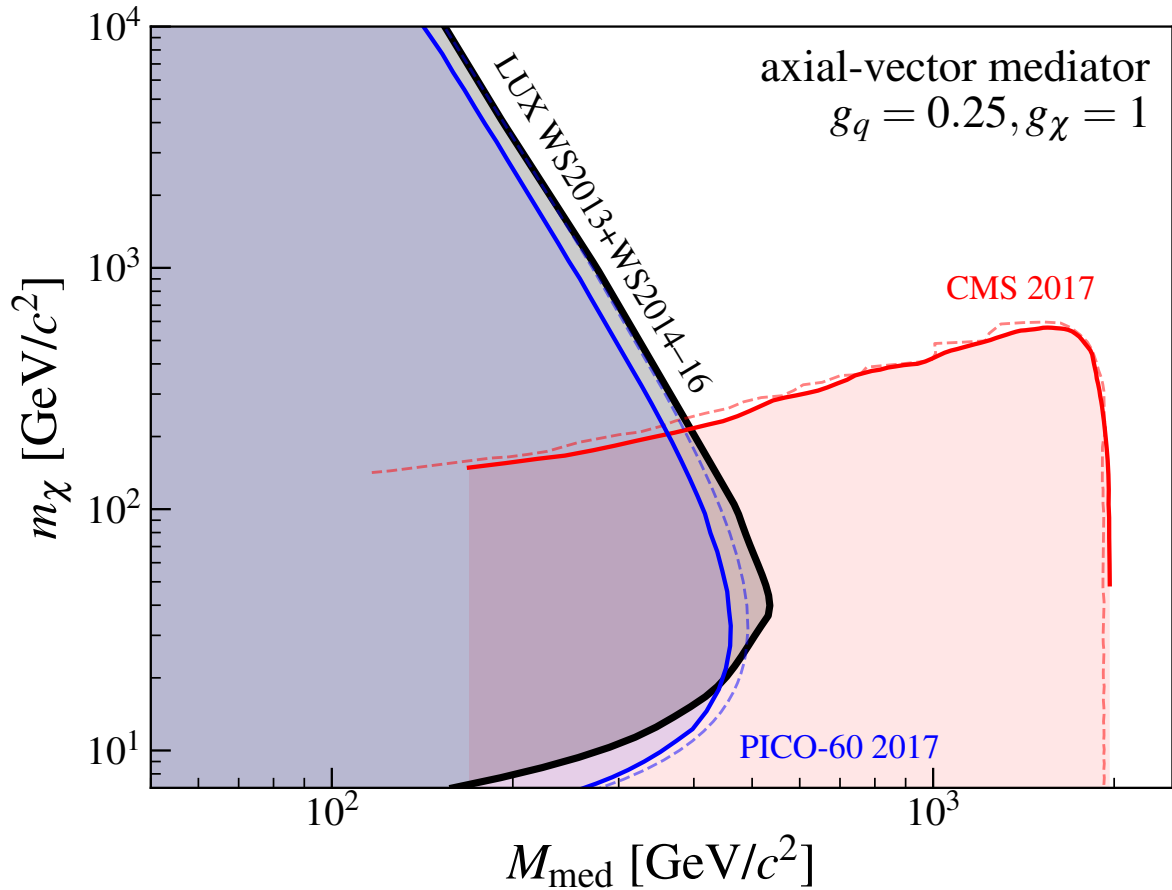


Figure 7.8: 95% CL exclusion regions in the mass-mass plane for axial vector  $Z'$  mediated coupling simplified models. Shaded area bounded by the black curve shows LUX combined results (newly calculated); the red curves show CMS results from [28]; the blue curves show the PICO results [34]. For the latter two results, the solid curves comprise points taken from analogous plots in the respective publications, whereas the dashed lines are calculated from the 90% CL cross section limits according to the procedure described in the text (these are shown simply as a cross-check of the method).

The EFT machinery of this  $Z'$  model also allows us to examine  $Z$ -portal DM, i.e. DM interactions mediated by the SM  $Z^0$  boson (see e.g. [174–176]). Supposing again that vector coupling is cancelled, the only unknown parameters in this theory are  $g_\chi$  and  $m_\chi$ ; the mass of the  $Z$  and its axial-vector couplings to quarks are known. Since  $g_q \propto T_3$  (weak isospin), the couplings for quarks differ by a sign between up- and down-types. Thus, by eqs. 7.31 and 7.33,  $a_n \neq a_p$ :

$$\frac{a_p}{a_n} = \frac{\Delta_u^{(p)} g_u + \Delta_d^{(p)} g_d + \Delta_s^{(p)} g_s}{\Delta_u^{(n)} g_u + \Delta_d^{(n)} g_d + \Delta_s^{(n)} g_s} \quad (7.36)$$

$$= \frac{-\Delta_u^{(p)} + \Delta_d^{(p)} + \Delta_s^{(p)}}{-\Delta_d^{(p)} + \Delta_u^{(p)} + \Delta_s^{(p)}} \quad (7.37)$$

$$\approx -1.15 \quad . \quad (7.38)$$

In fact, this precise relationship can be seen in the GAMBIT region shown in Fig. 7.6, which has slope  $\sim -1.2 \neq -1$  due to the nonzero strange quark contribution to nucleon spin (see eq. 7.38). Fig. 2 of Ref. [175] shows direct detection limits on  $m_\chi$  vs.  $g_\chi$  in this model, as well as the curve that would give rise to a thermal relic matching the observed cosmological DM density. The LUX results exclude a large fraction of this parameter space.

Consideration of the relic DM density introduces a serious caveat to the naive translation of direct detection results into the mass-mass plane of the  $Z'$  simplified models. With the couplings  $g_q$  and  $g_\chi$  fixed, points in  $M_{\text{med}}-m_\chi$  parameter space correspond to complete models of DM implying exact values of  $\Omega_{\text{DM}}$ . Since the LHC signal models are

independent of  $\Omega_{\text{DM}}$ , this concern does not affect their results. Direct detection limits, on the other hand, are proportional to the local DM density  $\rho_\chi$ , which is typically fixed to the canonical value of  $0.3 \text{ GeV } c^{-2} \text{ cm}^{-3}$ . In  $\Lambda\text{CDM}$ , this local density should be proportional to the cosmological abundance  $\Omega_{\text{DM}}$ . If the WIMP posited by this theory is only a subcomponent of the total DM density ( $\Omega_\chi/\Omega_{\text{DM}} < 1$ ), then  $\rho_\chi$  would have to be rescaled accordingly, changing the results from direct detection experiments. This subtlety prompts the authors of Ref. [86] to explicitly advise against displaying direct detection results as in Fig. 7.8. In Ref. [37], Chala *et al.* actually perform the relic density calculations and rescale an approximated LUX result, shown in Fig. 7.9.

On the other hand, an argument could be made that physics processes not described by the simplified model and inapplicable to LHC signals could alter the relic density calculation, allowing for  $\Omega_\chi/\Omega_{\text{DM}} = 1$  at values of  $M_{\text{med}}$  and  $m_\chi$  other than expected (Ref. [86] points to [177] as an appropriate reference motivating this line of reasoning).

Regardless of which approach is used, if LHC and direct detection results are to be compared using simplified models, the running of the couplings between the respective energy scales should be considered. The case for this is elegantly made in Ref. [39], which introduces a code for explicit calculation of the effects. An example of this renormalization group evolution is shown in Fig. 7.10, which shows the correction that should be applied to collider search results presented in the WIMP mass vs. WIMP-nucleon cross section plane. This correction has been applied in Fig. 7.11, which is identical to Fig. 7.3 aside from the rescaling of the LHC constraints.

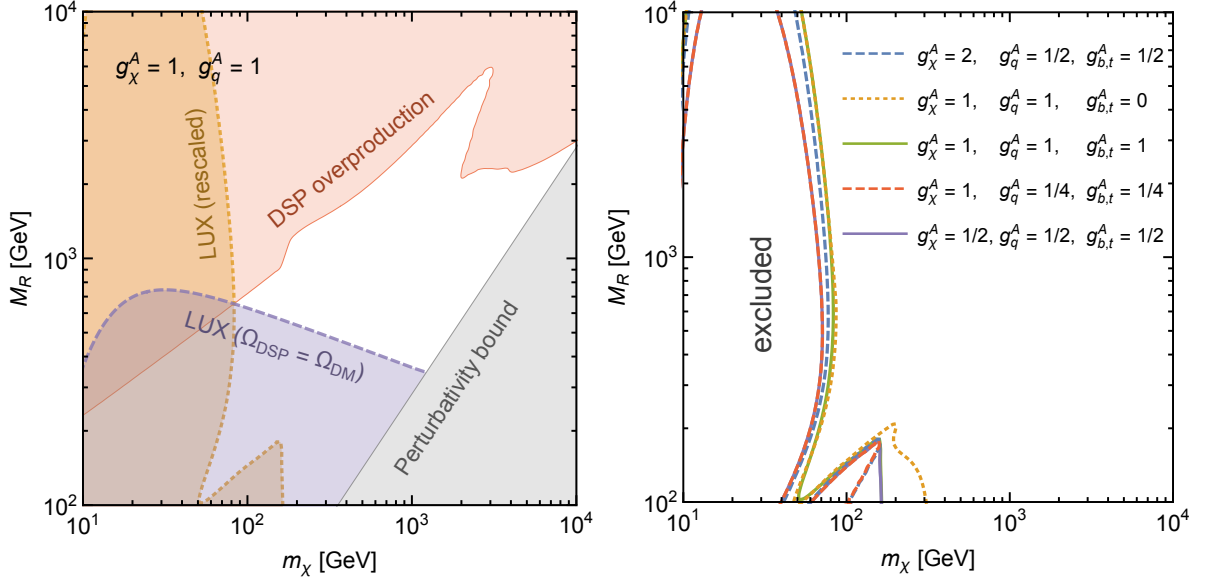


Figure 7.9: Effect of relic density rescaling on LUX limits, taken from Ref. [37] (where  $M_R$  refers to  $M_{\text{med}}$ ). At left, the rescaling procedure is illustrated by showing the raw LUX 95% CL bound with fixed  $\rho_\chi$  (purple), the region where the calculated  $\Omega_\chi/\Omega_{\text{DM}}^{\text{obs}} > 1$  (red), and the rescaled LUX limit (orange). Near  $m_\chi = 80$  GeV, all three contours overlap by construction: here, the calculated  $\Omega_\chi/\Omega_{\text{DM}}^{\text{obs}} = 1$ , which matches the assumption implicit in the purple curve, so that the rescaling multiplier is unity. Elsewhere, this is not true, and the discrepancy is corrected for by the rescaling. The purple region is estimated from LUX’s first SI result [18] (since this publication predates Refs. [17, 25, 38]), and furthermore differs from Fig. 7.8 by a factor of  $(1/0.25)^{2 \times 1/4} = 1/2$  due to the different values of  $g_q$  assumed. Still, the constraint is very close to that shown in Fig. 7.8, and the rescaled result is thus a good approximation of what might be obtained by applying this procedure to the most recent LUX bounds. The left panel also shows the “perturbativity bound”  $m_\chi < \sqrt{4\pi} M_{\text{med}}/g_\chi$ , which ensures that the  $\chi Z'$  Yukawa interaction is perturbative. In the right panel, the rescaled constraint contours are shown for various choices of mediator couplings.

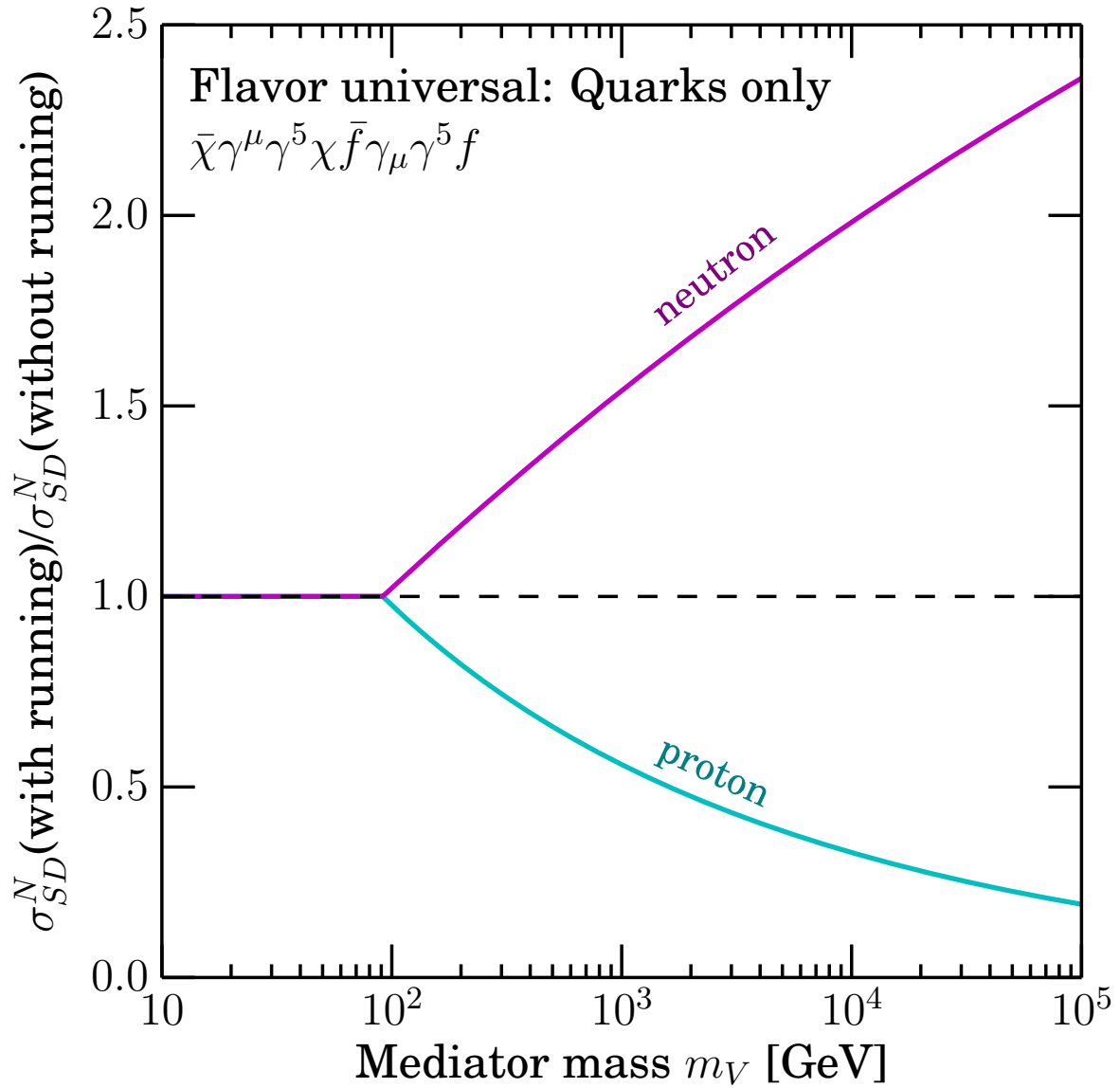


Figure 7.10: Comparison of SD WIMP-nucleon cross sections when the running of the couplings is taken into account, taken from Ref. [39]. These corrections should be applied to LHC constraints when comparing them to direct detection limits.

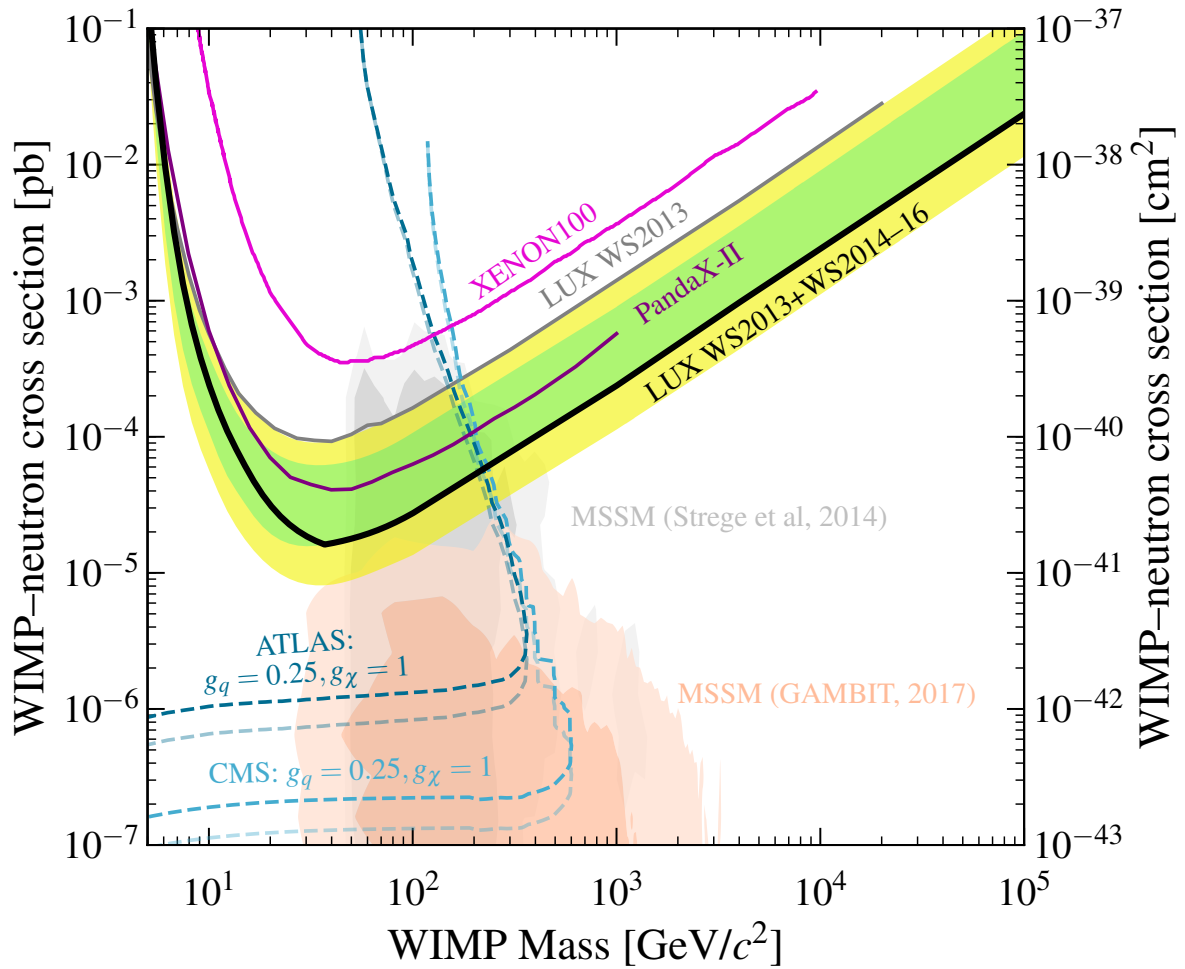


Figure 7.11: WIMP–neutron cross section limits, identical to Fig. 7.3 except for the LHC contours. The transparent CMS and ATLAS dashed curves are the same as in Fig. 7.3 (and as shown in Refs. [28] and [29], respectively). The solid dashed curves have been scaled by the correction factor shown in Fig. 7.10, following the procedure laid out in Ref. [39]. The effect is most pronounced at small cross sections since these correspond to large mediator mass.

## 7.7 Conclusion

In conclusion, the complete LUX dataset has been analyzed to set limits on SD WIMP-nucleon scattering. World-leading constraints are presented for neutron-only coupling, complementing searches for particle production at the LHC. Further complementarity with the PICO-60 result is achieved in the 2D  $a_n$ - $a_p$  plane. Future work will investigate a more complete set of EFT interaction operators, beyond those that define the standard SI and SD paradigm.

# Appendix A

## Annual velocity modulation

As discussed in Section 2.2.4, the relative velocity of the Earth with respect to the rest frame of the dark halo affects the expected nuclear recoil spectrum from WIMP scattering. In Ref. [40], Savage *et al.* derive the speed  $v_{\text{obs}}$  (or  $v_e$  in McCabe’s notation [8]) of an Earth-borne observer over the course of the year:

$$v_{\text{obs}}(t) \approx v_{\odot} \left[ 1 + b \frac{V_{\oplus}}{v_{\odot}} \cos \omega(t - t_c) \right] \quad , \quad (\text{A.1})$$

where  $\mathbf{v}_{\odot} = \mathbf{v}_{\text{LSR}} + \mathbf{v}_{\odot, \text{pec}}$  is the velocity of the Sun,  $V_{\oplus}$  is the Earth’s orbital speed around the Sun (see Table 2.1 for numerical values),  $b = 0.49$  is a geometrical factor accounting for the angle between the Earth’s orbital plane and the Sun’s motion,  $\omega = 2\pi/\text{year}$  is the modulation period,  $t$  is the time in years since Jan. 1, and  $t_c = 0.415$  years (June 1) is the SHM estimate for the time at which the relative Earth velocity is maximized.

In direct detection experiments, one can strive to discriminate background events and search for WIMPs in a cleaned-up signal region (as in the LUX analyses), or instead look

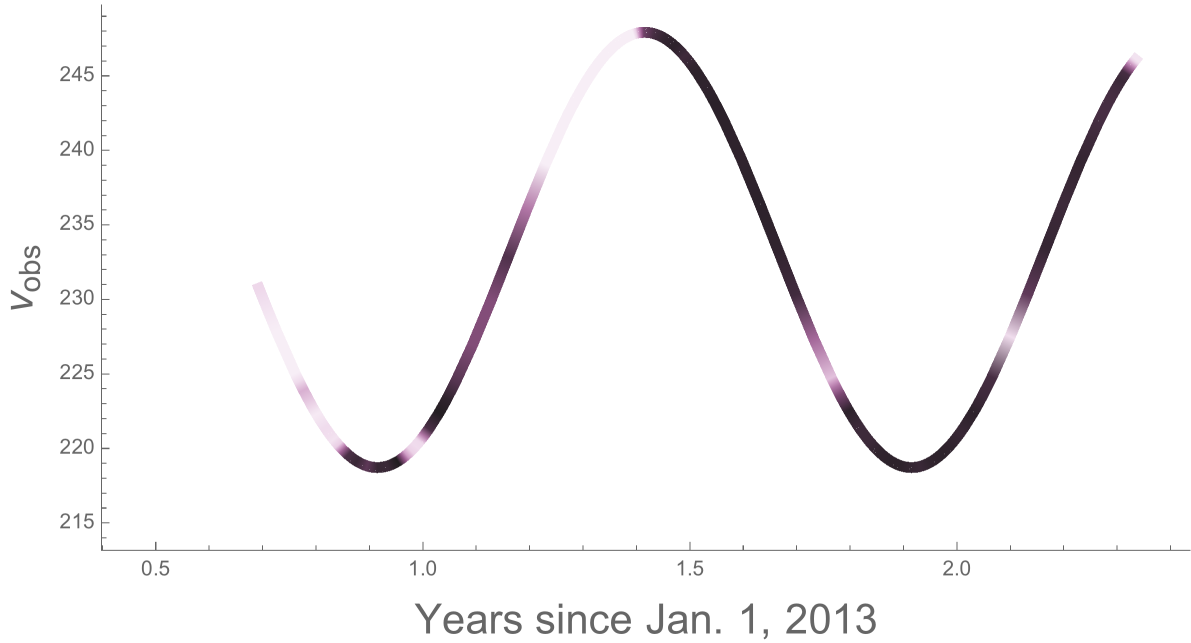


Figure A.1: Relative Earth velocity  $v_{\text{obs}}(t)$  during the LUX WS2014–16 exposure. Line color indicates the relative data-taking efficiency: lighter periods show times of calibration or detector shut-down, darker periods indicate closer to 100% efficiency.

for annual modulation of total event rate in a less strictly defined event parameter space (as in the DAMA result). In the former approach, the averaged  $\langle v_{\text{obs}}(t) \rangle$  value is used to construct the nuclear recoil spectrum used in the signal model. For very long exposures, this becomes simply:

$$\langle v_{\text{obs}}(t) \rangle \rightarrow v_{\odot} \approx 233 \text{ km/s} \quad . \quad (\text{A.2})$$

Otherwise, a more careful calculation can be done:

$$\langle v_{\text{obs}}(t) \rangle = \frac{\int v_{\text{obs}}(t) \epsilon(t) dt}{\int \epsilon(t) dt} \quad , \quad (\text{A.3})$$

with  $\epsilon(t)$  quantifying the time-dependent data-taking efficiency of the detector.

Figure A.1 shows  $v_{\text{obs}}(t)$  over the course of the LUX WS2014–16 exposure, with line darkness indicating the data-taking efficiency  $\epsilon(t)$ . The weighted average comes to

230 km/s. On the other hand, the shorter WS2013 exposure took place during the high velocity summer months, and clocks in at 245 km/s. Due to an oversight, this WS2013 value for  $\langle v_{\text{obs}}(t) \rangle$  was used in the WS2014–16 SI analysis [20], though it was corrected to the appropriate value in the SD analysis [38]. It is worth noting not only that the effect of this error on the computed limit was indiscernible (only a  $\sim 20\%$  shift at very low WIMP masses, invisible on the log-log scale), but also that the uncertainties on  $v_{\text{LSR}}$  and  $v_{\text{esc}}$  are larger and have more significant repercussions on sensitivity [8]. Figure A.2 shows the minute change in SD recoil spectra introduced by this shift in  $\langle v_{\text{obs}}(t) \rangle$ .

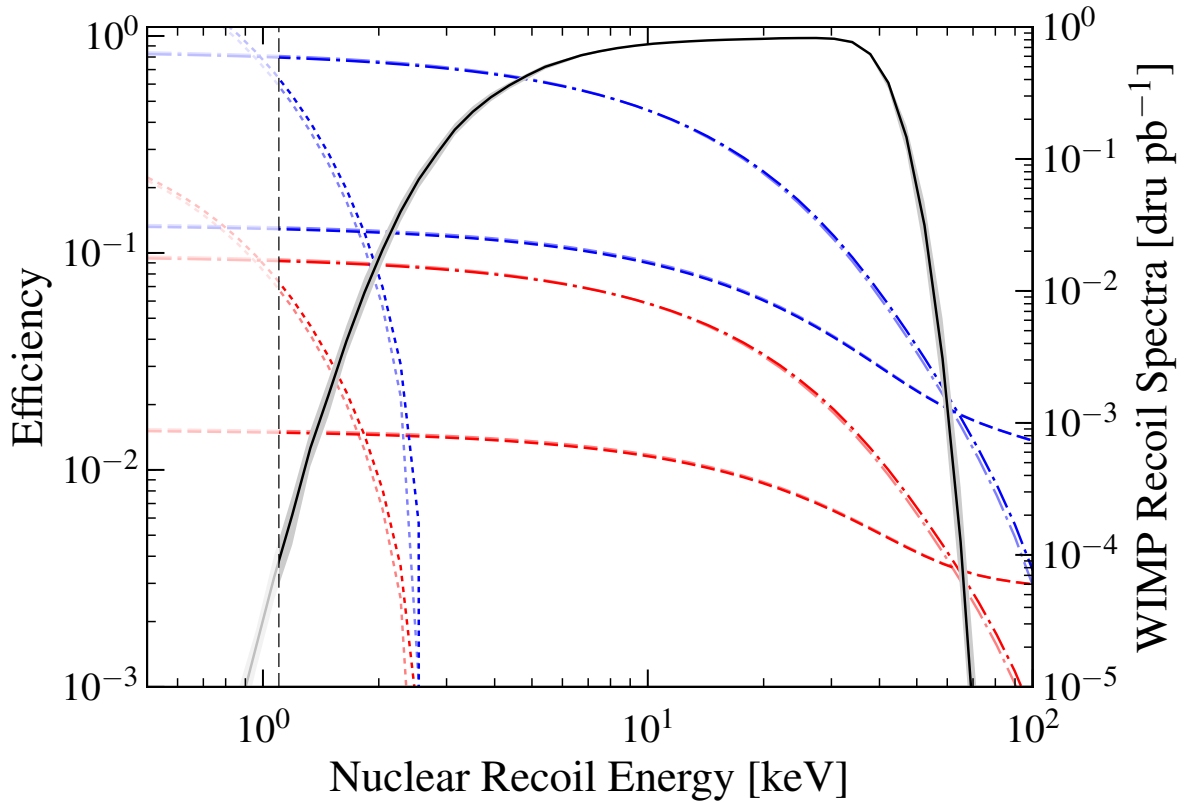


Figure A.2: Efficiency plot and SD recoil spectra as in Fig. 7.1. The fainter curves have been calculated using the correct WS2014–16 value of  $\langle v_{\text{obs}}(t) \rangle$  (230 km/s), and the darker curves using the WS2013 value (245 km/s). A visible change is only apparent in the 5 GeV WIMP curves, since the tail of the Maxwellian distribution is responsible for the recoil spectra at these energies.

# Appendix B

## Cut-and-count limits with likelihood ratios

In Chapter 6, the PLR test statistic is introduced for the purpose of limit setting. The much simpler “cut-and-count” approach using the Feldman-Cousins ordering principle is far less computationally expensive, and serves as a useful cross-check of the PLR result. The natural question, then, is how to make the “cut”? The Neyman-Pearson optimal observable is the likelihood ratio, which we can define on a per-event basis. Specifically, we can freeze the nuisance parameters to their nominal values, and calculate the likelihood ratio  $f_s(\mathbf{x})/f_b(\mathbf{x})$  for each event and make a cut in this 1D parameter space.

By way of an example, let’s look at the WS2014–16 SI analysis. To keep things simple, we shall consider only the  $(S1, \log_{10} S2)$ -space PDFs, restricting our background model to just the uniform energy ER population (i.e. only the betas and Comptons). The new

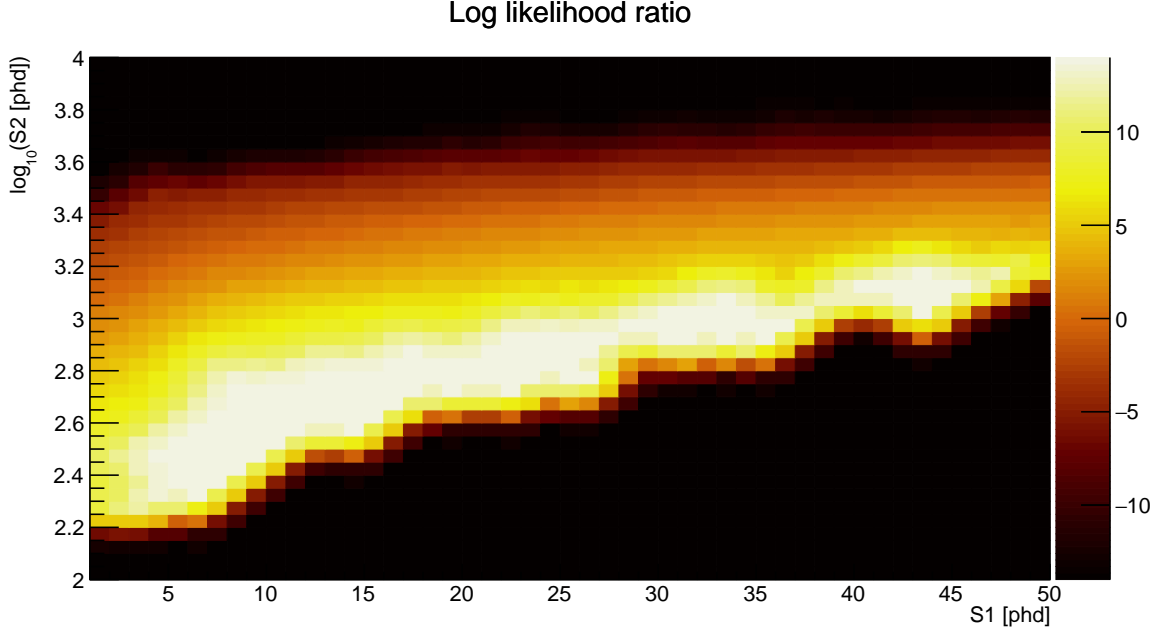


Figure B.1:  $\Lambda$  as a function of  $(S1, \log_{10} S2)$ , for a 50 GeV WIMP. This is the result of dividing a normalized Fig. 6.28 by a normalized Fig. 6.17 and taking the natural logarithm. (The blotchiness is only the result of smoothing a histogram with limited statistics.) Making a cut  $\Lambda > \Lambda_c$  would be equivalent to making a cut in  $(S1, \log_{10} S2)$ -space defined by closed regions satisfying  $\Lambda > \Lambda_c$ .

observable calculated for each event is

$$\Lambda = \ln \left[ \frac{f_s(S1, \log_{10} S2 | m_\chi)}{f_{\text{ER}}(S1, \log_{10} S2)} \right] . \quad (\text{B.1})$$

Since this is just a rough validation, we can arbitrarily choose one of the date bin/ $z$ -slice models to work with. The signal PDF of NR events will of course depend on the WIMP mass we are testing.

Figure B.1 shows the value of log likelihood ratio variable evaluated in  $(S1, \log_{10} S2)$ -space. Figure B.2 shows the distributions of background and signal events in  $\Lambda$ -space. From the CDFs implied by these, the acceptance curve in Fig. B.3 can be calculated. Repeating this exercise for many WIMP masses, we can calculate the signal acceptance

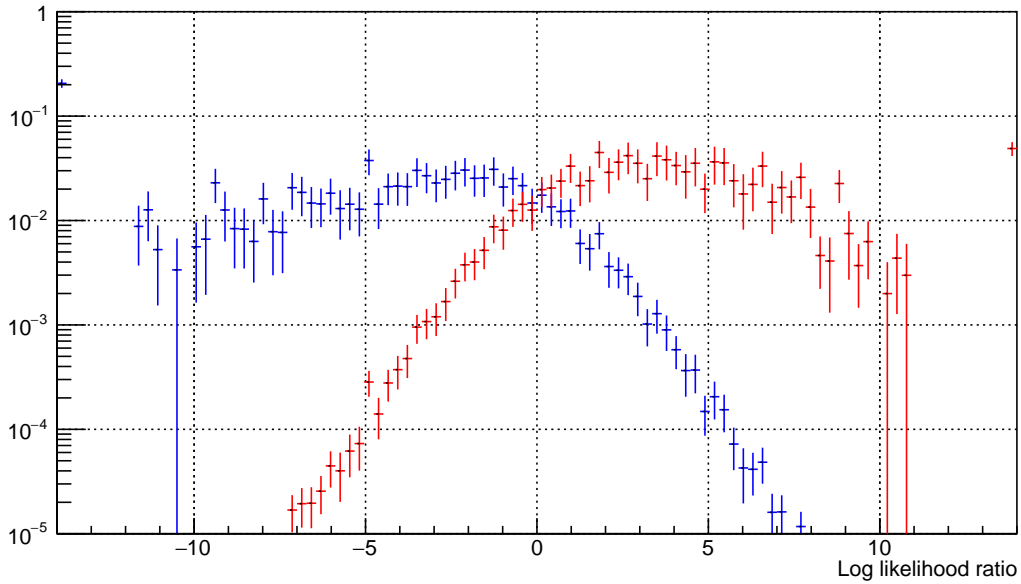


Figure B.2: PDFs in  $\Lambda$  for background events (blue) and signal events (red), in the case of a 50 GeV WIMP. One could imagine cutting at  $\Lambda > 5$  to achieve high background rejection.

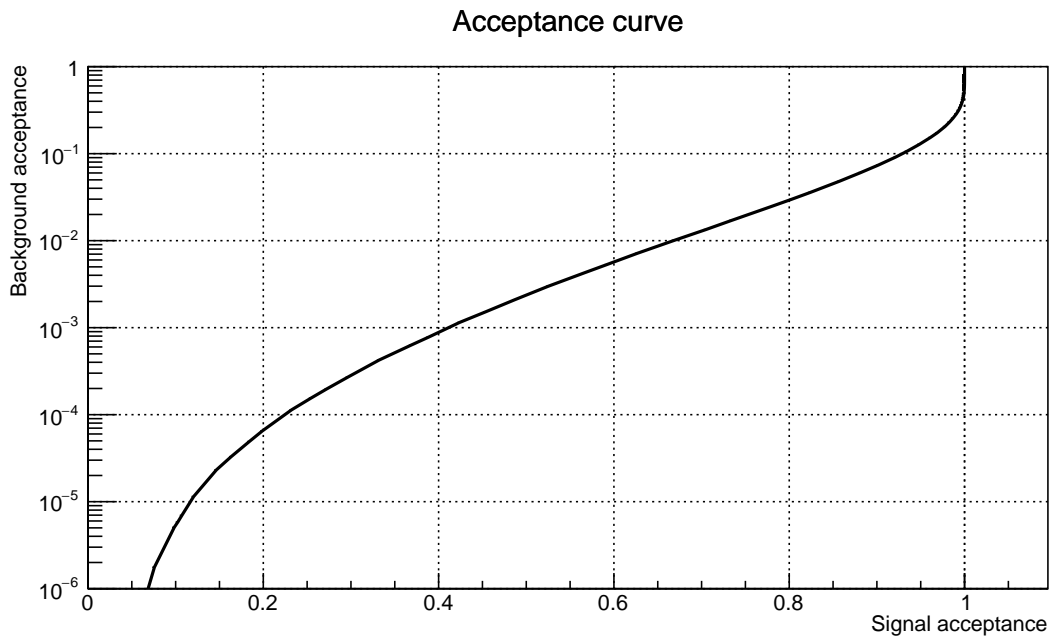


Figure B.3: Acceptance curve for ER background and 50 GeV WIMP. We can see that making a cut on  $\Lambda$  that achieves 40% signal acceptance will eliminate  $1 - 10^{-3} = 99.9\%$  of background events.

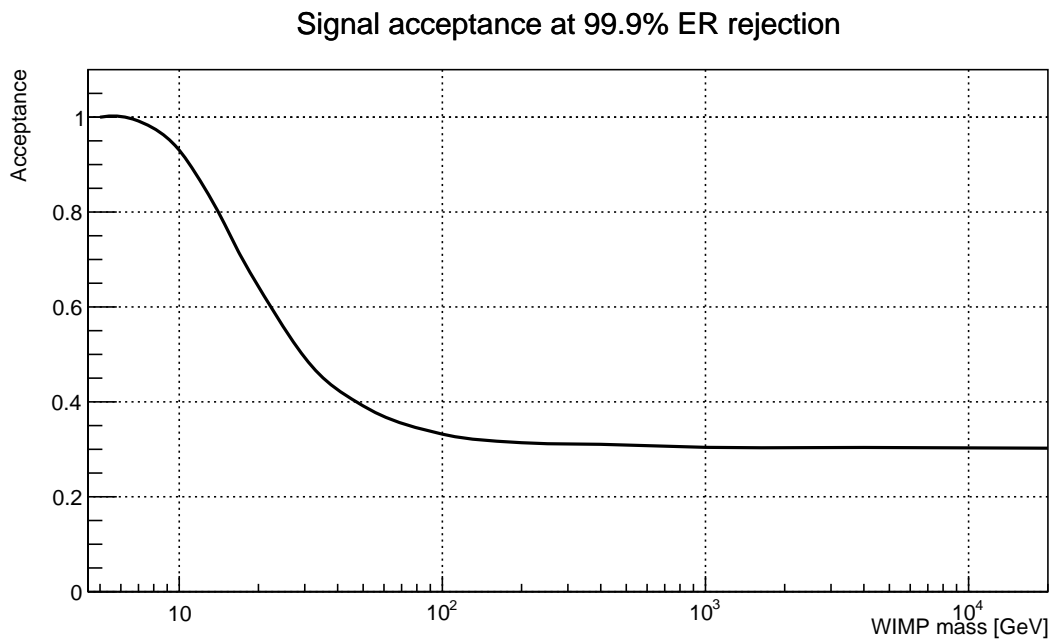


Figure B.4: Signal acceptance as a function of WIMP mass, following a cut on  $\Lambda$  that achieves 99.9% rejection of ER background events. Since the NR spectrum converges to a roughly constant shape as WIMP mass increases, the signal acceptance reaches a plateau. The NR and ER bands are better separated at lower energies, leading to the superior acceptance of light WIMPs for constant ER rejection.

for a given background rejection rate, as shown in Fig. B.4. Acceptance improves with decreasing WIMP mass because the NR population is actually more separated from the ER band at low recoil energies. Light WIMPs are kinematically limited to imparting only small amounts of momentum to Xe nuclei, and thus are more readily distinguished from ER backgrounds.

Note that this is *not* saying that LUX is most sensitive to low mass WIMPs. Consider the following scenario: 10 NR events pass our selection, as well as 1000 ER background events. If the NRs follow the recoil distribution of a 10 GeV WIMP, we can devise a cut that will include  $\sim 9$  signal events, and only 1 ER event (on average). On the other hand, if the NRs are the result of collisions with 50 GeV WIMPs, then our optimal cut will accept  $\sim 3$  signal events while allowing 1 ER event to leak in. However, if 10 signal events pass our selection criteria, this implies a much higher cross section for 10 GeV WIMPs than it does for 50 GeV WIMPs due to the NR detection efficiency at low energies.

To compare our cut-and-count expected limits to those predicted by the PLR procedure, we must first estimate how many background events will make it past our cut on  $\Lambda$ . If we choose to cut such that 99.9% of ER events are rejected, then we would expect  $\sim 1$  ER event to pass from the  $\sim 1200$  predicted by the background model. The Feldman-Cousins expected 90% CL upper limit for  $b = 1.0$  is 3.28 events (see Table XII of Ref. [22]). Dividing this by the signal acceptance gives us the expected upper limit on the total number of signal events passing selection criteria. Dividing again by the detection rate (in events per zb) for the WIMP mass being tested gives the expected

90% CL upper limit on WIMP-nucleon cross section. The bottom edge of the blue band in Fig. B.5 shows the results of this calculation.

Note that in the previous estimate, we have ignored background events from the wall and accidental coincidences. Looking at Table 6.3, we can conservatively estimate that all  $\sim 15$  expected events from these two sources will pass our cut on  $\Lambda$ . The corresponding Feldman-Cousins expected upper limit is 7.99 signal events. The WIMP-nucleon cross section derived from this calculation defines the upper bound of the blue band in Fig. B.5. As such, the blue band indicates a range of limits we might expect to make using our simple cut-and-count technique. The green band shows the  $1\text{-}\sigma$  expected limits from the full PLR analysis.

The two bands show reasonable overlap over a wide range of WIMP masses. For heavier WIMPs, it seems that our generous assumption that no wall events leak past the cut on  $\Lambda$  is more appropriate (this makes sense if one considers the shapes of the PDFs). Furthermore, with position discrimination, our ER leakage should be even less than  $10^{-3}$ . Thus, it stands to reason that the PLR expected limits are stronger than our cut-and-count estimates. For lighter WIMPs, however, the wall events *do* begin to contaminate our sample drawn from the  $\Lambda$  cut, and the upper edge of the blue band becomes a more reasonable estimate. Even this conservative estimate is not conservative enough, it seems, at  $m_\chi = 5$  GeV, where the PLR expected limits are weaker than the cut-and-count. This can be attributed to our freezing of nuisance parameters: the uncertainties in  $k_{\text{Lind}}$  and the wall event rate are considered in the PLR, but not in our

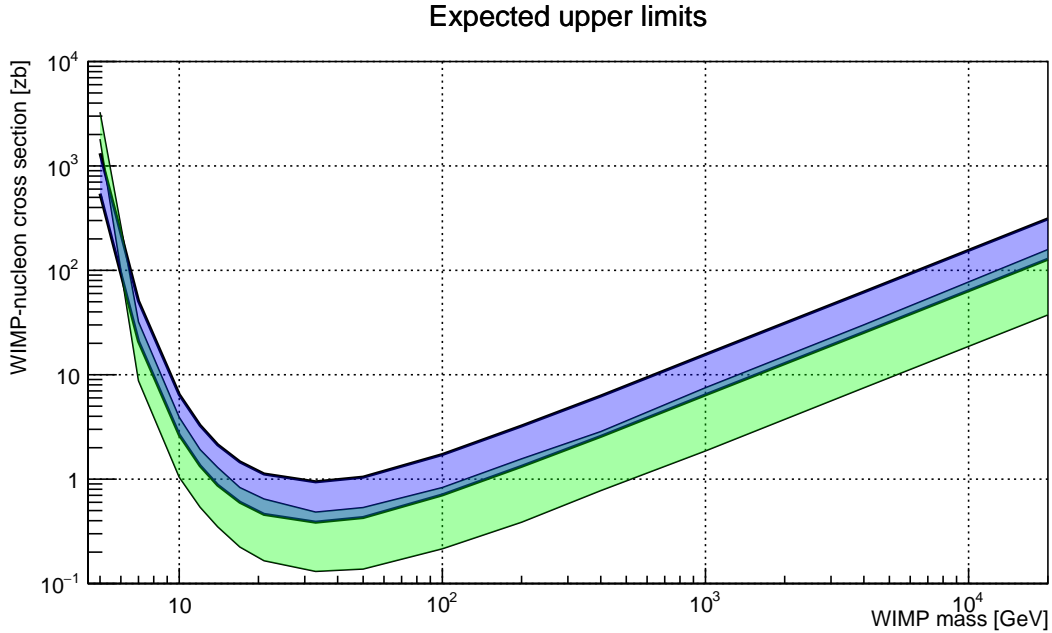


Figure B.5: In blue: a range of 90% CL upper limits on SI WIMP-nucleon cross section from an approximate cut-and-count analysis of the WS2014–16 dataset. The lower edge of the band is defined by a FC  $b = 15$  expected limit, the upper edge uses  $b = 1$ . In green: the  $1\text{-}\sigma$  range of expected limits from the full PLR analysis.

Feldman-Cousins analysis. One could improve the cut-and-count estimate to address this by using the technique proposed by Rolke *et al.* [142], which allows for uncertainties in signal acceptance and mean background rate.

This simple example is meant to be instructive, but one could imagine refining the likelihood function to include not just the ER backgrounds, but also the wall events and the accidentals. Furthermore, we could include the position and date observables into the likelihood functions, replicating the full structure of  $\mathcal{L}_{\text{WS2014-16}}$  (see eq. 6.24). In the end, the PLR is a more reliable tool, but cut-and-count analyses (using the Neyman-Pearson optimal observable) can serve as excellent validations or exploratory sensitivity studies, due to their extremely lightweight computational requirements.

# Bibliography

- [1] V. C. Rubin, W. K. Ford, Jr., and N. Thonnard, “Rotational properties of 21 SC galaxies with a large range of luminosities and radii, from NGC 4605 /R = 4kpc/ to UGC 2885 /R = 122 kpc/,” *Astrophys. J.* **238**, 471–487 (1980).
- [2] K. G. Begeman, A. H. Broeils, and R. H. Sanders, “Extended rotation curves of spiral galaxies: Dark haloes and modified dynamics,” *Mon. Not. Roy. Astron. Soc.* **249**, 523 (1991).
- [3] G. Jungman, M. Kamionkowski, and K. Griest, “Supersymmetric dark matter,” *Phys. Rep.* **267**, 195–373 (1996), [arXiv:hep-ph/9506380 \[hep-ph\]](#) .
- [4] G. Bertone, D. Hooper, and J. Silk, “Particle dark matter: Evidence, candidates and constraints,” *Phys. Rep.* **405**, 279–390 (2005), [arXiv:hep-ph/0404175 \[hep-ph\]](#) .
- [5] D. Clowe, M. Bradac, A. H. Gonzalez, M. Markevitch, S. W. Randall, C. Jones, and D. Zaritsky, “A direct empirical proof of the existence of dark matter,” *Astrophys. J.* **648**, L109–L113 (2006), [arXiv:astro-ph/0608407 \[astro-ph\]](#) .
- [6] P. A. R. Ade *et al.* (Planck), “Planck 2015 results. XIII. Cosmological parameters,” *Astron. Astrophys.* **594**, A13 (2016), [arXiv:1502.01589 \[astro-ph.CO\]](#) .
- [7] J. L. Feng, “Dark Matter Candidates from Particle Physics and Methods of Detection,” *Ann. Rev. Astron. Astrophys.* **48**, 495–545 (2010), [arXiv:1003.0904 \[astro-ph.CO\]](#) .
- [8] C. McCabe, “The Astrophysical Uncertainties Of Dark Matter Direct Detection Experiments,” *Phys. Rev. D* **82**, 023530 (2010), [arXiv:1005.0579 \[hep-ph\]](#) .
- [9] D. S. Akerib *et al.* (LUX Collaboration), “The Large Underground Xenon (LUX) Experiment,” *Nucl. Instrum. Meth. A* **704**, 111–126 (2013), [arXiv:1211.3788 \[physics.ins-det\]](#) .

- [10] D. S. Akerib *et al.* (LUX), “FPGA-based Trigger System for the LUX Dark Matter Experiment,” *Nucl. Instrum. Meth. A* **818**, 57–67 (2016), [arXiv:1511.03541 \[physics.ins-det\]](#) .
- [11] D. S. Akerib *et al.* (LUX), “Calibration, event reconstruction, data analysis and limits calculation for the LUX dark matter experiment,” (2017), in preparation.
- [12] D. S. Akerib *et al.* (LUX), “Position Reconstruction in LUX,” (2017), [arXiv:1710.02752 \[physics.ins-det\]](#) .
- [13] D. S. Akerib *et al.* (LUX), “ $^{83\text{m}}\text{Kr}$  calibration of the 2013 LUX dark matter search,” (2017), [arXiv:1708.02566 \[physics.ins-det\]](#) .
- [14] D. S. Akerib *et al.* (LUX), “Tritium calibration of the LUX dark matter experiment,” *Phys. Rev. D* **93**, 072009 (2016), [arXiv:1512.03133 \[physics.ins-det\]](#) .
- [15] D. S. Akerib *et al.* (LUX), “Low-energy (0.7-74 keV) nuclear recoil calibration of the LUX dark matter experiment using D-D neutron scattering kinematics,” (2016), [arXiv:1608.05381 \[physics.ins-det\]](#) .
- [16] D. S. Akerib *et al.*, “Radiogenic and Muon-Induced Backgrounds in the LUX Dark Matter Detector,” *Astropart. Phys.* **62**, 33–46 (2015), [arXiv:1403.1299 \[astro-ph.IM\]](#) .
- [17] D. S. Akerib *et al.* (LUX Collaboration), “Improved Limits on Scattering of Weakly Interacting Massive Particles from Reanalysis of 2013 LUX Data,” *Phys. Rev. Lett.* **116**, 161301 (2016), [arXiv:1512.03506 \[astro-ph.CO\]](#) .
- [18] D. S. Akerib *et al.* (LUX Collaboration), “First results from the LUX dark matter experiment at the Sanford Underground Research Facility,” *Phys. Rev. Lett.* **112**, 091303 (2014), [arXiv:1310.8214 \[astro-ph.CO\]](#) .
- [19] D. S. Akerib *et al.* (LUX), “3D Modeling of Electric Fields in the LUX Detector,” (2017), [arXiv:1709.00095 \[physics.ins-det\]](#) .
- [20] D. S. Akerib *et al.* (LUX), “Results from a search for dark matter in the complete LUX exposure,” *Phys. Rev. Lett.* **118**, 021303 (2017), [arXiv:1608.07648 \[astro-ph.CO\]](#) .
- [21] E. A. Bagnaschi *et al.*, “Supersymmetric Dark Matter after LHC Run 1,” *Eur. Phys. J.* **C75**, 500 (2015), [arXiv:1508.01173 \[hep-ph\]](#) .
- [22] G. J. Feldman and R. D. Cousins, “A Unified approach to the classical statistical analysis of small signals,” *Phys. Rev. D* **57**, 3873–3889 (1998), [arXiv:physics/9711021 \[physics.data-an\]](#) .

- [23] K. Cranmer, “Practical Statistics for the LHC,” in *Proceedings, 2011 European School of High-Energy Physics (ESHEP 2011): Cheile Gradistei, Romania, September 7-20, 2011* (2015) pp. 267–308, [,247(2015)], [arXiv:1503.07622 \[physics.data-an\]](#) .
- [24] P. Klos, J. Menéndez, D. Gazit, and A. Schwenk, “Large-scale nuclear structure calculations for spin-dependent WIMP scattering with chiral effective field theory currents,” *Phys. Rev. D* **88**, 083516 (2013), [Erratum: Phys. Rev.D89,no.2,029901(2014)], [arXiv:1304.7684 \[nucl-th\]](#) .
- [25] D. S. Akerib *et al.* (LUX Collaboration), “Results on the Spin-Dependent Scattering of Weakly Interacting Massive Particles on Nucleons from the Run 3 Data of the LUX Experiment,” *Phys. Rev. Lett.* **116**, 161302 (2016), [arXiv:1602.03489 \[astro-ph.CO\]](#) .
- [26] E. Aprile *et al.* (XENON100), “Limits on spin-dependent WIMP-nucleon cross sections from 225 live days of XENON100 data,” *Phys. Rev. Lett.* **111**, 021301 (2013), [arXiv:1301.6620 \[astro-ph.CO\]](#) .
- [27] C. Fu *et al.* (PandaX-II), “Spin-Dependent Weakly-Interacting-Massive-Particle–Nucleon Cross Section Limits from First Data of PandaX-II Experiment,” *Phys. Rev. Lett.* **118**, 071301 (2017), [arXiv:1611.06553 \[hep-ex\]](#) .
- [28] A. M. Sirunyan *et al.* (CMS), “Search for dark matter produced with an energetic jet or a hadronically decaying W or Z boson at  $\sqrt{s} = 13$  TeV,” (2017), [arXiv:1703.01651 \[hep-ex\]](#) .
- [29] M. Aaboud *et al.* (ATLAS), “Search for dark matter at  $\sqrt{s} = 13$  TeV in final states containing an energetic photon and large missing transverse momentum with the ATLAS detector,” (2017), [arXiv:1704.03848 \[hep-ex\]](#) .
- [30] P. Athron *et al.* (GAMBIT), “A global fit of the MSSM with GAMBIT,” (2017), [arXiv:1705.07917 \[hep-ph\]](#) .
- [31] C. Strege, G. Bertone, G. J. Besjes, S. Caron, R. Ruiz de Austri, A. Strubig, and R. Trotta, “Profile likelihood maps of a 15-dimensional MSSM,” *JHEP* **09**, 081 (2014), [arXiv:1405.0622 \[hep-ph\]](#) .
- [32] C. Savage, G. Gelmini, P. Gondolo, and K. Freese, “Compatibility of DAMA/LIBRA dark matter detection with other searches,” *J. Cosmol. Astropart. Phys.* **0904**, 010 (2009), [arXiv:0808.3607 \[astro-ph\]](#) .
- [33] C. Amole *et al.* (PICO), “Improved dark matter search results from PICO-2L Run 2,” *Phys. Rev. D* **93**, 061101 (2016), [arXiv:1601.03729 \[astro-ph.CO\]](#) .

- [34] C. Amole *et al.* (PICO), “Dark Matter Search Results from the PICO-60 C<sub>3</sub>F<sub>8</sub> Bubble Chamber,” *Phys. Rev. Lett.* **118**, 251301 (2017), [arXiv:1702.07666 \[astro-ph.CO\]](#) .
- [35] K. Choi *et al.* (Super-Kamiokande), “Search for neutrinos from annihilation of captured low-mass dark matter particles in the Sun by Super-Kamiokande,” *Phys. Rev. Lett.* **114**, 141301 (2015), [arXiv:1503.04858 \[hep-ex\]](#) .
- [36] M. G. Aartsen *et al.* (IceCube), “Search for annihilating dark matter in the Sun with 3 years of IceCube data,” *Eur. Phys. J. C* **77**, 146 (2017), [arXiv:1612.05949 \[astro-ph.HE\]](#) .
- [37] M. Chala, F. Kahlhoefer, M. McCullough, G. Nardini, and K. Schmidt-Hoberg, “Constraining Dark Sectors with Monojets and Dijets,” *JHEP* **07**, 089 (2015), [arXiv:1503.05916 \[hep-ph\]](#) .
- [38] D. S. Akerib *et al.* (LUX), “Limits on spin-dependent WIMP-nucleon cross section obtained from the complete LUX exposure,” *Phys. Rev. Lett.* **118**, 251302 (2017), [arXiv:1705.03380 \[astro-ph.CO\]](#) .
- [39] F. D’Eramo, B. J. Kavanagh, and P. Panci, “You can hide but you have to run: direct detection with vector mediators,” *JHEP* **08**, 111 (2016), [arXiv:1605.04917 \[hep-ph\]](#) .
- [40] C. Savage, K. Freese, and P. Gondolo, “Annual Modulation of Dark Matter in the Presence of Streams,” *Phys. Rev. D* **74**, 043531 (2006), [arXiv:astro-ph/0607121 \[astro-ph\]](#) .
- [41] J. Mock, *LuxDB00000489: Run4 libNEST models*, Tech. Rep. (2016).
- [42] J. H. Oort, “The force exerted by the stellar system in the direction perpendicular to the galactic plane and some related problems,” *Bulletin of the Astronomical Institutes of the Netherlands* **6**, 249 (1932).
- [43] F. Zwicky, “Die Rotverschiebung von extragalaktischen Nebeln,” *Helvetica Physica Acta* **6**, 110–127 (1933).
- [44] S. van den Bergh, “The Early history of dark matter,” *Publ. Astron. Soc. Pac.* **111**, 657 (1999), [arXiv:astro-ph/9904251 \[astro-ph\]](#) .
- [45] V. C. Rubin and W. K. Ford, Jr., “Rotation of the Andromeda Nebula from a Spectroscopic Survey of Emission Regions,” *Astrophys. J.* **159**, 379 (1970).
- [46] V. C. Rubin, W. K. Ford, Jr., N. Thonnard, and D. Burstein, “Rotational properties of 23 SB galaxies,” *Astrophys. J.* **261**, 439–456 (1982).

## BIBLIOGRAPHY

---

- [47] M. Milgrom, “A Modification of the Newtonian dynamics as a possible alternative to the hidden mass hypothesis,” *Astrophys. J.* **270**, 365–370 (1983).
- [48] A. G. Riess *et al.* (Supernova Search Team), “Observational evidence from supernovae for an accelerating universe and a cosmological constant,” *Astron. J.* **116**, 1009–1038 (1998), [arXiv:astro-ph/9805201 \[astro-ph\]](#) .
- [49] S. Perlmutter *et al.* (Supernova Cosmology Project), “Measurements of Omega and Lambda from 42 high redshift supernovae,” *Astrophys. J.* **517**, 565–586 (1999), [arXiv:astro-ph/9812133 \[astro-ph\]](#) .
- [50] P. J. E. Peebles, “Recombination of the Primeval Plasma,” *Astrophys. J.* **153**, 1 (1968).
- [51] Y. B. Zeldovich and R. A. Sunyaev, “The interaction of matter and radiation in a hot-model universe,” *Astrophysics and Space Science* **4**, 301–316 (1969).
- [52] D. J. Fixsen, “The Temperature of the Cosmic Microwave Background,” *Astrophys. J.* **707**, 916–920 (2009), [arXiv:0911.1955](#) .
- [53] W. Hu and S. Dodelson, “Cosmic microwave background anisotropies,” *Ann. Rev. Astron. Astrophys.* **40**, 171–216 (2002), [arXiv:astro-ph/0110414 \[astro-ph\]](#) .
- [54] T. M. C. Abbott *et al.* (DES), “Dark Energy Survey Year 1 Results: Cosmological Constraints from Galaxy Clustering and Weak Lensing,” (2017), [arXiv:1708.01530 \[astro-ph.CO\]](#) .
- [55] G. Arcadi, M. Dutra, P. Ghosh, M. Lindner, Y. Mambrini, M. Pierre, S. Profumo, and F. S. Queiroz, “The Waning of the WIMP? A Review of Models, Searches, and Constraints,” (2017), [arXiv:1703.07364 \[hep-ph\]](#) .
- [56] P. Tisserand *et al.* (EROS-2), “Limits on the Macho Content of the Galactic Halo from the EROS-2 Survey of the Magellanic Clouds,” *Astron. Astrophys.* **469**, 387–404 (2007), [arXiv:astro-ph/0607207 \[astro-ph\]](#) .
- [57] B. P. Abbott *et al.* (Virgo, LIGO Scientific), “Observation of Gravitational Waves from a Binary Black Hole Merger,” *Phys. Rev. Lett.* **116**, 061102 (2016), [arXiv:1602.03837 \[gr-qc\]](#) .
- [58] B. Carr, F. Kuhnel, and M. Sandstad, “Primordial Black Holes as Dark Matter,” *Phys. Rev. D* **94**, 083504 (2016), [arXiv:1607.06077 \[astro-ph.CO\]](#) .
- [59] R. Panek, “The father of dark matter.” *Discover* **30**, 80 – 87 (2009).
- [60] S. Scoles, “How Vera Rubin discovered dark matter.” *Astronomy* **44**, 26 – 31 (2016).

- [61] R. Bernabei *et al.*, “Final model independent result of DAMA/LIBRA-phase1,” *Eur. Phys. J. C* **73**, 2648 (2013), [arXiv:1308.5109 \[astro-ph.GA\]](#) .
- [62] E. Barbosa de Souza *et al.* (DM-Ice), “First search for a dark matter annual modulation signal with NaI(Tl) in the Southern Hemisphere by DM-Ice17,” *Phys. Rev. D* **95**, 032006 (2017), [arXiv:1602.05939 \[physics.ins-det\]](#) .
- [63] J. Amaré *et al.*, “The ANAIS Dark Matter Project: Status and Prospects,” in *14th Marcel Grossmann Meeting on Recent Developments in Theoretical and Experimental General Relativity, Astrophysics, and Relativistic Field Theories (MG14) Rome, Italy, July 12-18, 2015* (2016) [arXiv:1601.01184 \[astro-ph.IM\]](#) .
- [64] J. M. Gaskins, “A review of indirect searches for particle dark matter,” *Contemp. Phys.* **57**, 496–525 (2016), [arXiv:1604.00014 \[astro-ph.HE\]](#) .
- [65] L. Baudis, G. Kessler, P. Klos, R. F. Lang, J. Menéndez, S. Reichard, and A. Schwenk, “Signatures of Dark Matter Scattering Inelastically Off Nuclei,” *Phys. Rev. D* **88**, 115014 (2013), [arXiv:1309.0825 \[astro-ph.CO\]](#) .
- [66] D. Tucker-Smith and N. Weiner, “Inelastic dark matter,” *Phys. Rev. D* **64**, 043502 (2001), [arXiv:hep-ph/0101138 \[hep-ph\]](#) .
- [67] M. W. Goodman and E. Witten, “Detectability of Certain Dark Matter Candidates,” *Phys. Rev. D* **31**, 3059 (1985).
- [68] W. Guo and D. N. McKinsey, “Concept for a dark matter detector using liquid helium-4,” *Phys. Rev. D* **87**, 115001 (2013), [arXiv:1302.0534 \[astro-ph.IM\]](#) .
- [69] P. J. Fox and E. Poppitz, “Leptophilic Dark Matter,” *Phys. Rev. D* **79**, 083528 (2009), [arXiv:0811.0399 \[hep-ph\]](#) .
- [70] J. Kopp, V. Niro, T. Schwetz, and J. Zupan, “DAMA/LIBRA and leptonically interacting Dark Matter,” *Phys. Rev. D* **80**, 083502 (2009), [arXiv:0907.3159 \[hep-ph\]](#) .
- [71] R. Essig, J. Mardon, and T. Volansky, “Direct Detection of Sub-GeV Dark Matter,” *Phys. Rev. D* **85**, 076007 (2012), [arXiv:1108.5383 \[hep-ph\]](#) .
- [72] R. Essig, M. Fernandez-Serra, J. Mardon, A. Soto, T. Volansky, and T.-T. Yu, “Direct Detection of sub-GeV Dark Matter with Semiconductor Targets,” *JHEP* **05**, 046 (2016), [arXiv:1509.01598 \[hep-ph\]](#) .
- [73] S. Derenzo, R. Essig, A. Massari, A. Soto, and T.-T. Yu, “Direct Detection of sub-GeV Dark Matter with Scintillating Targets,” *Phys. Rev. D* **96**, 016026 (2017), [arXiv:1607.01009 \[hep-ph\]](#) .

- [74] A. K. Drukier, K. Freese, and D. N. Spergel, “Detecting Cold Dark Matter Candidates,” *Phys. Rev. D* **33**, 3495–3508 (1986).
- [75] K. Freese, J. A. Frieman, and A. Gould, “Signal Modulation in Cold Dark Matter Detection,” *Phys. Rev. D* **37**, 3388–3405 (1988).
- [76] D. Lynden-Bell, “Statistical mechanics of violent relaxation in stellar systems,” *Monthly Notices of the Royal Astronomical Society* **136**, 101–121 (1967).
- [77] J. Herzog-Arbeitman, M. Lisanti, and L. Necib, “The Metal-Poor Stellar Halo in RAVE-TGAS and its Implications for the Velocity Distribution of Dark Matter,” (2017), [arXiv:1708.03635 \[astro-ph.GA\]](#) .
- [78] J. D. Lewin and P. F. Smith, “Review of mathematics, numerical factors, and corrections for dark matter experiments based on elastic nuclear recoil,” *Astropart. Phys.* **6**, 87–112 (1996).
- [79] C. McCabe, “The Earth’s velocity for direct detection experiments,” *J. Cosmol. Astropart. Phys.* **1402**, 027 (2014), [arXiv:1312.1355 \[astro-ph.CO\]](#) .
- [80] R. H. Helm, “Inelastic and Elastic Scattering of 187-Mev Electrons from Selected Even-Even Nuclei,” *Phys. Rev.* **104**, 1466–1475 (1956).
- [81] J. Engel, “Nuclear form-factors for the scattering of weakly interacting massive particles,” *Phys. Lett. B* **264**, 114–119 (1991).
- [82] G. Duda, A. Kemper, and P. Gondolo, “Model Independent Form Factors for Spin Independent Neutralino-Nucleon Scattering from Elastic Electron Scattering Data,” *J. Cosmol. Astropart. Phys.* **0704**, 012 (2007), [arXiv:hep-ph/0608035 \[hep-ph\]](#) .
- [83] J. Engel, S. Pittel, and P. Vogel, “Nuclear physics of dark matter detection,” *Int. J. Mod. Phys. E***1**, 1–37 (1992).
- [84] J. Goodman, M. Ibe, A. Rajaraman, W. Shepherd, T. M. P. Tait, and H.-B. Yu, “Constraints on Dark Matter from Colliders,” *Phys. Rev. D* **82**, 116010 (2010), [arXiv:1008.1783 \[hep-ph\]](#) .
- [85] A. Rajaraman, W. Shepherd, T. M. P. Tait, and A. M. Wijangco, “LHC Bounds on Interactions of Dark Matter,” *Phys. Rev. D* **84**, 095013 (2011), [arXiv:1108.1196 \[hep-ph\]](#) .
- [86] G. Busoni *et al.*, “Recommendations on presenting LHC searches for missing transverse energy signals using simplified  $s$ -channel models of dark matter,” (2016), [arXiv:1603.04156 \[hep-ex\]](#) .

- [87] A. L. Fitzpatrick, W. Haxton, E. Katz, N. Lubbers, and Y. Xu, “The Effective Field Theory of Dark Matter Direct Detection,” *JCAP* **1302**, 004 (2013), [arXiv:1203.3542 \[hep-ph\]](#) .
- [88] C. Arina, E. Del Nobile, and P. Panci, “Dark Matter with Pseudoscalar-Mediated Interactions Explains the DAMA Signal and the Galactic Center Excess,” *Phys. Rev. Lett.* **114**, 011301 (2015), [arXiv:1406.5542 \[hep-ph\]](#) .
- [89] S. Scopel, K.-H. Yoon, and J.-H. Yoon, “Generalized spin-dependent WIMP-nucleus interactions and the DAMA modulation effect,” *JCAP* **1507**, 041 (2015), [arXiv:1505.01926 \[astro-ph.CO\]](#) .
- [90] R. Catena, A. Ibarra, and S. Wild, “DAMA confronts null searches in the effective theory of dark matter-nucleon interactions,” *JCAP* **1605**, 039 (2016), [arXiv:1602.04074 \[hep-ph\]](#) .
- [91] A. Rubbia, “ArDM: A Ton-scale liquid Argon experiment for direct detection of dark matter in the universe,” *TAUP 2005. Proceedings, 9th International Conference on topics in astroparticle and underground physics, Zaragoza, September 10, 2005*, *J. Phys. Conf. Ser.* **39**, 129–132 (2006), [arXiv:hep-ph/0510320 \[hep-ph\]](#) .
- [92] P. Agnes *et al.* (DarkSide), “Results from the first use of low radioactivity argon in a dark matter search,” *Phys. Rev. D* **93**, 081101 (2016), [Addendum: *Phys. Rev. D* 95, no.6, 069901 (2017)], [arXiv:1510.00702 \[astro-ph.CO\]](#) .
- [93] D. R. Nygren, “The Time Projection Chamber: A New 4 pi Detector for Charged Particles,” *1974 PEP summer study*, eConf **C740805**, 58 (1974).
- [94] J. Mock, N. Barry, K. Kazkaz, M. Szydagis, M. Tripathi, S. Uvarov, M. Woods, and N. Walsh, “Modeling Pulse Characteristics in Xenon with NEST,” *JINST* **9**, T04002 (2014), [arXiv:1310.1117 \[physics.ins-det\]](#) .
- [95] T. Takahashi, S. Konno, T. Hamada, M. Miyajima, S. Kubota, A. Nakamoto, A. Hitachi, E. Shibamura, and T. Doke, “Average energy expended per ion pair in liquid xenon,” *Phys. Rev. A* **12**, 1771–1775 (1975).
- [96] C. E. Dahl, *The physics of background discrimination in liquid xenon, and first results from Xenon10 in the hunt for WIMP dark matter*, Ph.D. thesis, Princeton University (2009).
- [97] J. Lindhard *et al.*, *Matt. Fys. Medd. Dan. Vid. Selsk* **33**, 10 (1963).
- [98] T. Doke, A. Hitachi, J. Kikuchi, K. Masuda, H. Okada, and E. Shibamura, “Absolute scintillation yields in liquid argon and xenon for various particles,” *Japanese Journal of Applied Physics* **41**, 1538 (2002).

## BIBLIOGRAPHY

---

- [99] B. Lenardo, K. Kazkaz, A. Manalaysay, J. Mock, M. Szydagis, and M. Tripathi, “A Global Analysis of Light and Charge Yields in Liquid Xenon,” *IEEE Trans. Nuc. Sci.* **62**, 3387–3396 (2015), [arXiv:1412.4417 \[astro-ph.IM\]](#) .
- [100] J. Thomas and D. A. Imel, “Recombination of electron-ion pairs in liquid argon and liquid xenon,” *Phys. Rev. A* **36**, 614–616 (1987).
- [101] A. Dobi, *Measurement of the Electron Recoil Band of the LUX Dark Matter Detector With a Tritium Calibration Source*, Ph.D. thesis, Maryland U., College Park (2014).
- [102] E. Aprile and T. Doke, “Liquid Xenon Detectors for Particle Physics and Astrophysics,” *Rev. Mod. Phys.* **82**, 2053–2097 (2010), [arXiv:0910.4956 \[physics.ins-det\]](#) .
- [103] E. Pease, *Rare-event searches in liquid xenon with the LUX and LUX-ZEPLIN detectors*, Ph.D. thesis, Yale University (2017).
- [104] E. Aprile, C. E. Dahl, L. DeViveiros, R. Gaitskell, K. L. Giboni, J. Kwong, P. Majewski, K. Ni, T. Shutt, and M. Yamashita, “Simultaneous measurement of ionization and scintillation from nuclear recoils in liquid xenon as target for a dark matter experiment,” *Phys. Rev. Lett.* **97**, 081302 (2006), [arXiv:astro-ph/0601552 \[astro-ph\]](#) .
- [105] D. M. Mei, Z. B. Yin, L. C. Stonehill, and A. Hime, “A Model of Nuclear Recoil Scintillation Efficiency in Noble Liquids,” *Astropart. Phys.* **30**, 12–17 (2008), [arXiv:0712.2470 \[nucl-ex\]](#) .
- [106] R. Davis, Jr., D. S. Harmer, and K. C. Hoffman, “Search for neutrinos from the sun,” *Phys. Rev. Lett.* **20**, 1205–1209 (1968).
- [107] D. S. Akerib *et al.* (LUX Collaboration), “Radio-assay of Titanium samples for the LUX Experiment,” (2011), [arXiv:1112.1376](#) .
- [108] D. S. Akerib *et al.* (LUX), “Chromatographic separation of radioactive noble gases from xenon,” (2016), [arXiv:1605.03844 \[physics.ins-det\]](#) .
- [109] D. S. Akerib *et al.* (LUX Collaboration), “The LUX Prototype Detector: Heat Exchanger Development,” *Nucl. Instrum. Meth. A* **709**, 29 (2013).
- [110] A. Dobi, C. G. Davis, C. Hall, T. Langford, S. Slutsky, and Y.-R. Yen, “Detection of krypton in xenon for dark matter applications,” *Nucl. Instrum. Meth. A* **665**, 1–6 (2011), [arXiv:1103.2714 \[astro-ph.IM\]](#) .
- [111] A. Dobi *et al.*, “Xenon purity analysis for EXO-200 via mass spectrometry,” *Nucl. Instrum. Meth. A* **675**, 40–46 (2012), [arXiv:1109.1046 \[physics.ins-det\]](#) .

- [112] R. Mannino, *Measuring backgrounds from  $^{85}\text{Kr}$  and  $^{210}\text{Bi}$  to improve sensitivity of dark matter detectors*, Ph.D. thesis, Texas A&M University (2017).
- [113] C. H. Faham, *Prototype, Surface Commissioning and Photomultiplier Tube Characterization for the Large Underground Xenon (LUX) Direct Dark Matter Search Experiment*, Ph.D. thesis, Brown University (2014).
- [114] C. H. Faham *et al.*, “Measurements of wavelength-dependent double photoelectron emission from single photons in VUV-sensitive photomultiplier tubes,” (2015), [arXiv:1506.08748 \[physics.ins-det\]](#) .
- [115] D. S. Akerib *et al.* (LUX Collaboration), “Data Acquisition and Readout System for the LUX Dark Matter Experiment,” *Nucl. Instrum. Meth. A* **668**, 1–8 (2012), [arXiv:1108.1836 \[astro-ph.IM\]](#) .
- [116] E. F. Druszkiewicz, *Digital Advances in Triggering and Data Acquisition Systems for Large Scale Dark Matter Search Experiments*, Ph.D. thesis, University of Rochester (2017).
- [117] V. N. Solovov *et al.*, “Position Reconstruction in a Dual Phase Xenon Scintillation Detector,” *IEEE Trans. Nuc. Sci.* **59**, 3286–3293 (2012), [arXiv:1112.1481 \[physics.ins-det\]](#) .
- [118] S. Agostinelli *et al.* (GEANT4), “GEANT4: A Simulation toolkit,” *Nucl. Instrum. Meth. A* **506**, 250–303 (2003).
- [119] D. S. Akerib *et al.*, “LUXSim: A Component-Centric Approach to Low-Background Simulations,” *Nucl. Instrum. Meth. A* **675**, 63–77 (2012), [arXiv:1111.2074 \[physics.data-an\]](#) .
- [120] C. Lee, *Mitigation of Backgrounds for the Large Underground Xenon Dark Matter Experiment*, Ph.D. thesis, Case Western Reserve University (2015).
- [121] D. Mei and A. Hime, “Muon-induced background study for underground laboratories,” *Phys. Rev. D* **73**, 053004 (2006), [arXiv:astro-ph/0512125 \[astro-ph\]](#) .
- [122] C. Patrignani *et al.* (Particle Data Group), “Review of Particle Physics,” *Chin. Phys.* **C40**, 100001 (2016).
- [123] D. E. Groom, N. V. Mokhov, and S. I. Striganov, “Muon stopping power and range tables 10-MeV to 100-TeV,” *Atom. Data Nucl. Data Tabl.* **78**, 183–356 (2001).
- [124] A. Lindote, H. M. Araujo, V. A. Kudryavtsev, and M. Robinson, “Simulation of neutrons produced by high-energy muons underground,” *Astropart. Phys.* **31**, 366–375 (2009), [arXiv:0810.1682 \[hep-ex\]](#) .

- [125] F. Halzen and S. R. Klein, “IceCube: An Instrument for Neutrino Astronomy,” *Rev. Sci. Instrum.* **81**, 081101 (2010), [arXiv:1007.1247 \[astro-ph.HE\]](#) .
- [126] I. M. Frank and I. E. Tamm, “Coherent visible radiation of fast electrons passing through matter,” *Compt. Rend. Acad. Sci. URSS* **14**, 109–114 (1937), [*Usp. Fiz. Nauk*93,no.2,388(1967)].
- [127] Y. Fukuda *et al.* (Super-Kamiokande), “The Super-Kamiokande detector,” *Advanced computing and analysis techniques in physics research. Proceedings, 8th International Workshop, ACAT 2002, Moscow, Russia, June 24-28, 2002*, *Nucl. Instrum. Meth. A* **501**, 418–462 (2003).
- [128] T. S. Light, “Temperature dependence and measurement of resistivity of pure water,” *Analytical Chemistry* **56**, 1138–1142 (1984), <http://dx.doi.org/10.1021/ac00271a019> .
- [129] M. Hanhardt, *Water Shield PMT Characterization and Muon Flux Surface Measurement for LUX Dark Matter Search*, Master’s thesis, South Dakota School of Mines and Technology (2011).
- [130] E. Aprile *et al.* (XENON), “First Dark Matter Search Results from the XENON1T Experiment,” *Phys. Rev. Lett.* **119**, 181301 (2017), [arXiv:1705.06655 \[astro-ph.CO\]](#) .
- [131] X. Cui *et al.* (PandaX-II), “Dark Matter Results From 54-Ton-Day Exposure of PandaX-II Experiment,” *Phys. Rev. Lett.* **119**, 181302 (2017), [arXiv:1708.06917 \[astro-ph.CO\]](#) .
- [132] J. Angle *et al.* (XENON10), “A search for light dark matter in XENON10 data,” *Phys. Rev. Lett.* **107**, 051301 (2011), [Erratum: *Phys. Rev. Lett.*110,249901(2013)], [arXiv:1104.3088 \[astro-ph.CO\]](#) .
- [133] P. Sorensen and K. Kamdin, “Evidence for metastable excimer states as the source of electron train backgrounds in liquid xenon emission detectors,” (2017), [arXiv:1711.07025 \[physics.ins-det\]](#) .
- [134] F. Bezrukov, F. Kahlhoefer, M. Lindner, F. Kahlhoefer, and M. Lindner, “Interplay between scintillation and ionization in liquid xenon Dark Matter searches,” *Astropart. Phys.* **35**, 119–127 (2011), [arXiv:1011.3990 \[astro-ph.IM\]](#) .
- [135] Y. Mei, *Direct Dark Matter Search with the XENON100 Experiment*, Ph.D. thesis, Rice University (2011).
- [136] G.-J. Zhang, K. Yang, W.-B. Zhao, and Z. Yan, “On the surface trapping parameters of polytetrafluoroethylene block,” *Applied Surface Science* **253**, 1995–1998 (2006).

## BIBLIOGRAPHY

---

- [137] R. Kressmann, G. M. Sessler, and P. Gunther, “Space-charge electrets,” *IEEE Transactions on Dielectrics and Electrical Insulation* **3**, 607–623 (1996).
- [138] “COMSOL Multiphysics<sup>®</sup>,” <http://www.comsol.com>.
- [139] R. Knoche, *Signal corrections and calibrations in the LUX dark matter detector*, Ph.D. thesis, University of Maryland (2016).
- [140] M. Szydagis, A. Fyhrie, D. Thorngren, and M. Tripathi, “Enhancement of nest capabilities for simulating low-energy recoils in liquid xenon,” *JINST* **8**, C10003 (2013).
- [141] J. Neyman, “Outline of a Theory of Statistical Estimation Based on the Classical Theory of Probability,” *Phil. Trans. Roy. Soc. Lond.* **A236**, 333–380 (1937).
- [142] W. A. Rolke, A. M. Lopez, and J. Conrad, “Limits and confidence intervals in the presence of nuisance parameters,” *Nucl. Instrum. Meth. A* **551**, 493–503 (2005), [arXiv:physics/0403059](https://arxiv.org/abs/physics/0403059) [physics] .
- [143] J. Neyman and E. S. Pearson, “On the Problem of the Most Efficient Tests of Statistical Hypotheses,” *Philosophical Transactions of the Royal Society of London Series A* **231**, 289–337 (1933).
- [144] A. L. Read, “Modified frequentist analysis of search results (The CL(s) method),” in *Workshop on confidence limits, CERN, Geneva, Switzerland, 17-18 Jan 2000: Proceedings* (2000) pp. 81–101.
- [145] G. Cowan, K. Cranmer, E. Gross, and O. Vitells, “Power-Constrained Limits,” (2011), [arXiv:1105.3166](https://arxiv.org/abs/1105.3166) [physics.data-an] .
- [146] G. Cowan, K. Cranmer, E. Gross, and O. Vitells, “Asymptotic formulae for likelihood-based tests of new physics,” *Eur. Phys. J. C* **71**, 1554 (2011), [Erratum: *Eur. Phys. J. C* **73**, 2501(2013)], [arXiv:1007.1727](https://arxiv.org/abs/1007.1727) [physics.data-an] .
- [147] C.-S. CHUANG and T. L. LAI, “Resampling methods for confidence intervals in group sequential trials,” *Biometrika* **85**, 317–332 (1998).
- [148] C.-S. Chuang and T. L. Lai, “Hybrid resampling methods for confidence intervals,” *Statistica Sinica* **10**, 1–33 (2000).
- [149] B. Sen, M. Walker, and M. Woodroffe, “On the unified method with nuisance parameters,” *Statistica Sinica* **19**, 301–314 (2009).
- [150] G. Servant and T. M. P. Tait, “Is the lightest Kaluza-Klein particle a viable dark matter candidate?” *Nucl. Phys.* **B650**, 391–419 (2003), [arXiv:hep-ph/0206071](https://arxiv.org/abs/hep-ph/0206071) [hep-ph] .

- [151] A. Birkedal, A. Noble, M. Perelstein, and A. Spray, “Little Higgs dark matter,” *Phys. Rev. D* **74**, 035002 (2006), [arXiv:hep-ph/0603077 \[hep-ph\]](#) .
- [152] L. Kastens *et al.*, “Calibration of a liquid xenon detector with  $^{83}\text{Kr}^m$ ,” *Phys. Rev. C* **80**, 045809 (2009).
- [153] L. W. Kastens, S. Bedikian, S. B. Cahn, A. Manzur, and D. N. McKinsey, “A 83 kr m source for use in low-background liquid xenon time projection chambers,” *JINST* **5**, P05006 (2010).
- [154] A. Manalaysay, T. M. Undagoitia, A. Askin, L. Baudis, A. Behrens, *et al.*, “Spatially uniform calibration of a liquid xenon detector at low energies using 83m-Kr,” *Rev. Sci. Instrum.* **81**, 073303 (2010), [arXiv:0908.0616 \[astro-ph.IM\]](#) .
- [155] J. R. Verbus *et al.*, “Proposed low-energy absolute calibration of nuclear recoils in a dual-phase noble element TPC using D-D neutron scattering kinematics,” *Nucl. Instrum. Meth. A* **851**, 68–81 (2017), [arXiv:1608.05309 \[physics.ins-det\]](#) .
- [156] D. R. Tovey, R. J. Gaitskell, P. Gondolo, Y. A. Ramachers, and L. Roszkowski, “A New model independent method for extracting spin dependent (cross-section) limits from dark matter searches,” *Phys. Lett. B* **488**, 17–26 (2000), [arXiv:hep-ph/0005041 \[hep-ph\]](#) .
- [157] A. Bailey, *Dark matter searches and study of electrode design in LUX and LZ*, Ph.D. thesis, Imperial College London (2016).
- [158] *Procedure for the LHC Higgs boson search combination in Summer 2011*, Tech. Rep. CMS-NOTE-2011-005. ATL-PHYS-PUB-2011-11 (CERN, Geneva, 2011).
- [159] L. Moneta, K. Cranmer, G. Schott, and W. Verkerke (2010) p. 57, [arXiv:1009.1003 \[physics.data-an\]](#) .
- [160] O. Buchmueller, M. J. Dolan, S. A. Malik, and C. McCabe, “Characterising dark matter searches at colliders and direct detection experiments: Vector mediators,” *JHEP* **01**, 037 (2015), [arXiv:1407.8257 \[hep-ph\]](#) .
- [161] L. Bergstrom and P. Gondolo, “Limits on direct detection of neutralino dark matter from  $b \rightarrow s$  gamma decays,” *Astropart. Phys.* **5**, 263–278 (1996), [arXiv:hep-ph/9510252 \[hep-ph\]](#) .
- [162] P. Athron *et al.* (GAMBIT), “GAMBIT: The Global and Modular Beyond-the-Standard-Model Inference Tool,” (2017), [arXiv:1705.07908 \[hep-ph\]](#) .
- [163] P. Athron *et al.* (GAMBIT), “Global fits of GUT-scale SUSY models with GAMBIT,” (2017), [arXiv:1705.07935 \[hep-ph\]](#) .

- [164] T. G. D. M. Workgroup *et al.*, “DarkBit: A GAMBIT module for computing dark matter observables and likelihoods,” (2017), [arXiv:1705.07920 \[hep-ph\]](#) .
- [165] T. G. M. Workgroup *et al.*, “SpecBit, DecayBit and PrecisionBit: GAMBIT modules for computing mass spectra, particle decay rates and precision observables,” (2017), [arXiv:1705.07936 \[hep-ph\]](#) .
- [166] A. Tan *et al.* (PandaX-II), “Dark Matter Results from First 98.7 Days of Data from the PandaX-II Experiment,” *Phys. Rev. Lett.* **117**, 121303 (2016), [arXiv:1607.07400 \[hep-ex\]](#) .
- [167] A. Crivellin, F. D’Eramo, and M. Procura, “New Constraints on Dark Matter Effective Theories from Standard Model Loops,” *Phys. Rev. Lett.* **112**, 191304 (2014), [arXiv:1402.1173 \[hep-ph\]](#) .
- [168] F. D’Eramo and M. Procura, “Connecting Dark Matter UV Complete Models to Direct Detection Rates via Effective Field Theory,” *JHEP* **04**, 054 (2015), [arXiv:1411.3342 \[hep-ph\]](#) .
- [169] F. Giuliani and T. A. Girard, “Model-independent limits from spin-dependent WIMP dark matter experiments,” *Phys. Rev. D* **71**, 123503 (2005), [arXiv:hep-ph/0502232 \[hep-ph\]](#) .
- [170] C. McCabe, private communication.
- [171] J. Beringer *et al.* (Particle Data Group), “Review of Particle Physics (RPP),” *Phys. Rev. D* **86**, 010001 (2012).
- [172] E. S. Ageev *et al.* (COMPASS), “Spin asymmetry  $A_1(d)$  and the spin-dependent structure function  $g_1(d)$  of the deuteron at low values of  $x$  and  $Q^{*2}$ ,” *Phys. Lett. B* **647**, 330–340 (2007), [arXiv:hep-ex/0701014 \[hep-ex\]](#) .
- [173] A. Airapetian *et al.* (HERMES), “Precise determination of the spin structure function  $g(1)$  of the proton, deuteron and neutron,” *Phys. Rev. D* **75**, 012007 (2007), [arXiv:hep-ex/0609039 \[hep-ex\]](#) .
- [174] G. Arcadi, Y. Mambrini, and F. Richard, “Z-portal dark matter,” *JCAP* **1503**, 018 (2015), [arXiv:1411.2985 \[hep-ph\]](#) .
- [175] M. Escudero, A. Berlin, D. Hooper, and M.-X. Lin, “Toward (Finally!) Ruling Out Z and Higgs Mediated Dark Matter Models,” *JCAP* **1612**, 029 (2016), [arXiv:1609.09079 \[hep-ph\]](#) .
- [176] J. Kearney, N. Orlofsky, and A. Pierce, “Z boson mediated dark matter beyond the effective theory,” *Phys. Rev. D* **95**, 035020 (2017), [arXiv:1611.05048 \[hep-ph\]](#) .
- [177] G. Gelmini and P. Gondolo, “DM Production Mechanisms,” (2010), [arXiv:1009.3690 \[astro-ph.CO\]](#) .